

AWARD NUMBER: W81XWH-10-1-1036

TITLE: *Simulation of Blast Loading on an Ultrastructurally-based Computational Model of the Ocular Lens*

PRINCIPAL INVESTIGATOR: Richard A. Regueiro, Ph.D.

CONTRACTING ORGANIZATION:  
Regents of the University of Colorado  
Boulder, CO 80309

REPORT DATE: October 2012

TYPE OF REPORT: Cnnual

PREPARED FOR:  
U.S. Army Medical Research and Materiel Command  
Fort Detrick, Maryland 21702-5012

DISTRIBUTION STATEMENT:  
Approved for public release; distribution unlimited

The views, opinions and/or findings contained in this report are those of the author(s) and should not be construed as an official Department of the Army position, policy or decision unless so designated by other documentation

REPORT DOCUMENTATION PAGE				Form Approved OMB No. 0704-0188	
Public reporting burden for this collection of information is estimated to average 1 hour per response, including the time for reviewing instructions, searching existing data sources, gathering and maintaining the data needed, and completing and reviewing this collection of information. Send comments regarding this burden estimate or any other aspect of this collection of information, including suggestions for reducing this burden to Department of Defense, Washington Headquarters Services, Directorate for Information Operations and Reports (0704-0188), 1215 Jefferson Davis Highway, Suite 1204, Arlington, VA 22202-4302. Respondents should be aware that notwithstanding any other provision of law, no person shall be subject to any penalty for failing to comply with a collection of information if it does not display a currently valid OMB control number. PLEASE DO NOT RETURN YOUR FORM TO THE ABOVE ADDRESS.					
1. REPORT DATE (DD-MM-YYYY) 1 October 2012		2. REPORT TYPE Annual		3. DATES COVERED (From - To) Sept 30, 2011 to Sept 29, 2012	
4. TITLE AND SUBTITLE Simulation of Blast Loading on an Ultrastructurally-based Computational Model of the Ocular Lens				5a. CONTRACT NUMBER W81XWH-10-1-1036	
				5b. GRANT NUMBER	
				5c. PROGRAM ELEMENT NUMBER	
6. AUTHOR(S) Richard A. Regueiro  tlej ctf tgi wgtqB eqmtcf qQfw				5e. TASK NUMBER	
				5f. WORK UNIT NUMBER	
				8. PERFORMING ORGANIZATION REPORT NUMBER	
7. PERFORMING ORGANIZATION NAME(S) AND ADDRESS(ES) Regents of the University of Colorado Boulder, CO 80309-0001					
9. SPONSORING / MONITORING AGENCY NAME(S) AND ADDRESS(ES) U.S. Army Medical Research and Materiel Command Fort Detrick, Maryland 21702-5012				10. SPONSOR/MONITOR'S ACRONYM(S)	
				11. SPONSOR/MONITOR'S REPORT NUMBER(S)	
12. DISTRIBUTION / AVAILABILITY STATEMENT Approved for public release; distribution unlimited					
13. SUPPLEMENTARY NOTES					
14. ABSTRACT The report summarizes the research accomplishments during the second year of the project. Research focused on experimental tasks in support of the development of a multiscale finite element model to be used to simulate blast loading of ocular lenses. Smooth indent creep tests were conducted on porcine and human lens capsules. Potentially better images were obtained of type IV collagen meshwork ultrastructure via cryo-electron tomography. Confocal laser scanning microscopy was used to identify structure of the lens fiber cells. High strain rate compression (stress relaxation), impulse, and puncture tests were conducted on whole porcine lenses in Dr. Tusit Weerasooriya's laboratory at the Army Research Laboratory (ARL), Aberdeen Proving Ground (APG).					
15. SUBJECT TERMS ocular lens mechanical experiments, lens capsule ultrastructure, lens fiber cell ultrastructure, finite element analysis, high strain rate testing					
16. SECURITY CLASSIFICATION OF:			17. LIMITATION OF ABSTRACT	18. NUMBER OF PAGES 160	19a. NAME OF RESPONSIBLE PERSON
a. REPORT	b. ABSTRACT	c. THIS PAGE			19b. TELEPHONE NUMBER (include area code)

# Contents

<b>1</b>	<b>Introduction</b>	<b>1</b>
<b>2</b>	<b>Body</b>	<b>1</b>
<b>3</b>	<b>Key Research Accomplishments</b>	<b>11</b>
<b>4</b>	<b>Reportable Outcomes</b>	<b>11</b>
<b>5</b>	<b>Conclusion</b>	<b>11</b>
<b>A</b>	<b>Master of Science Thesis</b>	<b>ii</b>

# 1 Introduction

In the life of a combat soldier, traumatic cataract in ocular lenses may result from blast loading, whereby (i) the lens capsule (Fig.1) is perforated by intraocular foreign bodies (IOFBs [Walter, 1962, Mader et al., 1993, Parver et al., 1993, Wong et al., 1997, Mader et al., 2006, Weichel and Colyer, 2008]) which in turn damage the lens fiber cells, (ii) the lens is loaded fluid dynamically by the surrounding aqueous and vitreous humors [Banitt et al., 2009] (see Fig.1), and/or (iii) the lens internal substance (crystallins lens fiber cells) is stressed by the passing shock wave. Traumatic cataract can result in a partially or fully clouded lens, complete dislocation of the lens (floating between aqueous and vitreous humors, see Fig.1), or zonule rupture such that partial or full vision loss may occur. The mechanisms of traumatic cataract formation that may require cataract surgery (implantation of an intraocular lens (IOL)) are not well understood in comparison to the mature and ever-improving surgical technology and procedures. The **hypothesis of the research** is that an ultrastructurally-based computational finite element model of the ocular lens subjected to blast loading can assist in better understanding how traumatic cataract is formed in the combat soldier, and in turn improve our understanding of traumatic cataract in civilians whose eyes are subjected to impact loading. The **scope of the research** is to develop a multi-scale, ultrastructurally-based, computational model of the ocular lens subjected to blast loading, in conjunction with imaging methods to identify lens capsule and internal substance structure and mechanical experiments for calibrating material model parameters.

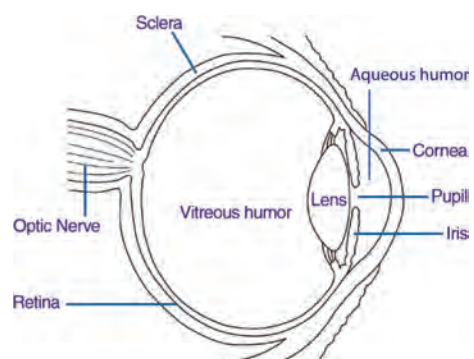


Figure 1. Eye cross-section.  
[www.nei.nih.gov](http://www.nei.nih.gov).

## 2 Body

The research tasks that have been focussed on to date are primarily the experimental ones: Tasks 4, 5, and 6. These Tasks have been worked on by my graduate student, Mr. Christopher Bay, which culminated in his Master of Science (MS) thesis *Biomechanics and Ultrastructure of the Ocular Lens*, included as an Appendix. Thus, the Body of this Annual Report refers primarily to Mr. Bay's MS thesis, with the exception to recent results obtained by Mr. Bay when visiting and conducting higher strain rate experiments on ocular lenses in Dr. Tusit Weerasooriya's laboratory at the Army Research Laboratory (ARL), Aberdeen Proving Ground (APG). These results are discussed in a separate section entitled **Higher Strain Rate Axial Compression Experiments on Whole Porcine Ocular Lenses** at the end of this Body under **Task 4b**.

A new PhD student, Ms. Xuwei Peng, has been recruited to focus on the modeling and computational mechanics Tasks 1, 2, and 3. This is the focus of future work, with a No Cost Extension (NCE) expected to be filed through September 2016.

Here, the Tasks are summarized, with details referred to Chapters in Mr. Bay's MS thesis.



**4a. Conduct unconfined compression tests at slower strain rates (0.001/s) to measure force versus time mechanical response, and image before and after testing the lens fiber cell geometry using CSLM in subtask 6a (months 1-6).**

The slower strain rate unconfined compression test results, and associated constitutive model parameter fitting, are discussed in Chapter 3. It was observed that a finite strain, isotropic, viscoelastic constitutive model [Reese and Govindjee, 1998] used in the lens capsule and internal lens substance meshes separately (Fig. 3.15), with related but separate constitutive parameters, was able to model the stress relaxation response of whole porcine lenses for various hold strains and strain rates (Figs. 3.17, 3.19, 3.21, 3.23, 3.25, 3.27, 3.29, 3.31). An approximation that is not valid for human lenses is ignoring differences in mechanical properties between the nucleus and cortex [Burd et al., 2002]. This can be resolved as confocal laser scanning microscopy (CSLM) identifies the structure of human lens tissue. But for the porcine lens data, a journal article is in preparation.

CSLM was used to identify ultrastructure of the internal lens substance, the lens fiber cells in Chapter 7. It was observed the fiber cell membrane walls could be discerned in green color, longitudinally and cross-sectionally. We are in the process of obtaining more images at various slices in the lens to see how an overall lens fiber ultrastructure can be reconstructed from these slice images.

CSLM was not conducted after unconfined compression because the methods are still being refined to identify the lens fiber cell structure.

**Task 5. smooth and sharp nanoindentation testing on porcine lenses to approximate lens capsule multiscale elasticity and strength parameters, and mechanical parameters of internal lens substance material (months 12-24):**

**5a. Design and fabricate a fixture to clamp lens capsules for nanoindentation onto samples immersed in aqueous solution (months 12-15).**

**5b. Test use of new fixture in nanoindentation machine (month 16).**

**5c. Conduct smooth nanoindents on porcine lens capsules (months 16-18).**

The procedure of nanoindentation, including substrate design and fabrication (Fig. 5.2), and preliminary results for creep testing with a  $1\ \mu\text{m}$  spherical tip (Figs. 5.4-5.27), is described in Chapter 5. We learned that the standard hold times (not surprising) for metals are too short to enable full creep of the lens capsules. Thus, we are in the process of testing in creep at longer hold times, approximately 5 minutes (300 seconds), compared to the 30-40 second hold times in the results in Figs. 5.4-5.27. It is clear a steady-state strain (displacement) has not been achieved. We plan to simulate with finite element analysis the same initial boundary value problem (IBVP) in order to calibrate gross viscoelastic properties of the capsule, and also the fibril viscoelastic properties for the three-dimensional finite strain beam model representing the type IV meshwork ultrastructure (**Task 6b**).

The next step is continuing smooth nanoindentation to longer creep times, and then conduct sharp nanoindentation (**Task 5d**) to measure the cutting force of lens capsules and possibly its time dependence. Nanoindentation on whole lenses most likely will not be conducted (**Tasks 5e and 5f**) because we are collecting data on large puncture tests of whole lenses (Chapter 4). These puncture data are more meaningful for understanding gross whole lens puncture resistance.

**6a. Before and after whole porcine lens unconfined compression, image lens fiber cell geometry using CLSM (low strain rate subtask 4a: months 1-4; higher strain rate subtask 4b: months 6-8).**

CLSM is discussed in Chapter 7 on porcine lenses. We are still refining the procedure of CLSM for identifying the ultrastructure, at various cross-sections through the whole lens, of the internal lens fiber cells. Thus, we are focussing our efforts on as-received porcine lenses and one human lens.

**6b. On as-received porcine lens capsules, image type IV collagen ultrastructure in lens capsule using cyro-electron tomography (months 1-4).**

Identification of type IV collagen meshwork ultrastructure in the lens capsule using cyro-electron microscopy/tomography is described in Chapter 6. Through standard freeze-substitution sample preparation methods, in conjunction with electron tomography (ET) to generate a stack of images (see attached movie `lens_freeze_sub_ET.wmv`), we see in Figs. 6.5-6.7 structure that begins to resemble type IV collagen meshwork ultrastructure identified in other works [Barnard et al., 1992, Inoue, 1994]. We plan to use this structure to then construct our 3D beam finite element mesh of the type IV collagen for our multiscale modeling in **Task 1**. Figure 6.8 demonstrates the initial procedure for obtaining a beam finite element mesh from such images.

One current focus of the research is to determine if the images in Figs. 6.5-6.7 are indeed structure, or if they are an artifact of the freezing process. There is currently a dispute among our collaborators in the Molecular, Cellular, and Development Biology (MCDB) Department at the University of Colorado, Boulder, about this topic. More experiments are being conducted to determine whether what we are seeing is structure or artifact, and gelatin is being used as a control.

**Higher Strain Rate Axial Compression Experiments on Whole Porcine Ocular Lenses**

**4b. Conduct unconfined compression tests at higher strain rates (up to 1/s) to measure force versus time mechanical response, and image before and after testing the lens fiber cell geometry using CSLM in subtask 6a to see if traumatic cataracts are generated (months 6-12).**

First, we would like to acknowledge the support of Dr. Tusit Weerasooriya and his Member of Technical Staff, Dr. Brett Sanborn, in using their high strain rate experimental laboratory at ARL APG. They provided assistance to Mr. Bay during his one week visit to ARL in July 2012 to obtain the preliminary results presented here, in order to determine which high strain rate experiments on which to focus for future research.

For all compression tests, whether high strain rate compress and hold, or high strain rate impulse and release, or high strain rate puncture, the test apparatus shown in Figs.2-5 was used in Dr. Weerasooriya's lab at ARL APG. Just as at CU Boulder, all lenses were compressed along their posterior-anterior poles, because this is how the lenses normally rest on a flat surface when placed in the BSS bath, except for puncture tests we can also test the anterior side (Fig.4.5 of Bay [2012]).

As an example of a high strain rate compression and hold experiment for stress relaxation, see attached movie `2+yr_10perc_1000mm-per-sec_eye1.wmv` (does not show very much, as compared to the impulse and puncture tests below) and associated force versus time curve in Fig.6. This test involved a 1000 mm/s axial displacement rate to 10% axial strain and then held for  $\approx 350$  seconds. With a lens height of 8.67 mm, this leads to an axial strain rate nominally of 115/s. We can use these data, and for a range of strain rates, to calibrate the viscoelastic and poroelastic parameters of the material models. But further experiments are required to ensure repeatability of the

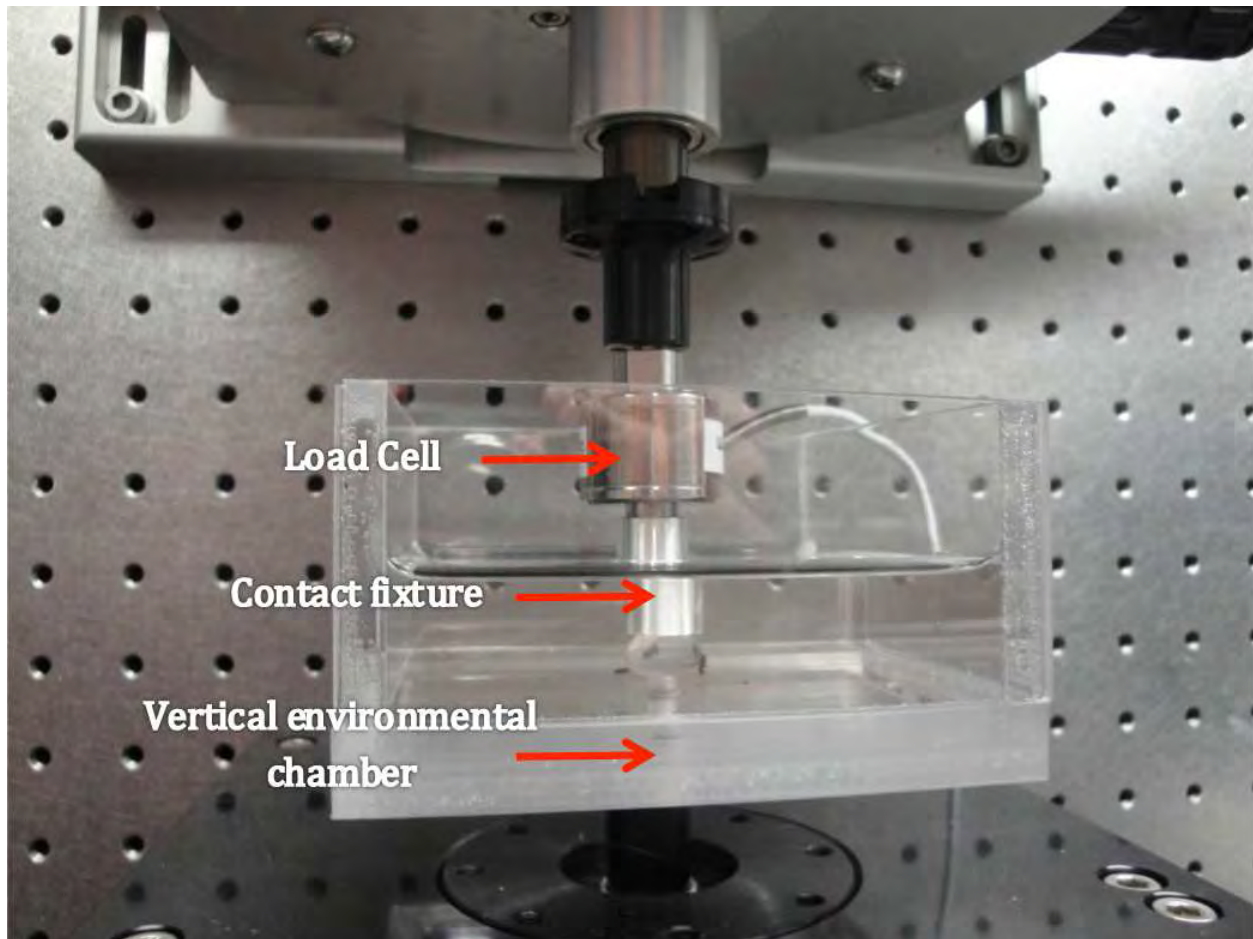


Figure 2. Close-up of test setup with Bose Electroforce vertically compressing an ocular lens in Balance Salt Solution (BSS), with a porcine lens beneath the contact fixture. The load cell is rated at 250 g.

data before material model parameter calibration.

As an example of a high strain rate impulse test on a lens, see attached movie 2+yr\_20perc\_500mm-per-sec\_eye3.wmv and associated force versus time curve in Fig.7. This test involved a 500 mm/s axial displacement rate to 20% axial strain and then released. With a lens height of 8.963 mm, this leads to an axial strain rate nominally of 56/s. The results in Fig.7(top) are interesting, in that after the application of the impulse at  $\approx 0.024\text{sec}$ , there is wave propagation axially through the lens as it contacts the contact fixture and the flat bottom surface of the environmental chamber. There is also dependence on the height of the contact fixture after impulse loading. For a 1000 mm/s axial displacement rate to 60% axial strain, with higher release of the contact fixture after impulse, we see in 2+yr\_60perc\_1000mm-per-sec\_eye1.wmv larger motion of the lens dynamically after impulse loading. There clearly is a fluid dynamic effect of the BSS on the lens after impulse for this experiment.

We can use these data, and for a range of strain rates, to calibrate the viscoelastic and poroelastic parameters of the material models. But further experiments are required to ensure repeatability of the data before material model parameter calibration.

As an example of a high strain rate puncture test on a lens, see attached movie



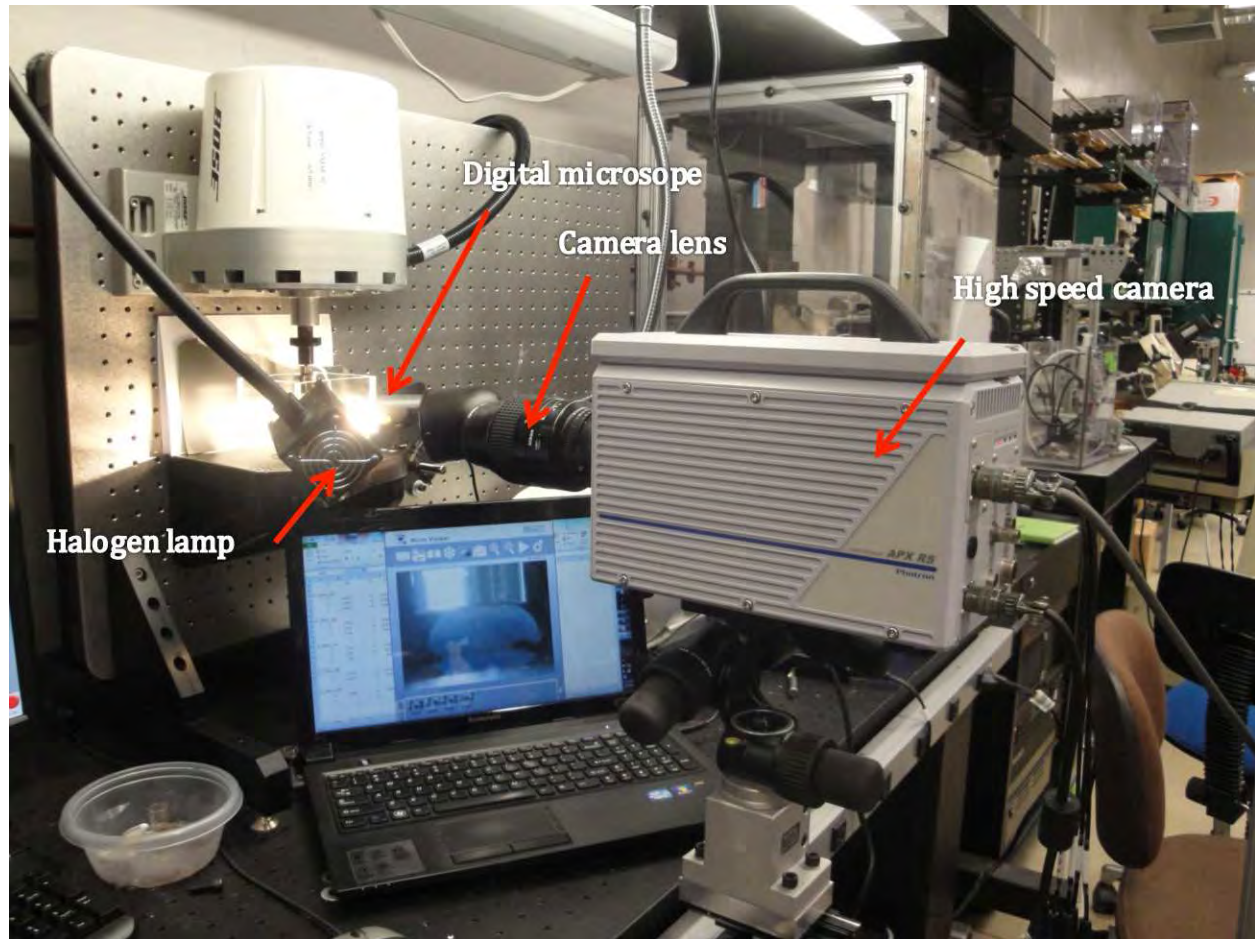


Figure 3. Overall test setup, showing the Bose Electroforce vertically mounted, the halogen lamp lighting the test bath with ocular lens, the high speed digital camera, and the image of the compressed lens on the laptop screen.

1mm\_flat\_post\_1000mm-per-sec\_eye5.wmv and associated force versus time curve in Fig.8. This test involved a 1000 mm/s axial displacement rate through puncture, with 1mm diameter fat circular post. The results in Fig.8(top) show the quick ramp up of load over 0.25sec, and then decrease after the lens capsule punctured. Figure 8(bottom) attempts to show corresponding deformed lenses during the puncture process.

We can use these data, and for a range of strain rates, to calibrate the viscoelastic and poroelastic parameters of the material models. But further experiments are required to ensure repeatability of the data before material model parameter calibration.

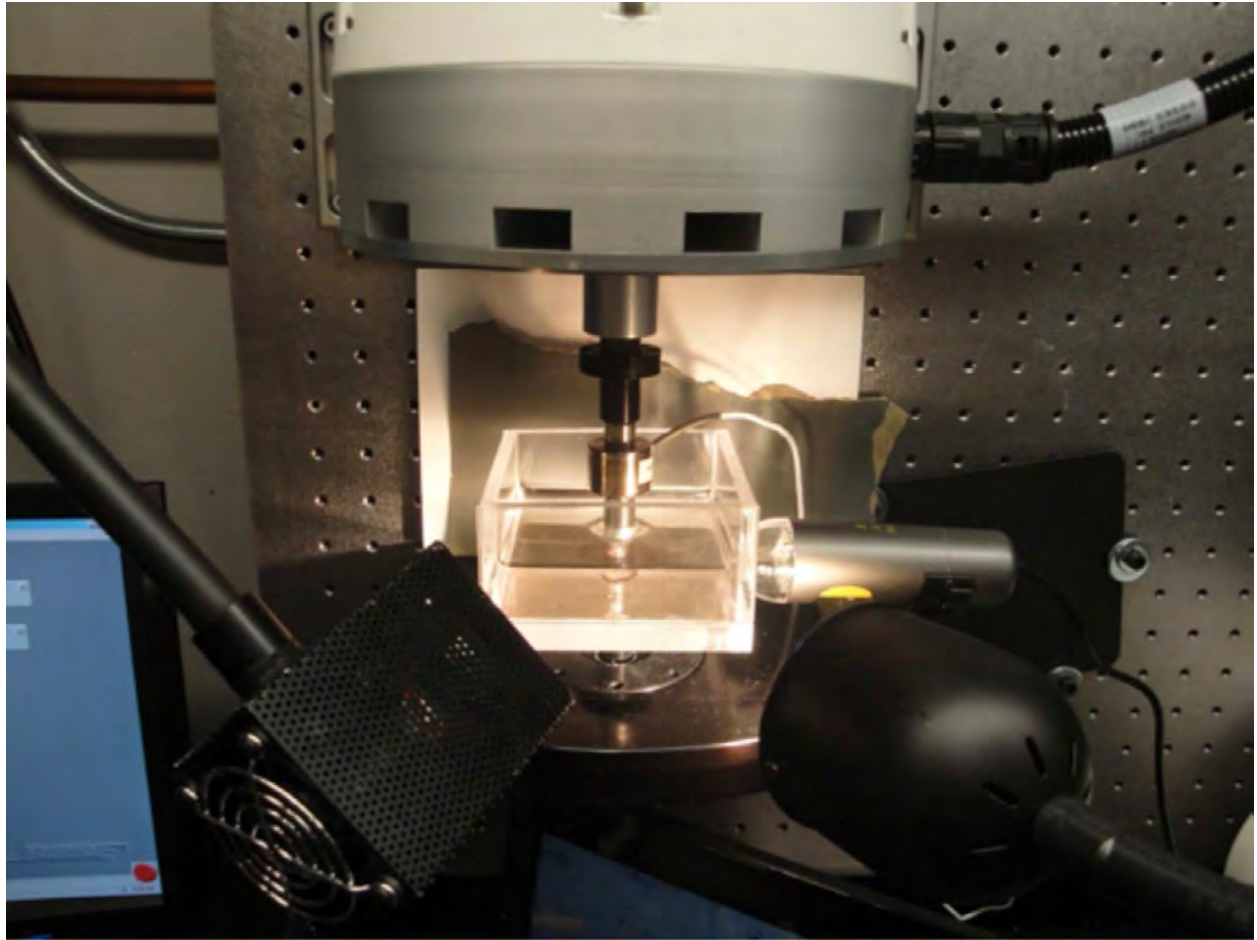


Figure 4. Closeup of setup with halogen lamps, and a lower resolution digital scope at the right for checking configuration of the contact on the lens during compression.

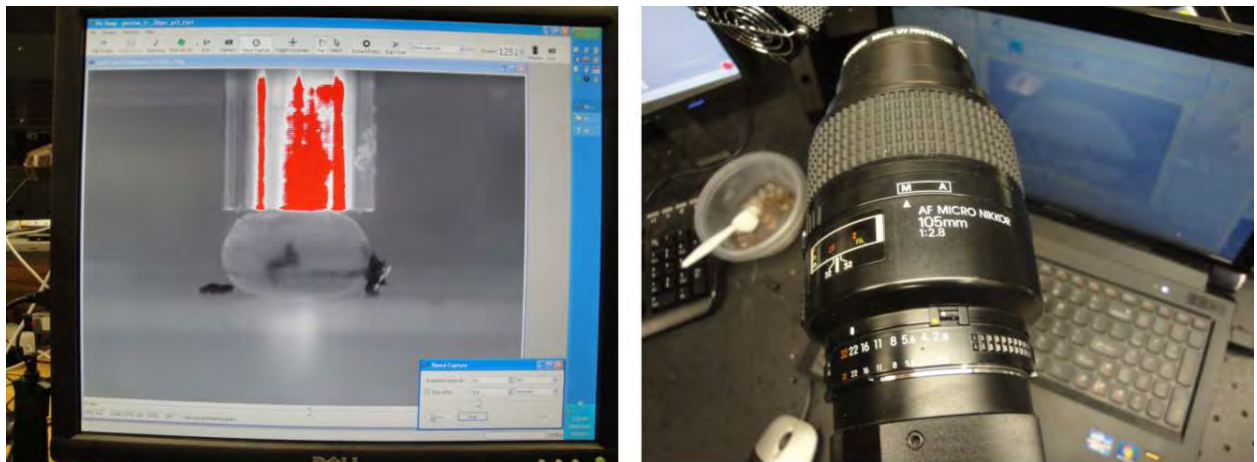


Figure 5. (left) Image from the high speed camera on the porcine ocular lens. (right) The high speed camera lens itself.

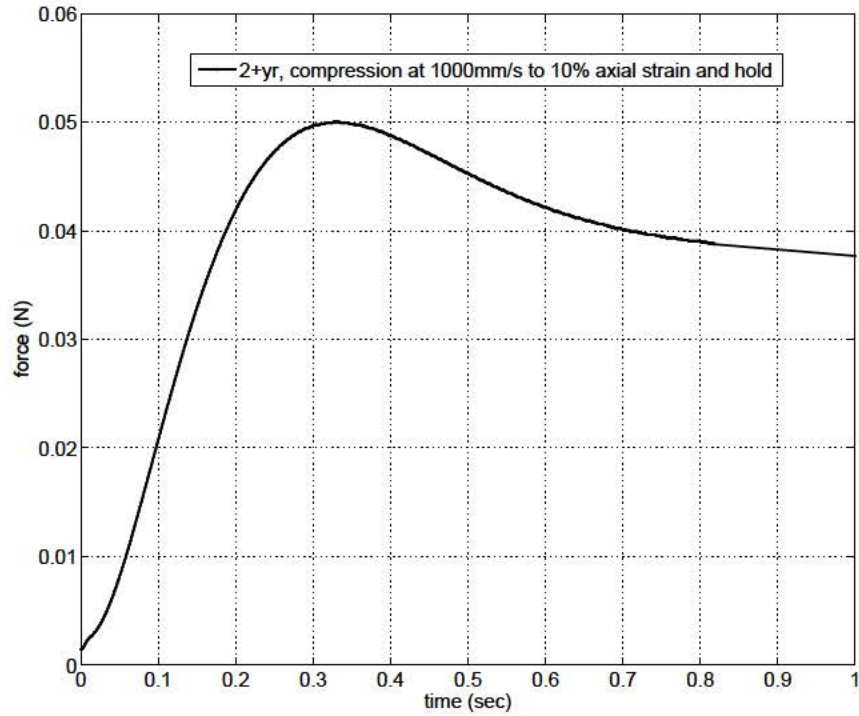
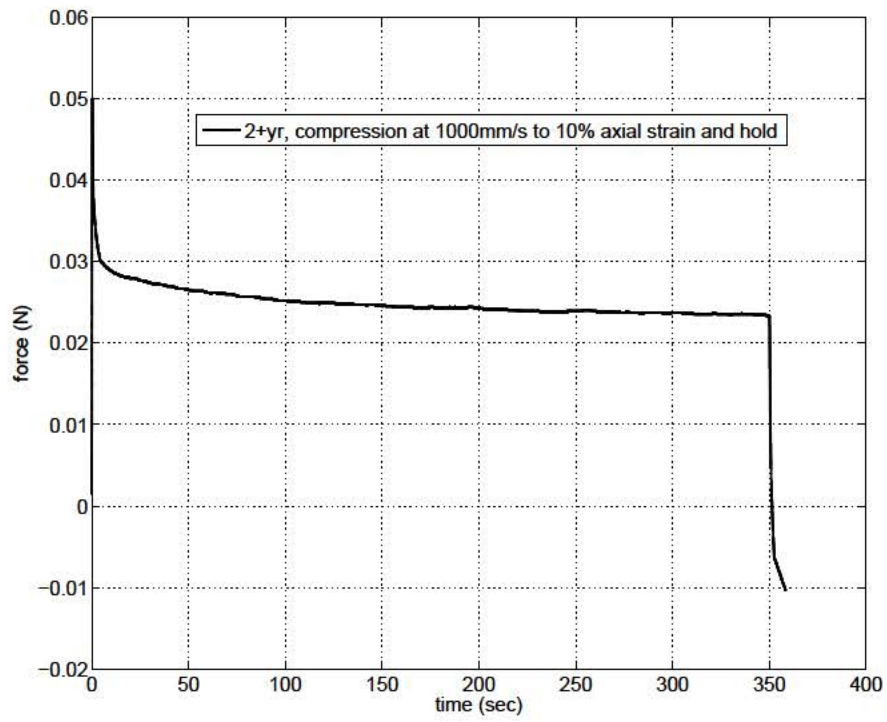


Figure 6. (top) Force versus time curve for a high strain rate stress relaxation test on a 2+year old porcine lens. (bottom) Zoom in plot of the same curve, showing smooth peak force and transition to relaxation.



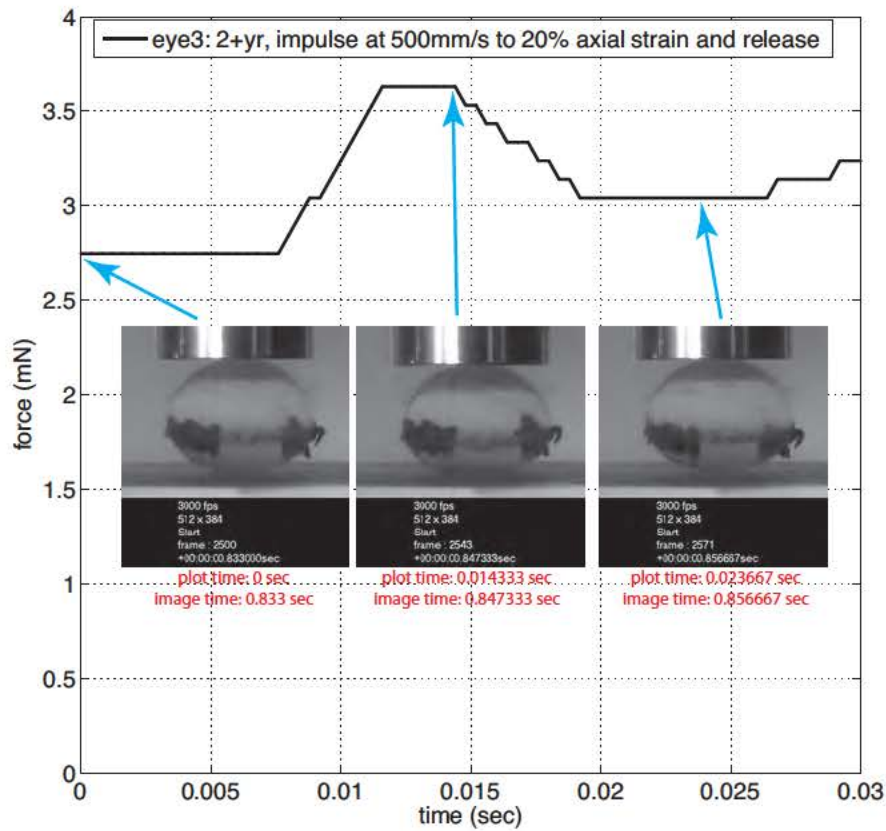
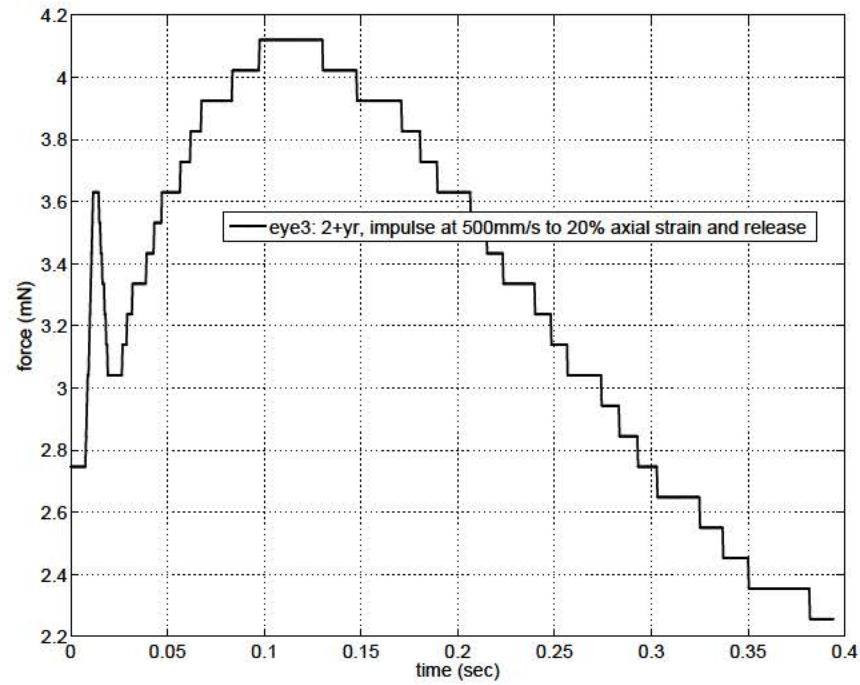


Figure 7. (top) Force versus time curve for a high strain rate impulse test on a 2+year old porcine lens. (bottom) Zoom in plot of the same curve, showing the impulse load profile, and associated deformed lens images.

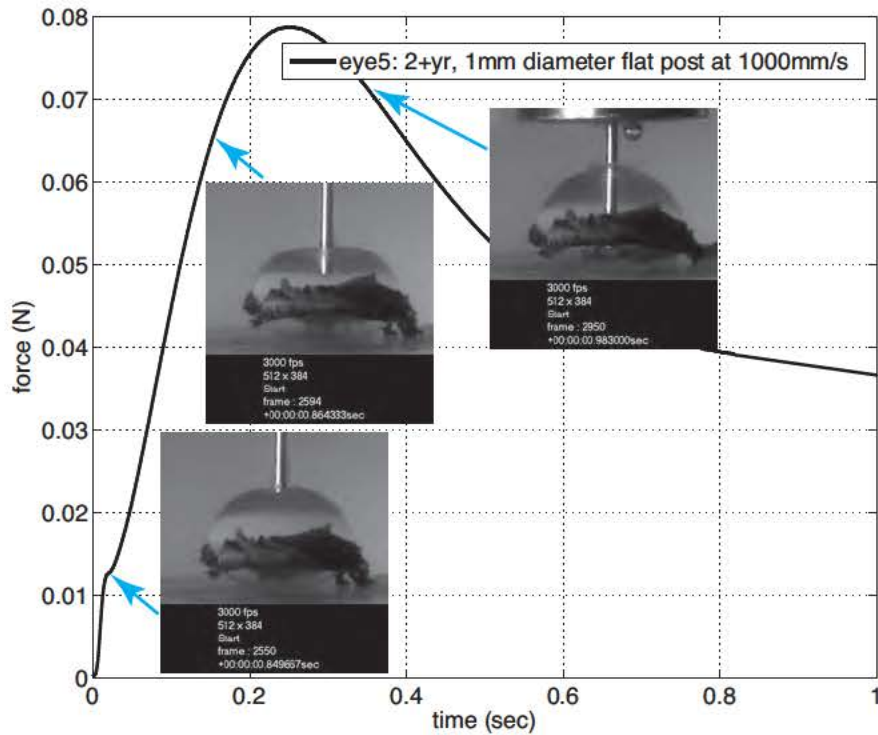
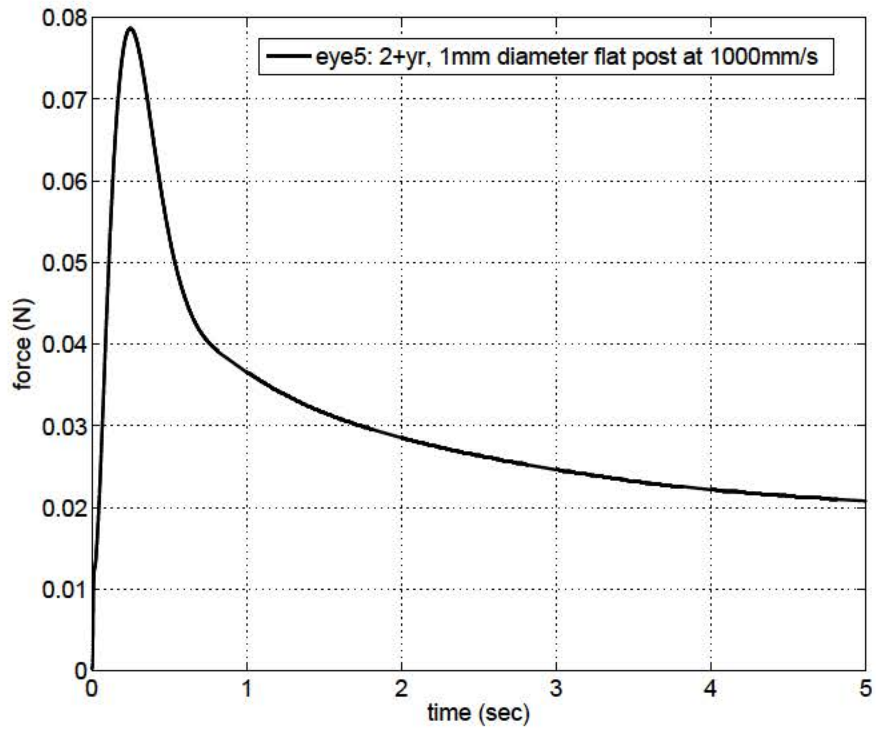


Figure 8. (top) Force versus time curve for a high strain rate puncture test on a 2+year old porcine lens. (bottom) Zoom in plot of the same curve, showing the peak load, and associated deformed lens images.



### Future Testing at ARL APG

Future testing at ARL APG in Dr. Weerasooriya's lab would focus on expanding the data set that was initially generated. This would be done by repeating tests that were completed, and conducting new tests with the younger porcine tissue (6-9 month old). If there is enough confidence in the testing of the porcine lenses, testing on human lenses would be performed as well. The response of the lens would be recorded with a dynamic load cell in addition to the Bose Electroforce load cell to ensure that we are capturing the full response of the lens, especially with the higher strain rate tests. The tables below describe tests that would be completed.

Compression (Stress Relaxation) Testing			
Age of tissue	Strain (%)	Rate (mm/s)	# samples
2+ year	10, 20	0.1, 0.3, 10, 30, 100, 300, 600, 1000	5
6-9 month	10, 20	0.1, 0.3, 10, 30, 100, 300, 600, 1000	5
Total tests			160

Impulse Testing			
Age of tissue	Strain (%)	Rate (mm/s)	# samples
2+ year	10, 20, 40, 60	10, 30, 100, 300, 600, 1000	5
6-9 month	10, 20, 40, 60	10, 30, 100, 300, 600, 1000	5
Total tests			240

Puncture Testing			
Age of tissue	Surface	Rate (mm/s)	# samples
2+ year	Anterior, Posterior	5, 50, 250, 500, 1000	5
6-9 month	Anterior, Posterior	5, 50, 250, 500, 1000	5
Total tests			240

### 3 Key Research Accomplishments

- Quasi-static puncture testing data were presented on 2+ year old and 6-9 month old porcine eyes, which will be used to calibrate parameters for failure modeling of the lens capsule, and internal lens substance (lens fiber cells).
- Preliminary creep data for spherical tip nanoindentation testing were presented, which will be used to calibrate directly the multiscale, 3D beam network model of type IV collagen meshwork in the lens capsule.
- CLSM was applied to internal lens substance to provide preliminary images of the lens fiber cell ultrastructure. This will be used to identify the lens fiber cell structure for the multiscale modeling of the internal lens substance.
- Electron Tomography (ET) images are beginning to provide identification of type IV collagen meshwork ultrastructure, although our MCDB collaborators are determining whether this is structure or an artifact of the freezing process.
- Preliminary high strain rate compression (stress relaxation), impulse, and puncture tests were conducted in Dr. Weerasooriya's lab at ARL APG. The results are promising, and we hope to have the opportunity to conduct more tests.

### 4 Reportable Outcomes

1. ARVO posters:
  - (a) Experiments and Finite Element Modeling of Indentation and Puncture of the Lens. C. Bay (presenter), R. Regueiro. *ARVO 2012*. #1349. Ft. Lauderdale, FL.
  - (b) Experiments and Finite Element Analysis of Stress Relaxation upon Compression of Whole Porcine Lenses. R. Regueiro (presenter), C. Bay. *ARVO 2012*. #1350. Ft. Lauderdale, FL.
2. Chris Bay's MS thesis: Bay, C.J. (2012) *Biomechanics and Ultrastructure of the Ocular Lens*, MS thesis, University of Colorado, Boulder.
3. Chris Bay recruited to Mechanical Engineering PhD program at Texas A&M (not necessarily a good thing for PI Regueiro, because now I have a big drop-off in activity on the experimental side of the research)

### 5 Conclusion

The research progress to date has focussed on the experimental portion of the research, ranging from unconfined compression with flat platen and puncture tips for estimating material constitutive parameters and puncture resistance, smooth indent creep testing for nanoindentation of lens capsules, structure identification of the lens capsule using cryo-electron microscopy and tomography,

structure identification of the internal lens fiber cells using confocal laser scanning microscopy, and preliminary high strain rate compression, impulse, and puncture testing in Dr. Tusit Weerasooriya's laboratory at the Army Research Laboratory (ARL), Aberdeen Proving Ground (APG). We would like to conduct future tests at ARL APG, if possible, given the preliminary data are promising.

All these data and images of structure will provide the basis for the multiscale computational finite element models of the ultrastructural response of whole lenses under dynamic loading.

The next main phase of the research, upon recruiting a PhD student, Ms. Xuewei Peng, is the development and application of the multiscale computational modeling framework to blast loading of the ocular lens.

## References

- MR. Banitt, JB. Malta, SL. Mian, and H.K Soong. Rupture of anterior lens capsule from blunt ocular injury. *JOURNAL OF CATARACT AND REFRACTIVE SURGERY*, 35(5):943–945, MAY 2009. ISSN 0886-3350. doi: 10.1016/j.jcrs.2008.11.066.
- K Barnard, SA Burgess, DA Carter, and DM Woolley. Three-dimensional structure of type IV collagen in the mammalian lens capsule. *J. Struct. Biol.*, 108(1):6–13, JAN-FEB 1992. ISSN 1047-8477.
- C.J. Bay. Biomechanics and Ultrastructure of the Ocular Lens. Ms thesis, University of Colorado at Boulder, 2012.
- HJ Burd, SJ Judge, and JA Cross. Numerical modelling of the accommodating lens. *Vis. Res.*, 42(18):2235–2251, AUG 2002. ISSN 0042-6989.
- S Inoue. Basic structure of basement-membranes is a fine network of cords, irregular anastomosing strands. *MICROSCOPY RESEARCH AND TECHNIQUE*, 28(1):29–47, MAY 1 1994. ISSN 1059-910X. doi: 10.1002/jemt.1070280105.
- T.H. Mader, J.V. Aragonés, A.C. Chandler, J.A. Hazlehurst, J. Heier, J.D. Kingham, and E. Stein. Ocular and ocular adnexal injuries treated by United States military ophthalmologists during operations Desert Shield and Desert Storm. *Ophthalmology*, 100(10):1462–1467, OCT 1993.
- T.H. Mader, R.D. Carroll, C.S. Slade, R.K. George, J.P. Ritchey, and S.P. Neville. Ocular war injuries of the Iraqi insurgency, January-September 2004. *Ophthalmology*, 113(1):97–104, JAN 2006.
- L.M. Parver, A.L. Dannenberg, B. Blacklow, C.J. Fowler, R.J. Brechner, and J.M. Tielsch. Characteristics and causes of penetrating eye injuries reported to the National Eye Trauma System Registry, 1985-91. *PUBLIC HEALTH REPORTS*, 108(5):625–632, SEP-OCT 1993.
- S. Reese and S. Govindjee. A theory of finite viscoelasticity and numerical aspects. *Int. J. Solids Struct.*, 35:3455–3482, 1998.
- W.L. Walter. Intralenticular foreign body - as a cause of traumatic cataract. *AMERICAN JOURNAL OF OPHTHALMOLOGY*, 54(5):856–&, 1962.
- Eric D. Weichel and Marcus H. Colyer. Combat ocular trauma and systemic injury. *CURRENT OPINION IN OPHTHALMOLOGY*, 19(6):519–525, NOV 2008. ISSN 1040-8738. doi: 10.1097/ICU.0b013e3283140e98.
- TY Wong, MB Seet, and CL Ang. Eye injuries in twentieth century warfare: A historical perspective. *SURVEY OF OPHTHALMOLOGY*, 41(6):433–459, MAY-JUN 1997. ISSN 0039-6257.

## **A Master of Science Thesis**

The appendix includes the Master of Science Thesis of Mr. Christopher Bay, to which is referred in early sections of this Annual Report.

# **Biomechanics and Ultrastructure of the Ocular Lens**

by

**Christopher Joseph Bay**

B.S., University of Colorado Boulder, 2012

A thesis submitted to the  
Faculty of the Graduate School of the  
University of Colorado in partial fulfillment  
of the requirements for the degree of  
Masters of Science  
Department of Mechanical Engineering

2012

This thesis entitled:  
Biomechanics and Ultrastructure of the Ocular Lens  
written by Christopher Joseph Bay  
has been approved for the Department of Mechanical Engineering

---

Richard Regueiro

---

Virginia Ferguson

---

Mark Rentschler

Date \_\_\_\_\_

The final copy of this thesis has been examined by the signatories, and we find that both the content and the form meet acceptable presentation standards of scholarly work in the above mentioned discipline.

Bay, Christopher Joseph (M.S., Mechanical Engineering)

Biomechanics and Ultrastructure of the Ocular Lens

Thesis directed by Associate Professor Richard Regueiro

Study of the biomechanics of the ocular lens is imperative to increasing our understanding of the role of the ocular lens in accommodation, to improving current surgical methods (cataract and intraocular lens replacement), and to better qualify the nature and mechanics of injuries sustained to the ocular lens (lens dehiscence, lens perforation, and traumatic cataract). Previous work done to determine and model the mechanical properties of the ocular lens includes non-ideal experimental assumptions and lack of qualified data. The goal of this work is to produce and analyze data suitable for the creation of an ultrastructurally based computational model of the ocular lens and make progress toward the generation of such a model.

The creation of a model requires the determination of the material properties as well as identification of the ultrastructure of the tissue to be modeled. Unconfined compression testing of the whole porcine ocular lens, puncture testing of the whole porcine ocular lens, and nanoindentation of the anterior porcine and human lens capsule were performed to generate data from which to calculate material properties of the lens. Cryo-electron tomography and confocal scanning LASER microscopy were employed to determine the ultrastructure of the porcine lens capsule and porcine lens fiber cells, respectively.

Test data were produced from the mechanical tests and the fitting of parameters to calculate material properties were started. Potential identification of the type-IV collagen meshwork of the lens capsule and positive identification of the lens fiber cells were achieved. Preliminary modeling work was started with the data available using Abaqus (simulia.com) and Tahoe (tahoe.sourceforge.net).



## Dedication

First and foremost, this thesis is dedicated to my mom, Sharon, and my two younger sisters, Crystal and Kayla. Thank you mom, for your constant support in the pursuit of my dreams, the occasional Chipotle gift card to curb my hunger, and for helping to keep me going when I thought different. Crystal, thank you for reminding me of my humility and showing me the importance of serving others through your studies and work. And Kayla, thank you for keeping me grounded in reality while encouraging me to shoot past the stars. I love you all and would not be who I am today without you.

Secondly, I would like to thank my uncle Wayne for being such a positive influence throughout my life. You have only begun showing me the secrets of, as well as how to so thoroughly enjoy the art of fishing, and I hope we can reel 'em in for years to come.

Next, I would like to thank my good friend Kyle Blackmer. You have been, and always will be a brother to me. Thank you for your guidance, your wisdom, and your unconditional friendship throughout my college career and beyond. I love you man.

Lastly, I would like to thank my girlfriend, Laura Willson. Your support and encouragement throughout this whole ordeal has been tremendous. From keeping me focused, to providing comedic interludes, I couldn't have completed this without your help. Thank you for all the baking sustenance, hours of laughs, and escapes from reality. You mean the world to me and I love you.

## Acknowledgements

I would like to acknowledge financial support from a research grant awarded and administered by the U.S. Army Medical Research & Materiel Command (USAMRMC) and the Telemedicine & Advanced Technology Research Center (TATRC), at Fort Detrick, MD under Award Number W81XWH-10-1-1036. I would also like to thank Professor Jerry Qi (CU Boulder) for use of his 2N load cell, Professor Virginia Ferguson (CU Boulder) and Dr. Corrine Packard (Colorado School of Mines) for their assistance with nanoindentation, and Greg Potts for use of the ME machine shop. I would like to acknowledge Adam Blanchard for designing and testing the prototype unconfined compression apparatus, Ralph Burns for designing and fabricating the current pedestal apparatus, Professor Vicky Nguyen (Johns Hopkins U.) for implementing the finite strain isotropic viscoelasticity model into Tahoe, and Dr. Reese Jones (Sandia) for implementing the Dakota-Tahoe interface for parameter optimization. I also thank Jacqui Trujillo of Rocky Mtn. Lions Eye Institute for BSS and microsurgery tools. Preliminary funding for this research was provided by the University of Colorado, Boulder, Graduate School Seed Grant, and the College of Engineering and Applied Science Discovery Learning Apprenticeship Program. I thank Sai Radha, Sri Radha, and Chad Hottimsky for their help and enthusiasm for the project. Lastly, I want to express my sincere gratitude towards Professor Richard Regueiro. He has been a wonderful mentor and a bottomless resource for all the questions I have had. Thank you for your belief in me and allowing me the opportunity to do research and learn with you.

# Contents

## Chapter

<b>1</b>	Introduction	1
<b>2</b>	Background	3
2.1	Characteristics of the Lens . . . . .	3
2.1.1	Capsule . . . . .	5
2.1.2	Lens Fiber Cells . . . . .	6
2.2	Previous Research . . . . .	7
2.2.1	Capsule . . . . .	7
2.2.2	Lens Fiber Cells . . . . .	8
2.3	What is Needed . . . . .	9
<b>3</b>	Parameter Fitting of Unconfined Compression Testing Data	10
3.1	Previous Testing Done . . . . .	11
3.2	Methods of Fitting Parameters . . . . .	19
3.3	Sample Preparation . . . . .	20
3.4	Experimental Setup . . . . .	21
3.5	Experimental Method . . . . .	22
3.6	Results . . . . .	22
3.7	Discussion . . . . .	36

<b>4</b>	<b>Puncture Testing of the Whole Lens</b>	<b>45</b>
4.1	Sample Preparation . . . . .	45
4.2	Experimental Setup . . . . .	46
4.3	Experimental Method . . . . .	49
4.4	Theoretical Modeling . . . . .	51
4.5	Results . . . . .	52
4.6	Discussion . . . . .	59
<b>5</b>	<b>Nanoindentation of the Capsule</b>	<b>65</b>
5.1	Sample Preparation . . . . .	66
5.2	Experimental Setup . . . . .	66
5.3	Experimental Method . . . . .	67
5.4	Results . . . . .	68
5.5	Discussion . . . . .	81
<b>6</b>	<b>Electron Microscopy and Tomography of the Lens Capsule</b>	<b>83</b>
6.1	Sample Preparation . . . . .	84
6.2	Experimental Setup . . . . .	86
6.3	Experimental Method . . . . .	86
6.4	Results . . . . .	87
6.5	Discussion . . . . .	92
<b>7</b>	<b>Confocal Scanning Laser Microscopy of the Lens Fiber Cells</b>	<b>94</b>
7.1	Sample Preparation . . . . .	94
7.2	Experimental Setup . . . . .	98
7.3	Experimental Method . . . . .	99
7.4	Results . . . . .	99
7.5	Discussion . . . . .	109

<b>8</b>	<b>Discussion</b>	<b>111</b>
<b>9</b>	<b>Recommendations</b>	<b>113</b>
9.1	Determine Material Properties from Data . . . . .	113
9.2	Additional Imaging and Modeling . . . . .	113
9.3	Confocal Imaging of Deformed/Damaged Lenses . . . . .	114
9.4	Posterior Lens Capsule Testing . . . . .	114
9.5	Human Tissue Testing . . . . .	115
9.6	Higher Strain Rate Testing . . . . .	115
9.7	Determine Properties/Structure of Zonules/Ciliary Body . . . . .	116
<b>10</b>	<b>Conclusion</b>	<b>117</b>
	<b>Bibliography</b>	<b>119</b>

## Tables

### Table

3.1	Unconfined Compression Testing Conditions and Number of Whole Ocular Porcine Lenses Tested With Preconditioning. . . . .	14
3.2	Unconfined Compression Testing Conditions and Number of Whole Ocular Porcine Lenses Tested With No Preconditioning . . . . .	22
3.3	Average Parameters Fitted of Tissue 2 Years or Older . . . . .	36
3.4	Average Parameters Fitted of Tissue 6-9 Months Old . . . . .	37
3.5	Tahoe Parameters vs Abaqus Parameters . . . . .	44
4.1	Testing Configurations and Number of Lenses Tested . . . . .	46
4.2	Average Puncture Force & Average Time to Puncture. . . . .	60
5.1	Average Displacement Values from Human Anterior Lens Capsule Creep Tests . . . .	82

## Figures

### Figure

2.1	General Anatomy of the Eye (nei.nih.gov). . . . .	4
2.2	Theory of How Accommodation Occurs: On the left in the lens is shown in the un-accommodated state, where the zonules are in tension. On the right the lens is shown in the accommodated state, where the zonules are not in tension due to the contraction of the ciliary muscle [McLeod et al., 2003]. . . . .	4
2.3	Detailed Anatomy of the Ocular Lens [Kessel and Kardon, 1979]. . . . .	5
3.1	Dissection of Globe to Remove Ocular Lens. . . . .	11
3.2	Removing Excess Zonules from Ocular Lens with Tissue Paper. . . . .	12
3.3	Test Setup for Unconfined Compression Testing. . . . .	13
3.4	Shape of Lens (Anterior Surface Facing Down) Testing in Testing Platform, Showing Upper Load Platen. . . . .	13
3.5	Example Showing Data with Preconditioning. . . . .	14
3.6	Graph of all eyes from the 2+ year 10% strain 0.1 mm/s Group. . . . .	15
3.7	Graph of all eyes from the 2+ year 10% strain 0.3 mm/s Group. . . . .	15
3.8	Graph of all eyes from the 2+ year 20% strain 0.1 mm/s Group. . . . .	16
3.9	Graph of all eyes from the 2+ year 20% strain 0.3 mm/s Group. . . . .	16
3.10	Graph of all eyes from the 6-9 month 10% strain 0.1 mm/s Group. . . . .	17
3.11	Graph of all eyes from the 6-9 month 10% strain 0.3 mm/s Group. . . . .	17

3.12	Graph of all eyes from the 6-9 month 20% strain 0.1 mm/s Group. . . . .	18
3.13	Graph of all eyes from the 6-9 month 20% strain 0.3 mm/s Group. . . . .	18
3.14	Analogy of Model Implemented in Tahoe to a Standard Linear Solid. . . . .	20
3.15	Example of Lens Mesh Generated by CUBIT - Notice the two sections: the exterior lens capsule (yellow and purple) and the interior lens fiber cells (green). . . . .	21
3.16	Graph of Eye2 and Eye3 from the 2+ year 10% strain 0.1 mm/s Group. . . . .	23
3.17	Graph of Eye2 and Eye3 vs Tahoe from the 2+ year 10% strain 0.1 mm/s Group. . .	23
3.18	Graph of Eye1 and Eye2 from the 2+ year 10% strain 0.3 mm/s Group. . . . .	24
3.19	Graph of Eye1 and Eye2 vs Tahoe from the 2+ year 10% strain 0.3 mm/s Group. . .	24
3.20	Graph of Eye5 and Eye7 from the 2+ year 20% strain 0.1 mm/s Group. . . . .	25
3.21	Graph of Eye5 and Eye7 vs Tahoe from the 2+ year 20% strain 0.1 mm/s Group. . .	25
3.22	Graph of Eye9 and Eye10 from the 2+ year 20% strain 0.3 mm/s Group. . . . .	26
3.23	Graph of Eye9 and Eye10 vs Tahoe from the 2+ year 20% strain 0.3 mm/s Group. .	26
3.24	Graph of Eye10 and Eye3 from the 6-9 month 10% strain 0.1 mm/s Group. . . . .	27
3.25	Graph of Eye10 and Eye3 vs Tahoe from the 6-9 month 10% strain 0.1 mm/s Group.	27
3.26	Graph of Eye7 and Eye1 from the 6-9 month 10% strain 0.3 mm/s Group. . . . .	28
3.27	Graph of Eye7 and Eye1 vs Tahoe from the 6-9 month 10% strain 0.3 mm/s Group.	28
3.28	Graph of Eye3 and Eye10 from the 6-9 month 20% strain 0.1 mm/s Group. . . . .	29
3.29	Graph of Eye3 and Eye10 vs Tahoe from the 6-9 month 20% strain 0.1 mm/s Group.	29
3.30	Graph of Eye7 and Eye9 from the 6-9 month 20% strain 0.3 mm/s Group. . . . .	30
3.31	Graph of Eye7 and Eye9 vs Tahoe from the 6-9 month 20% strain 0.3 mm/s Group.	30
3.32	Graph of all eyes from the 2+ year 10% strain 0.1 mm/s with no Preconditioning Group. . . . .	32
3.33	Graph of all eyes from the 2+ year 10% strain 0.3 mm/s with no Preconditioning Group. . . . .	32
3.34	Graph of all eyes from the 2+ year 20% strain 0.1 mm/s with no Preconditioning Group. . . . .	33



3.35 Graph of all eyes from the 2+ year 20% strain 0.3 mm/s with no Preconditioning Group. . . . .	33
3.36 Graph of all eyes from the 6-9 month 10% strain 0.1 mm/s with no Preconditioning Group. . . . .	34
3.37 Graph of all eyes from the 6-9 month 10% strain 0.3 mm/s with no Preconditioning Group. . . . .	34
3.38 Graph of all eyes from the 6-9 month 20% strain 0.1 mm/s with no Preconditioning Group. . . . .	35
3.39 Graph of all eyes from the 6-9 month 20% strain 0.3 mm/s with no Preconditioning Group. . . . .	35
3.40 Simulation of Unconfined Compression on Whole Porcine Ocular Lens - Beginning of simulation. . . . .	38
3.41 Abaqus Simulation of Unconfined Compression on Whole Porcine Ocular Lens - Full loading has been reached; can see stress in the capsule along the top and bottom. . .	39
3.42 Abaqus Simulation of Unconfined Compression on Whole Porcine Ocular Lens - End of simulation; stress has gradually relaxed in capsule. . . . .	40
3.43 Scaled contour of the Abaqus simulation showing the maximum stressed state of the lens fiber cells. . . . .	41
3.44 Scaled contour of the Abaqus simulation showing the stressed state of the lens fiber cells at the end of the simulation. . . . .	42
3.45 Overlay of the Abaqus simulation with an image of the compressed lens. . . . .	43
3.46 Graph of Data Produced From Tahoe Simulation and Abaqus Simulation . . . . .	44
4.1 2N Load Cell and Puncture Tip Apparatus Attached to MTS Insight II. . . . .	47
4.2 Puncture Loading Tip Geometries with Various Diameters $d$ and Angles $\Theta$ . . . . .	47
4.3 Environmental Chamber with Testing Pedestal Placed Inside. . . . .	48
4.4 Example of Image Taken Before Each Test to get Geometry Data. . . . .	49

4.5	Sample Holder inside of Environmental Chamber. . . . .	50
4.6	Graph of 1 mm Spherical Anterior Data. . . . .	53
4.7	Graph of 1 mm Spherical Posterior Data. . . . .	53
4.8	Graph of 1 mm Cylindrical Anterior Data. . . . .	54
4.9	Graph of 1 mm Cylindrical Posterior Data. . . . .	54
4.10	Graph of 2 mm Spherical Anterior Data. . . . .	55
4.11	Graph of 2 mm Spherical Posterior Data. . . . .	55
4.12	Graph of 2 mm Cylindrical Anterior Data. . . . .	56
4.13	Graph of 2 mm Cylindrical Posterior Data. . . . .	56
4.14	Graph of 30 deg Conical Anterior Data. . . . .	57
4.15	Graph of 30 deg Conical Posterior Data. . . . .	57
4.16	Graph of 45 deg Conical Anterior Data. . . . .	58
4.17	Graph of 45 deg Conical Posterior Data. . . . .	58
4.18	Image series showing the lens at the begining of the test (top left), after the initial puncture (top right,) and subsequent tearing (bottom left and right) during a 30 degree conical puncture test. . . . .	59
4.19	Abaqus Simulation of Puncture Testing of Whole Porcine Ocular Lens - Beginning of simulation. . . . .	62
4.20	Abaqus Simulation of Puncture Testing of Whole Porcine Ocular Lens - As far as simulation will complete. . . . .	63
4.21	Abaqus Simulation of Puncture Testing of Whole Porcine Ocular Lens - Scaled con- tour to better show stresses in lens fibers. . . . .	64
5.1	Hysitron TI-950 TriboIndenter Nanoindenter Located at the Colorado School of Mines.	67
5.2	Drawing of Nanoindentation Substrate with Dome-Shaped Surface and Liquid Well.	67
5.3	Image of Lens Capsule Being Held in Place by a Small Metallic Washer Within the Nanoindenter. . . . .	68

5.4	Graph of Nanoindentation Creep Test Porcine Lens Capsule 1 - Load to 5 $\mu\text{N}$ , Hold for 30 seconds. The pre-load force necessary to get contact with the lens capsule is the cause of the non-zero starting force. . . . .	69
5.5	Graph of Nanoindentation Creep Test Porcine Lens Capsule 2 - Load to 5 $\mu\text{N}$ , Hold for 30 seconds. The pre-load force necessary to get contact with the lens capsule is the cause of the non-zero starting force. . . . .	69
5.6	Graph of Nanoindentation Creep Test Porcine Lens Capsule 3 - Load to 5 $\mu\text{N}$ , Hold for 30 seconds. The pre-load force necessary to get contact with the lens capsule is the cause of the non-zero starting force. . . . .	70
5.7	Graph of Nanoindentation Creep Test Porcine Lens Capsule 4 - Load to 5 $\mu\text{N}$ , Hold for 30 seconds. The pre-load force necessary to get contact with the lens capsule is the cause of the non-zero starting force. . . . .	70
5.8	Graph of Nanoindentation Creep Test Porcine Lens Capsule 5 - Load to 5 $\mu\text{N}$ , Hold for 30 seconds. The pre-load force necessary to get contact with the lens capsule is the cause of the non-zero starting force. . . . .	71
5.9	Graph of Nanoindentation Creep Test Porcine Lens Capsule 6 - Load to 15 $\mu\text{N}$ , Hold for 30 seconds. The pre-load force necessary to get contact with the lens capsule is the cause of the non-zero starting force. . . . .	71
5.10	Graph of Nanoindentation Creep Test Human Lens Capsule 1 - Load to 5 $\mu\text{N}$ , Hold for 30 seconds. The pre-load force necessary to get contact with the lens capsule is the cause of the non-zero starting force. . . . .	72
5.11	Graph of Nanoindentation Creep Test Human Lens Capsule 2 - Load to 5 $\mu\text{N}$ , Hold for 30 seconds. The pre-load force necessary to get contact with the lens capsule is the cause of the non-zero starting force. . . . .	72
5.12	Graph of Nanoindentation Creep Test Human Lens Capsule 3 - Load to 10 $\mu\text{N}$ , Hold for 30 seconds. The pre-load force necessary to get contact with the lens capsule is the cause of the non-zero starting force. . . . .	73

5.13	Graph of Nanoindentation Creep Test Human Lens Capsule 4 - Load to 10 $\mu\text{N}$ , Hold for 30 seconds. The pre-load force necessary to get contact with the lens capsule is the cause of the non-zero starting force. . . . .	73
5.14	Graph of Nanoindentation Creep Test Human Lens Capsule 5 - Load to 15 $\mu\text{N}$ , Hold for 30 seconds. The pre-load force necessary to get contact with the lens capsule is the cause of the non-zero starting force. . . . .	74
5.15	Graph of Nanoindentation Creep Test Human Lens Capsule 6 - Load to 15 $\mu\text{N}$ , Hold for 30 seconds. The pre-load force necessary to get contact with the lens capsule is the cause of the non-zero starting force. . . . .	74
5.16	Graph of Nanoindentation Creep Test Human Lens Capsule 7 - Load to 20 $\mu\text{N}$ , Hold for 30 seconds. The pre-load force necessary to get contact with the lens capsule is the cause of the non-zero starting force. . . . .	75
5.17	Graph of Nanoindentation Creep Test Human Lens Capsule 8 - Load to 20 $\mu\text{N}$ , Hold for 30 seconds. The pre-load force necessary to get contact with the lens capsule is the cause of the non-zero starting force. . . . .	75
5.18	Graph of Nanoindentation Creep Test Human Lens Capsule 9 - Load to 25 $\mu\text{N}$ , Hold for 30 seconds. The pre-load force necessary to get contact with the lens capsule is the cause of the non-zero starting force. . . . .	76
5.19	Graph of Nanoindentation Creep Test Human Lens Capsule 10 - Load to 25 $\mu\text{N}$ , Hold for 30 seconds. The pre-load force necessary to get contact with the lens capsule is the cause of the non-zero starting force. . . . .	76
5.20	Graph of Nanoindentation Creep Test Human Lens Capsule 11 - Load to 30 $\mu\text{N}$ , Hold for 30 seconds. The pre-load force necessary to get contact with the lens capsule is the cause of the non-zero starting force. . . . .	77
5.21	Graph of Nanoindentation Creep Test Human Lens Capsule 12 - Load to 30 $\mu\text{N}$ , Hold for 30 seconds. The pre-load force necessary to get contact with the lens capsule is the cause of the non-zero starting force. . . . .	77

5.22	Graph of Nanoindentation Creep Test Human Lens Capsule 13 - Load to 35 $\mu\text{N}$ , Hold for 30 seconds. The pre-load force necessary to get contact with the lens capsule is the cause of the non-zero starting force. . . . .	78
5.23	Graph of Nanoindentation Creep Test Human Lens Capsule 14 - Load to 35 $\mu\text{N}$ , Hold for 30 seconds. The pre-load force necessary to get contact with the lens capsule is the cause of the non-zero starting force. . . . .	78
5.24	Graph of Nanoindentation Creep Test Human Lens Capsule 15 - Load to 40 $\mu\text{N}$ , Hold for 30 seconds. The pre-load force necessary to get contact with the lens capsule is the cause of the non-zero starting force. . . . .	79
5.25	Graph of Nanoindentation Creep Test Human Lens Capsule 16 - Load to 40 $\mu\text{N}$ , Hold for 30 seconds. The pre-load force necessary to get contact with the lens capsule is the cause of the non-zero starting force. . . . .	79
5.26	Graph of Nanoindentation Creep Test Human Lens Capsule 17 - Load to 45 $\mu\text{N}$ , Hold for 30 seconds. The pre-load force necessary to get contact with the lens capsule is the cause of the non-zero starting force. . . . .	80
5.27	Graph of Nanoindentation Creep Test Human Lens Capsule 18 - Load to 45 $\mu\text{N}$ , Hold for 30 seconds. The pre-load force necessary to get contact with the lens capsule is the cause of the non-zero starting force. . . . .	80
6.1	BalTec HPM 010 High Pressure Freezer. . . . .	85
6.2	Phillips CM-100 Transmission Electron Microscope. . . . .	86
6.3	FEI Tecnai TF30 300kV IVEM Microscope. . . . .	86
6.4	Initial Image Collected on Phillips CM-100 at 245,000X with 60 nm scale bar. . . . .	88
6.5	Reconstructed Image from Tilt-Series: taken at 23,000X, 1 image per degree from -60° to 60° with 50 nm scale bar. . . . .	89
6.6	Zoomed in Region of Reconstructed Image from Tilt-Series: taken at 23,000X, 1 image per degree from -60° to 60° with 100 nm scale bar. . . . .	90

6.7	Reconstructed Image from Tilt-Series: taken at 23,000X, 1 image per degree from -60° to 60° with 50 nm scale bar. . . . .	91
6.8	Modeling of Perceived Structure from ET Images using IMOD. . . . .	93
7.1	Confocal LASER Scanning Microscopy Images of Porcine Lens Capsule. . . . .	95
7.2	Confocal LASER Scanning Microscopy Images of Porcine Lens Capsule After Color Addition Through Post-Processing. . . . .	96
7.3	Channels 1 & 2 of Confocal LASER Scanning Microscopy Images of Porcine Lens Capsule Combined Into Composite Image With Post-Processing. . . . .	97
7.4	Olympus Fluoview FV1000 Confocal Microscope. . . . .	98
7.5	Confocal Image of Lens Fibers: 3x5 stitched image, each individual image was taken with the 40x(NA=1.30) objective in oil. Each image is 512 x 512 pixels and 317.331 x 317.331 $\mu\text{m}$ , resulting in an overall image size of 1586.655 x 951.993 $\mu\text{m}$ . The anterior surface can be identified at the bottom of the image by the nuclei stained with DAPI shown in cyan. The waves seen on the bottom of the sample are artifacts from the sectioning process. Notice the fine, honeycomb-like structure of the lens fibers in the bottom left area of the tissue. . . . .	100
7.6	Confocal Image of Lens Fibers: Image was taken with the 20x(NA=0.75) objective in air. The image size is 800 x 800 pixels, or 635.205 x 635.205 $\mu\text{m}$ . Again, the anterior surface of the samples is identified by the stained nuclei in cyan. The fine structure of the lens fibers can be seen in the upper portion of the of the sample. . .	101
7.7	Confocal Image of Lens Fibers: Image was taken with the 40x(NA=1.30) objective in oil. The image is 512 x 512 pixels and has a size of 317.331 x 317.331 $\mu\text{m}$ . The the lens fiber structure appears to be somewhat regular, with an exception along the anterior surface. This could be due to deformation of the tissue during the sectioning process. . . . .	102

7.8	Confocal Image of Lens Fibers: Image was taken with the 100x(NA=1.40) objective in oil. The image is 512 x 512 pixels and has a size of 126.728 x 126.728 $\mu\text{m}$ . This image provides a detailed view of the lens fiber cells near the anterior surface. . . . .	103
7.9	Confocal Image of Lens Fibers: Image was taken with the 40x(NA=1.30) objective in oil. The image is 512 x 512 pixels and has a size of 317.331 x 317.331 $\mu\text{m}$ . Lens fiber structure moving towards the middle of the section. . . . .	104
7.10	Confocal Image of Lens Fibers: Image was taken with the 40x(NA=1.30) objective in oil. The image is 512 x 512 pixels and has a size of 317.331 x 317.331 $\mu\text{m}$ . The structure of the lens fibers is harder to distinguish. This could be due to inadequate staining in the middle of the sample. . . . .	105
7.11	Confocal Image of Lens Fibers: Image was taken with the 100x(NA=1.40) objective in oil. The image is 512 x 512 pixels and has a size of 126.728 x 126.728 $\mu\text{m}$ . This image provides a detailed view of the lens fiber cells towards the middle of the section.	106
7.12	Confocal Image of Lens Fibers: Image was taken with the 40x(NA=1.30) objective in oil. The image is 512 x 512 pixels and has a size of 317.331 x 317.331 $\mu\text{m}$ . Image shows area where lens fibers were torn, near edge of sample. . . . .	107
7.13	Confocal Image of Lens Fibers: Image was taken with the 40x(NA=1.30) objective in oil. The image is 512 x 512 pixels and has a size of 317.331 x 317.331 $\mu\text{m}$ . Potentially another tear in the sample, cleaner than in Figure 7.12. . . . .	108
7.14	Modeling of Lens Fiber Ultrastructure using IMOD. . . . .	110
9.1	CAD Drawing of Environmental Bath and Test Fixtures Adapted to a Bose Electro-force TestBench System to Allow for Intermediate Strain Rate Testing in Fluid. . . .	116

# **Chapter 1**

## **Introduction**

The benefits of understanding the biomechanics of the ocular lens have far reaching implications for the research community, armed forces, and general populace. For example, currently accommodation (the process of the ocular lens focussing) as well as presbyopia (the loss of accommodation over time) are not fully understood. This is partly due to a lack of adequate material property determination and structure identification of the ocular lens. While research has been done to find the material properties [Bailey et al., 1993, Krag et al., 1997, Yang et al., 1998a, Krag and Andreassen, 2003b] and identify the ultrastructure of the ocular lens, specifically the lens capsule [Barnard et al., 1992], the majority of data suffers from many assumptions made in regards to the experimental techniques, such as 1-D/uniaxial measurements and alterations to the native structure of the tissue. Recently, work has been done to measure the multiaxial properties of the lens capsule [Heistand et al., 2005, Pedrigi et al., 2007, David et al., 2007] and material properties of the lens fibers [Erpelding et al., 2005, Reilly and Ravi, 2009], more work is needed. An increased understanding of the biomechanics and structure of the ocular lens are necessary to answer the question of how accommodation occurs and why presbyopia happens.

With a better understanding of the material properties and structure of the ocular lens, current surgical treatments for presbyopia (mainly intraocular lens replacement surgery) and cataract surgery can be improved. Design specifications of the IOLs such as elasticity and geometry could be optimized for the human lens [McLeod et al., 2003]. With the study of lens properties in regards to age, IOLs could be individually customized for the patient. The interactions of surgical devices



and prostheses can be computationally modeled and studied, allowing for the advancement of IOL and surgical device design. This could result in lower rates of complications after surgery as well as decreases in healthcare costs related to ocular treatments. In order for this to take place, more study is needed of the mechanical properties and ultrastructure of the ocular lens.

Trauma can occur to the ocular lens, either through blunt force contact, blast-wave loading (due to a percussive wave generated from an explosion), or through the introduction of an intraocular foreign body (IOFB, commonly small pieces of metal or glass). Partial or complete dislocation of the ocular lens can occur [Jain et al., 2004, Kim et al., 2009], as well as the formation of traumatic cataracts [Fineman et al., 2000, Nguyen et al., 2002] and perforation of the ocular lens [Mader et al., 1993, Mader et al., 2006]. Trauma to the lens is of particular interest to the armed forces and their personnel, especially in light of the increased use of improvised explosive devices (IEDs) in recent military actions [Muzaffar et al., 2000, Mader et al., 2006, Weichel and Colyer, 2008, Weichel et al., 2008, Colyer et al., 2008]. Ocular trauma can also occur in civilians in workplace accidents or during everyday life [Lee and Song, 2001]. Better material properties and structure identification are needed for the creation of an ultrastructurally based computational mechanical model. With such a model, the lens could be simulated under such trauma conditions. Information from simulations such as these could be used to better understand the mechanics of the injuries suffered to the ocular lens and lead to the design of adequate protective gear and improved treatments.

The goal of this work was to gather and analyze data towards the production of an ultrastructurally based computational mechanical model. The model is part of a larger area of research towards modeling the entire eye in a variety of conditions and producing simulations that lead to increased understanding of the ocular lens. This was done through mechanical testing of the ocular lens to determine material properties, specifically the whole porcine ocular lens and anterior porcine lens capsule tissue, and imaging of the ocular lens ultrastructure, specifically the anterior porcine lens capsule and the porcine lens fibers.

## Chapter 2

### Background

#### 2.1 Characteristics of the Lens

The ocular lens is a relatively small, transparent body placed behind the cornea and aqueous humor in the eye (see Figure 2.1). It is suspended between the aqueous humor and the vitreous humor by ciliary zonules which attach near the equator of the lens. The ciliary zonules are anchored to the ciliary body, which encircles the opening that the lens is suspended in. Within the ciliary body is the ciliary muscle. Through a process called accommodation, the lens (coupled with the curvature of the cornea) allows for the focussing of near and far images by changing its shape. Currently, the most widely held theory of accommodation is the Helmholtz Theory [Burd et al., 1999, Glasser and Campbell, 1999, Martin et al., 2005, Stachs et al., 2005], originally introduced in 1855 [Helmholz, 1855]. The theory states the lens is accommodated and in its lowest stressed state when the tension in the zonules are relaxed [Krag and Andreassen, 2003a]. This occurs when the ciliary muscle contracts. With the ciliary muscle relaxed, the zonules are put into tension thus flattening the lens and putting it in the un-accommodated state. Figure 2.2 shows the un-accommodated state on the left and the accommodated state on the right.

Presbyopia is the loss of accommodation of the lens as we age. It has been proposed that presbyopia occurs due to a change in the mechanical properties of the eye over time. Some have attributed this to a change in the mechanical properties of the lens internal substance and the lens capsule [Beers and van der Heijde, 1996, Glasser and Campbell, 1998, Glasser and Campbell, 1999, Heys et al., 2004a, Breitenfeld et al., 2005, Richdale et al., 2008, Ziebarth et al., 2008] some to a

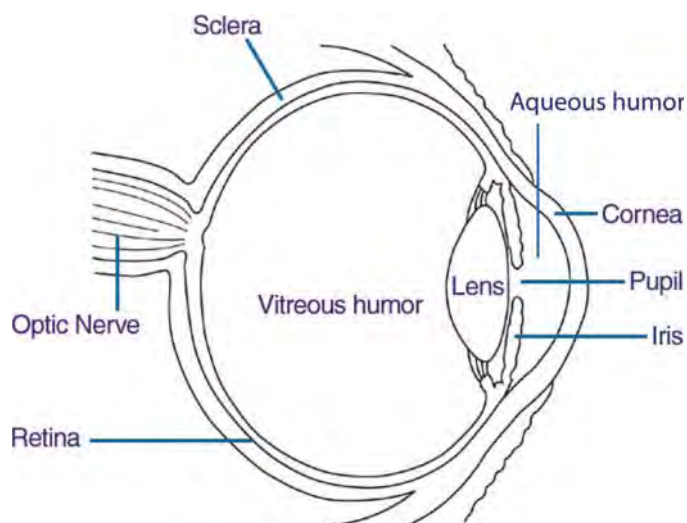


Figure 2.1: General Anatomy of the Eye (nei.nih.gov).

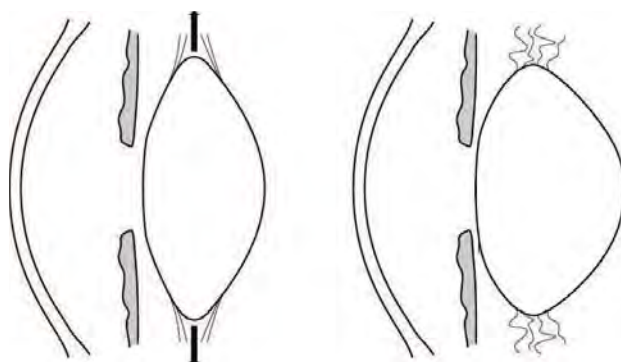


Figure 2.2: Theory of How Accommodation Occurs: On the left the lens is shown in the unaccommodated state, where the zonules are in tension. On the right the lens is shown in the accommodated state, where the zonules are not in tension due to the contraction of the ciliary muscle [McLeod et al., 2003].

change in the zonules [Stachs et al., 2005], and others to a change in the ability of the ciliary muscle to contract [Abolmaali et al., 2007]. Previous work has shown that a change in the lens's mechanical properties results in a decrease of the accommodative power of the lens [Krag and Andreassen, 1996, Krag et al., 1997, Glasser and Campbell, 1998, Krag and Andreassen, 2003a, Strenk et al., 2004, Heys et al., 2004a, Weeber et al., 2005]. Although prior work has been done to characterize the mechanical properties of the lens [Krag et al., 1997, Glasser and Campbell, 1999, Weeber et al., 2005, Heistand et al., 2005], there has not been enough work for people to agree on one set of properties or range of properties. To fully comprehend the mechanisms of presbyopia, an understanding of the mechanical properties of the ocular lens is needed. The ocular lens is comprised of 2 main parts, shown in Figure 2.3. A more detailed description of each part is provided below.

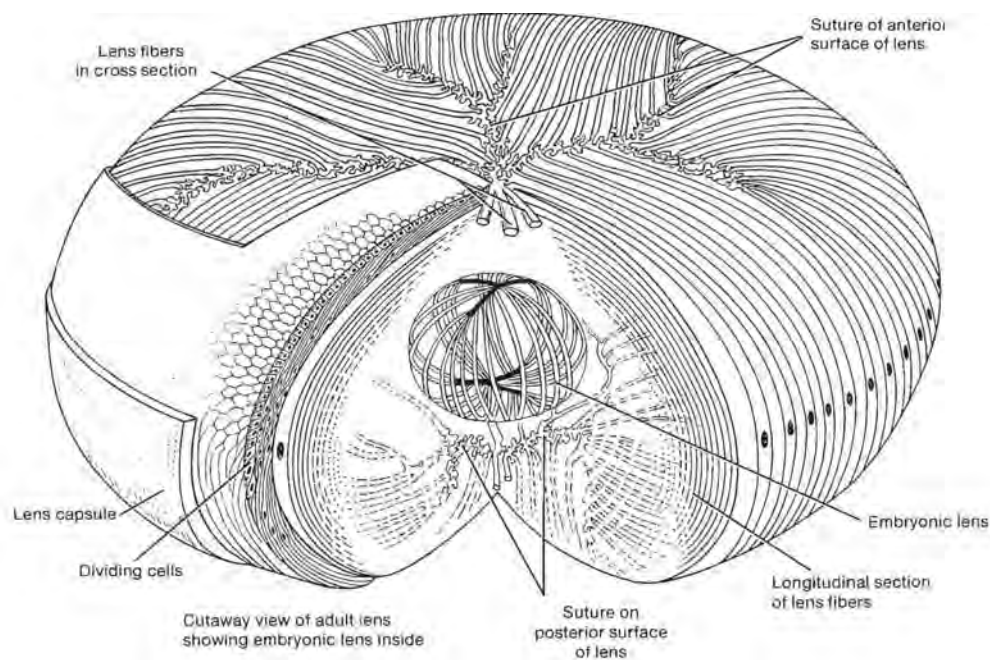


Figure 2.3: Detailed Anatomy of the Ocular Lens [Kessel and Kardon, 1979].

### 2.1.1 Capsule

The exterior portion of the ocular lens is the lens capsule. The capsule acts as a bag-like membrane for the lens, containing the lens fibers and helping to maintain the proper ionic

balance for the lens fibers. The ultrastructure of the lens capsule is a type-IV collagen 3-D mesh-work [Barnard et al., 1992]. This mesh-work provides for nearly 65% of the dry weight of the lens capsule, acting as a support structure [Barnard et al., 1992]. The human lens capsule thickness has been found to vary depending on radial location and anterior vs posterior surfaces. The anterior thickness varies from 11-33  $\mu\text{m}$  while the posterior thickness varies from 4-9  $\mu\text{m}$  [Krag et al., 1997, Krag and Andreassen, 2003b]. As mentioned earlier, ciliary zonules attach to the lens along its equator, interweaving with the lens capsule [Stachs et al., 2005]. Through this attachment, it is thought that the tension in the zonules is transmitted to the lens capsule, allowing it to deform the interior lens fibers when in the un-accommodated state [Beers and van der Heijde, 1996]. The lens capsule continues to grow throughout most of life [Krag and Andreassen, 2003a].

### **2.1.2 Lens Fiber Cells**

The lens fibers make up the majority of the volume of the ocular lens. They are contained within the lens capsule. A gel-like substance, the lens fibers cells are elongated cells comprised mainly of proteins called crystallins [Kaufman and Alm, 2003]. These cells are arranged in layers [Kessel and Kardon, 1979], much like an onion, as can be seen in Figure 2.3. The interior lens fibers are separated into 2 main regions: the inner nucleus, and the outer cortex [Kaufman and Alm, 2003]. It has been found in studies that the interior nucleus is stiffer than the cortex [Heys et al., 2004a, Erpelding et al., 2005]. Cross-sectional area of the lens fiber cells has been found to range from 5  $\mu\text{m}^2$  to 148  $\mu\text{m}^2$ , depending on the region [Taylor et al., 1996]. It has been shown that misalignment of the lens fiber cells by trauma or IOFBs can result in formation of cataracts [Rofagha et al., 2008]. New lens fibers are produced along the lens capsule throughout most of life [Kaufman and Alm, 2003].

## **2.2 Previous Research**

### **2.2.1 Capsule**

#### **2.2.1.1 Property Determination**

Various research has been completed to characterize the mechanical properties of the lens. One study done by Krag, et al. (1997) involved cutting the anterior lens capsule into circular segments using a laser and then stretching these circular segments uniaxially and measuring the force response. One issue with this test is that by sectioning the lens capsule into circular segments essentially destroys the native structure and in vivo stress condition of the lens capsule, resulting in a different force response than native tissue. Also, this test neglected preconditioning of the lens capsule, which is frequently necessary when testing biological tissue [Fung, 1993]. One study looked at puncturing whole lenses [Yang et al., 1998a]. The test was limited in its force measuring technique, based off of a spring with a weight attached, a machine to lower the spring, and a stopwatch. More recently, Heistand, et al. (2005) developed an experiment to measure the multiaxial mechanical behavior of the anterior lens capsule. The experiment involves two cameras measuring the displacement of microspherules on the anterior surface of the lens capsule as it is inflated with fluid [Heistand et al., 2005]. Other multiaxial strain research has been done [David et al., 2007, Pedrigi et al., 2007] as well as work involving a multiaxial lens stretcher [Reilly et al., 2008]; however, more data is needed to find conclusive results.

Additionally, several modeling studies involving the lens capsule assume it to be an elastic material [Burd et al., 2002, Burd et al., 1999, Liu et al., 2006, Pedrigi and Humphrey, 2011]. However, experiments have shown viscoelastic behavior of the lens capsule [Thim et al., 1993, Krag and Andreassen, 2003a].

#### **2.2.1.2 Structure Identification**

Little work has been done with regard to the identification of the ultrastructure of the lens capsule [Barnard et al., 1992]. Barnard utilized cryoelectron microscopy to image lens capsule

[Barnard et al., 1992]. The process involved with preparing the sample for the imaging, unfortunately, has the high probability of altering the native structure of the lens capsule. After being frozen in a high-pressure freezer, the samples were subjected to extraction in order to remove the material between the type-IV collagen fibers. This step can result in overall dimension and stress changes as the material between the mesh-work can act to support or even push apart the fibers. After extraction, samples underwent a platinum deposition, creating a replica of the type-IV collagen mesh-work. Due to the inconsistencies of the depositions layers inherent with the process, the true thickness and spacing of the fibers cannot be observed as they have been enlarged by unequal amounts. Additionally, the data presented was only 2-dimensional, when 3-dimensional structure identification is needed.

## **2.2.2 Lens Fiber Cells**

### **2.2.2.1 Property Determination**

Microindentation of the interior lens fibers was performed by Reilly, et al. (2009). Porcine lenses were immersed in preserving medium shortly after death and then fixed within a gel for sectioning [Reilly and Ravi, 2009]. Lenses were bisected along the optical axis or in the equatorial plane through the middle of the lens [Reilly and Ravi, 2009]. Lens fibers were then microindented and the force response was measured. The sectioning process involved can lead to the damaging of the lens fibers or the alteration of material properties. Another test involved using a fine conical probe to measure the resistance to penetration of different layers of the lens [Pau and Kranz, 1991]. Again, the damage done to the lens fiber cells is not ideal when measuring their material properties.

### **2.2.2.2 Structure Identification**

Transmission electron microscopy and scanning electron microscopy have both been done on the lens fibers to image the ultrastructure and organization of the fiber cells [Taylor et al., 1996, Kessel and Kardon, 1979]. This has resulted in decent results, but the preparation and fixation processes used can result in alteration of the native structure of the lens fibers. Additionally, fluores-

cent confocal microscopy has been done [O'Connor et al., 2008, Shestopalov and Bassnett, 2000], but more data is needed, specifically analysis of the 3-D nature of the structure to include in an ultrastructurally based computational model.

### **2.3 What is Needed**

While there has been an increased focus on researching the ocular lens, its properties, and behavior, an accurate model that is based off of the ultrastructure of the involved tissues has not been generated. We are aware of only one model that has included ultrastructure data in their model [Burd, 2009] for the lens capsule. Furthermore, majority of models do not model the lens as viscoelastic, neglecting this part of the tissues behavior nor the potential poroelasticity of the lens capsule (thickest basement membrane in the human body). What is needed is a ultrastructurally based computational finite element model which will allow for the simulation various conditions, leading to increased understanding of the ocular lens and its mechanics. In order for this to be possible, more testing is needed to generate data from which material properties can be calculated. Also, further imaging is needed of the ultrastructure of the lens capsule and lens fibers, focussing on the 3-D nature of the structure. The data gathered from the following work is a first step toward the creation of such a model.



## Chapter 3

### Parameter Fitting of Unconfined Compression Testing Data

In order to create a computational mechanical model of the ocular lens, the material properties of the lens must be known. While previous work has been completed on determining the material properties of the lens as mentioned earlier, varying methods and assumptions have not produced a defining set of material properties. Unconfined compression testing was completed in order to produce data that could be used to determine the material properties of the whole ocular lens, specifically  $\tau$  (relaxation time constant),  $\mu_{\text{EQ}}$  (equilibrium shear modulus), and  $\mu_{\text{NEQ}}$  (nonequilibrium shear modulus). From these properties, bulk moduli and viscosities can also be calculated, as described in the Methods of Fitting Parameters section. The data were fitted using DAKOTA (Design Analysis Kit for Optimization and Terascale Applications) which is developed by Sandia National Laboratories ([dakota.sandia.gov](http://dakota.sandia.gov)). Once approximate fits were found, meshes were generated using CUBIT, a geometry and mesh generation toolkit also developed by Sandia National Laboratories ([cubit.sandia.gov](http://cubit.sandia.gov)). Images of lenses before being tested were taken for 2 test groups. From these images, geometric data were collected and used in the generation of the meshes. With the parameters determined from the data fits and the mesh generations, simulations were run for particular cases of each test group using Tahoe, a research-oriented platform geared towards the development of numerical methods and material models. Tahoe was initially developed by Sandia National Laboratories ([tahoe.sourceforge.net](http://tahoe.sourceforge.net)) and is currently being developed by several academic and industry partners. Furthermore, preliminary modeling in Abaqus ([www.simulia.com](http://www.simulia.com)) is being completed, to compare with Tahoe results and investigate the material properties. The first round

of tests (completed by a previous student) included preconditioning (as described in the Previous Testing Done section). The idea being that the lens is in a preconditioned state within the eye as it constantly focuses and accommodates. Also, as mentioned earlier, it is known that biological tissue often requires preconditioning when collecting data [Fung, 1993]. A second round of tests has been completed without preconditioning and fits are currently being generated (the testing data are shown below in Section 3.6) for comparison with the preconditioned data and to show the lenses' initial response characteristics.

### 3.1 Previous Testing Done

A previous student, Laura Hatanaka, completed a series of unconfined compression testing on whole ocular porcine lenses. Whole ocular globes were collected and shipped by Animal Technologies, Inc. (Tyler, TX), overnight on wet ice. Upon receipt, the whole lenses were extracted by making an incision approximately midway in the sclera and cutting through the sclera until the lens could be accessed from the posterior direction (see Figure 3.1).



Figure 3.1: Dissection of Globe to Remove Ocular Lens.

Excess vitreous humor was removed with tweezers and scissors. The zonules were then cut around the lens, and the lens was fully extracted from the globe. Excess zonules were removed by rolling the lens along its equator on tissue paper (see Figure 3.2).

Lenses were then transported in Alcon Balanced Salt Solution (BSS) to the MTS Insight II electromechanical testing system for testing. A 2N load cell (sensitivity: 2.04 mv/V) was used to



Figure 3.2: Removing Excess Zonules from Ocular Lens with Tissue Paper.

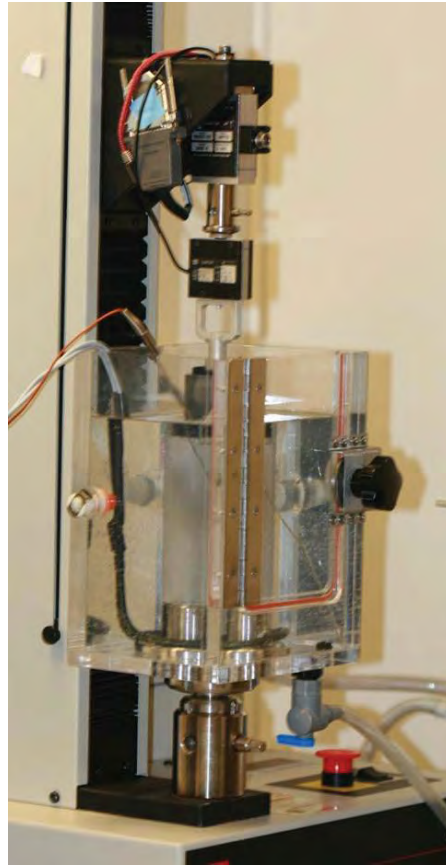
record the force exerted by the lens in each test. The lens was placed in a pedestal containing Alcon BSS (see Figure 3.3a ). The testing pedestal was surrounded by a heated water bath within an environmental chamber (see Figure 3.3b). The water bath was heated to 37 °C to help approximate in vivo conditions.

The lens was tested with the anterior surface facing downwards, due to the greater curvature of the posterior surface and the lens's natural tendency to rest on its anterior surface when free (see Figure 3.4). The lens was compressed by a flat platen (the platen can be seen at the top of Figure 3.4).

Tests were completed on tissue from two different tissue age groups: from pigs aged 6-9 months or pigs aged 2 or more years. Tissue from each age group was compressed to 2 strains (10% and 20%) at 2 loading rates (0.1 mm/s and 0.3 mm/s). For each test group, 10 samples were tested for a total of 80 lenses. A summary of the testing configurations and number of samples can be seen in Table 3.1. Lenses underwent preconditioning through 5 cycles of testing. The first 2 cycles would load and unload the lens to the desired strain 2 times and then load and hold the lens at the desired strain for 200 seconds. The last 3 cycles would load and unload the lens to the desired strain 3 times and then load and hold the lens at the desired strain for 350 seconds. See Figure 3.5 to view an example of preconditioning. For the parameter fitting, only the last load and hold curve was used.



(a) Testing Pedestal with BSS Solution in Testing Platform.



(b) Test Setup for Unconfined Compression Testing.

Figure 3.3: Test Setup for Unconfined Compression Testing.

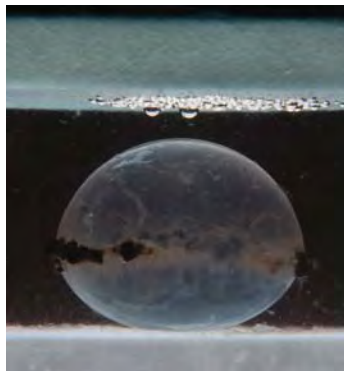


Figure 3.4: Shape of Lens (Anterior Surface Facing Down) Testing in Testing Platform, Showing Upper Load Platen.

Table 3.1: Unconfined Compression Testing Conditions and Number of Whole Ocular Porcine Lenses Tested With Preconditioning.

Loading Rate	Age of Tissue			
	Strain			
	6-9 month 10%	6-9 month 20%	2+ year 10%	2+ year 20%
0.1 mm/s	10	10	10	8
0.3 mm/s	10	10	10	10

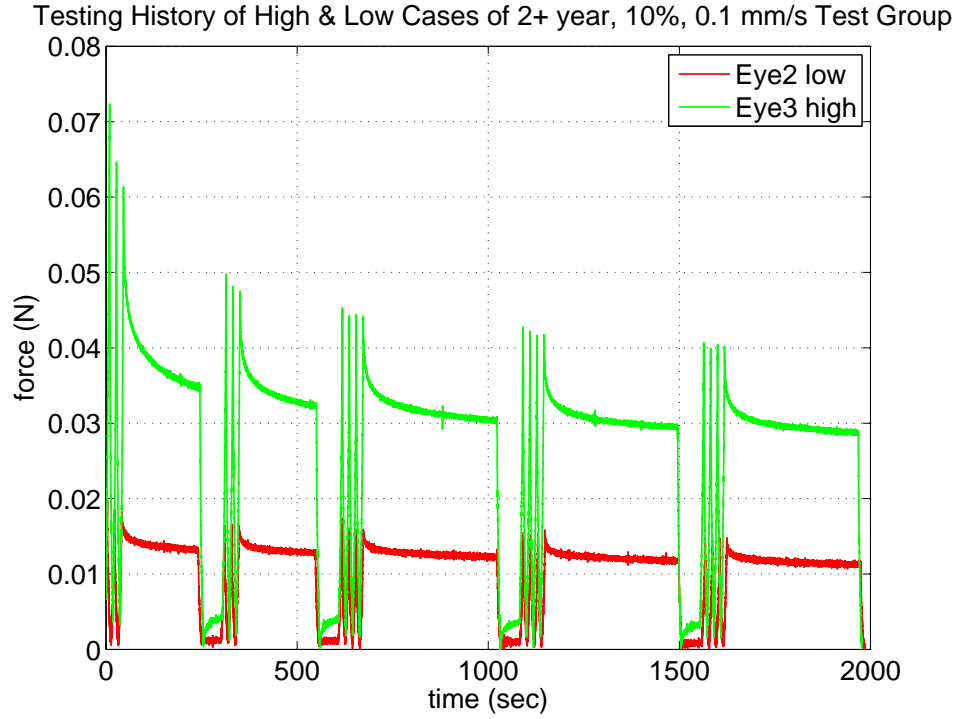


Figure 3.5: Example Showing Data with Preconditioning.

Below are graphs showing the previous data that were collected. As mentioned above, only the last load and hold curve of the test was used in the parameter fitting. Each graph shows the 10 eyes tested for that test group.

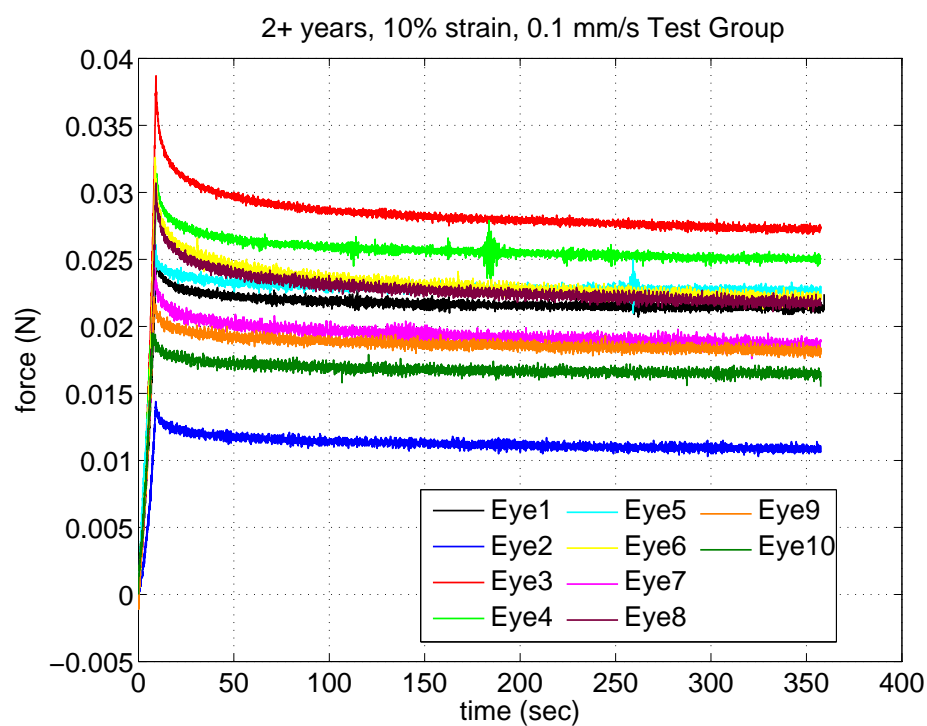


Figure 3.6: Graph of all eyes from the 2+ year 10% strain 0.1 mm/s Group.

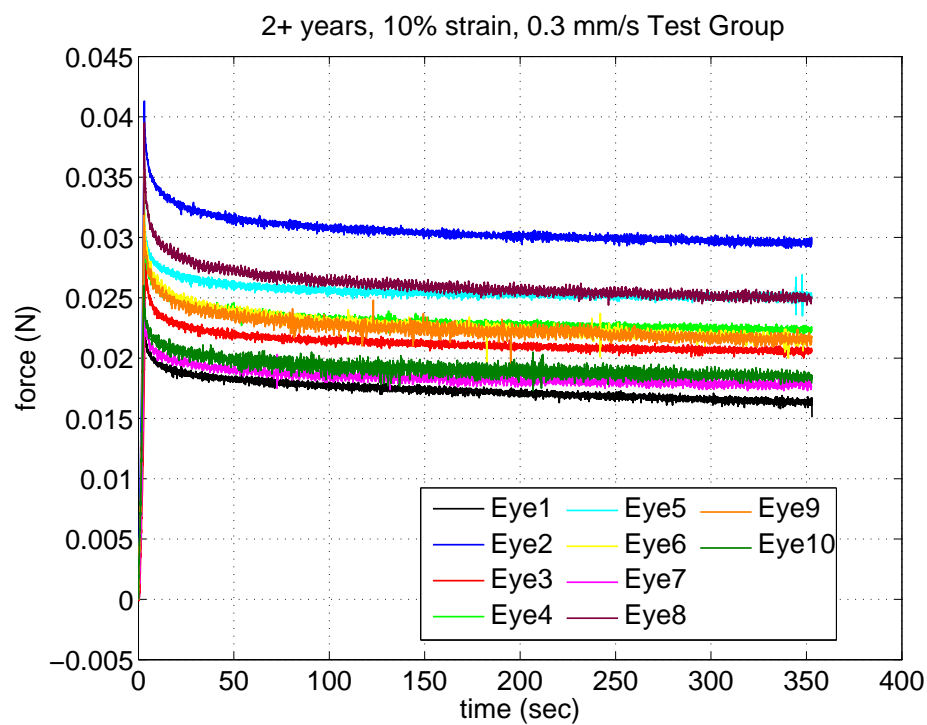


Figure 3.7: Graph of all eyes from the 2+ year 10% strain 0.3 mm/s Group.

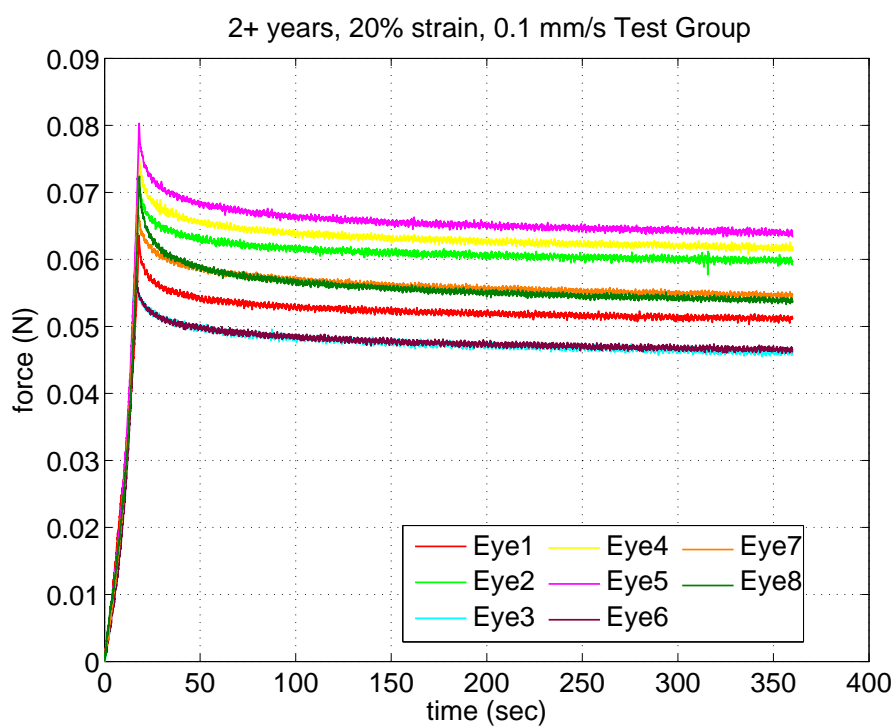


Figure 3.8: Graph of all eyes from the 2+ year 20% strain 0.1 mm/s Group.

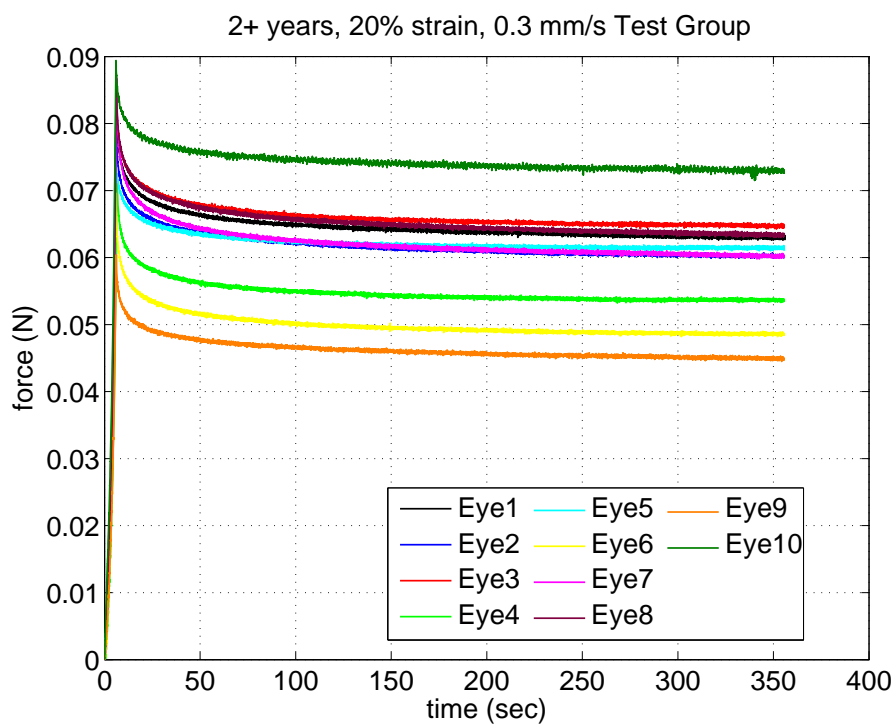


Figure 3.9: Graph of all eyes from the 2+ year 20% strain 0.3 mm/s Group.

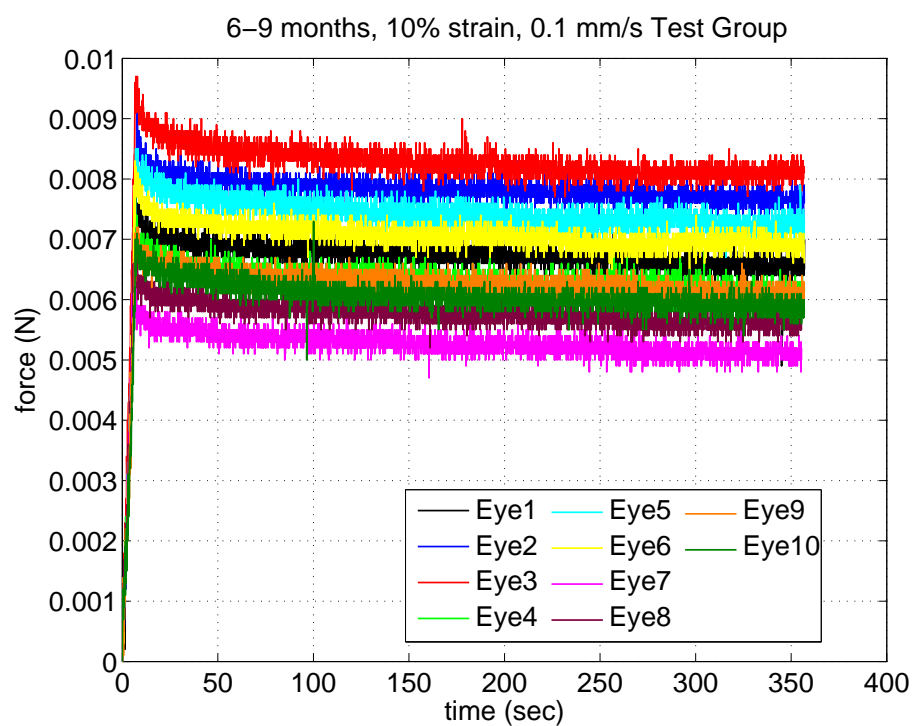


Figure 3.10: Graph of all eyes from the 6-9 month 10% strain 0.1 mm/s Group.

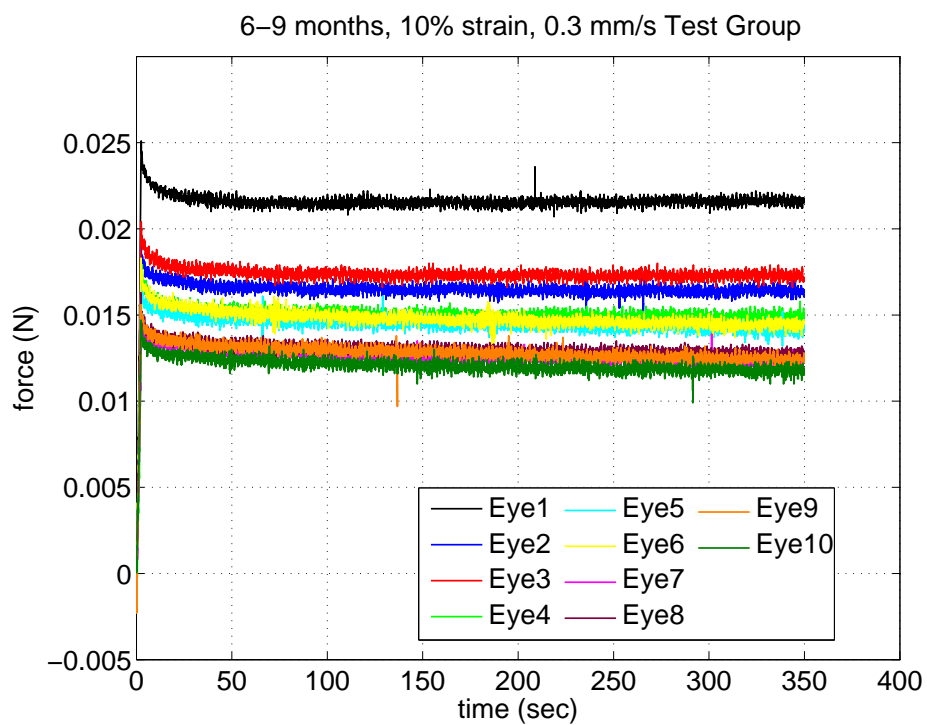


Figure 3.11: Graph of all eyes from the 6-9 month 10% strain 0.3 mm/s Group.



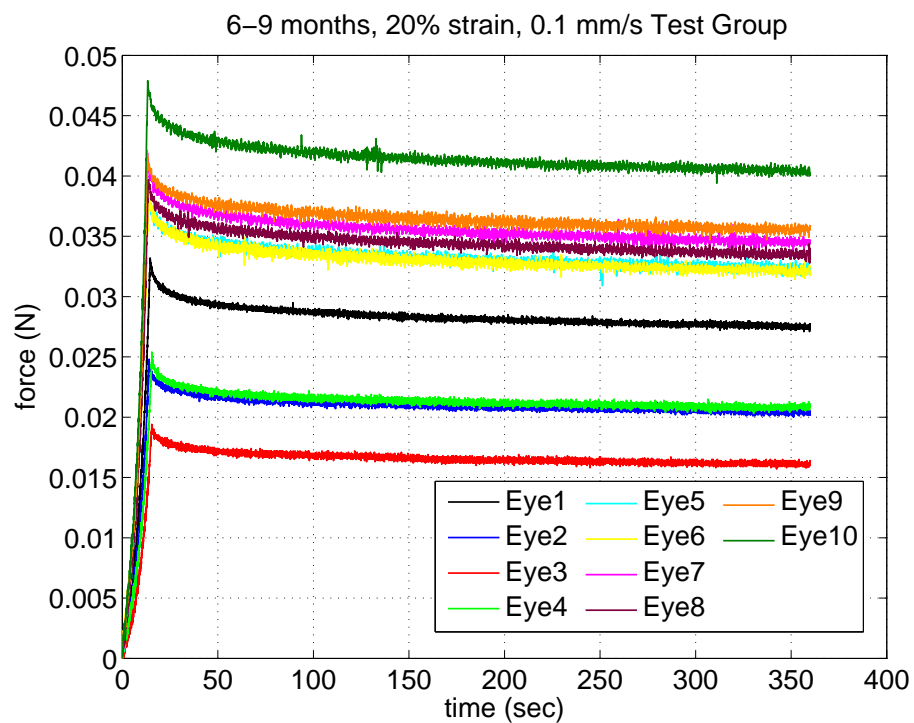


Figure 3.12: Graph of all eyes from the 6-9 month 20% strain 0.1 mm/s Group.

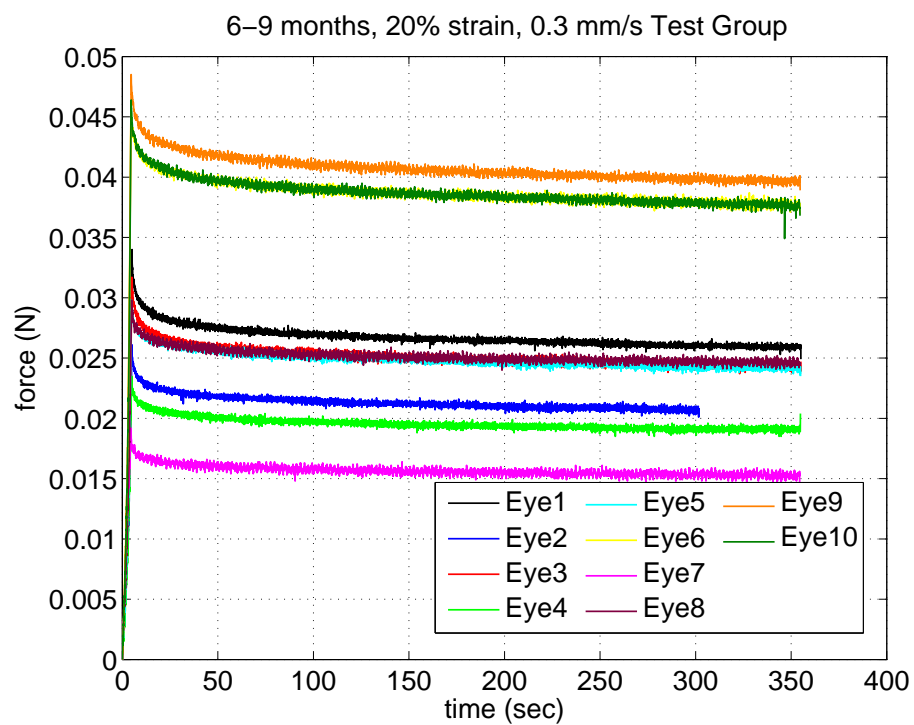


Figure 3.13: Graph of all eyes from the 6-9 month 20% strain 0.3 mm/s Group.

### 3.2 Methods of Fitting Parameters

DAKOTA (dakota.sandia.gov) was used for optimizing the parameters during the data fitting process. A constitutive framework based off of a finite deformation, isotropic, viscoelasticity model developed by Reese and Govindjee [Reese and Govindjee, 1998] was implemented within Tahoe (tahoe.sourceforge.net) by Prof. Thao (Vicky) Nguyen (Johns Hopkins University), and being used by Prof. Richard Regueiro (University of Colorado Boulder) and his research group. The input parameters for Tahoe are  $\tau$  (relaxation time constant),  $\mu_{EQ}$  (equilibrium shear modulus), and  $\mu_{NEQ}$  (nonequilibrium shear modulus). From these parameters, the bulk moduli and viscosities can be calculated. Equations 3.1 through 3.5 show how to calculate the bulk moduli ( $\kappa_{EQ}$  and  $\kappa_{NEQ}$ ) and the viscosities ( $\eta_D$  and  $\eta_V$ ). Figure 3.14 shows an analogy of the model implemented in Tahoe to a standard linear solid. The upper spring provides for the long-term elastic effects of the lens tissue while the bottom dashpot and spring in series provides for the viscoelastic properties.

$$\kappa_{EQ} = A\mu_{EQ} \quad (3.1)$$

$$\kappa_{NEQ} = A\mu_{NEQ} \quad (3.2)$$

$$\eta_D = \tau\mu_{NEQ} \quad (3.3)$$

$$\eta_V = \tau\kappa_{NEQ} \quad (3.4)$$

$$A = 100(\text{capsule}), 1000(\text{substance}) \quad (3.5)$$

Additionally, meshes were generated based off of the geometric data gathered from the images of the lenses. Images of the lenses were overlaid with a coordinate grid and coordinates were taken along the right side of the lens starting from the midpoint on the bottom of the lens to the midpoint at the top of the lens. These coordinates were normalized from 0 to 1 and then multiplied by the height of the lens, previously measured during testing. For lenses that were not imaged, an average set of coordinates normalize from 0 to 1 were used, multiplied by the height of the non-imaged lens. Using these coordinates, 2-D axisymmetric meshes (see Figure 3.15) were generated with the

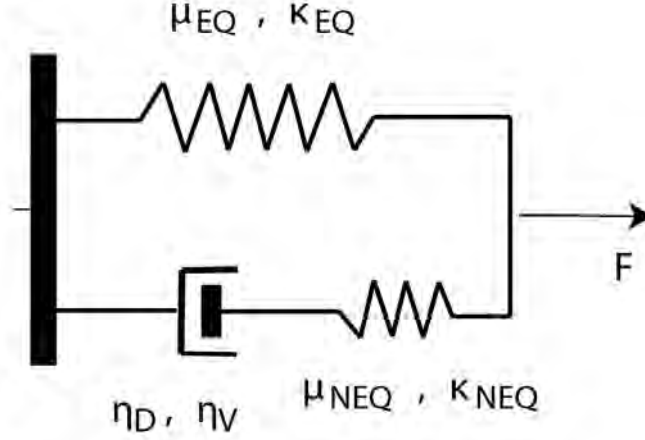


Figure 3.14: Analogy of Model Implemented in Tahoe to a Standard Linear Solid.

software CUBIT ([cubit.sandia.gov](http://cubit.sandia.gov)). Meshes were setup such that they had 2 sections: the outer lens capsule and the interior lens fibers (see Figure 3.15). The thickness of the capsule is  $60\text{ }\mu\text{m}$ , based off of the measurements of previous work [Krag and Andreassen, 1996].

An initial guess of the 3 material properties  $\tau$  (relaxation time constant),  $\mu_{EQ}$  (equilibrium shear modulus), and  $\mu_{NEQ}$  (nonequilibrium shear modulus) was made with lower and upper bounds for each parameter. DAKOTA then utilized the model in Tahoe and the generated mesh for each lens as it completed 27 different variations of the initial parameter guesses. Once finished, plots of force vs. time from the simulations were analyzed and used to adjust the parameter guesses. This process was completed until a satisfactory approximate fit was achieved. Out of each test group, the highest and lowest force vs. time curves were fitted.

### 3.3 Sample Preparation

Sample preparation for the first round of testing is described above in Previous Testing Done. Sample preparation for the second round of testing differed slightly and is described below. As before, whole ocular globes were collected and shipped by Animal Technologies, Inc. (Tyler, TX), overnight on wet ice. Upon receipt, the whole lenses were extracted by first removing the cornea. This was done by making a small incision in the cornea with a diamond-head scalpel and cutting

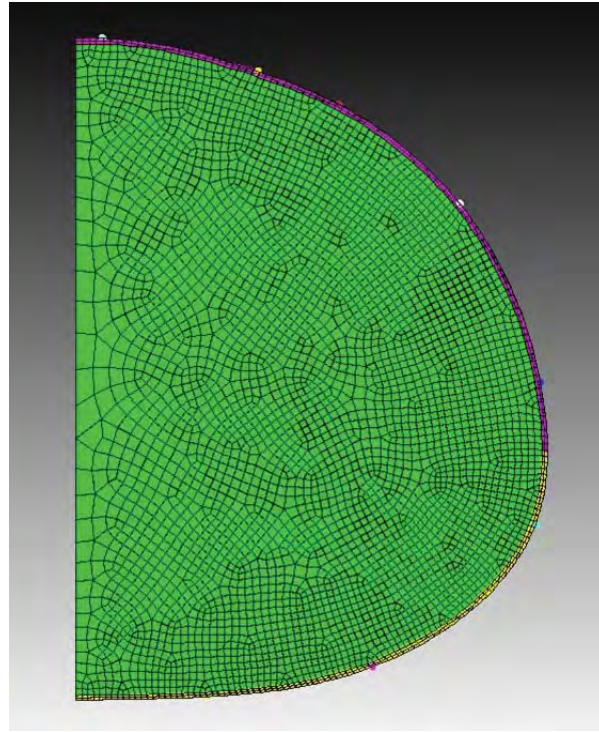


Figure 3.15: Example of Lens Mesh Generated by CUBIT - Notice the two sections: the exterior lens capsule (yellow and purple) and the interior lens fiber cells (green).

around the cornea with a pair of curved microsurgery scissors. Once the cornea was removed, the processed was repeated by making an incision through the zonules and cutting around the zonules until the whole lens was free. Excess zonules were removed as described earlier, and the whole lenses were transported in Alcon BSS to the MTS Insight II.

### 3.4 Experimental Setup

The same MTS Insight II testing system was used as describe earlier. Lenses were loaded in the same testing pedestal as used before (see Figure 3.3a) and used the same water bath heated to 37 °C. The same flat loading platen was used (can be seen in the top of Figure 3.4).

### 3.5 Experimental Method

Whole porcine ocular lenses were tested with the same test groups as before, only this time there were 5 samples per test group. No preconditioning was used and the lenses were loaded to the defined strain at the defined loading rate and held there for 350 seconds. A summary of the test configurations and samples per test can be seen below in Table 3.2. Images of each lens tested were taken pre-test and the tests were video recorded to get gross deformation of the lenses as they were loaded.

Table 3.2: Unconfined Compression Testing Conditions and Number of Whole Ocular Porcine Lenses Tested With No Preconditioning

Loading Rate	Age of Tissue			
	Strain			
	6-9 month 10%	6-9 month 20%	2+ year 10%	2+ year 20%
0.1 mm/s	5	5	5	5
0.3 mm/s	5	5	5	5

### 3.6 Results

Below are the overall testing history and parameter fits generated for the high and low curves of each test group with pre-conditioning. Fits are approximate and the next iteration of parameter fits will be done after adjustments to the constitutive framework within Tahoe.

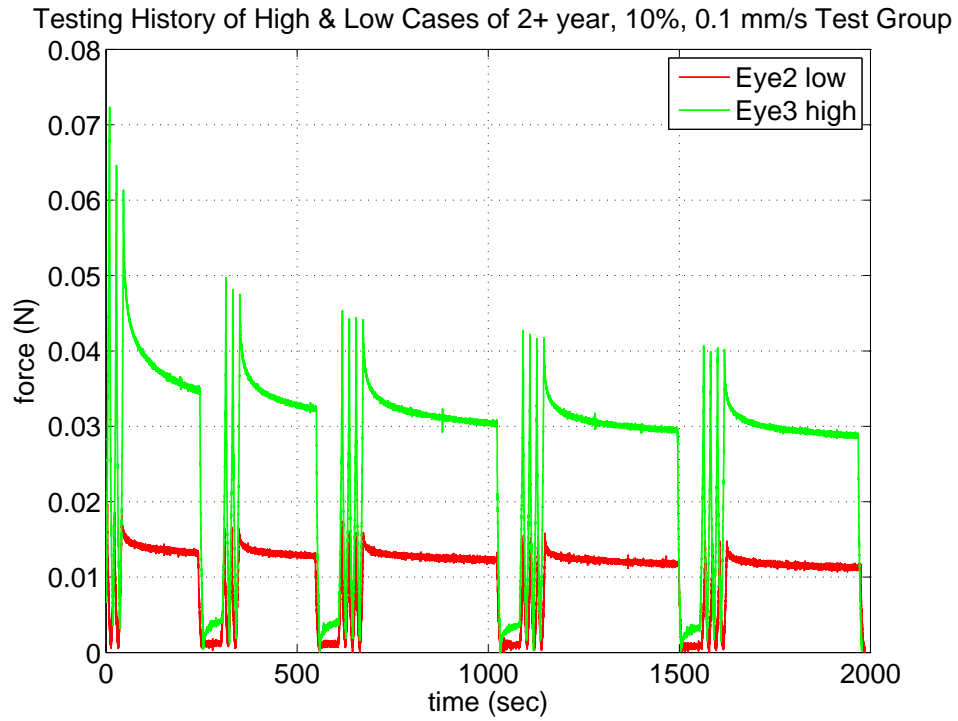


Figure 3.16: Graph of Eye2 and Eye3 from the 2+ year 10% strain 0.1 mm/s Group.

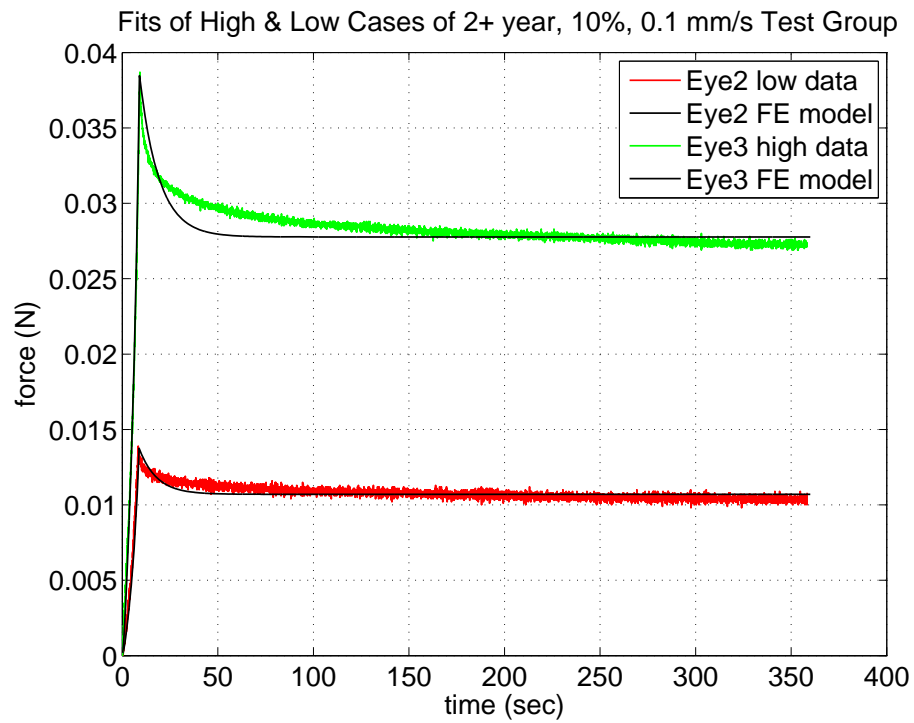


Figure 3.17: Graph of Eye2 and Eye3 vs Tahoe from the 2+ year 10% strain 0.1 mm/s Group.

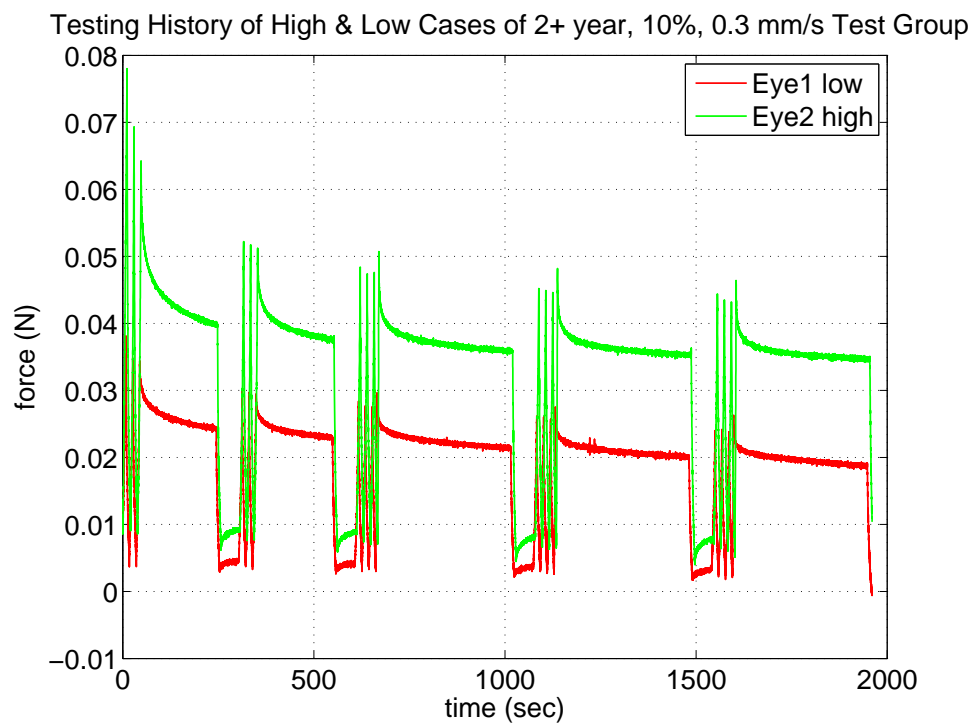


Figure 3.18: Graph of Eye1 and Eye2 from the 2+ year 10% strain 0.3 mm/s Group.

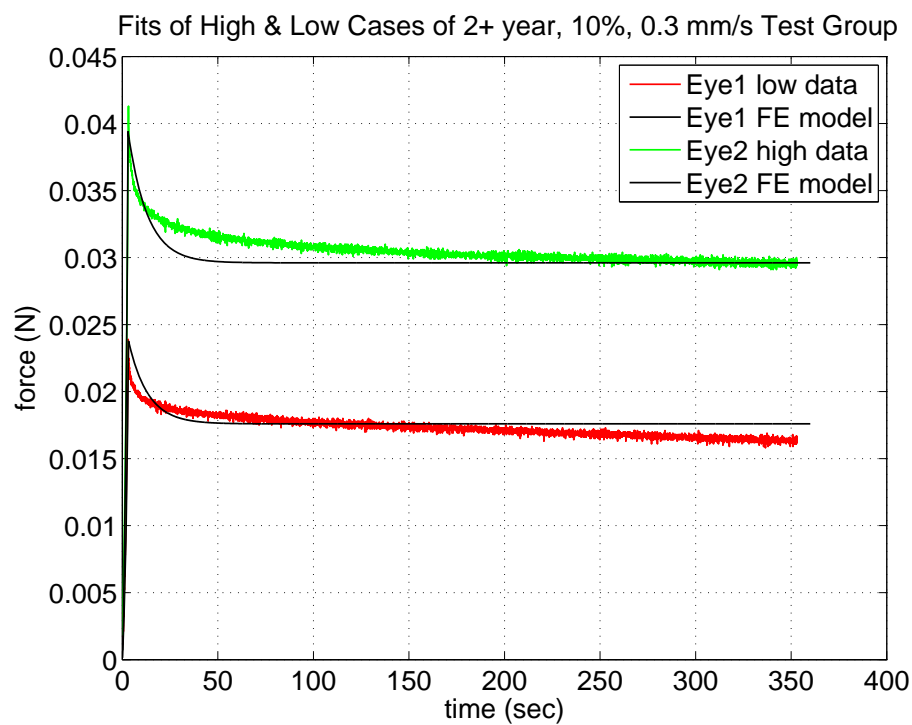


Figure 3.19: Graph of Eye1 and Eye2 vs Tahoe from the 2+ year 10% strain 0.3 mm/s Group.

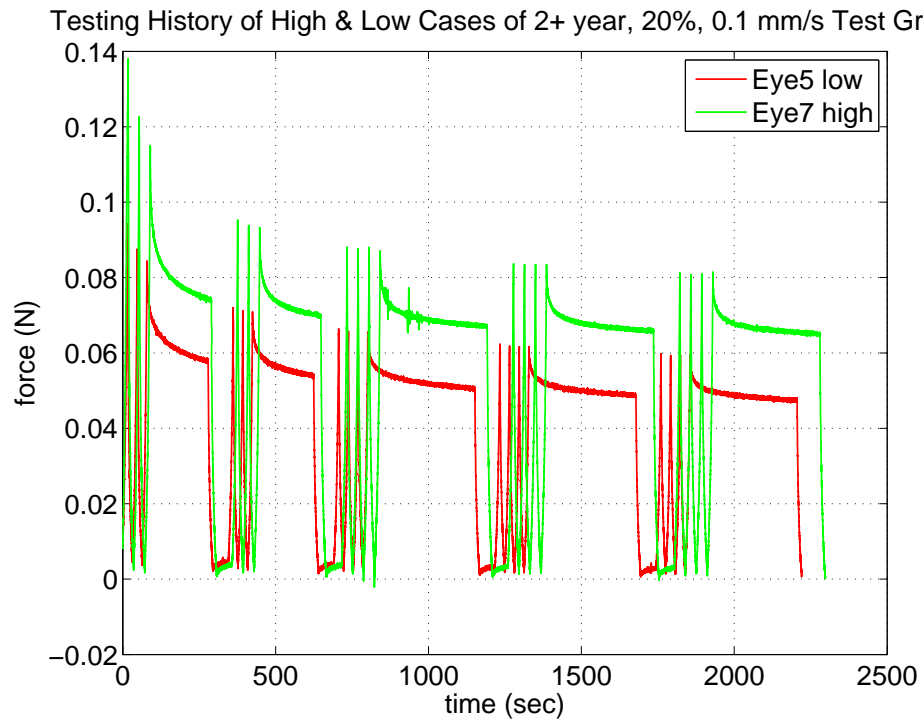


Figure 3.20: Graph of Eye5 and Eye7 from the 2+ year 20% strain 0.1 mm/s Group.

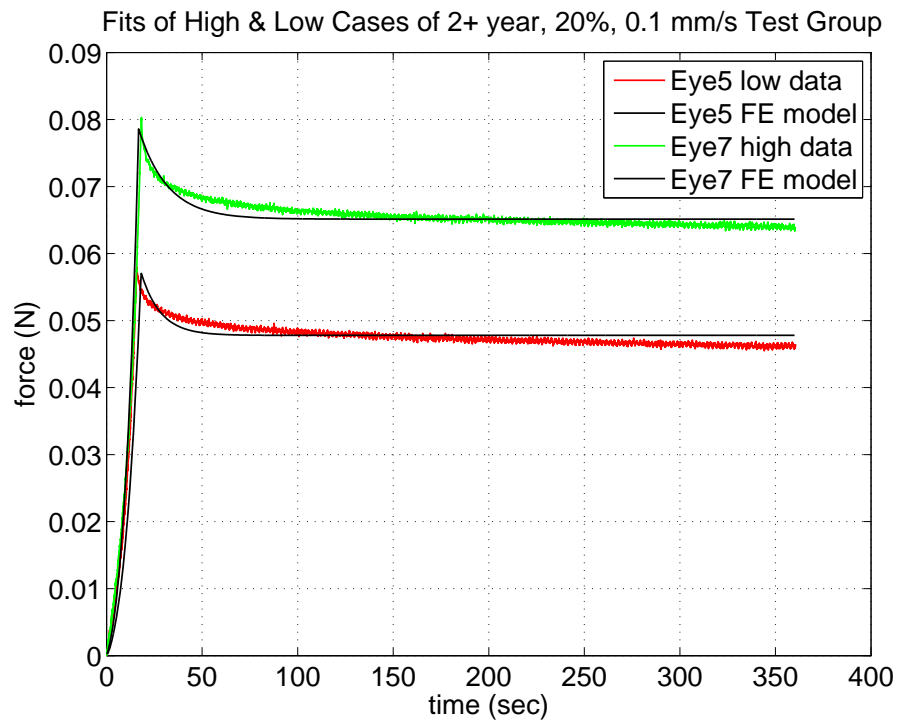


Figure 3.21: Graph of Eye5 and Eye7 vs Tahoe from the 2+ year 20% strain 0.1 mm/s Group.



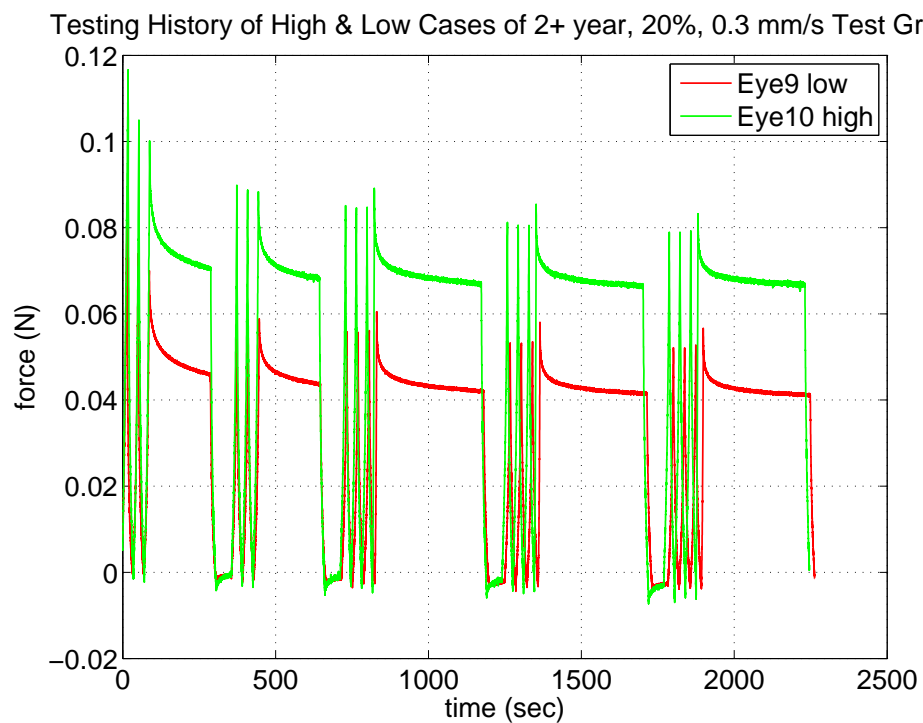


Figure 3.22: Graph of Eye9 and Eye10 from the 2+ year 20% strain 0.3 mm/s Group.

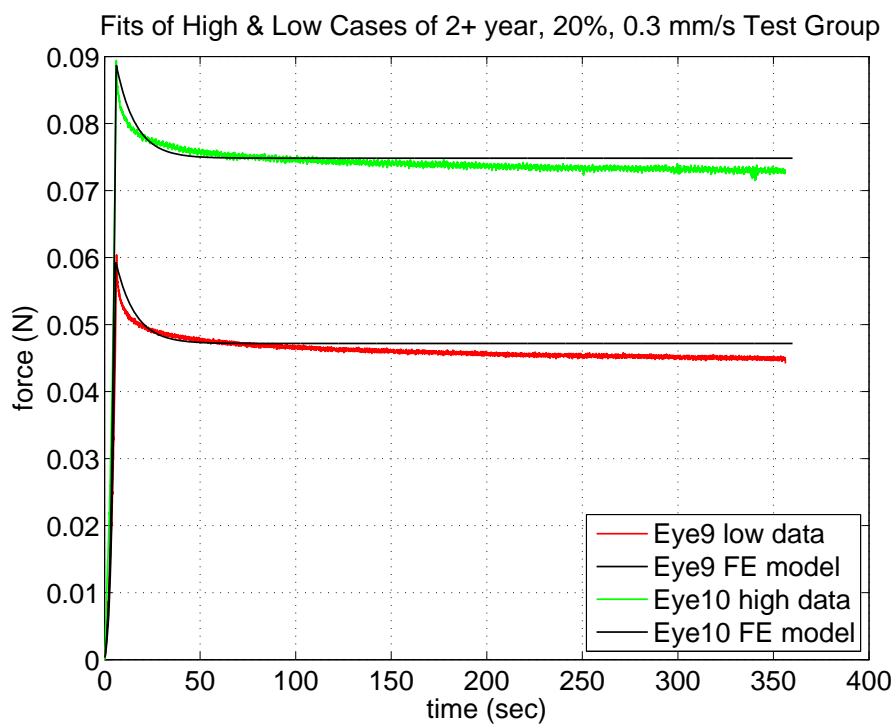


Figure 3.23: Graph of Eye9 and Eye10 vs Tahoe from the 2+ year 20% strain 0.3 mm/s Group.

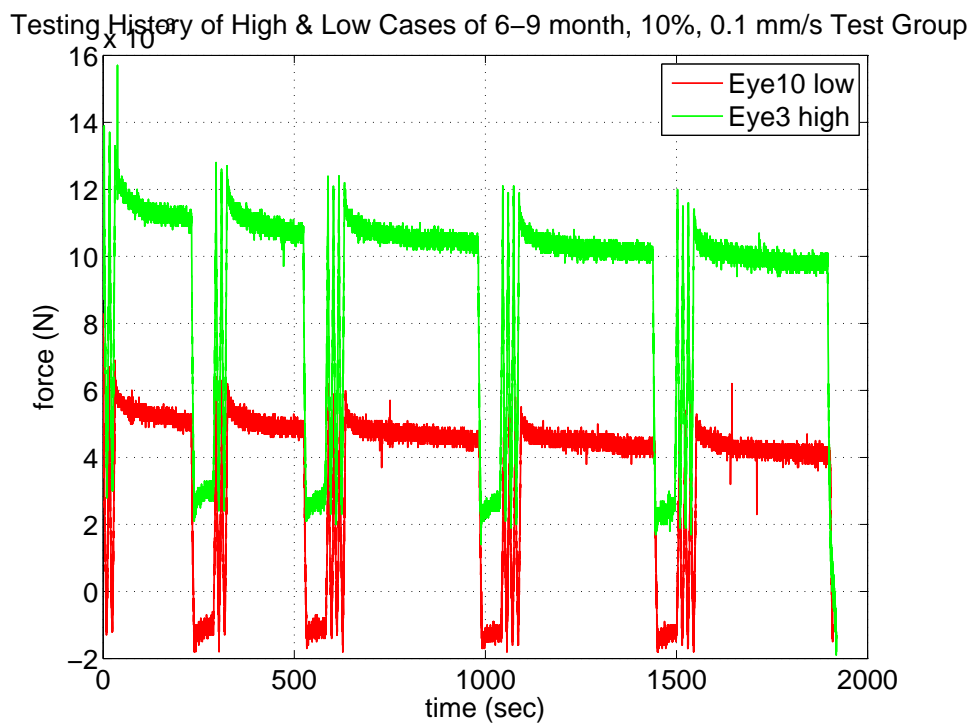


Figure 3.24: Graph of Eye10 and Eye3 from the 6-9 month 10% strain 0.1 mm/s Group.

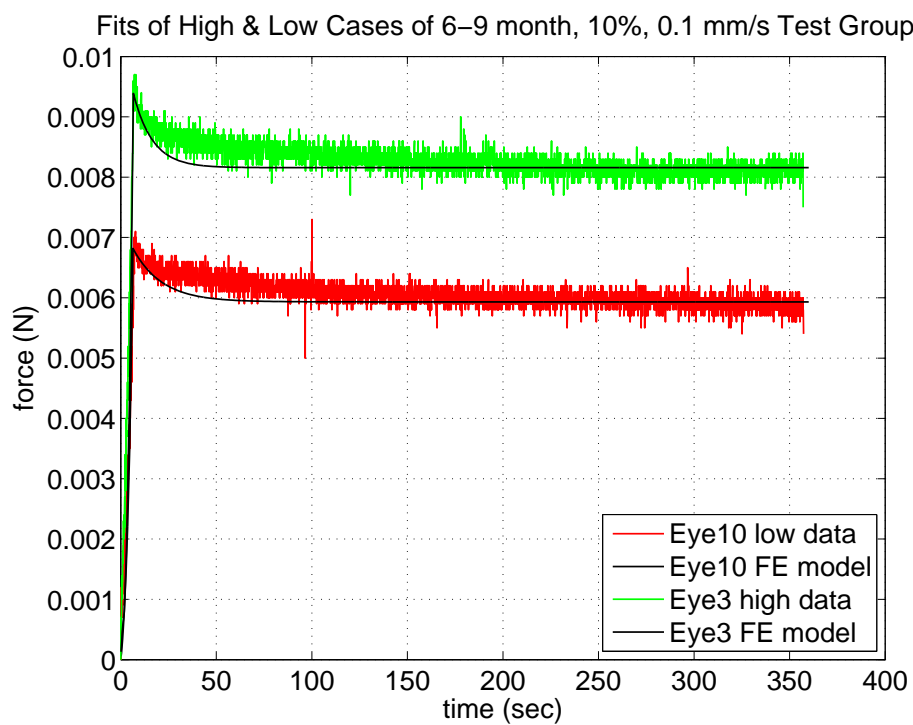


Figure 3.25: Graph of Eye10 and Eye3 vs Tahoe from the 6-9 month 10% strain 0.1 mm/s Group.

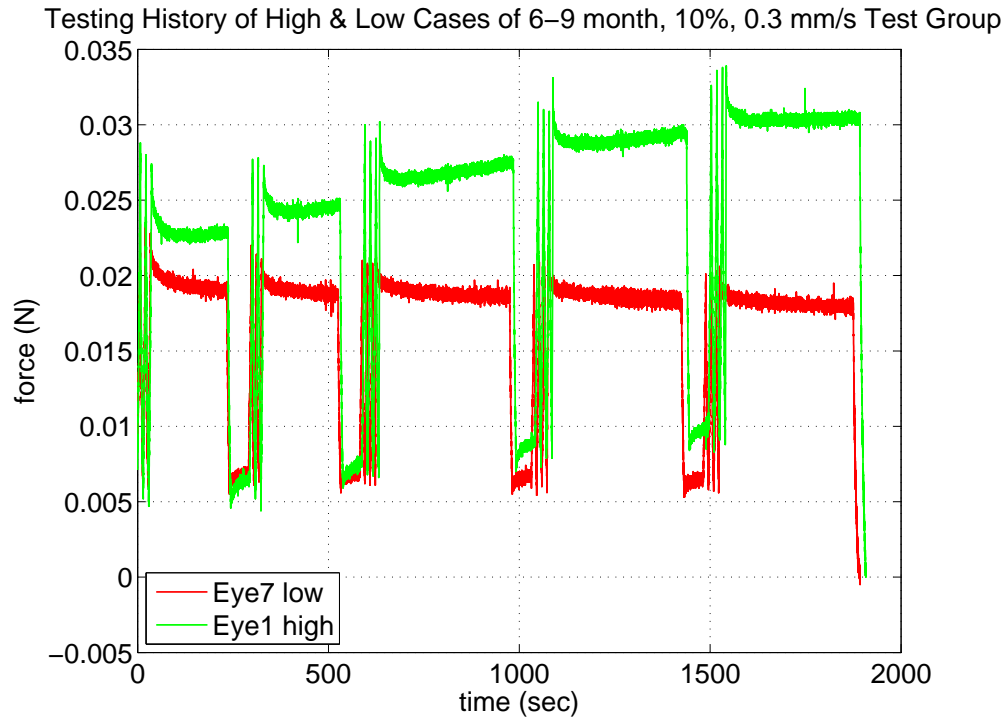


Figure 3.26: Graph of Eye7 and Eye1 from the 6–9 month 10% strain 0.3 mm/s Group.

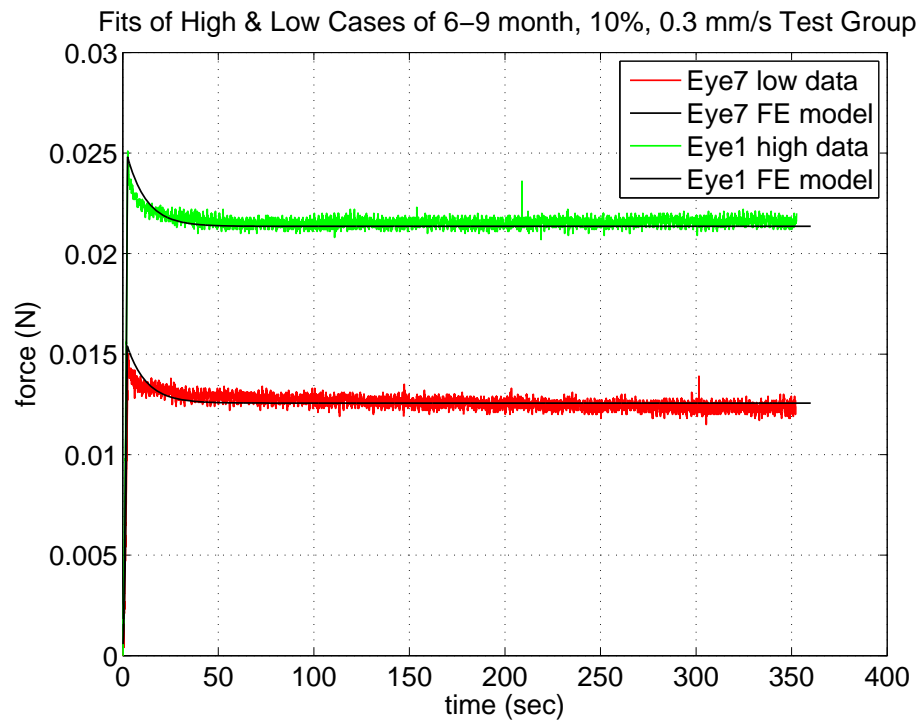


Figure 3.27: Graph of Eye7 and Eye1 vs Tahoe from the 6–9 month 10% strain 0.3 mm/s Group.

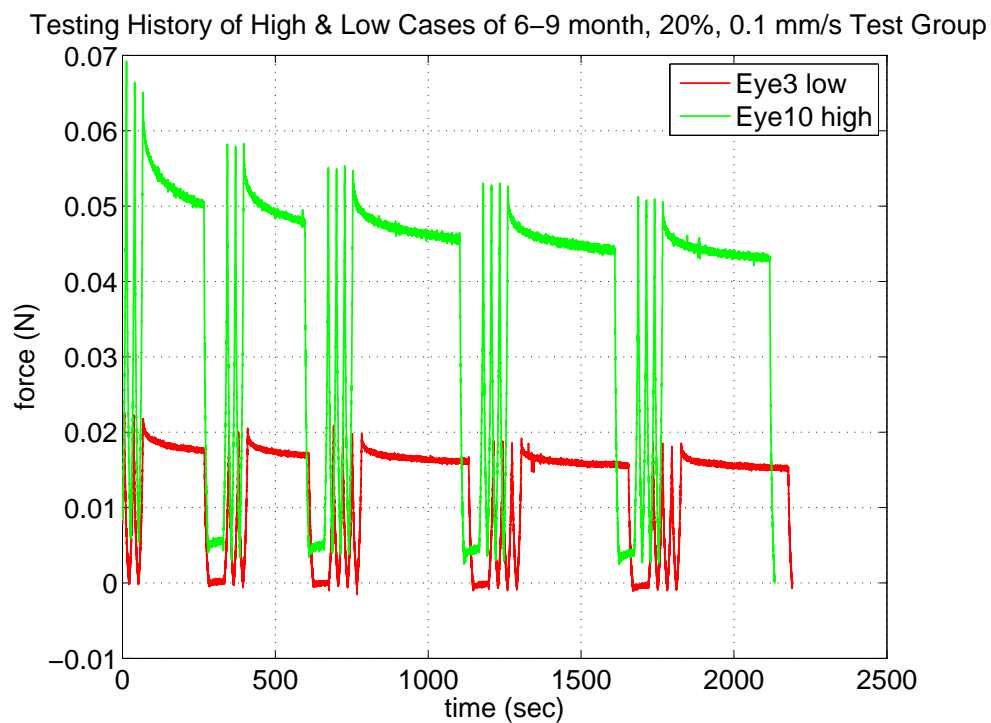


Figure 3.28: Graph of Eye3 and Eye10 from the 6–9 month 20% strain 0.1 mm/s Group.

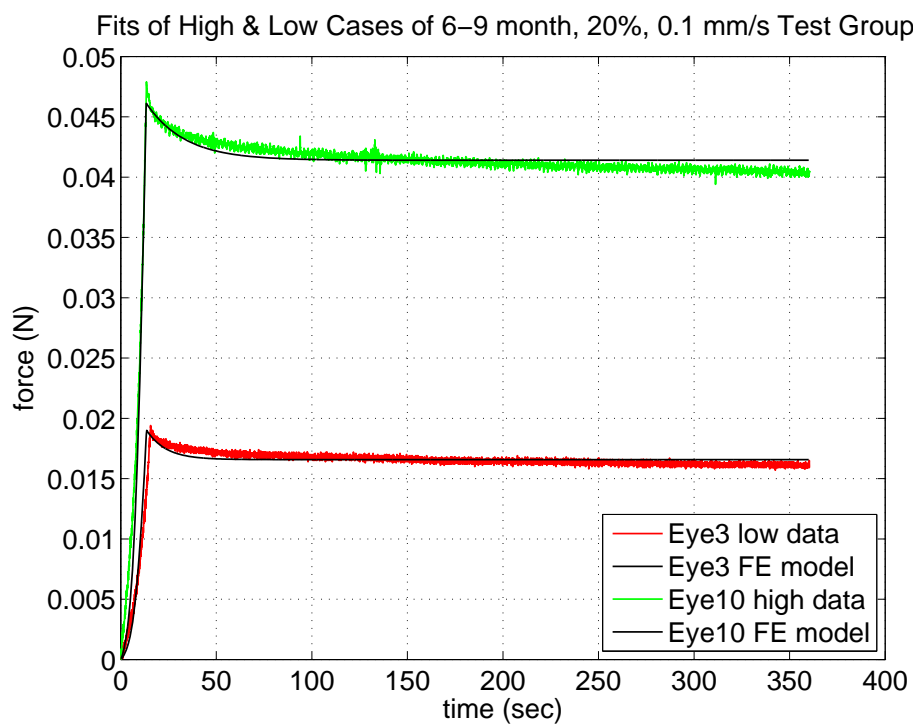


Figure 3.29: Graph of Eye3 and Eye10 vs Tahoe from the 6–9 month 20% strain 0.1 mm/s Group.

Testing History of High &amp; Low Cases of 6–9 month, 20%, 0.3 mm/s Test Group

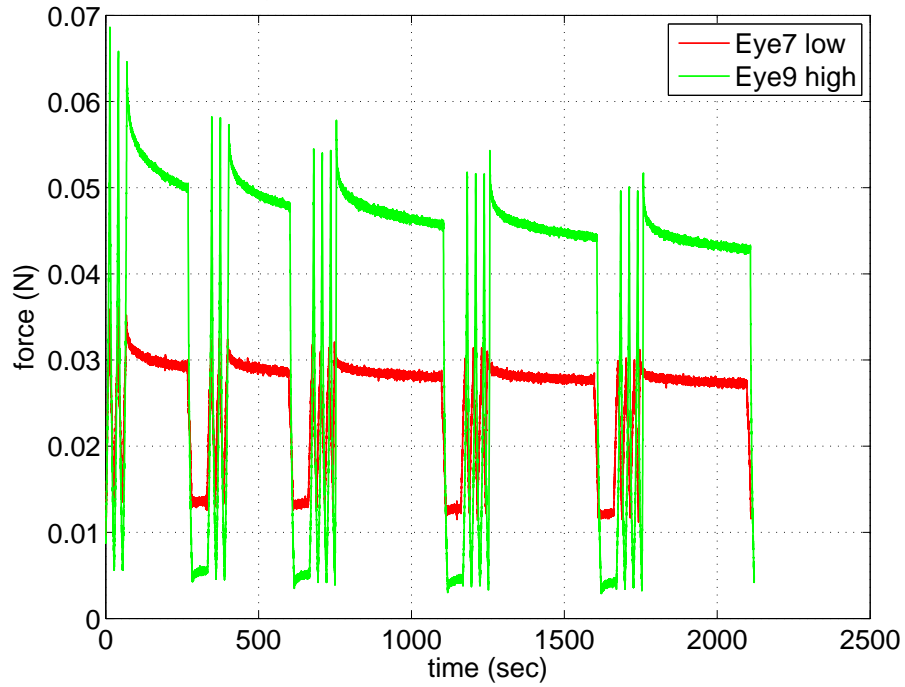


Figure 3.30: Graph of Eye7 and Eye9 from the 6-9 month 20% strain 0.3 mm/s Group.

Fits of High &amp; Low Cases of 6–9 month, 20%, 0.3 mm/s Test Group

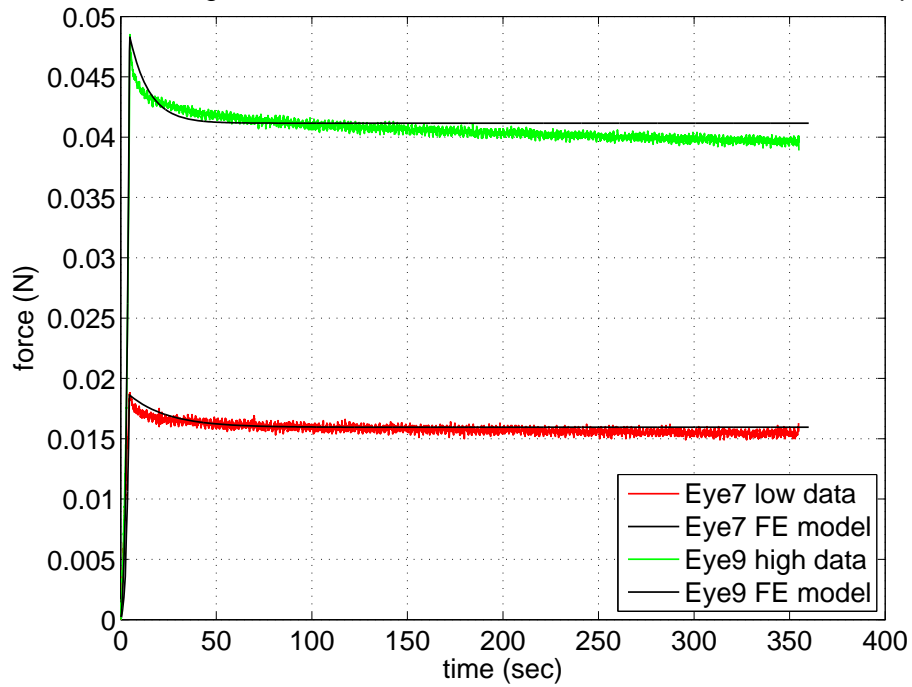


Figure 3.31: Graph of Eye7 and Eye9 vs Tahoe from the 6-9 month 20% strain 0.3 mm/s Group.

Below are graphs of the whole porcine ocular lenses tested in unconfined compression without preconditioning. Reviewing the test data, noise is apparent during some of the tests. The cause of this is unknown and another set of tests are currently being run to see if the noise still exists or not. These data are currently being fitted.

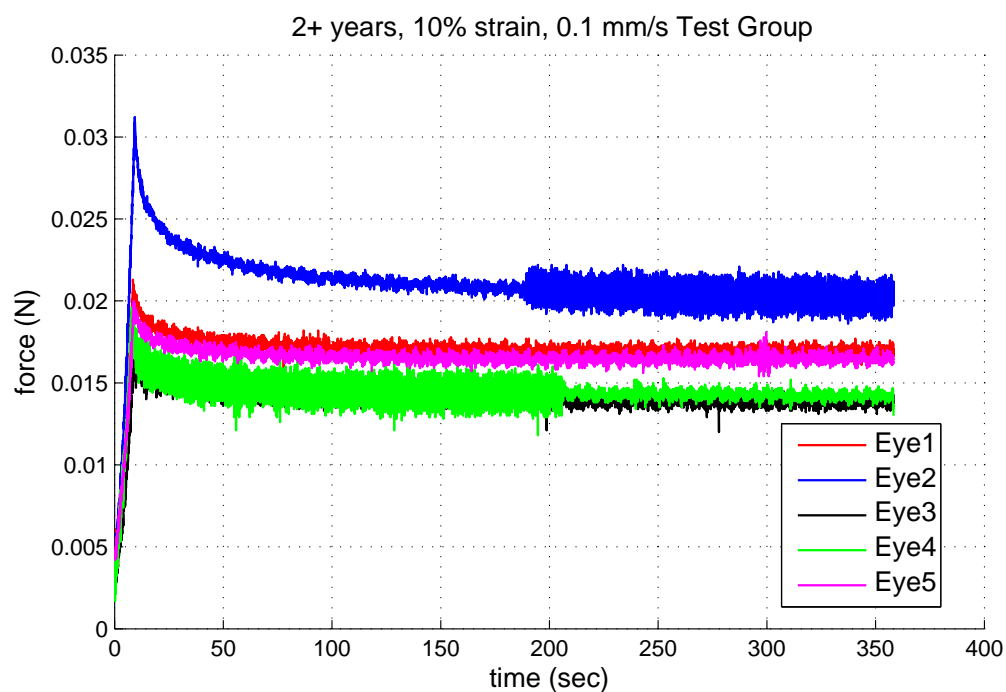


Figure 3.32: Graph of all eyes from the 2+ year 10% strain 0.1 mm/s with no Preconditioning Group.

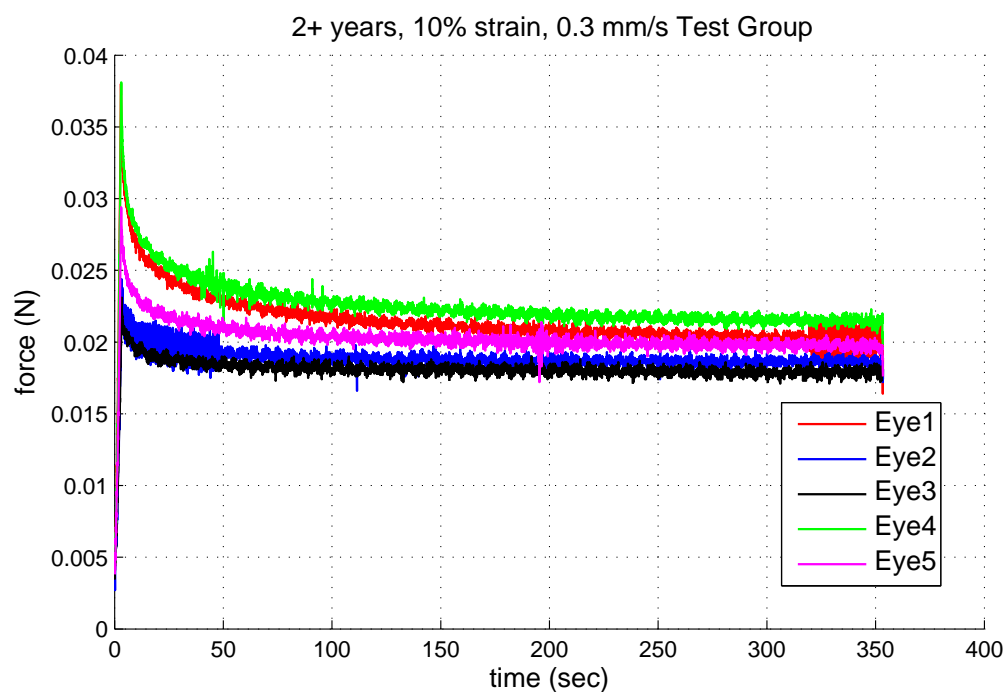


Figure 3.33: Graph of all eyes from the 2+ year 10% strain 0.3 mm/s with no Preconditioning Group.

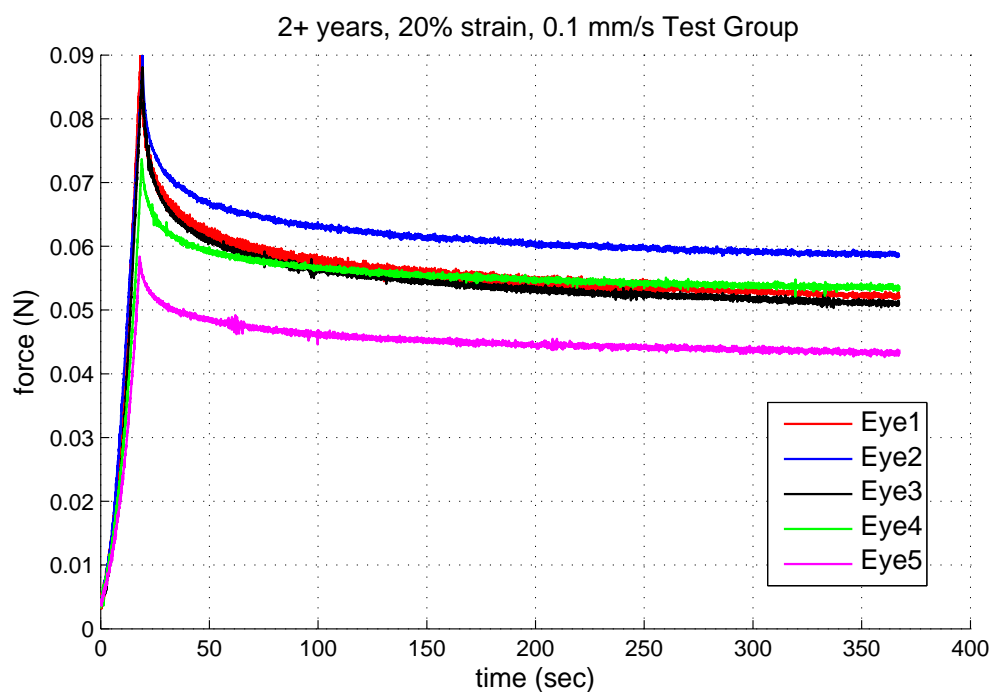


Figure 3.34: Graph of all eyes from the 2+ year 20% strain 0.1 mm/s with no Preconditioning Group.

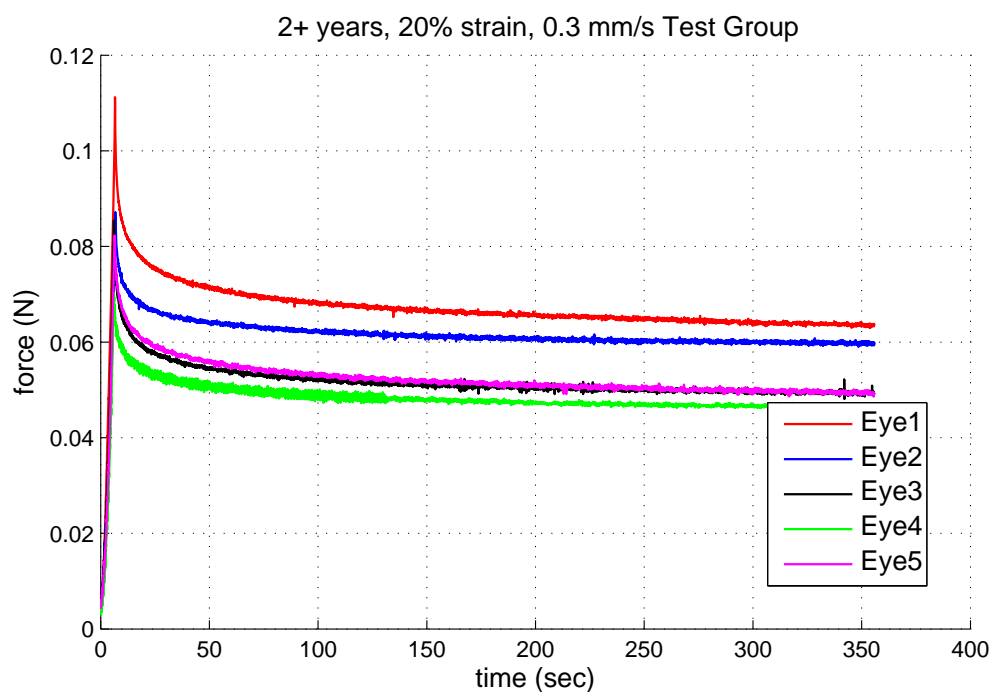


Figure 3.35: Graph of all eyes from the 2+ year 20% strain 0.3 mm/s with no Preconditioning Group.



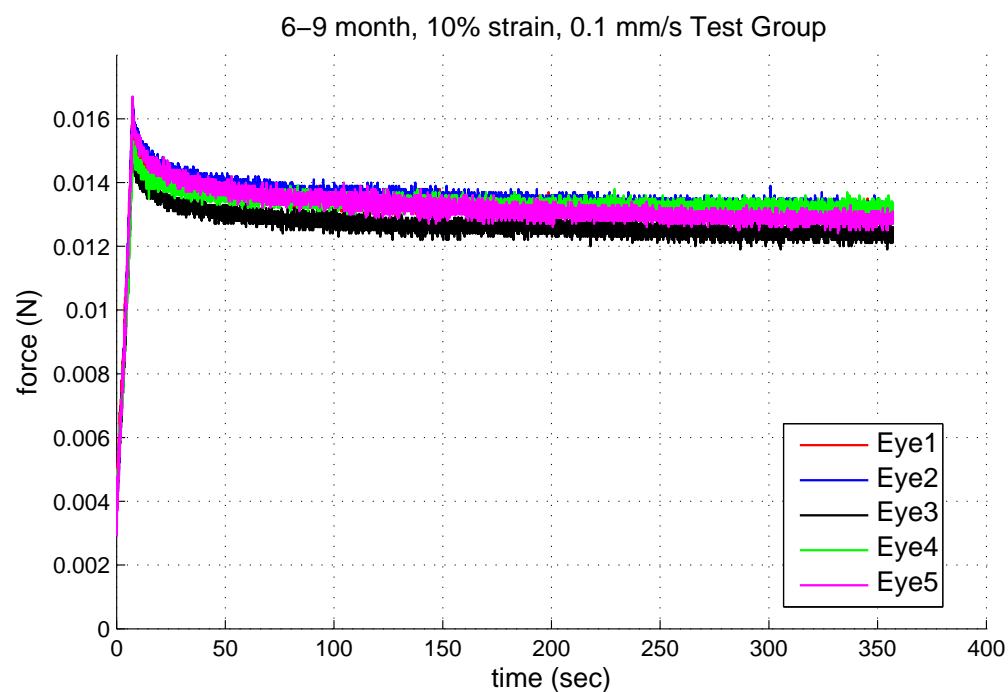


Figure 3.36: Graph of all eyes from the 6-9 month 10% strain 0.1 mm/s with no Preconditioning Group.

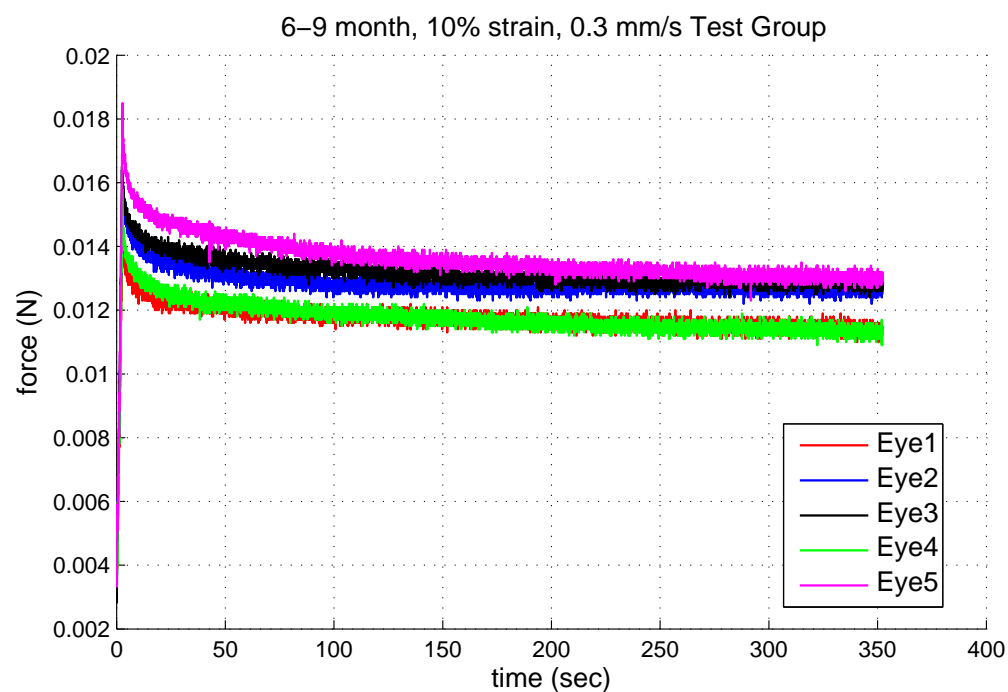


Figure 3.37: Graph of all eyes from the 6-9 month 10% strain 0.3 mm/s with no Preconditioning Group.

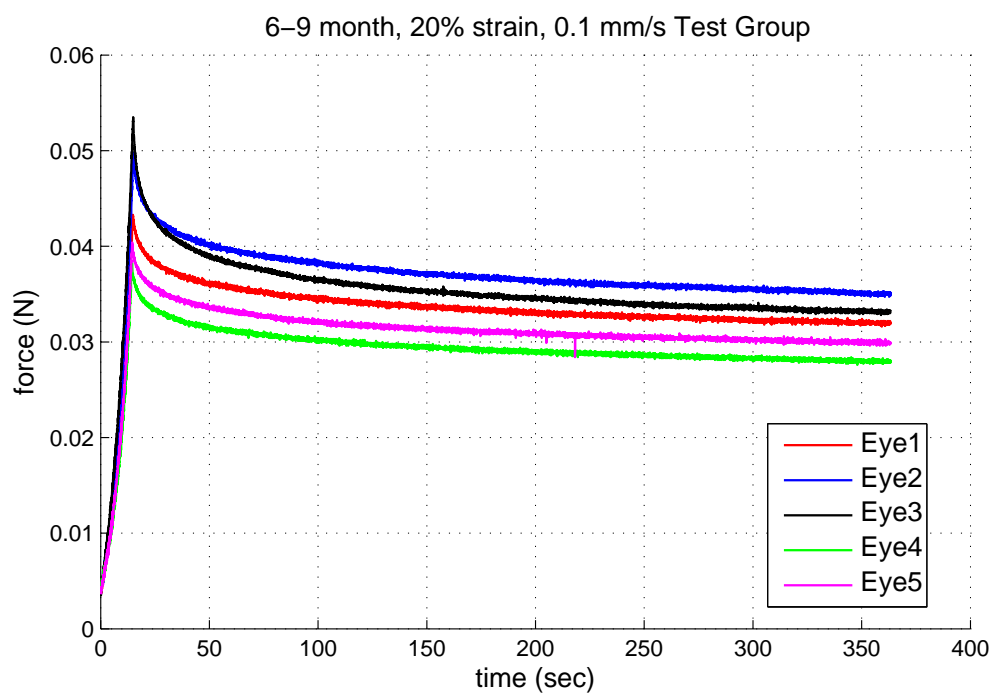


Figure 3.38: Graph of all eyes from the 6-9 month 20% strain 0.1 mm/s with no Preconditioning Group.

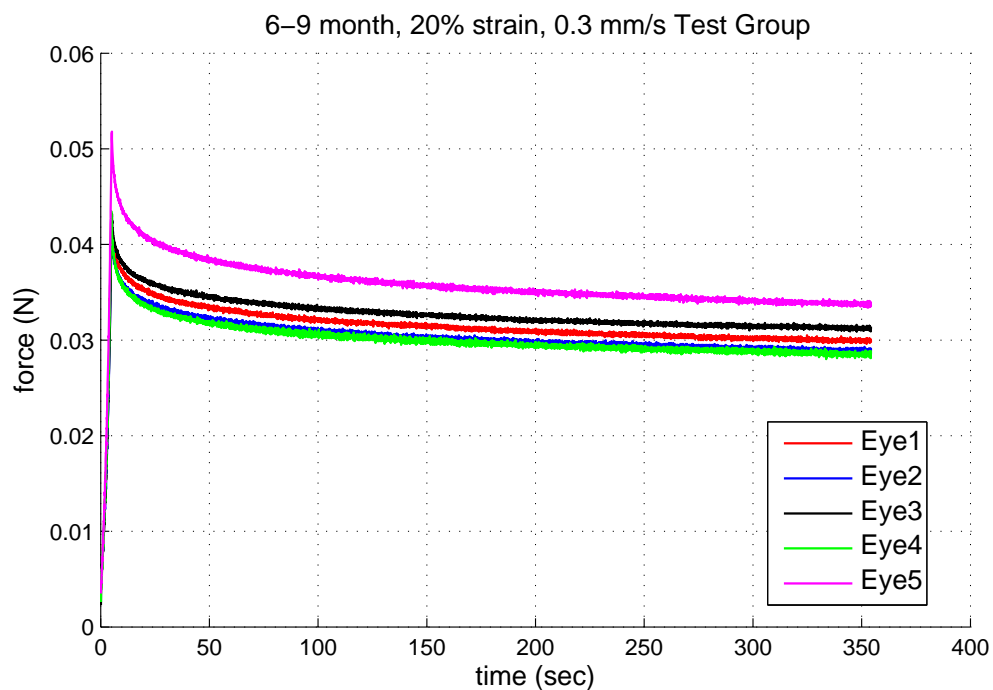


Figure 3.39: Graph of all eyes from the 6-9 month 20% strain 0.3 mm/s with no Preconditioning Group.

### 3.7 Discussion

As can be seen in the overall testing history for each lens that was fitted, the preconditioning resulted in a lower force in the last loading curve, with the exception of the high load curve for the 6-9 month, 10% strain, 0.3 mm/s loading rate test group. As for why the lens force became greater after more cycles, we are unsure. The viscoelasticity of the whole porcine ocular lens can also be seen in the testing history of each lens, showing a relaxation in the force over the hold time after each loading. This supports our reasoning that viscoelastic properties of the lens need to be included in ocular lens computational models as opposed to assuming the tissue is purely elastic or that the viscoelastic forces are negligible.

For each test group from the first round of testing, approximate fits were achieved. In order to get better fits for the initial drop of the curve, adjustments will need to be made to the constitutive model within Tahoe. The average parameters for the two different age test groups were calculated and are shown below. Table 3.3 shows the average values for the test group of tissue aged 2 years or more. Table 3.4 shows the average values for the test group of tissue aged 6-9 months. While these fits are just preliminary and not enough to determine significantly accurate material properties, it can be seen between the two age groups' viscosities that the older test group lenses are more viscous. This complies with the theory that the lens stiffens as we age, resulting in the loss of accommodation seen in presbyopia.

Table 3.3: Average Parameters Fitted of Tissue 2 Years or Older

	$\tau$ (s)	$\mu_{EQ}$ (MPa)	$\mu_{NEQ}$ (MPa)	$\kappa_{EQ}$ (MPa)	$\kappa_{NEQ}$ (MPa)	$\eta_D$ (MPa.s)	$\eta_V$ (MPa.s)
Capsule	11.1	0.84	0.29	84.0	29.4	3.27	327
Substance	11.1	8.4e-5	2.94e-5	0.084	0.0294	3.27e-4	0.327

Reviewing the no-preconditioning test groups, no immediate trend or difference can be seen between the test groups with preconditioning. It seems the force values of the no-preconditioning group generally fall within the range seen in the preconditioning test group. More data is needed to determine a difference in forces. It will be interesting to see the difference in material properties

Table 3.4: Average Parameters Fitted of Tissue 6-9 Months Old

	$\tau$ (s)	$\mu_{EQ}$ (MPa)	$\mu_{NEQ}$ (MPa)	$\kappa_{EQ}$ (MPa)	$\kappa_{NEQ}$ (MPa)	$\eta_D$ (MPa.s)	$\eta_V$ (MPa.s)
Capsule	13.1	0.71	0.135	71.0	13.5	1.77	177
Substance	13.1	7.1e-5	1.35e-5	0.071	0.0135	1.77e-4	0.177

when the fits are completed for the no-preconditioning test groups.

Some preliminary modeling of the unconfined compression of the whole porcine ocular lens has been completed in Abaqus. Figures 3.40, 3.41, and 3.42 show the various stages of the Abaqus simulation of Lens 3 (high load case) of the 2+ year, 10% strain, 0.1 mm/s loading rate test group. Figure 3.40 shows the beginning of the simulation, with the lens positioned with the anterior surface downward, the fixed platen at the bottom representing the testing pedestal, and the load platen at the top. In Figure 3.41 we can see the lens flattening against both the load platen and bottom surface and the stress in the lens capsule along the top and bottom surfaces of the lens. This image shows the simulation at the point where the lens has been deformed to the defined strain of 10%. When comparing Figure 3.42 at the end of the simulation to Figure 3.41 at the height of the force, the stress relaxation can be noticed in the lens capsule. Comparing Figure 3.43 and Figure 3.44 the relaxation of the stress in the lens fiber cells can be seen. The maximum stresses in the lens fiber cells can be seen located near the contact point of the platen. Figure 3.45 shows an overlay of the Abaqus model with an image of the compressed lens. The compressed model appears to match well with the actual compressed lens.

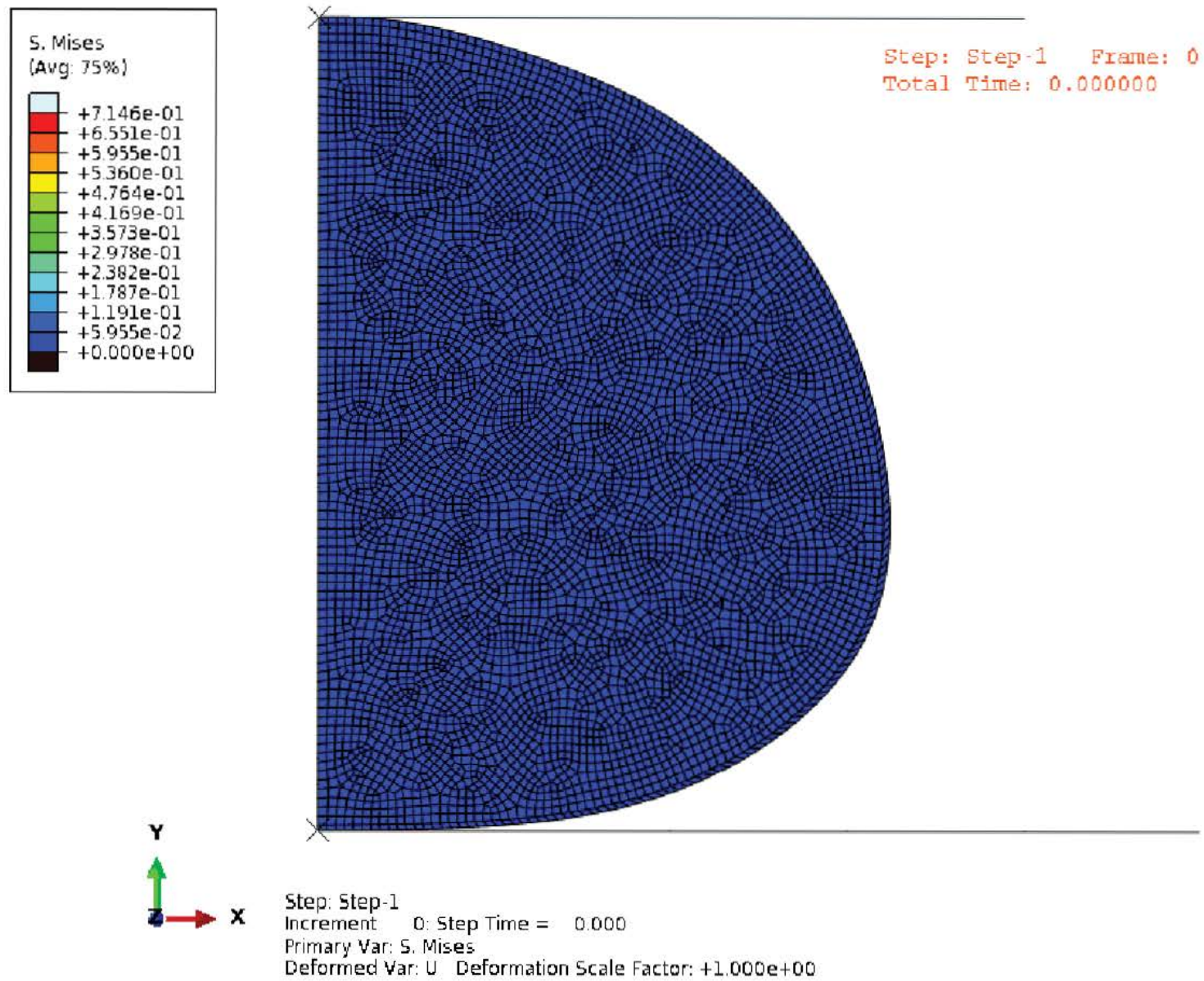


Figure 3.40: Simulation of Unconfined Compression on Whole Porcine Ocular Lens - Beginning of simulation.

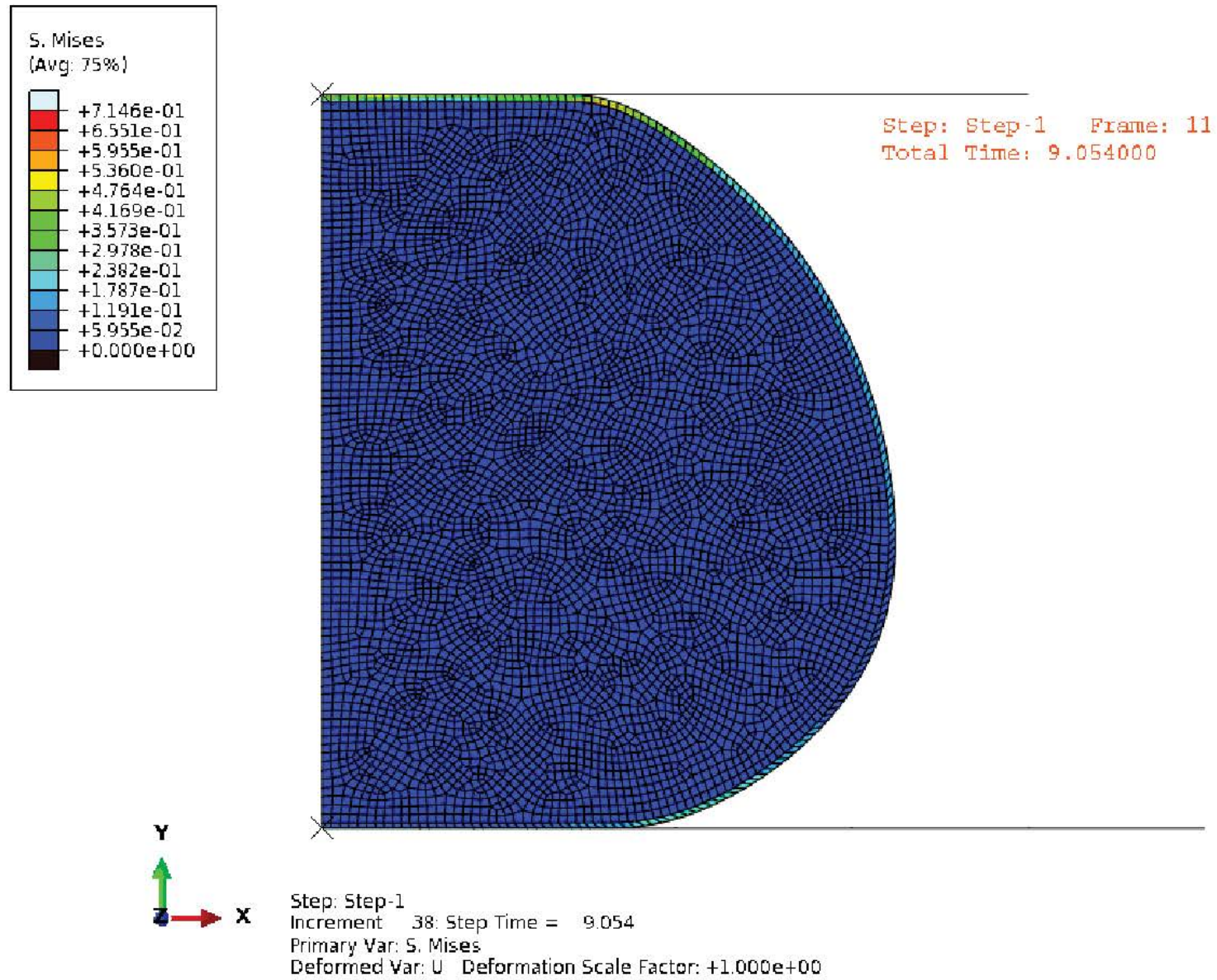


Figure 3.41: Abaqus Simulation of Unconfined Compression on Whole Porcine Ocular Lens - Full loading has been reached; can see stress<sub>33</sub> in the capsule along the top and bottom.



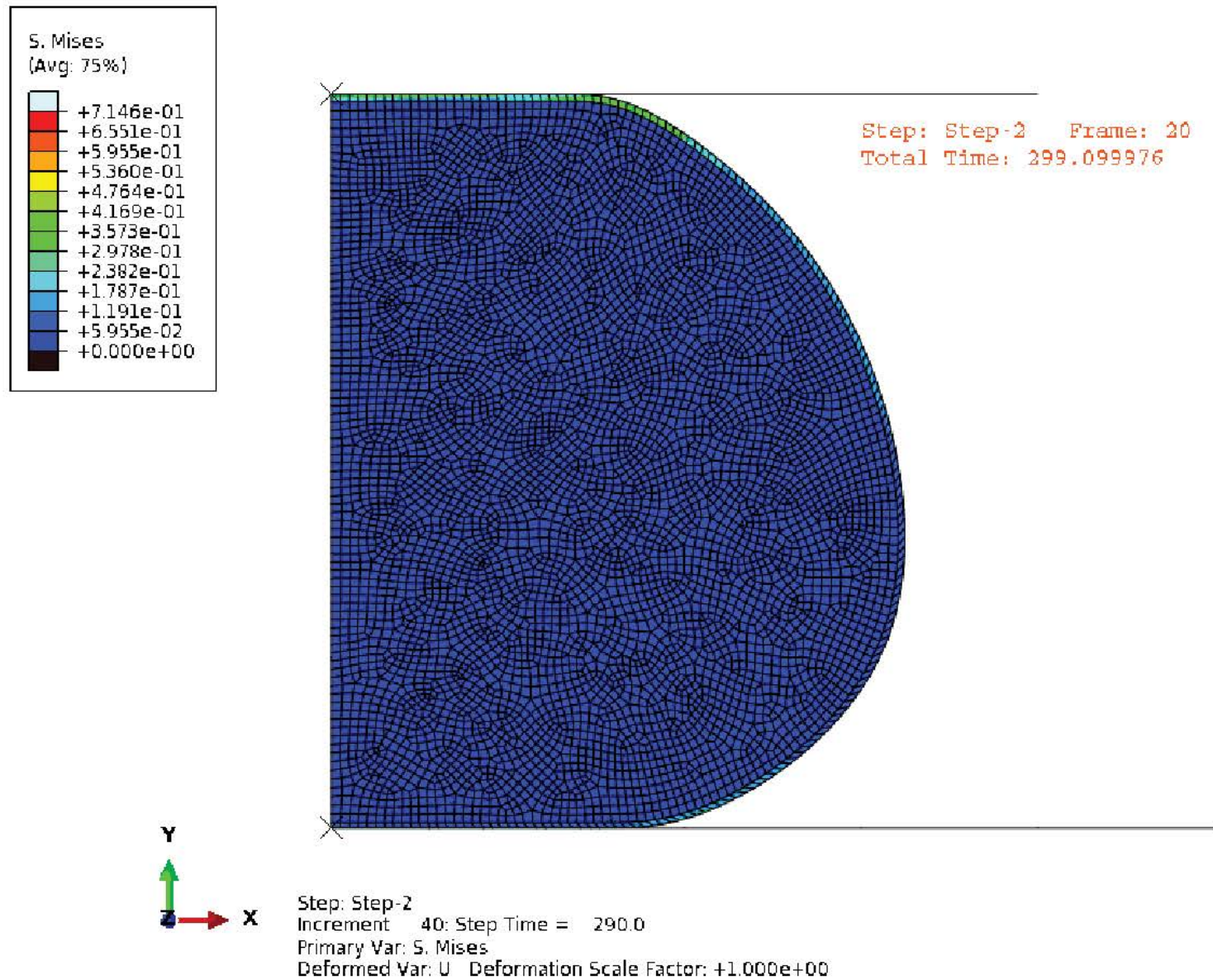


Figure 3.42: Abaqus Simulation of Unconfined Compression on Whole Porcine Ocular Lens - End of simulation; stress has gradually relaxed in capsule. 40

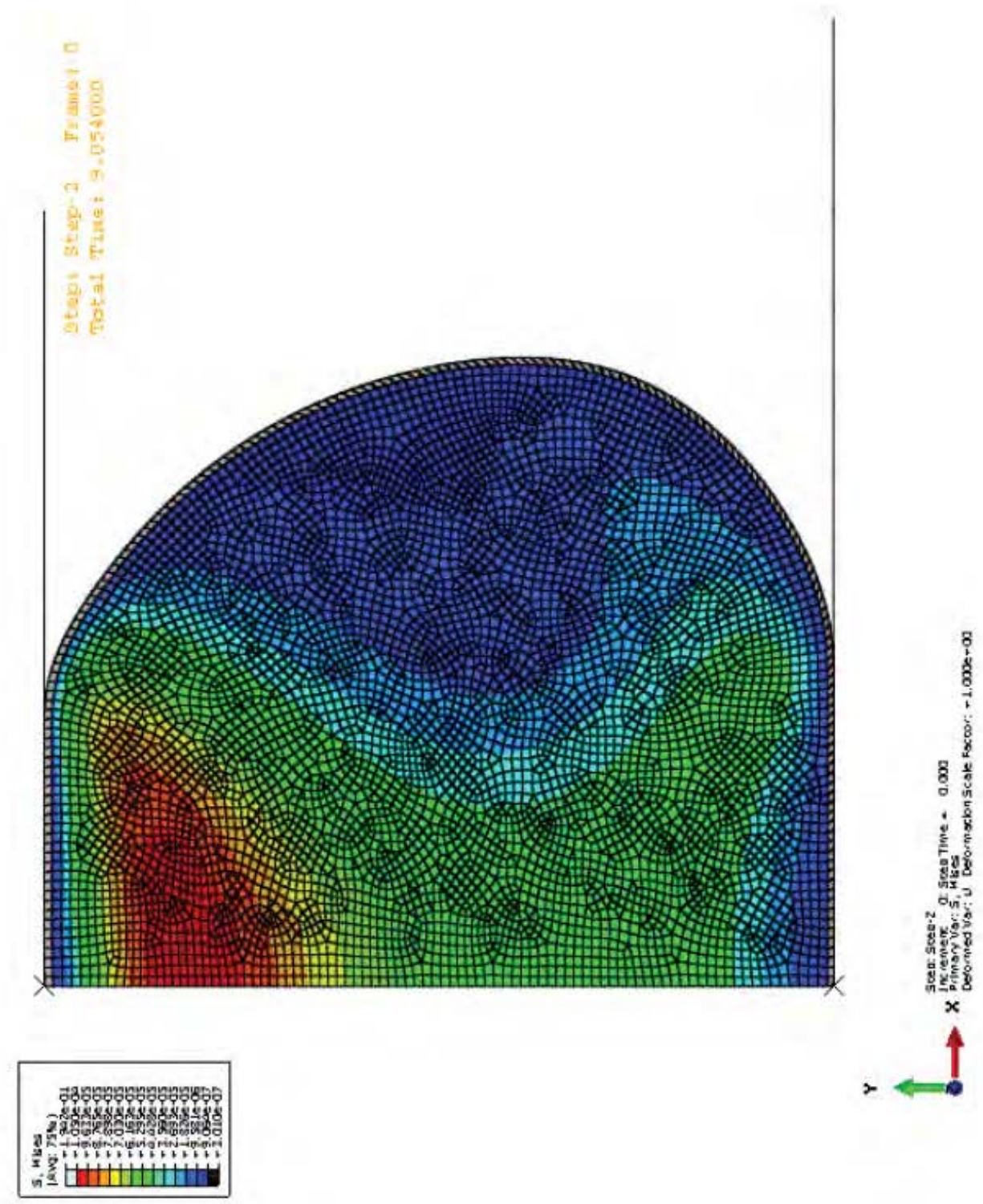


Figure 3.43: Scaled contour of the Abaqus simulation showing the maximum stressed state of the lens fiber cells.



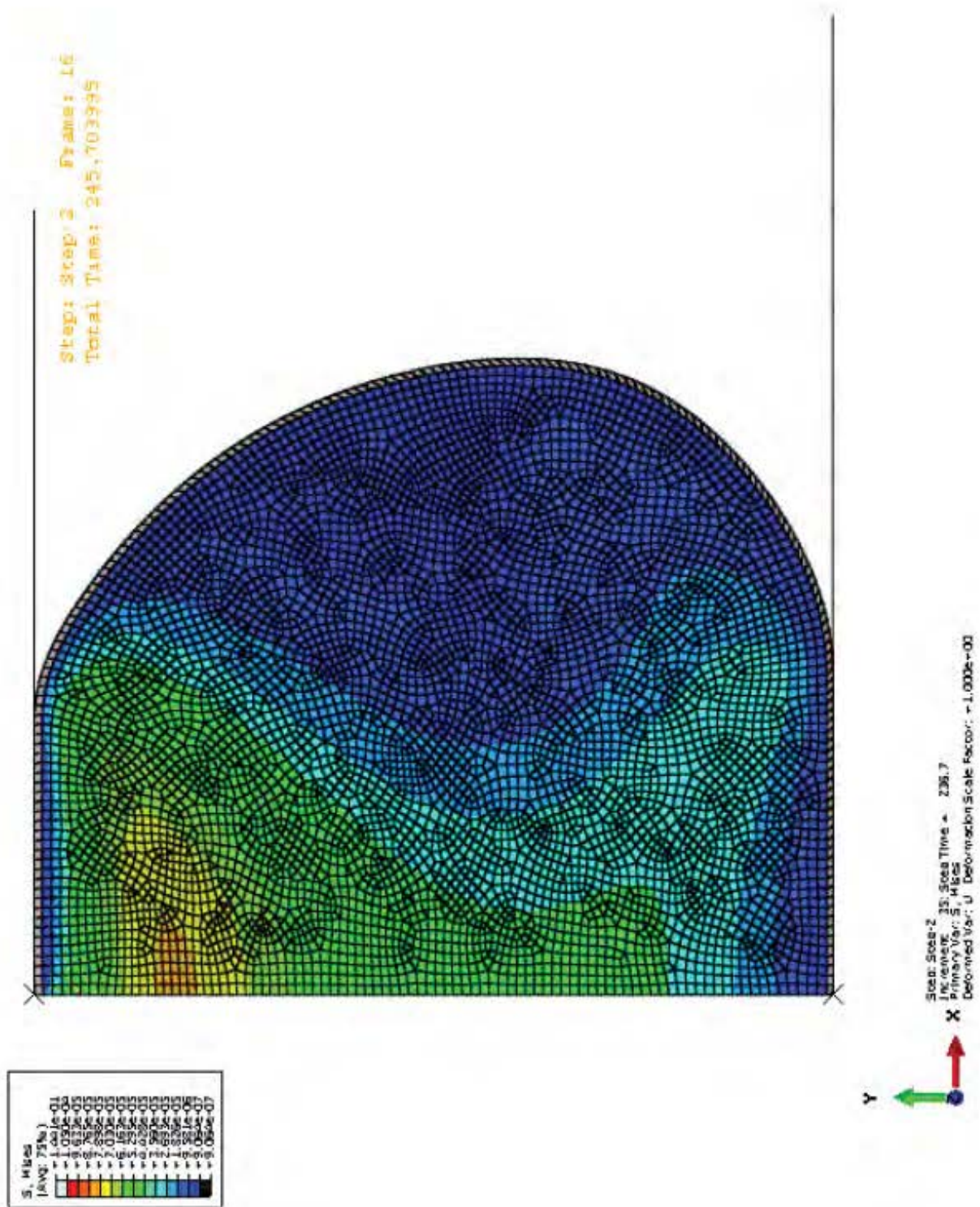


Figure 3.44: Scaled contour of the Abaqus simulation showing the stressed state of the lens fiber cells at the end of the simulation.

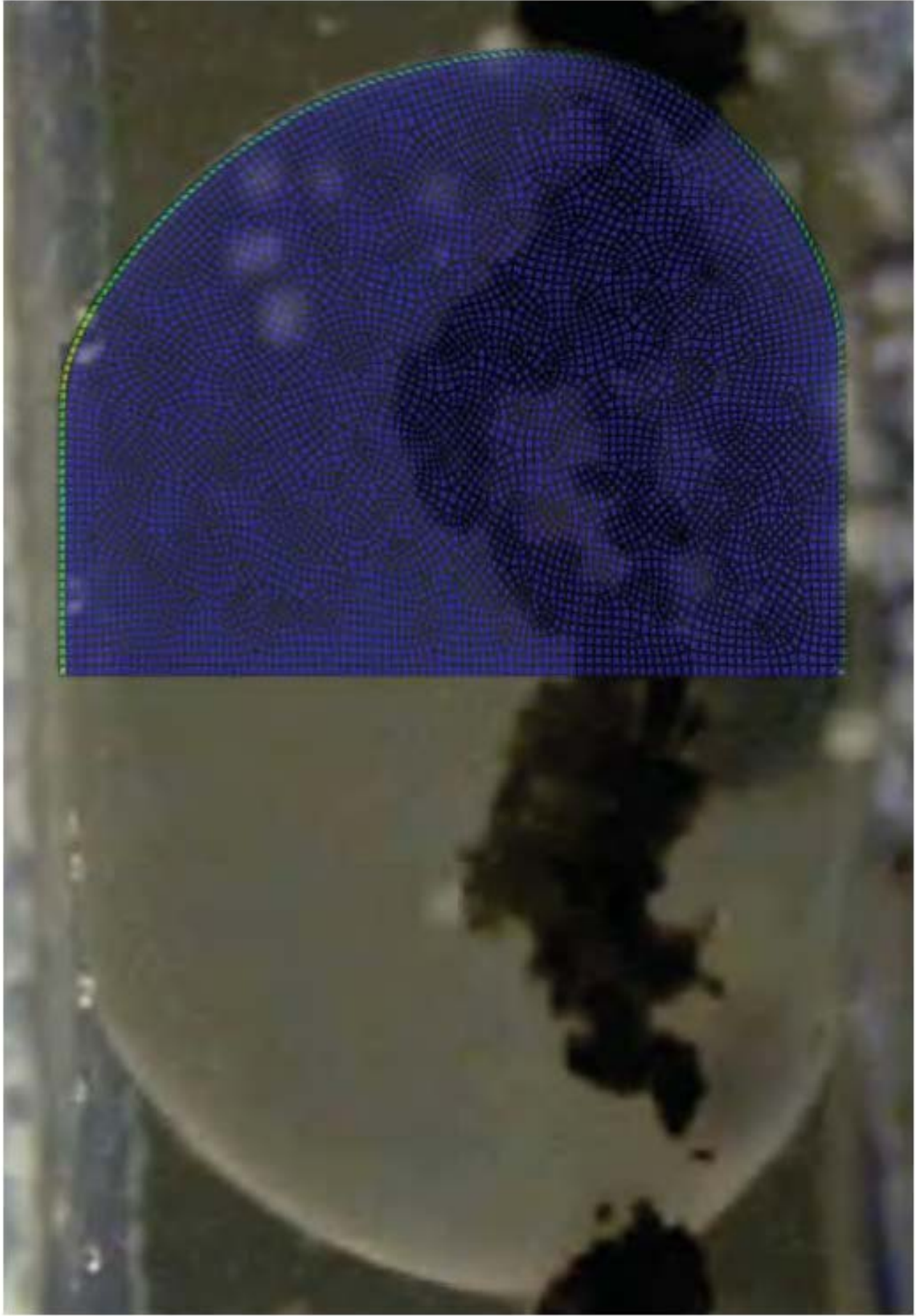


Figure 3.45: Overlay of the Abaqus simulation with an image of the compressed lens.

Figure 3.46 compares the theoretical data produced from Tahoe using the fitted parameters and the theoretical data produced by the simulation within Abaqus. In order to get the 2 sets of data to match, the material properties for Abaqus had to be slightly adjusted. This is likely due to the differences in constitutive governing equations used between the model implemented in Tahoe and the model in Abaqus. The Abaqus model properties were setup as isotropic viscoelastic. The 2 sets of parameters are shown below in Table 3.5. The difference in parameters are small and the data matching between the two simulations is encouraging towards the ends of determine the viscoelastic properties of the whole porcine ocular lens.

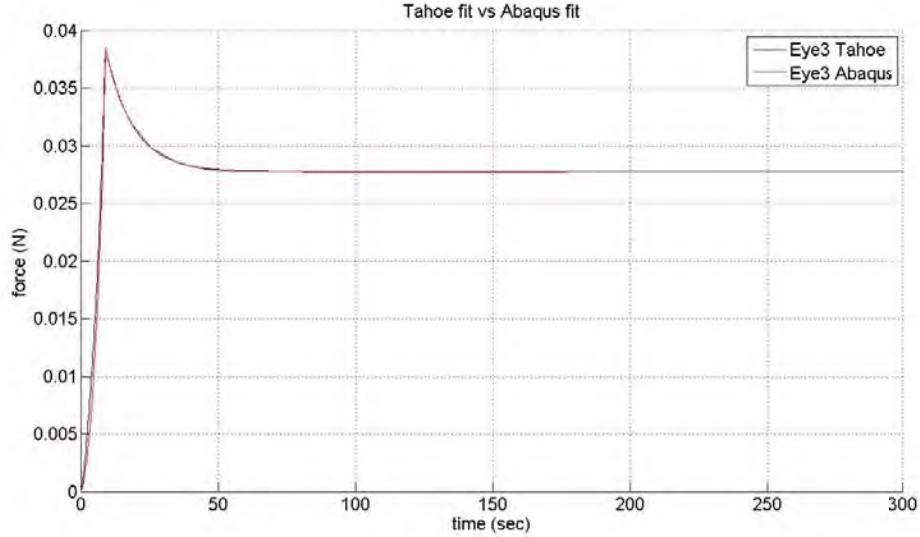


Figure 3.46: Graph of Data Produced From Tahoe Simulation and Abaqus Simulation

Table 3.5: Tahoe Parameters vs Abaqus Parameters

	$\tau$ (s)	$\mu_{EQ}$ (MPa)	$\mu_{NEQ}$ (MPa)	$\kappa_{EQ}$ (MPa)	$\kappa_{NEQ}$ (MPa)
Capsule (Tahoe)	10	1.275	0.65	127.5	65
Capsule (Abaqus)	10	1.479	0.49	147.9	49
Substance (Tahoe)	10	7.1e-5	1.35e-5	0.071	0.0135
Substance (Abaqus)	10	1.479e-4	4.9e-5	0.1479	0.049

## **Chapter 4**

### **Puncture Testing of the Whole Lens**

Puncture testing was completed to provide data that would be useful in modeling the interaction between the ocular lens and intraocular foreign bodies (IOFBs). This data will also allow for the calculation of material properties (similar to the method described in the Parameter Fitting of Unconfined Compression Testing Data Chapter at large deformations). Additionally, using the puncture testing protocol, tissue will be fixed and imaged using confocal LASER scanning microscopy to study the deformation/damage of the lens fibers after loading/puncture. Whole porcine ocular lenses were loaded past puncture using a MTS Insight II electromechanical testing system with 6 different puncture tip geometries, described below. The tests were recorded to gain information of the gross deformation of the lens under puncture. Force and displacement were recorded and the data were exported for future analysis and modeling. Preliminary modeling was done using Abaqus ([www.simulia.com](http://www.simulia.com)), described in more detail below.

#### **4.1 Sample Preparation**

Whole porcine globes were shipped on wet ice from Animal Technologies, Inc. in Tyler, TX. Tissue came from one age group: pigs aged 2 or more years. For puncture testing, the whole ocular lens was removed by excising the cornea and cutting through the iris and zonules. This was done by making a small incision with a diamond-head blade at the edge of the cornea and using curved microsurgery scissors to cut around the cornea. The same process is used to cut through the zonules. Excess zonules were removed by rolling the lens along its equator on tissue paper. Excess

vitreous was also removed by rolling the lens end over end on tissue paper and trimming away the vitreous that stuck to the paper. Lens were then placed in Alcon Laboratories, Inc. Balanced Salt Solution (BSS) for transport to the MTS Insight II for testing.

## 4.2 Experimental Setup

All puncture tests were completed on a MTS Insight II Electromechanical testing system. The Insight II is screw-driven machine. The tests utilized a 2N load cell (sensitivity: 2.04 mv/V) to measure the small force response of the ocular lens (see Figure 4.1). The puncture tip was connected to the load cell by a piece of polycarbonate designed so that tips could be interchanged (see Figure 4.1). Lenses were loaded and punctured with six different puncture geometries: 1) a 1 mm diameter cylindrical tip, 2) a 2 mm diameter cylindrical tip, 3) a 1 mm diameter spherical tip, 4) a 2 mm diameter spherical tip, 5) a 30 degree conical tip, 6 )and a 45 degree conical tip. The geometries and dimensions can be seen in Figure 4.2.

Table 4.1: Testing Configurations and Number of Lenses Tested

Tip Geometry (d, $\theta$ )	Loading Rate (mm/s)	Anterior Surface	Posterior Surface
1mm spherical	0.5	5	5
2mm spherical	0.5	5	5
1mm cylindrical	0.5	5	5
2mm cylindrical	0.5	5	5
30 deg conical	0.5	5	5
45 deg conical	0.5	5	5

The ocular lenses were tested at a single loading rate of 0.5 mm/s to 80% nominal axial strain. Test groups and samples per group can be seen in Table 4.1. All tests were performed in Alcon BSS. The overall test setup can be seen in Figure 4.3. The lens was placed in the Alcon BSS in a testing pedestal. The testing pedestal was situated inside of a water bath contained by an environmental testing chamber. The water bath was heated to 37 °C. The lenses were imaged before testing and recorded during testing using an Aven Hand-Held Digital Microscope



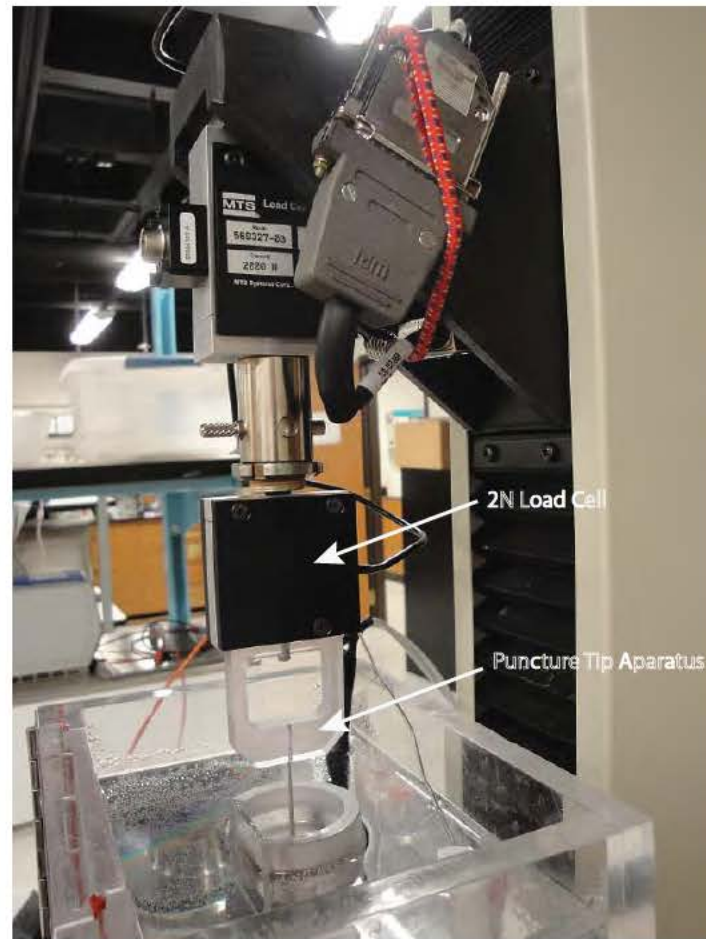


Figure 4.1: 2N Load Cell and Puncture Tip Apparatus Attached to MTS Insight II.

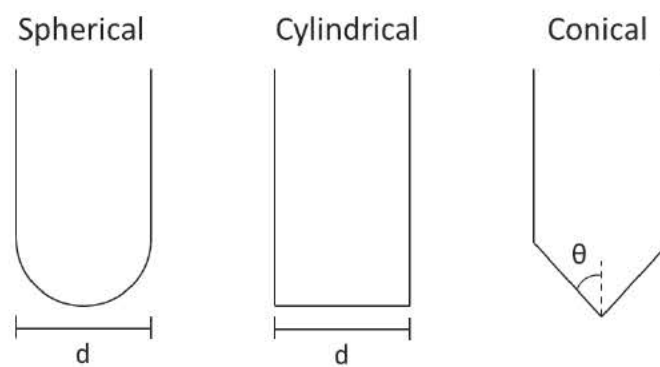


Figure 4.2: Puncture Loading Tip Geometries with Various Diameters  $d$  and Angles  $\theta$ .

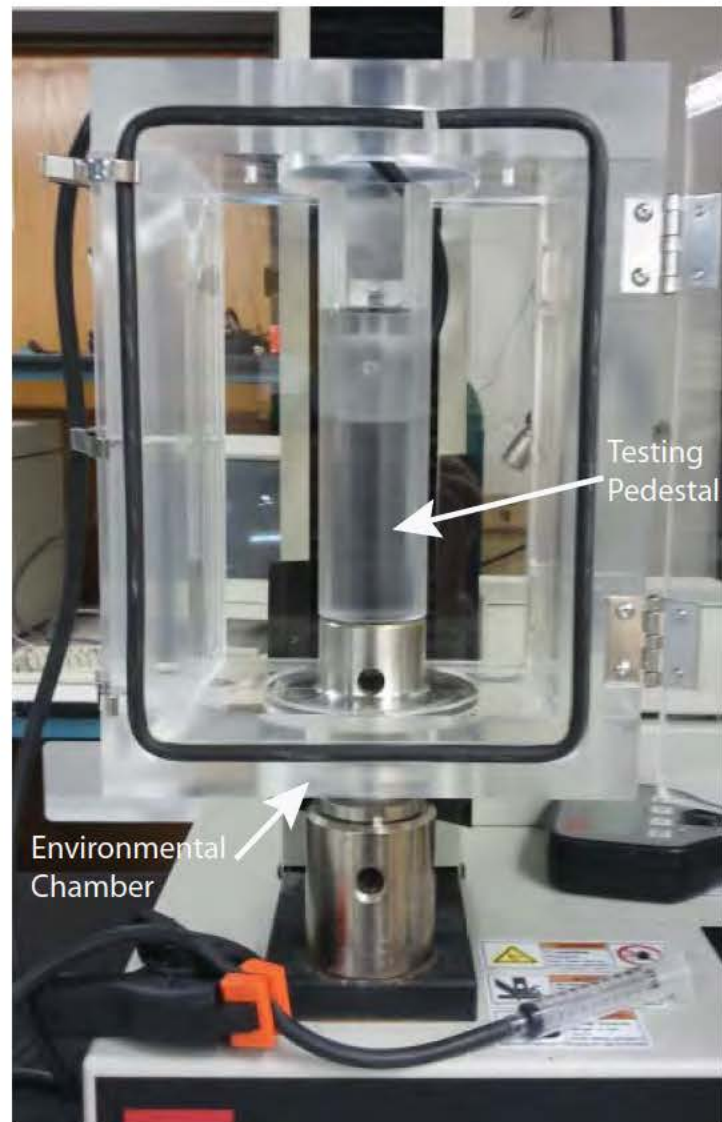


Figure 4.3: Environmental Chamber with Testing Pedestal Placed Inside.

(1.3 Megapixel)(see Figure 4.4). For posterior tests, the lens was centered in the pedestal and rested freely on its anterior surface. For anterior tests, it was required to manufacture a well to hold the lens with the anterior surface pointed up (see Figure 4.5).



Figure 4.4: Example of Image Taken Before Each Test to get Geometry Data.

This well was made out of acrylic and made to have the approximate shape of posterior surface of the lens. The software TestWorks 4 ([www.mts.com](http://www.mts.com)) was used in all of the tests to control the Insight II and collect all the data.

### 4.3 Experimental Method

A testing program was developed in TestWorks 4 allowing specification of displacement speed, strain to displace to, whether the anterior or posterior surface is being punctured, lens height, test date, test time, any observational notes about the lens pre-test, and how the lens failed post-test. Initially the puncture tip was brought into contact to determine where the testing pedestal or puncture well surface was, for calculating the lens height. The lens was then placed in the testing pedestal reservoir, either anterior surface up (with puncture well) or posterior surface up. The puncture tip was lowered to approximately 1 mm above the lens. The load cell was then zeroed and began approaching the lens. Once the pre-load force of 0.05 N was reached, the program displayed





Figure 4.5: Sample Holder inside of Environmental Chamber.

the lens height for the user to record. An image was taken of the lens using the digital microscope before testing. The user then entered all testing information (lens height, displacement speed, strain to displace to, puncture tip being used, surface being punctured, and any observational notes about the lens). Once all information was entered, video recording and the test began, collecting force and displacement data at a rate of 20 Hz. The lens was loaded at the specified testing rate (0.5 mm/s for all tests) to the desired strain (80%). Upon reaching 80%, the machine paused 3 seconds to ensure complete data collection and then the test ended. The user stopped the video recording and then entered how the lens failed (anterior puncture, posterior puncture, side blow-out, other), supplying any additional notes on the test/failure mode. The machine was then retracted and the punctured lens was removed. The Alcon BSS in the pedestal reservoir was removed after 5 consecutive tests in order to provide better imaging conditions. The Alcon BSS was allowed to acclimate to temperature after it was changed.

#### 4.4 Theoretical Modeling

Preliminary modeling was completed in the commercially available modeling software Abaqus ([www.simulia.com](http://www.simulia.com)). A 2-D, axisymmetric simulation was set up based off the geometry of a 2+ year aged porcine ocular lens from the 1 mm spherical posterior test group. The model of the lens was divided into 2 parts: the lens capsule and the interior lens fibers, each with separate material properties. Both sections were modeled using Abaqus' hyperelastic, isotropic, Neo-hookean material, which requires the definition of  $g_1 = \mu_{NEQ} \div \mu_{EQ}$  (shear modulus ratio),  $\kappa_1 = \kappa_{NEQ} \div \kappa_{EQ}$  (bulk modulus ratio),  $\tau_1$  (relaxation time constant),  $C10 = \mu_{EQ} \div 2$ , and  $D1 = 2 \div \kappa_{EQ}$ . Average material properties (  $\mu_{EQ}$ ,  $\mu_{NEQ}$ ,  $\kappa_{EQ}$ ,  $\kappa_{NEQ}$ , and  $\tau$  ) were calculated from the parameters given from the fitted experimental data from the unconfined compression testing as parameter fitting on the puncture testing data has not been completed. Both sections were meshed with quad elements. The 1 mm spherical puncture tip was modeled as a solid, incompressible surface. Contact was defined as frictionless. The puncture tip was fixed in the  $U1 = 0$  (x) and  $U3 = 0$  (rotational) direction. The lens was fixed at the bottom in the  $U1 = 0$ ,  $U2 = 0$  (y), and  $U3 = 0$  directions and

at the top in the  $U_2 = 0$  and  $U_3 = 0$  directions. A boundary condition was set up along the x-axis at the bottom to represent the testing pedestal surface. The simulation was set to run at 0.5 mm/s displacement to 80% strain.

## **4.5 Results**

Below are graphs of each test group, showing the 5 whole ocular lenses in each group.

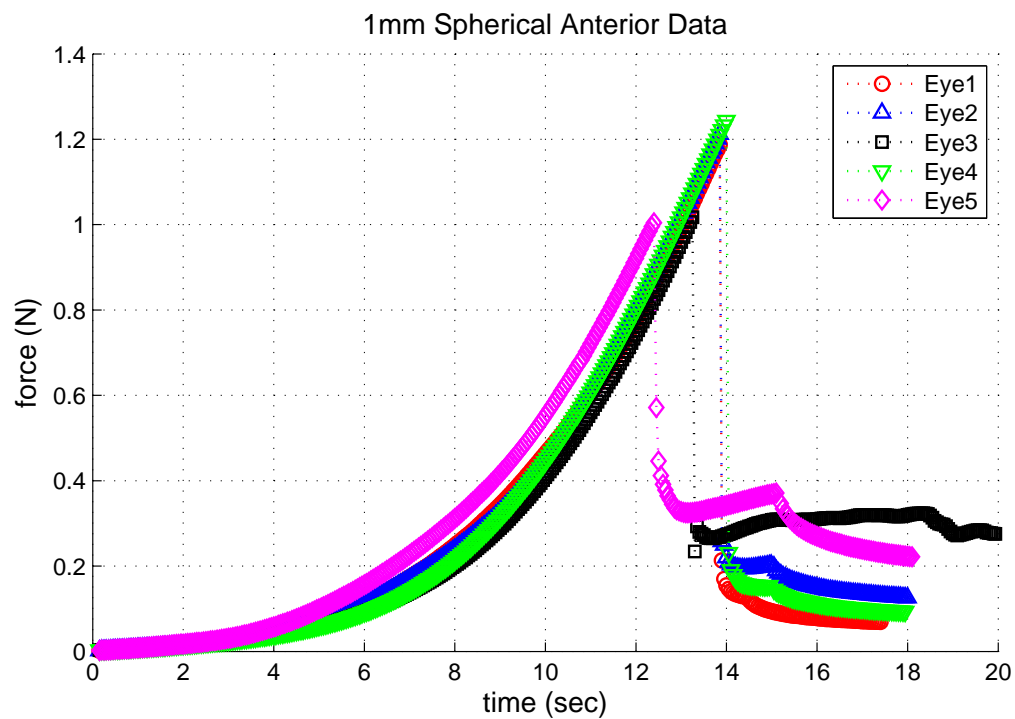


Figure 4.6: Graph of 1 mm Spherical Anterior Data.

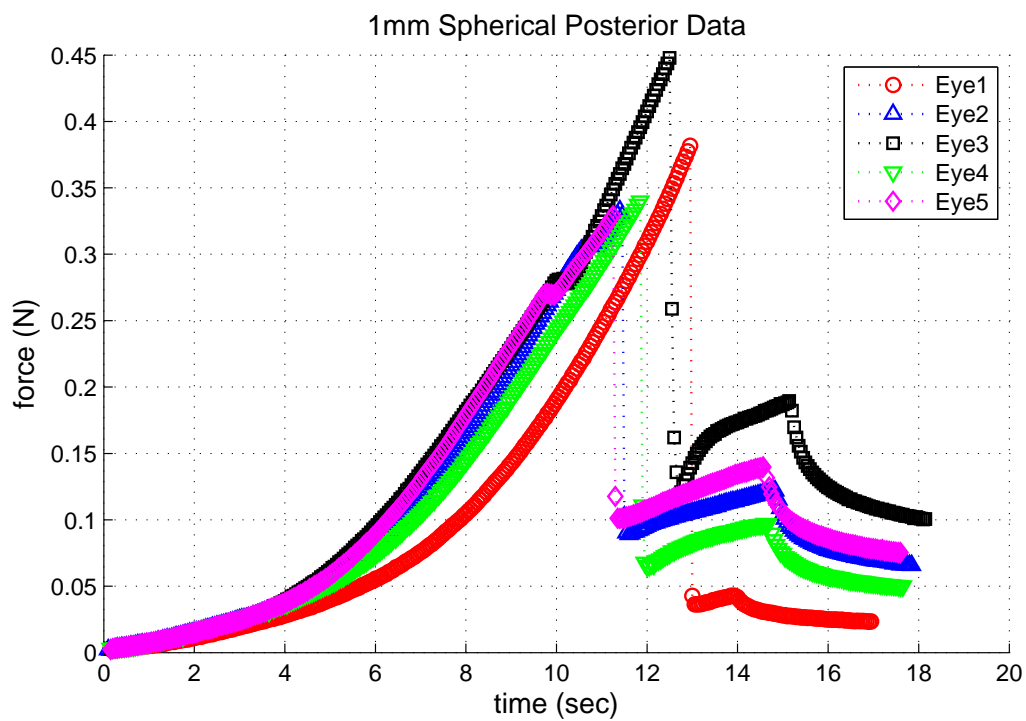


Figure 4.7: Graph of 1 mm Spherical Posterior Data.

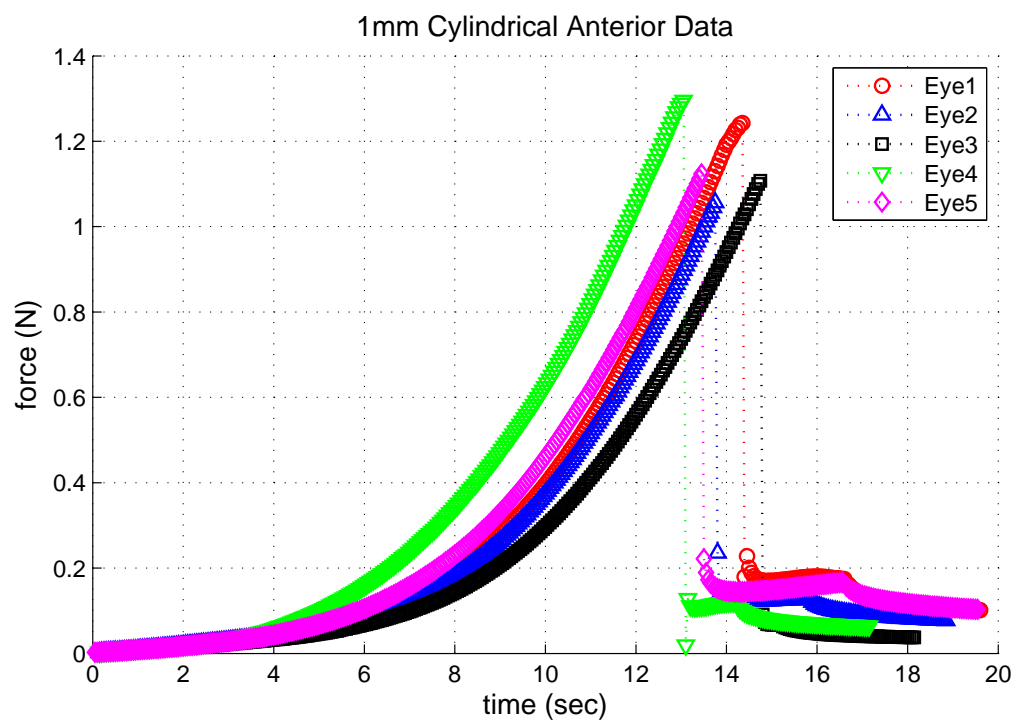


Figure 4.8: Graph of 1 mm Cylindrical Anterior Data.

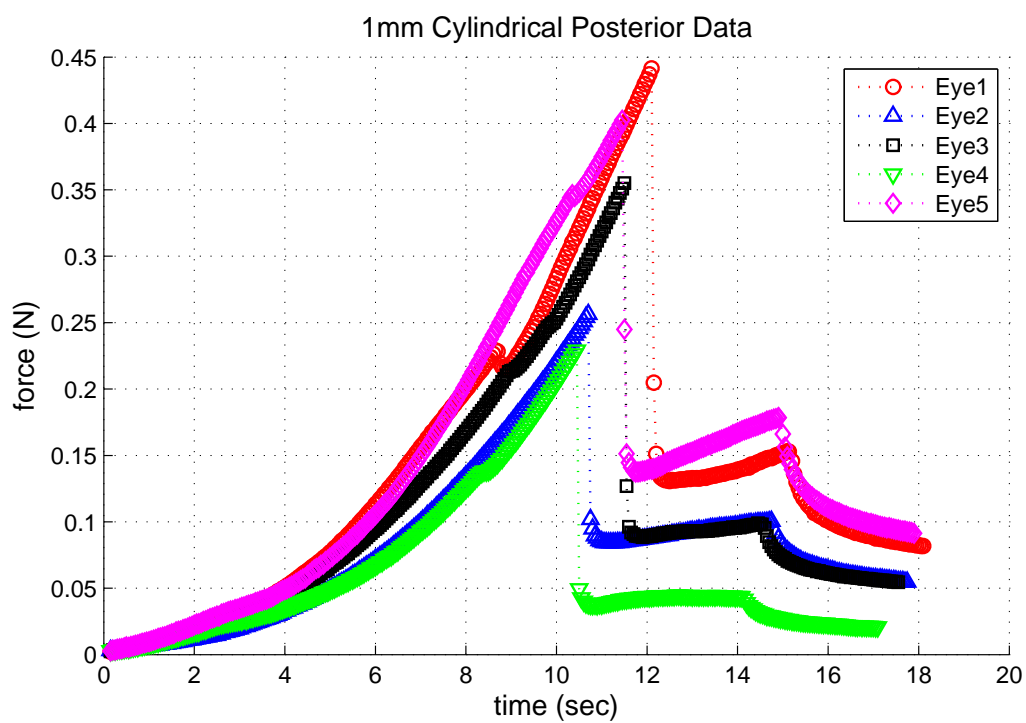


Figure 4.9: Graph of 1 mm Cylindrical Posterior Data.

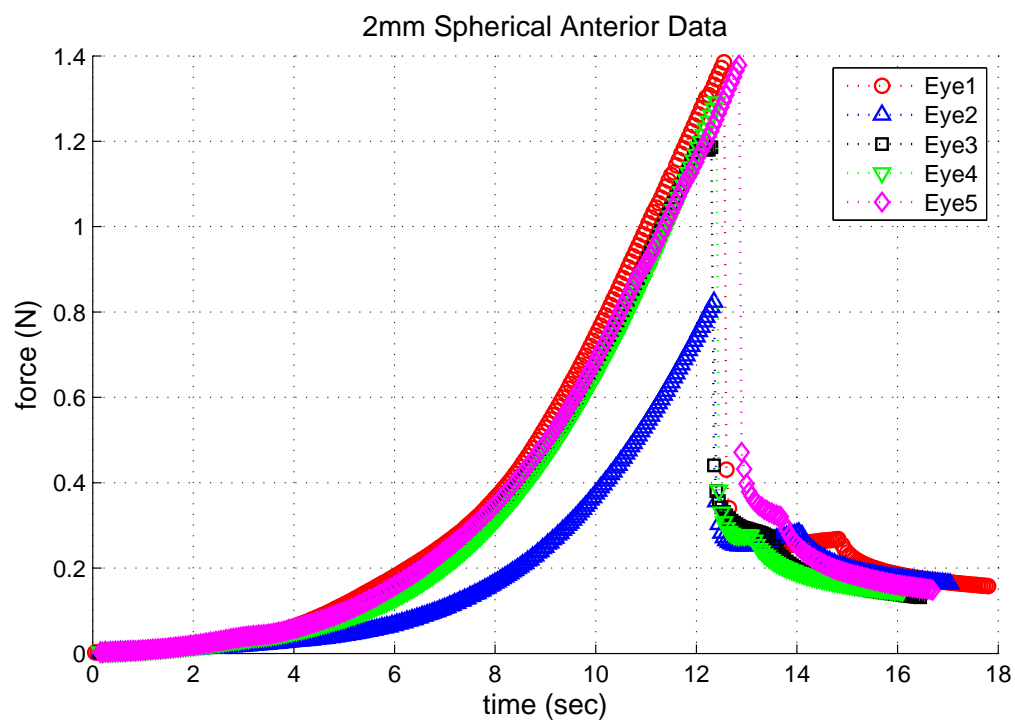


Figure 4.10: Graph of 2 mm Spherical Anterior Data.

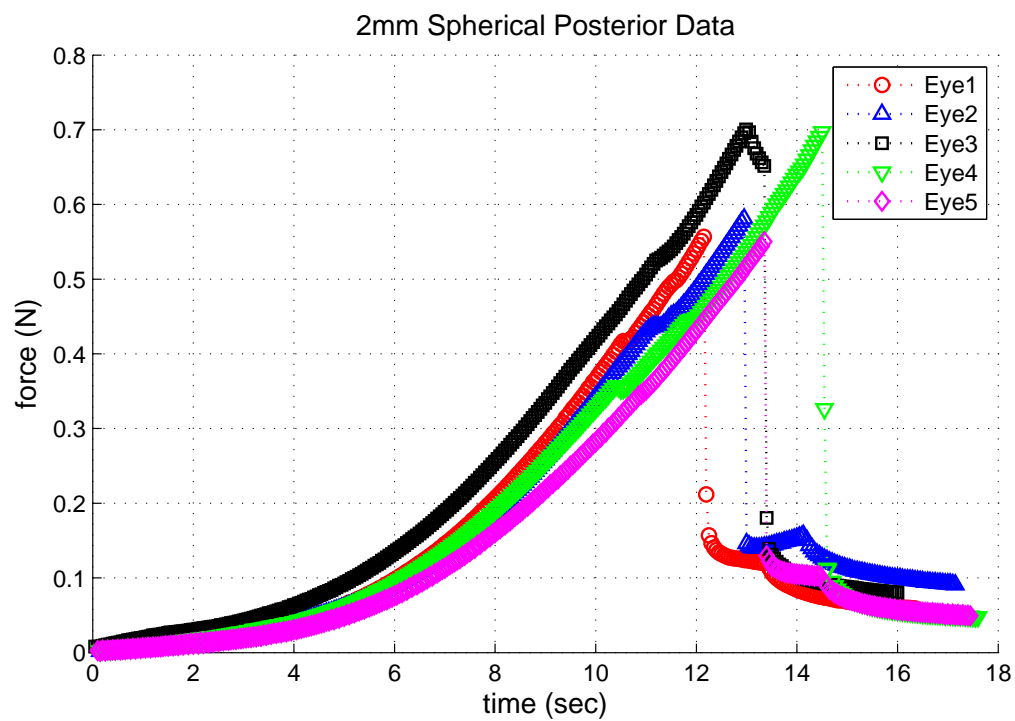


Figure 4.11: Graph of 2 mm Spherical Posterior Data.

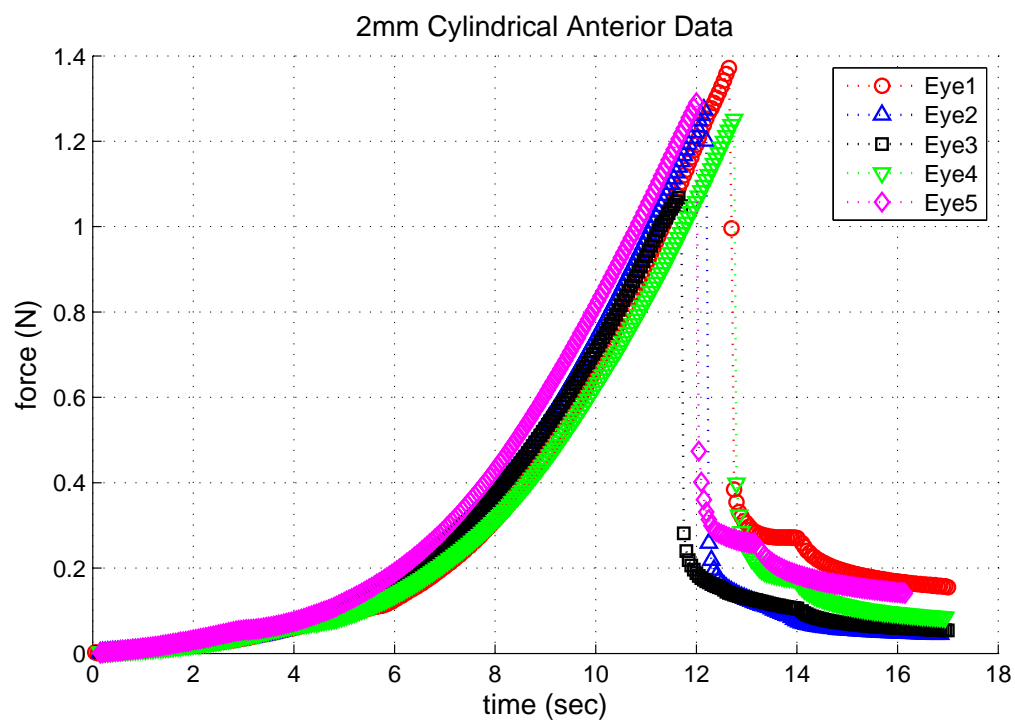


Figure 4.12: Graph of 2 mm Cylindrical Anterior Data.

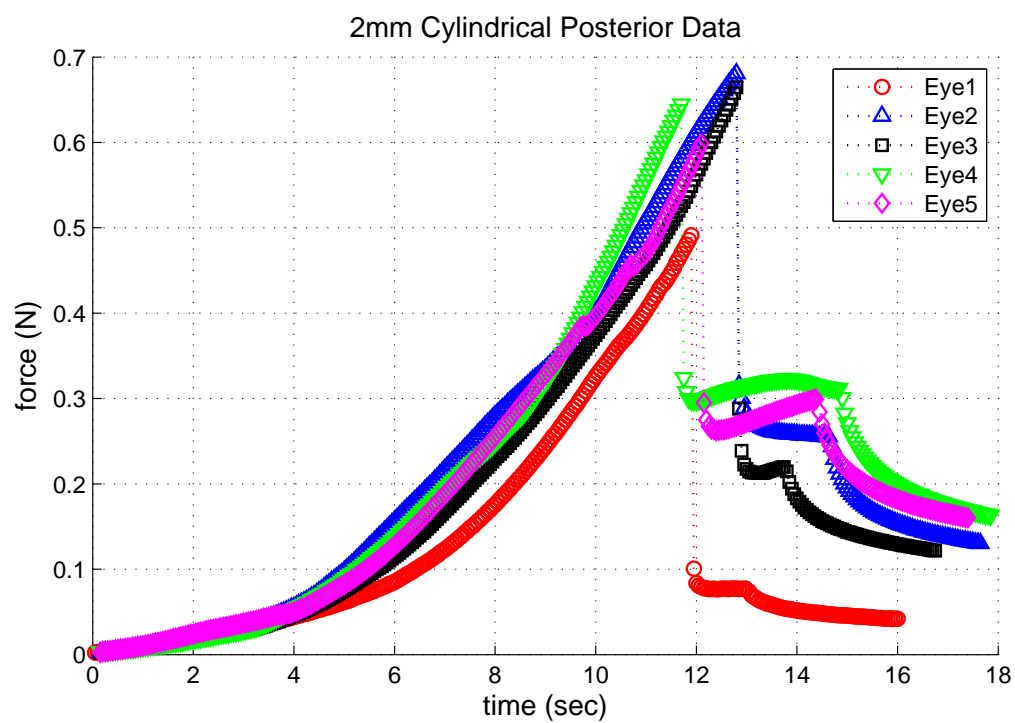


Figure 4.13: Graph of 2 mm Cylindrical Posterior Data.

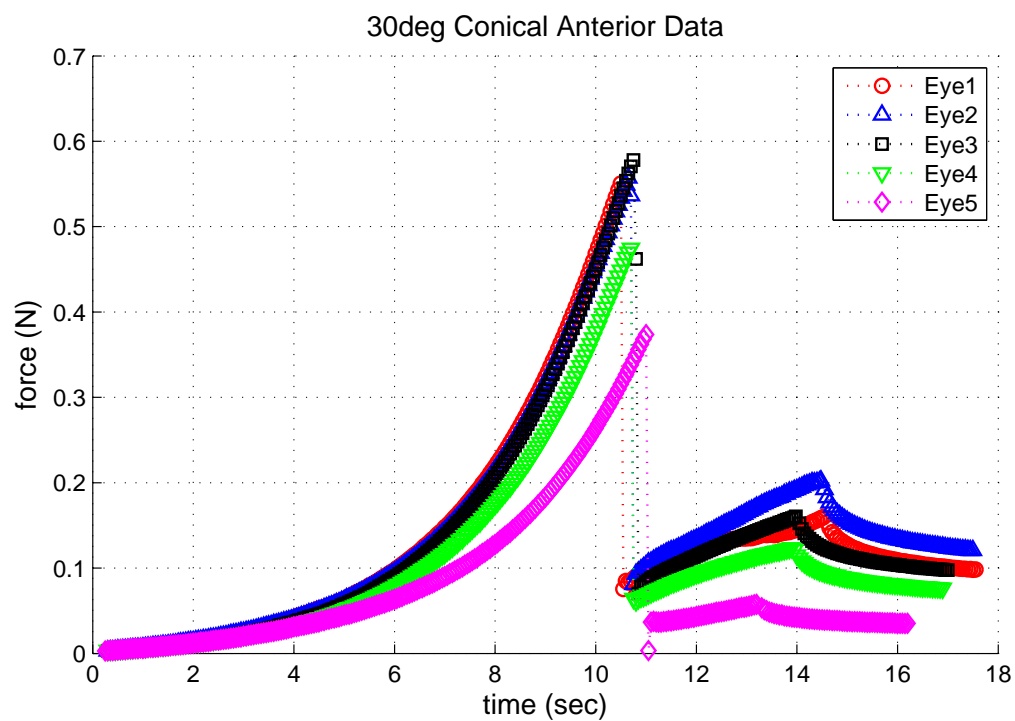


Figure 4.14: Graph of 30 deg Conical Anterior Data.

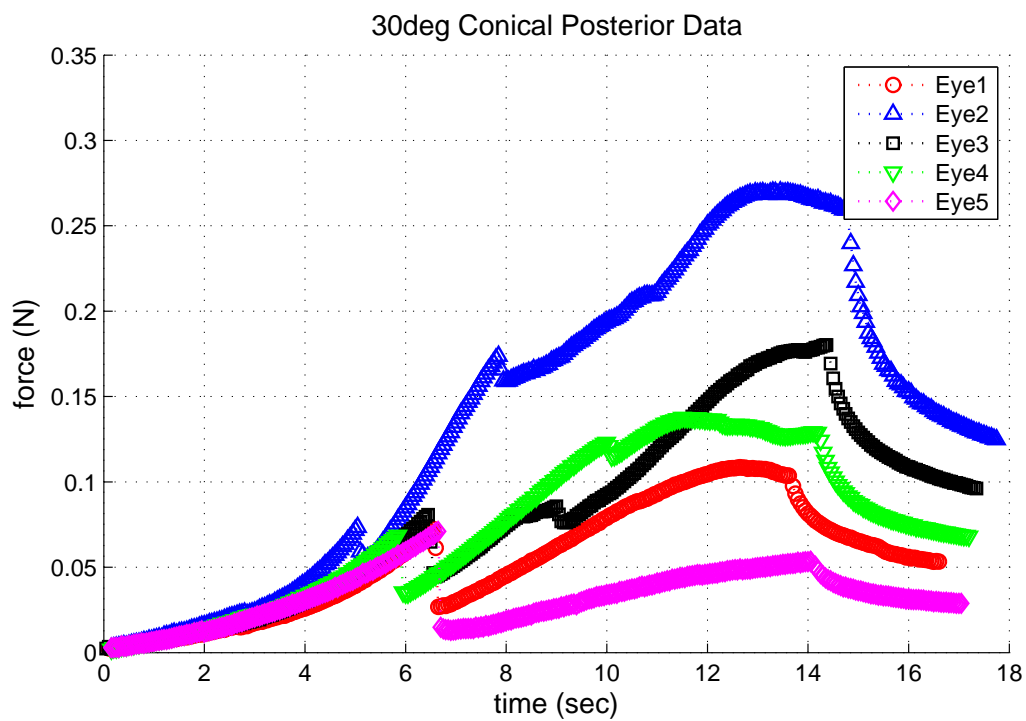


Figure 4.15: Graph of 30 deg Conical Posterior Data.



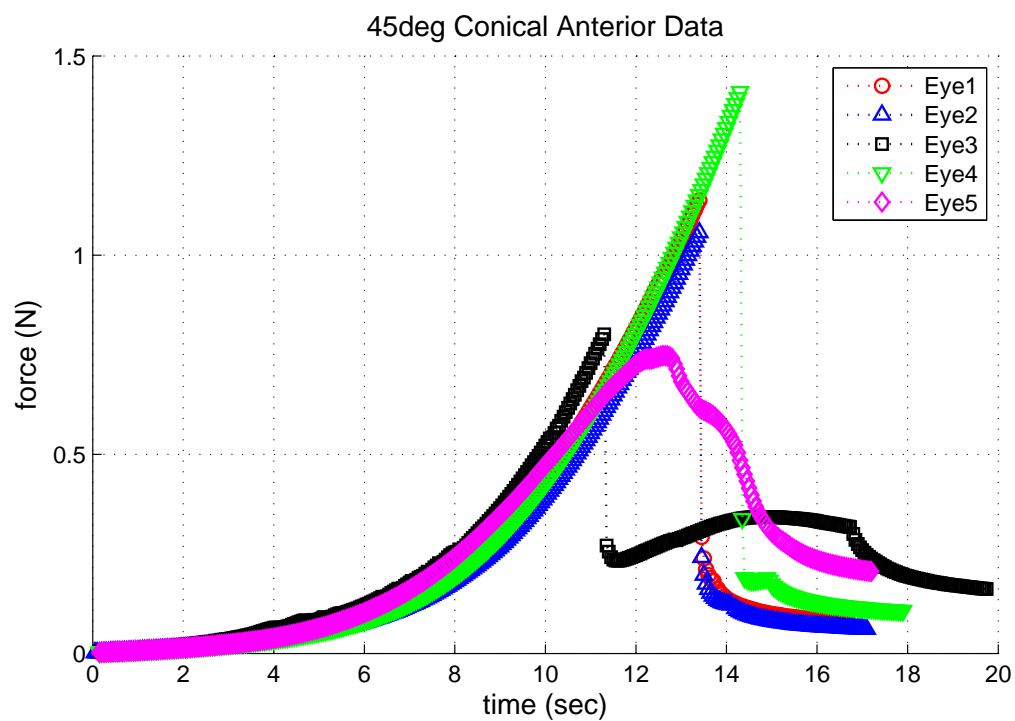


Figure 4.16: Graph of 45 deg Conical Anterior Data.

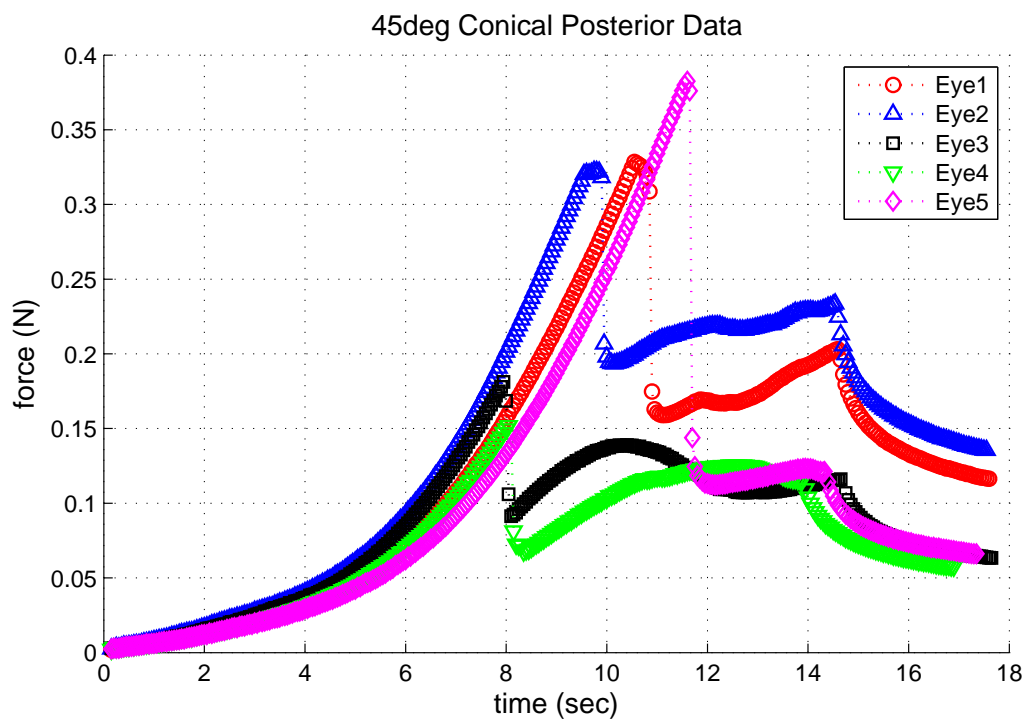


Figure 4.17: Graph of 45 deg Conical Posterior Data.

## 4.6 Discussion

Looking at the graphs for each test configuration, the data appear to have grouped well. All tests look similar with the exception of the 30 degree conical posterior test group. The tests show a very early puncture force, followed by a slight decrease in force, and then an increase in force to values greater than the puncture force by the end of the test. Upon further investigation of the data by reviewing the recorded video of the tests, it can be seen that after the initial puncture as the puncture tip continues downward, the capsule tears in addition to the original puncture (see Figure 4.18). The tears appear to go from the original puncture site down to the equator. After the tears, the lens shifts from being centrally located under the puncture tip as the puncture tip moves through the exposed lens fibers. We believe the puncture to occur earlier than the others due to the sharper nature of the 30 degree conical tip and that the posterior lens is weaker and thinner than the anterior lens [Krag et al., 1997, Yang et al., 1998a].

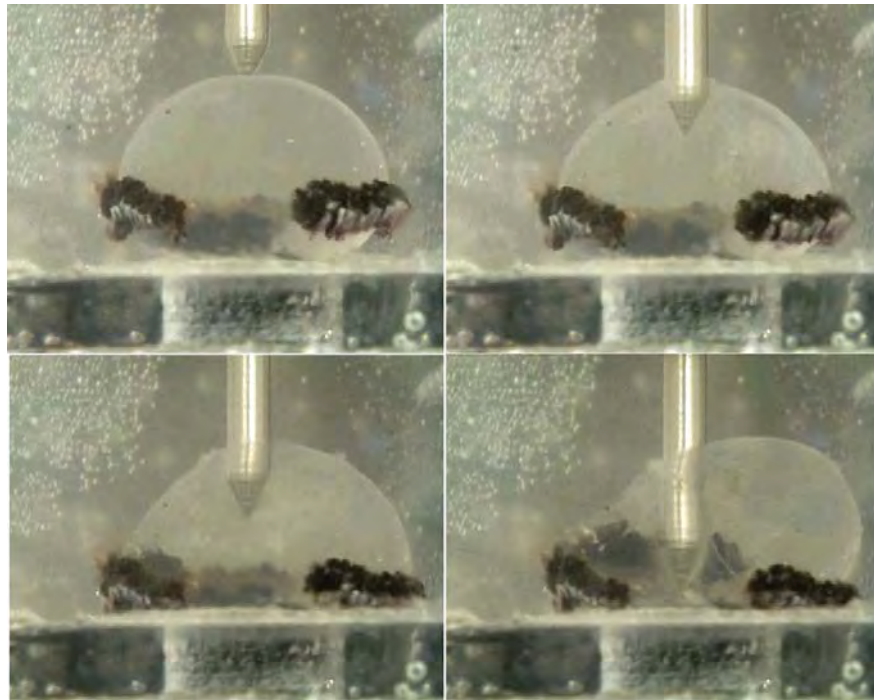


Figure 4.18: Image series showing the lens at the beginning of the test (top left), after the initial puncture (top right,) and subsequent tearing (bottom left and right) during a 30 degree conical puncture test.

Average puncture forces and the average time to puncture were calculated for each test group and can be seen in Table 4.2. It can be seen from the average values that the sharper (30 degree) and smaller diameter (1 mm) puncture tips had a smaller puncture force than their more blunt (45 degree) and larger (2 mm) counterparts. Also, the puncture forces for posterior tests are smaller than the puncture forces for the anterior tests for all groups. This supports Yang's findings that the anterior lens capsule is stronger than the posterior lens capsule [Yang et al., 1998a]. The puncture forces between the respective spherical and cylindrical tip sizes were approximately the same, with the 45 degree conical tip landing somewhere in between anteriorly and slightly below posteriorly. The 30 degree conical tip puncture force was much lower than all the others, due to its sharpness. Puncture times for the tips were longer on anterior tests than posterior tests except for the 2 mm cylindrical group and the 2 mm spherical group. In the 2 mm cylindrical tip group times were approximately the same between anterior and posterior tests. In the 2 mm spherical tip group, the average anterior time was lower than the average posterior time by 0.73 seconds. Although the posterior lens capsule is weaker than the anterior, perhaps the average puncture time for the 2 mm spherical posterior group was longer than the anterior group because of the non-sharp nature of the tip and the greater surface area of the posterior lens capsule (allowing for more deformation before failure with the non-sharp tip).

Table 4.2: Average Puncture Force & Average Time to Puncture.

Tip Geometry (d, $\Theta$ )	Anterior		Posterior	
	Force (N)	Time (s)	Force (N)	Time (s)
1 mm spherical	1.1329	13.47	0.3663	12.00
2 mm spherical	1.2929	12.48	0.6171	13.21
1 mm cylindrical	1.1651	13.89	0.3508	11.03
2 mm cylindrical	1.2510	12.16	0.6159	12.18
30 deg conical	0.5067	10.73	0.0672	5.61
45 deg conical	1.2399	13.18	0.2928	9.25

Preliminary modeling is being completed in Abaqus. Below Figures 4.19 and 4.20 show an Abaqus simulation for a 1 mm spherical posterior puncture test with a loading rate of 0.1 mm/s (we

started with a lower loading rate than actual to get the simulation to run the longest). Figure 4.19 shows the beginning of the simulation and Figure 4.20 shows as far as the simulation will run. The simulation is setup as a 2-D axisymmetric mesh with a fixed bottom platen and an incompressible 1 mm spherical puncture tip. The interactions between the lens and the tip and the lens and the bottom platen are frictionless. In Figure 4.20 the stress can be seen in the lens capsule near the contact point of the puncture tip. Figure 4.21 better shows the stresses in the lens fiber cells, with the highest stresses being located near the puncture tip contact point. We are trying to model the puncture test up to puncture (approximately 70% strain). Unfortunately, with Abaqus the simulation only runs to approximately 17% strain before failing to converge. Work is currently being done to model the lens capsule as a shell element and the interior lens fibers as a viscous incompressible fluid in hopes of getting the simulation to run to higher strains.

While modeling has been difficult, our data support Yang's findings that the anterior lens capsule is stronger than the posterior lens capsule [Yang et al., 1998a]. More importantly, the data gathered will be useful in calculating material properties of the whole porcine ocular lens with parameter fitting in Tahoe to compare with the properties calculated from the unconfined compression testing data. Additionally, the data will be useful when the model is developed enough to begin modeling the interaction between intraocular foreign bodies and the ocular lens.

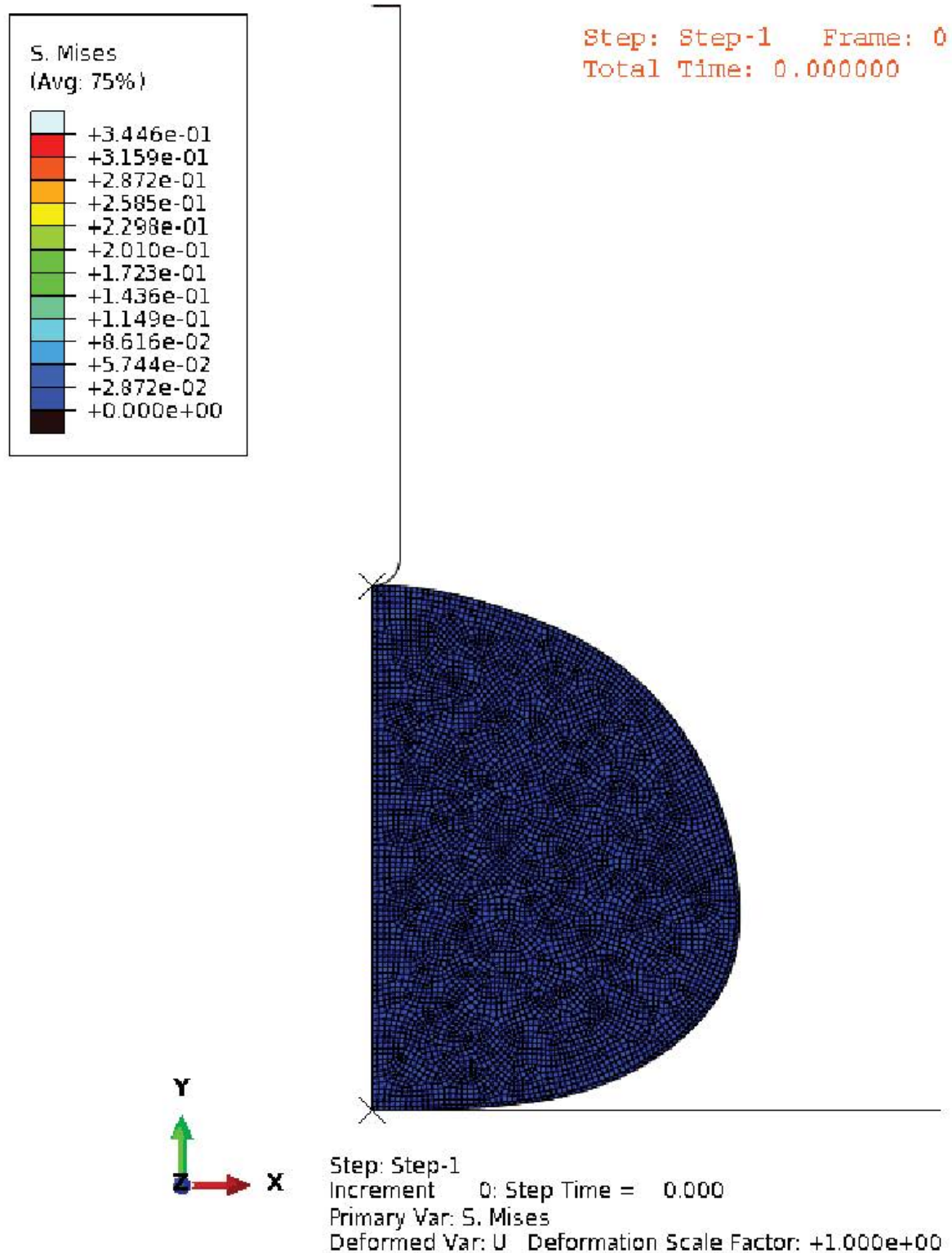


Figure 4.19: Abaqus Simulation of Puncture Testing of Whole Porcine Ocular Lens - Beginning of simulation.

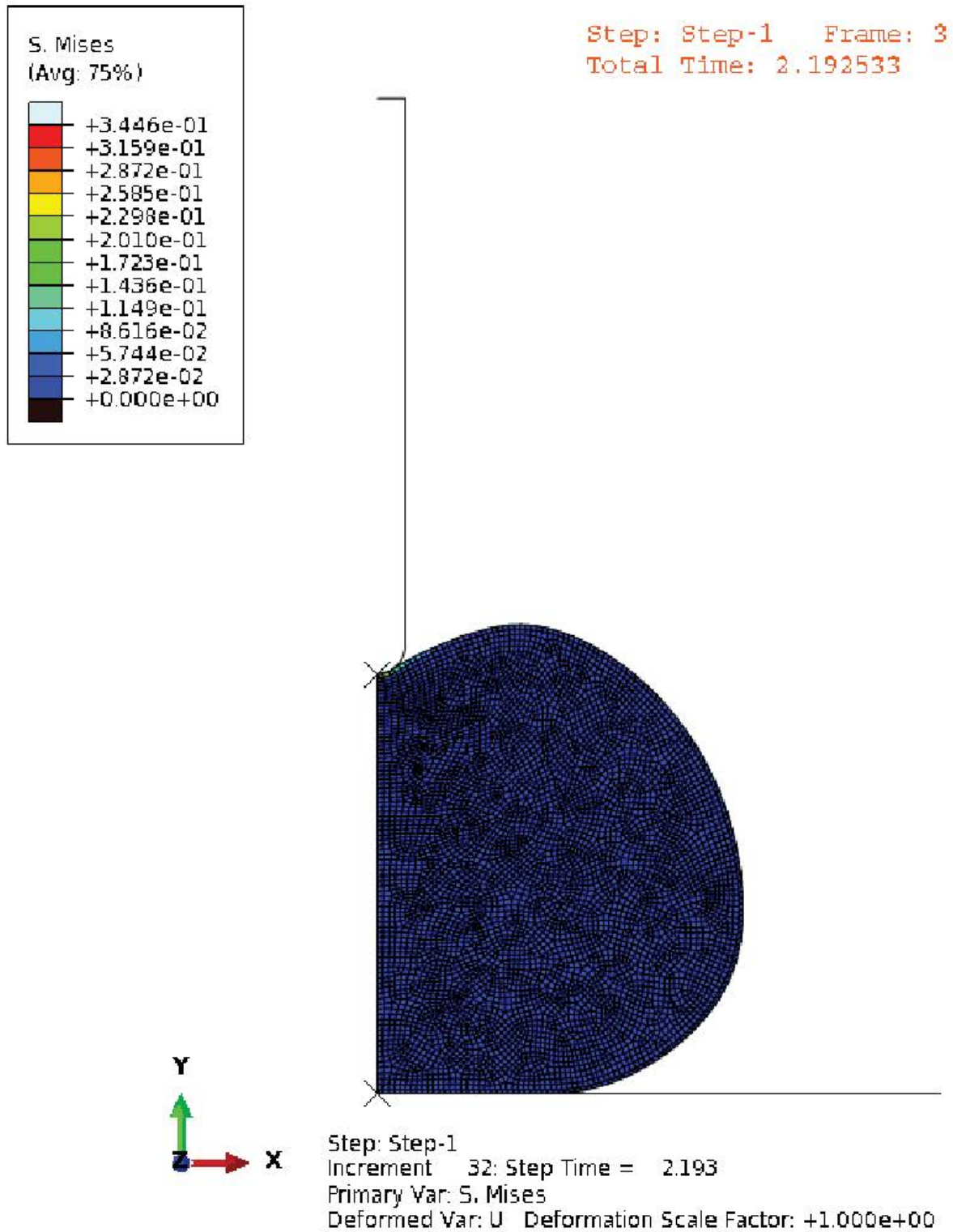


Figure 4.20: Abaqus Simulation of Puncture Testing of Whole Porcine Ocular Lens - As far as simulation will complete.



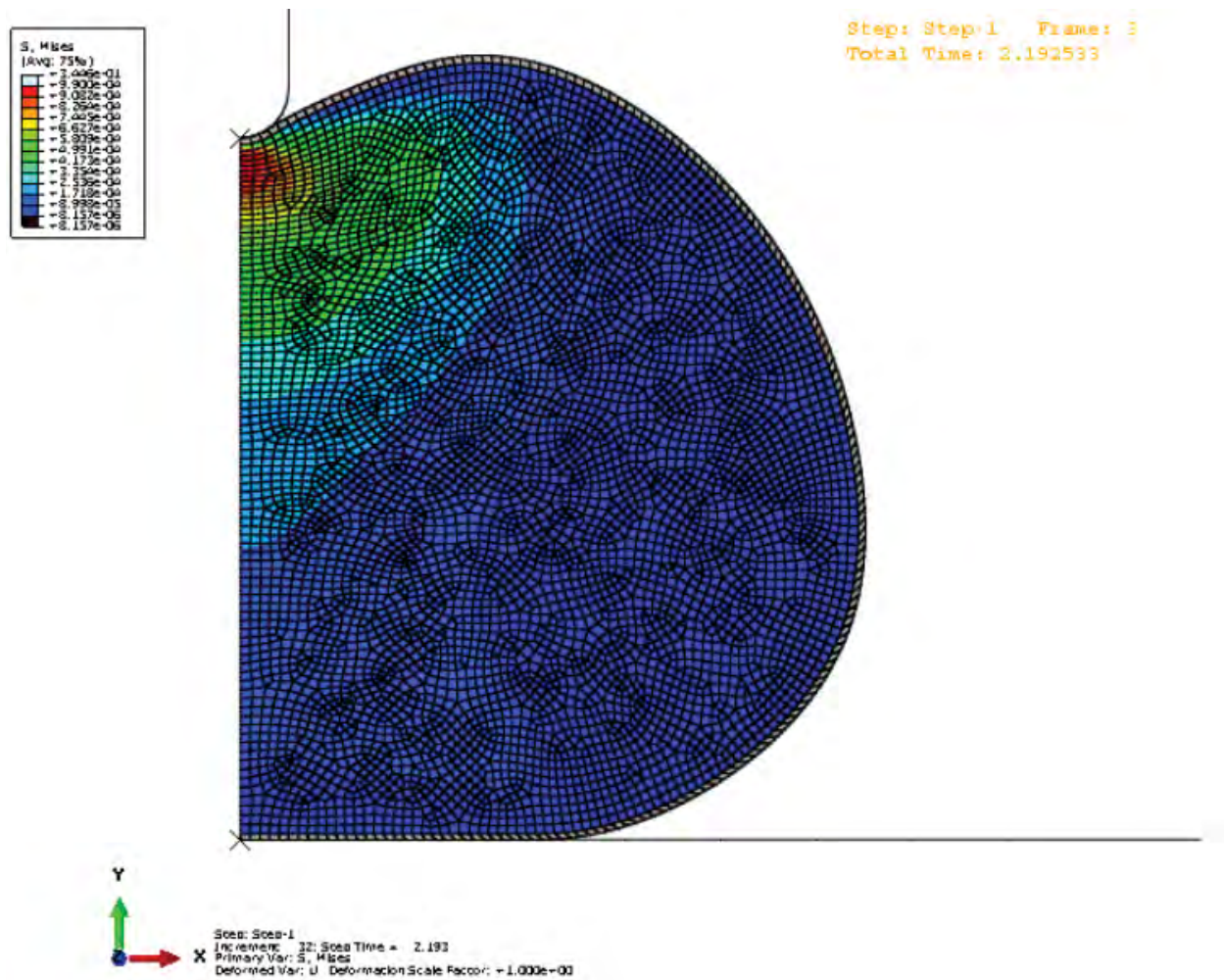


Figure 4.21: Abaqus Simulation of Puncture Testing of Whole Porcine Ocular Lens - Scaled contour to better show stresses in lens fibers.

## Chapter 5

### Nanoindentation of the Capsule

Nanoindentation can be used to determine the material properties of samples. This is done by indenting a material with known properties (the indentation tip) into a material's surface with unknown properties. The force and displacement are recorded during the test and later used with the tip geometry and indentation area to calculate the unknown material properties. For viscoelastic materials, frequently a stress-relaxation test or a creep test are used to determine material properties. In a stress-relaxation test, the indentation tip is lowered into the sample to a pre-defined depth at which the tip stops displacing and the material is allowed to relax over a pre-defined hold time, after which the indentation tip will retract. In a creep test, the indentation tip is lowered into the sample until a pre-defined force is reached. Once this force is reached, the indentation tip will continue to indent into the sample as it relaxes, maintaining that pre-defined force for a certain length of time, after which the indentation tip will retract. Nanoindentation is being used on the lens capsule to determine the capsules material properties (specifically  $\tau$  (relaxation time constant),  $\mu_{EQ}$  (equilibrium shear modulus), and  $\mu_{NEQ}$  (nonequilibrium shear modulus)). Because of the size of the indentation tips used in nanoindentation, very small volumes of material can be tested. This fits well with the lens capsule as the porcine anterior lens capsule is approximately  $60\ \mu m$  thick. Calculation of the parameters will be done using the same method employed in the parameter fitting of the unconfined compression data, described in detail in the previous Parameter Fitting of Unconfined Compression Testing Data Chapter. Determination of just the lens capsule properties will allow for the back calculation of the interior lens fiber material



properties from the whole lens data gathered from the unconfined compression data. The two material property sets will be used for the different materials in the computational model.

## 5.1 Sample Preparation

Anterior lens capsule tissue was collected by first removing the cornea as previously described in the Puncture Testing of the Whole Lens Chapter. Then, while applying slight pressure to the whole globe, a small incision was made with a diamond-head scalpel in the anterior surface of the ocular lens, near the attachment of the zonules. By gently widening this incision with the scalpel, the interior lens fibers slide out, intact, from the slight pressure being applied to the globe. With the interior lens fibers removed, the anterior portion of the capsule was then lifted by a pair of tweezers inserted through the previously made incision. Once lifted, the anterior capsule was collected by using a pair of micro scissors to cut the capsule near the zonule attachments around the perimeter. Once extracted, the anterior lens capsule tissue was placed in vials containing Alcon BSS and transported to the nanoindenter (at the Colorado School of Mines in Golden, CO) on wet-ice.

## 5.2 Experimental Setup

A TI-950 TriboIndenter made by Hysitron was used to perform the nanoindentation (see Figure 5.1). The machine was located at the Colorado School of Mines in Golden, CO under the direction of Assistant Professor Corrine Packard. A  $1\text{ }\mu\text{m}$  diameter, spherical fluid cell tip was used to test the lens capsule in Alcon BSS at room temperature (approximately  $21\text{ }^{\circ}\text{C}$ ). The anterior lens capsule tissue was placed on a polycarbonate substrate with the approximate curved shape of the anterior surface of the lens (see Figure 5.2). The substrate has a surrounding wall to contain the Alcon BSS that the lens capsule is immersed in. The lens capsule was held in place by a small metallic washer, preventing slippage of the tissue while being indented (see Figure 5.3).



Figure 5.1: Hysitron TI-950 TriboIndenter Nanoindenter Located at the Colorado School of Mines.

### 5.3 Experimental Method

TriboScan 9 software was utilized to perform the tests and export the data. After ensuring the correct calibration file was loaded, an air indent was performed to calibrate the indentation tip and system. This was followed by tip-to-optic calibration. The boundary was defined for an aluminium standard and an h-pattern indentation series was used to align the indentation tip with the optics. The sample tissue was then placed on the substrate, held in place by the small metallic washer, and immersed in Alcon BSS that had acclimated to the room temperature for at least 24 hours. The substrate and sample were then placed in the machine. After defining the boundary of the testing substrate, the indentation tip was positioned over the center of the testing substrate and lowered into the fluid so that the Alcon BSS could no longer be seen being pulled up the sides of the indentation tip but without contacting the lens capsule. A single tip-to-optic calibration indent

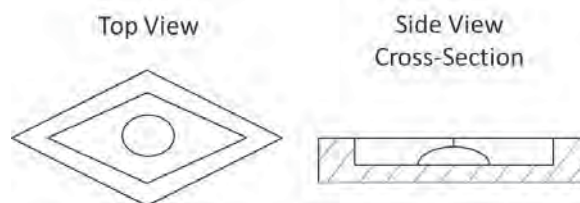


Figure 5.2: Drawing of Nanoindentation Substrate with Dome-Shaped Surface and Liquid Well.

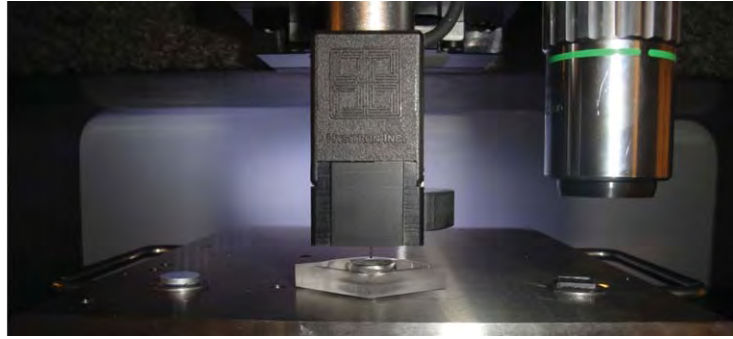


Figure 5.3: Image of Lens Capsule Being Held in Place by a Small Metallic Washer Within the Nanoindenter.

was performed on the lens capsule tissue to determine the height of the sample. The software was then switched into Imaging mode (normally used to create a 3-D image of a material's surface using the indentation tip). Single indents in Imaging mode were used to indent the sample. This allowed for more reliable finding of the surface of the lens capsule as the tip remains in constant contact with the lens capsule. Creep tests were performed with a hold load of  $5 \mu N$ . The tip loaded for 10 seconds, held the load for 30 seconds, and unloaded over 10 seconds. Test locations were separated by  $60 \mu m$  in the positive x-direction (to avoid any plastic deformation from previous indents) until 4 indents were completed. The test locations then moved  $60 \mu m$  in the negative y-direction and resumed testing, moving  $60 \mu m$  in the negative x-direction until 4 tests were completed. This process was repeated for all tests. Depth, load, and time were recorded for each test. Once the test was completed, the data were exported in text files for later analysis.

## 5.4 Results

Below are graphs showing creep test data from nanoindentation of the anterior porcine lens capsule and the anterior human lens capsule. The non-zero starting force on each graph is a product of the pre-load force necessary for the indentation tip to find contact. It was hard to avoid with such a small holding load.

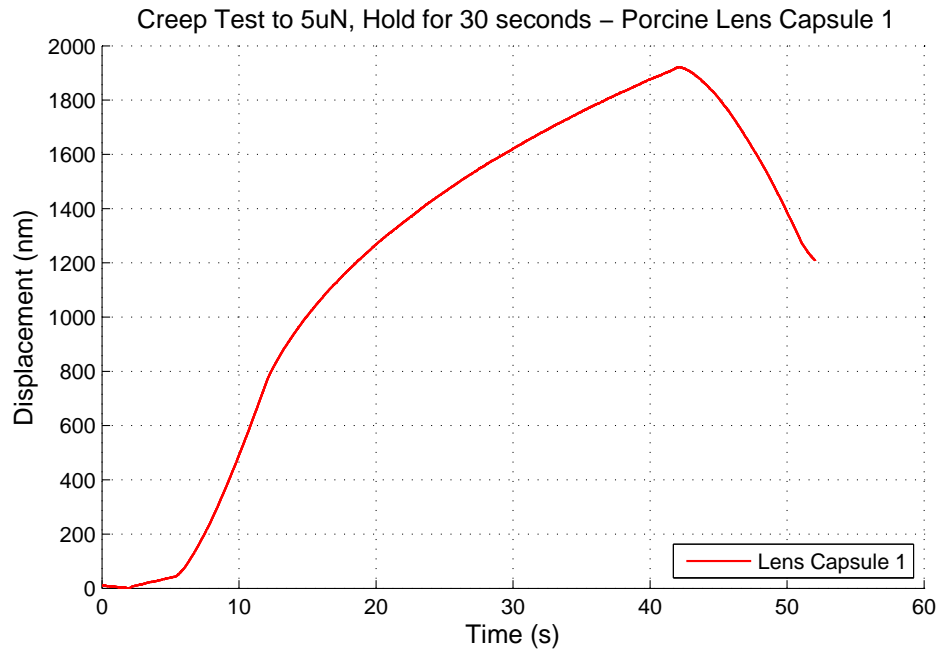


Figure 5.4: Graph of Nanoindentation Creep Test Porcine Lens Capsule 1 - Load to 5  $\mu\text{N}$ , Hold for 30 seconds. The pre-load force necessary to get contact with the lens capsule is the cause of the non-zero starting force.

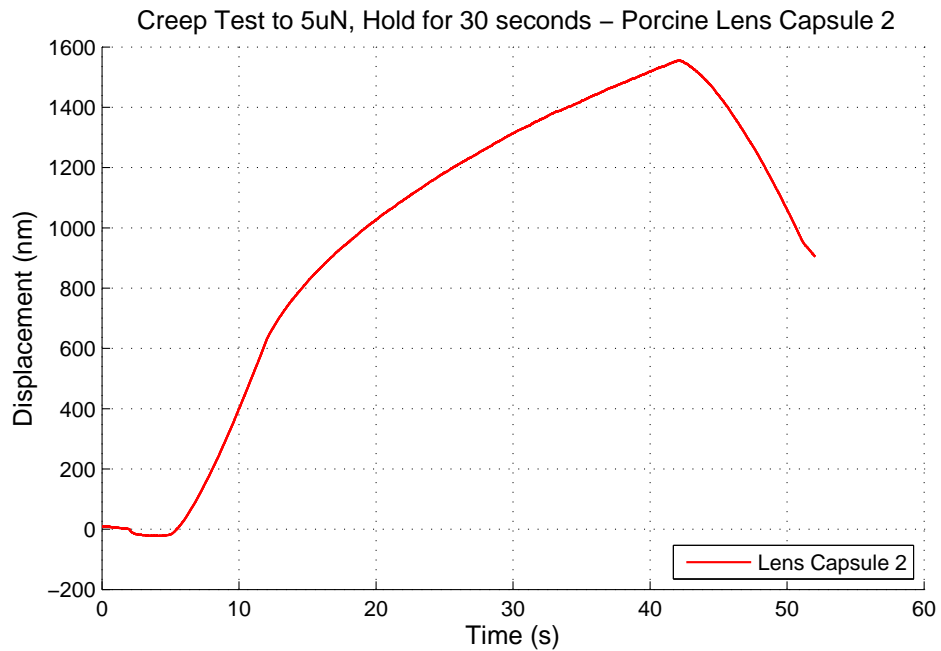


Figure 5.5: Graph of Nanoindentation Creep Test Porcine Lens Capsule 2 - Load to 5  $\mu\text{N}$ , Hold for 30 seconds. The pre-load force necessary to get contact with the lens capsule is the cause of the non-zero starting force.

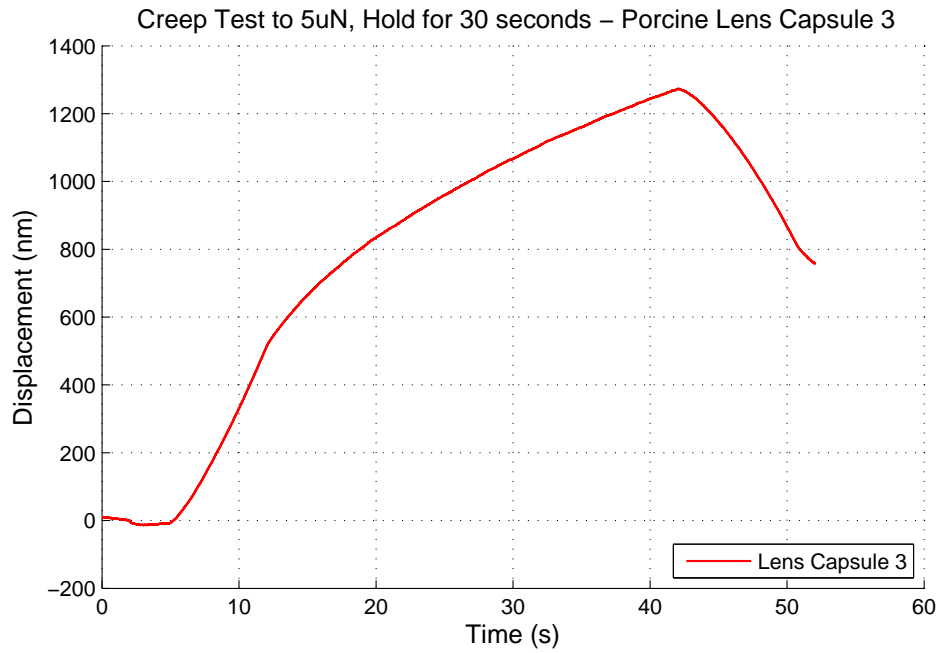


Figure 5.6: Graph of Nanoindentation Creep Test Porcine Lens Capsule 3 - Load to 5  $\mu\text{N}$ , Hold for 30 seconds. The pre-load force necessary to get contact with the lens capsule is the cause of the non-zero starting force.

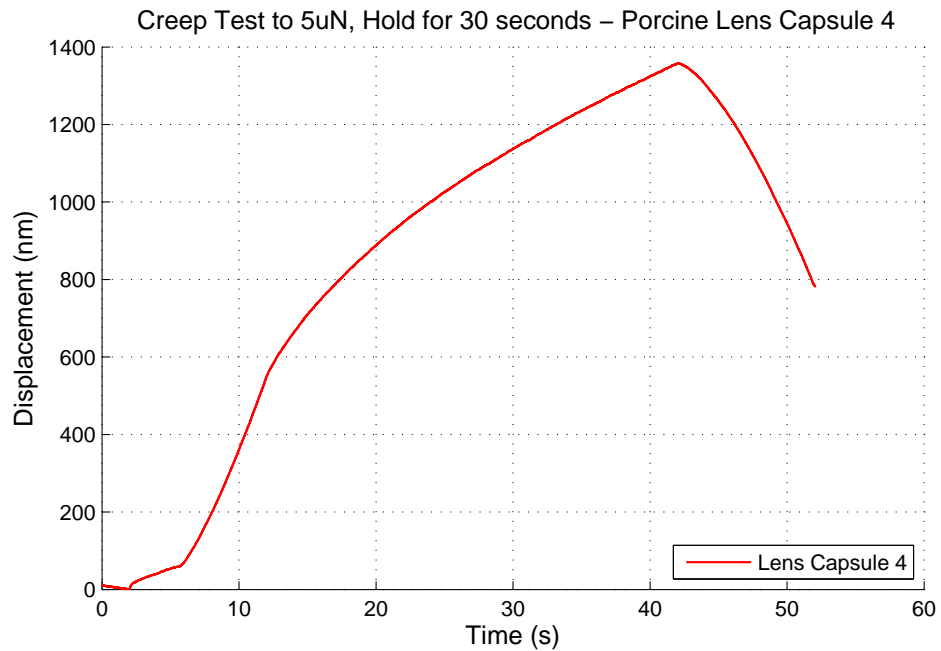


Figure 5.7: Graph of Nanoindentation Creep Test Porcine Lens Capsule 4 - Load to 5  $\mu\text{N}$ , Hold for 30 seconds. The pre-load force necessary to get contact with the lens capsule is the cause of the non-zero starting force.

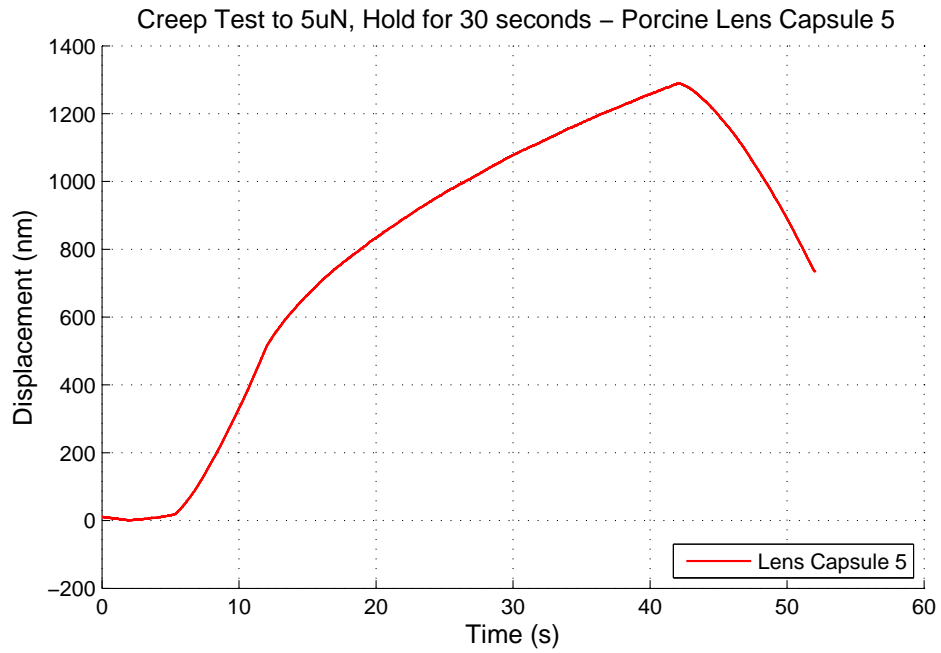


Figure 5.8: Graph of Nanoindentation Creep Test Porcine Lens Capsule 5 - Load to 5  $\mu\text{N}$ , Hold for 30 seconds. The pre-load force necessary to get contact with the lens capsule is the cause of the non-zero starting force.

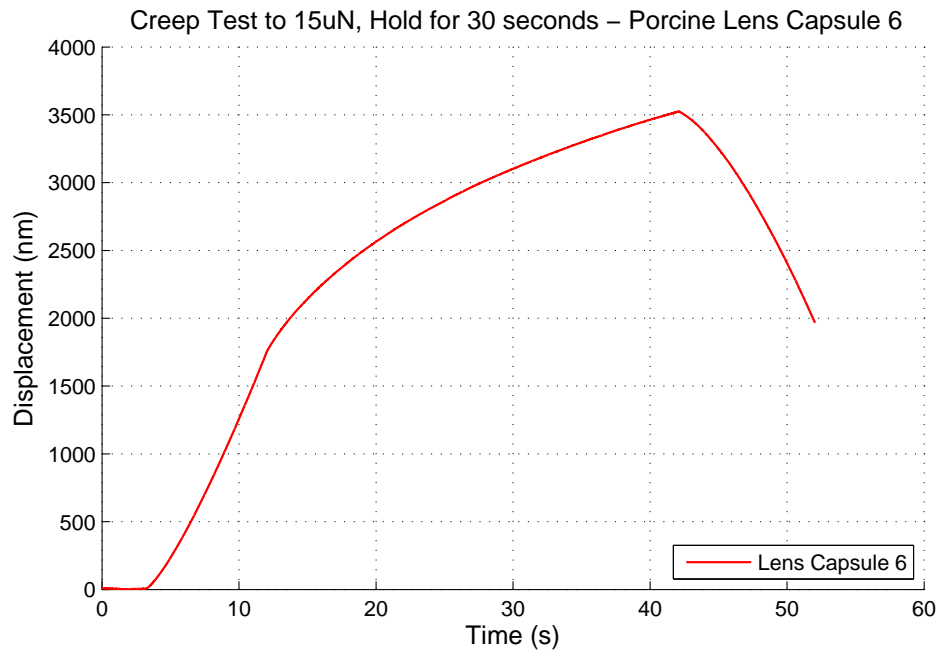


Figure 5.9: Graph of Nanoindentation Creep Test Porcine Lens Capsule 6 - Load to 15  $\mu\text{N}$ , Hold for 30 seconds. The pre-load force necessary to get contact with the lens capsule is the cause of the non-zero starting force.

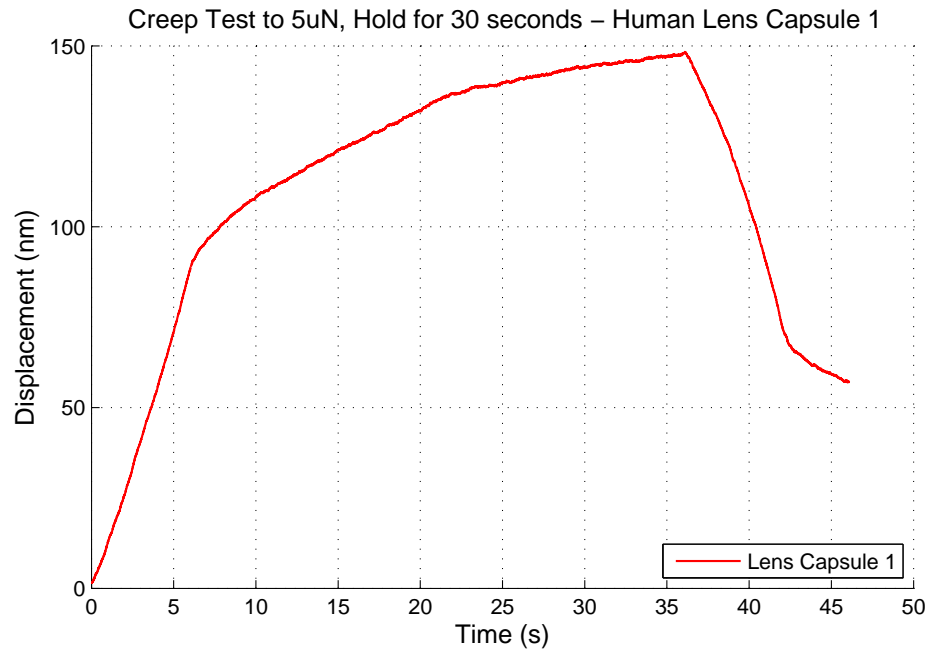


Figure 5.10: Graph of Nanoindentation Creep Test Human Lens Capsule 1 - Load to 5  $\mu\text{N}$ , Hold for 30 seconds. The pre-load force necessary to get contact with the lens capsule is the cause of the non-zero starting force.

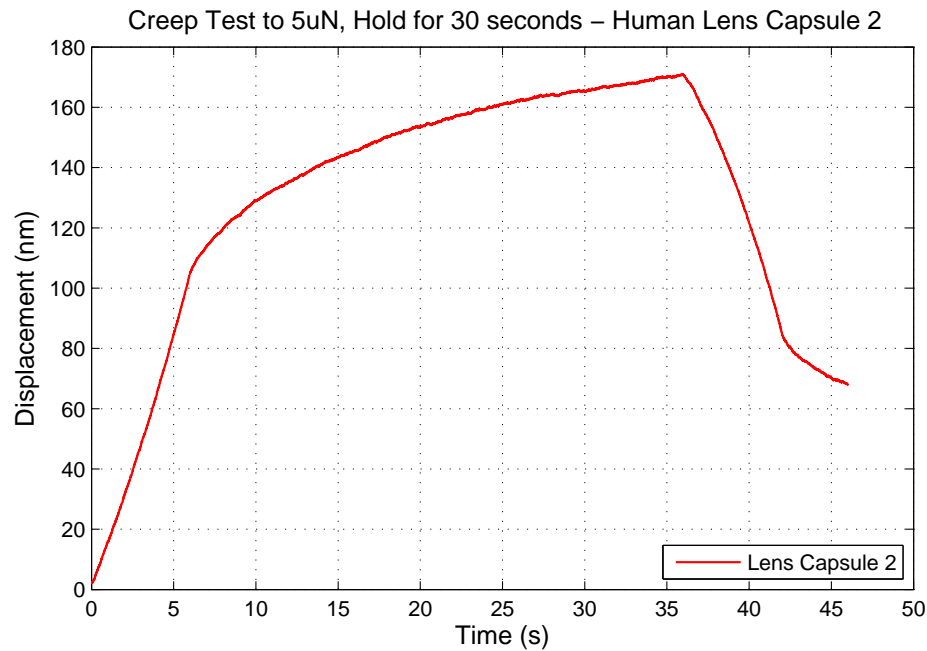


Figure 5.11: Graph of Nanoindentation Creep Test Human Lens Capsule 2 - Load to 5  $\mu\text{N}$ , Hold for 30 seconds. The pre-load force necessary to get contact with the lens capsule is the cause of the non-zero starting force.

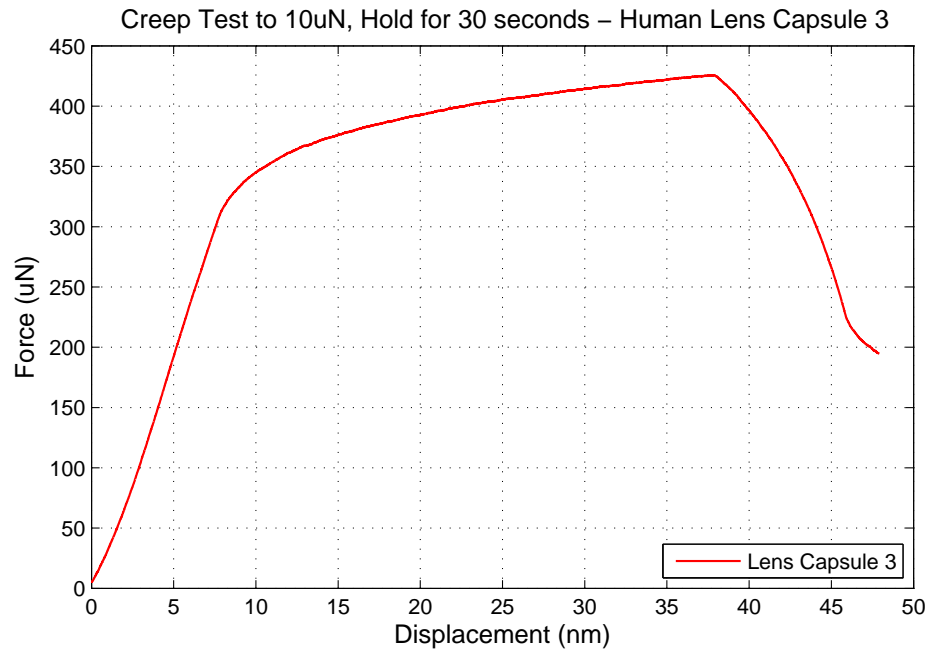


Figure 5.12: Graph of Nanoindentation Creep Test Human Lens Capsule 3 - Load to  $10 \mu\text{N}$ , Hold for 30 seconds. The pre-load force necessary to get contact with the lens capsule is the cause of the non-zero starting force.

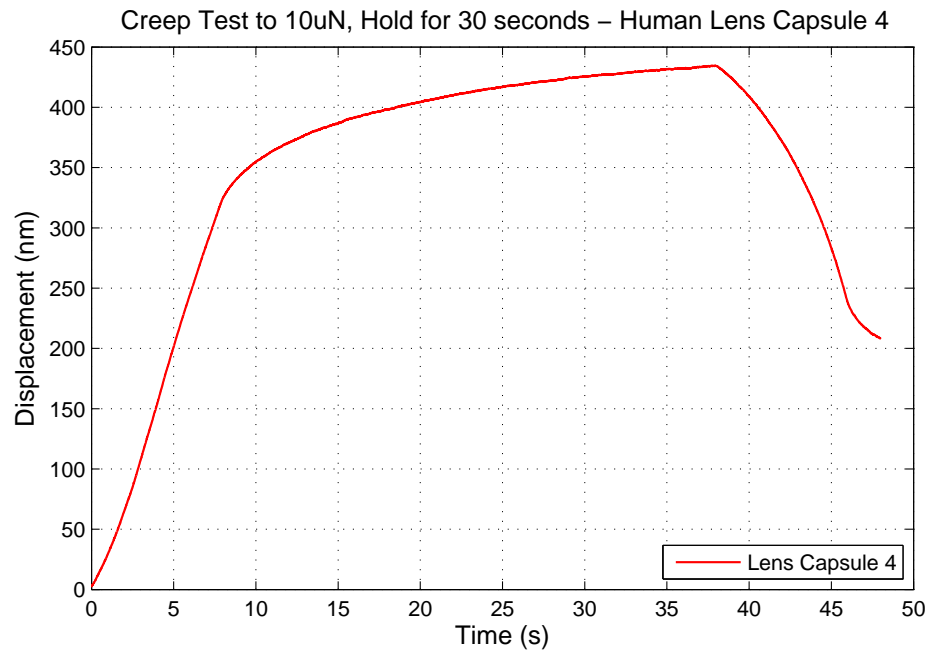


Figure 5.13: Graph of Nanoindentation Creep Test Human Lens Capsule 4 - Load to  $10 \mu\text{N}$ , Hold for 30 seconds. The pre-load force necessary to get contact with the lens capsule is the cause of the non-zero starting force.



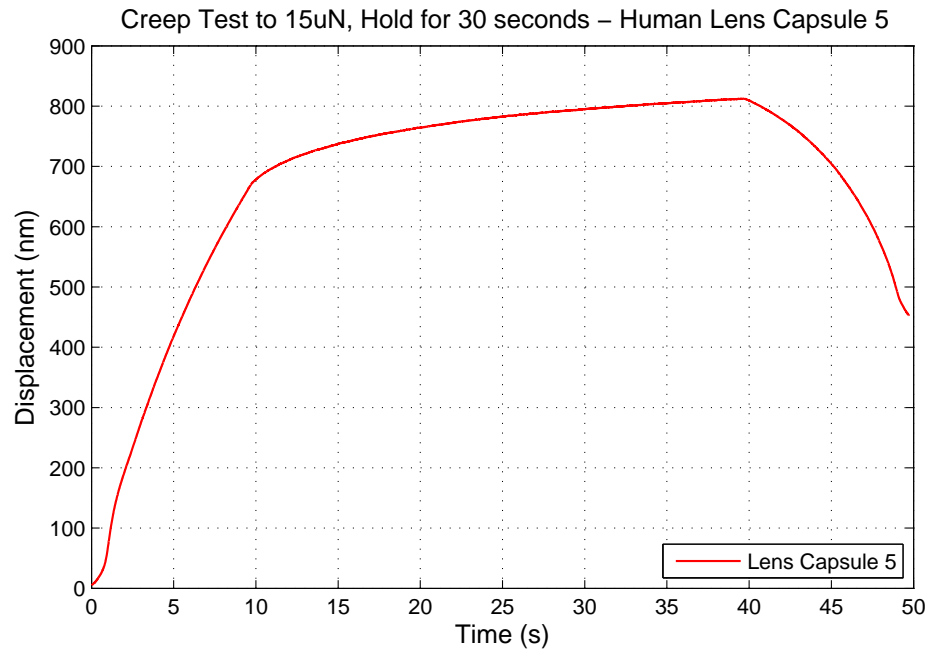


Figure 5.14: Graph of Nanoindentation Creep Test Human Lens Capsule 5 - Load to 15  $\mu\text{N}$ , Hold for 30 seconds. The pre-load force necessary to get contact with the lens capsule is the cause of the non-zero starting force.

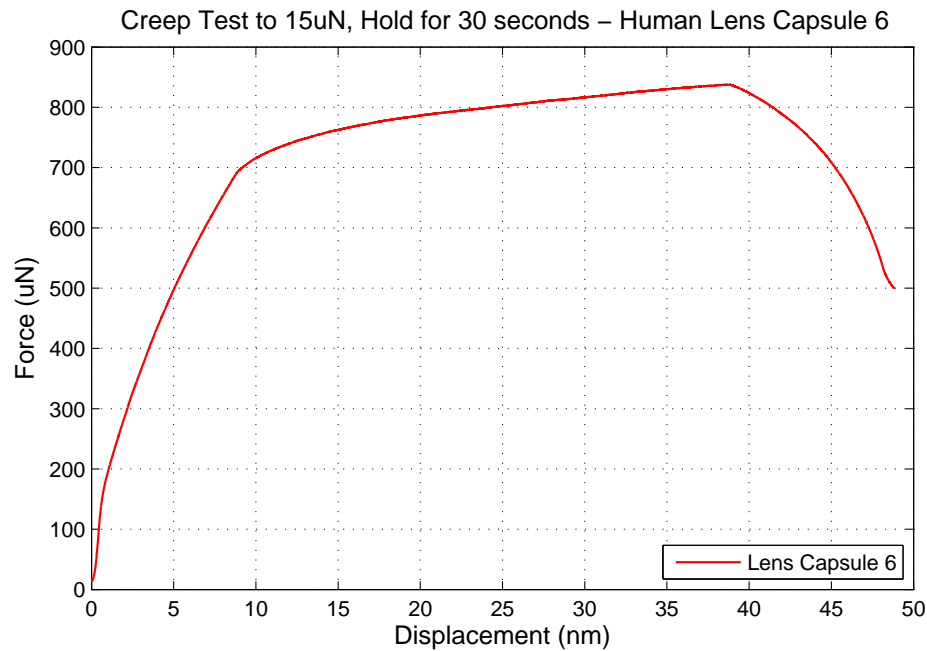


Figure 5.15: Graph of Nanoindentation Creep Test Human Lens Capsule 6 - Load to 15  $\mu\text{N}$ , Hold for 30 seconds. The pre-load force necessary to get contact with the lens capsule is the cause of the non-zero starting force.

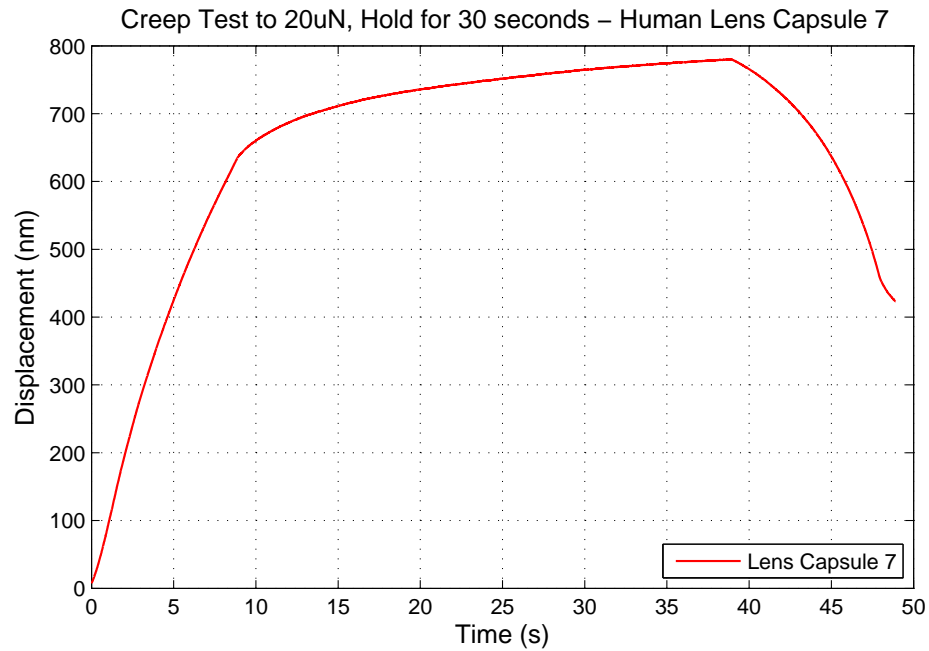


Figure 5.16: Graph of Nanoindentation Creep Test Human Lens Capsule 7 - Load to 20  $\mu\text{N}$ , Hold for 30 seconds. The pre-load force necessary to get contact with the lens capsule is the cause of the non-zero starting force.

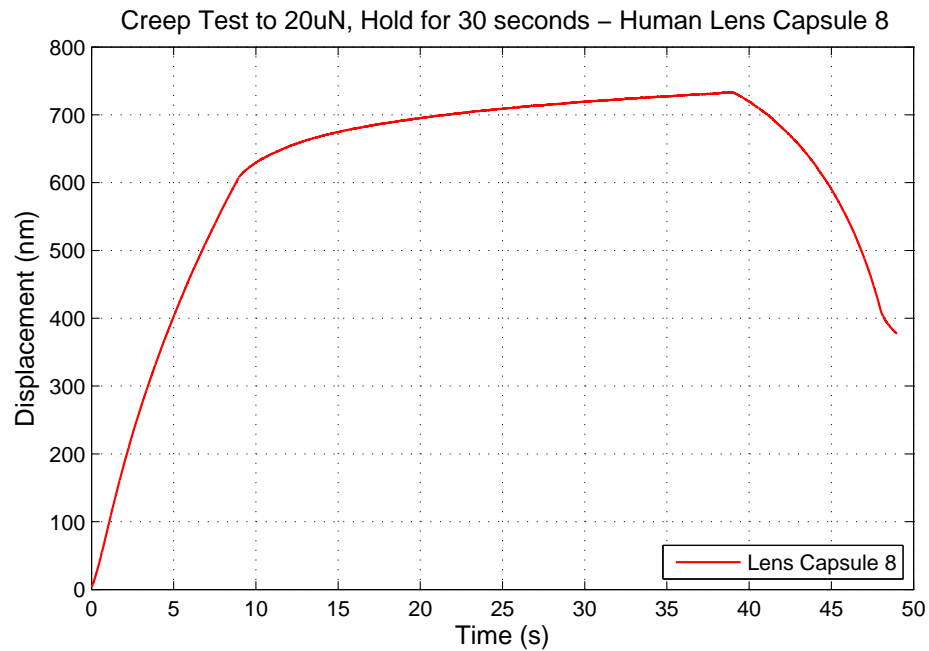


Figure 5.17: Graph of Nanoindentation Creep Test Human Lens Capsule 8 - Load to 20  $\mu\text{N}$ , Hold for 30 seconds. The pre-load force necessary to get contact with the lens capsule is the cause of the non-zero starting force.

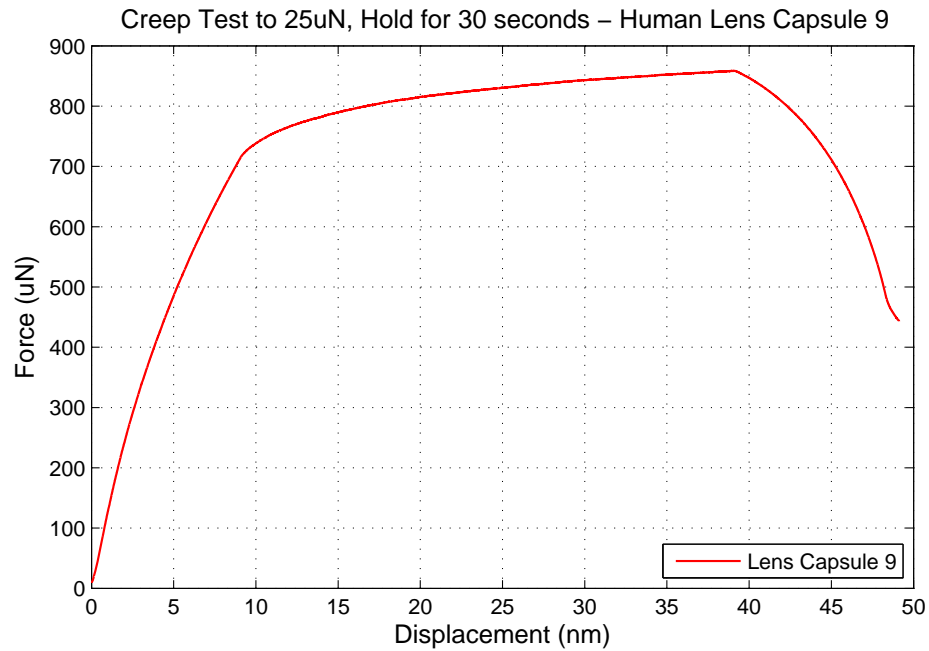


Figure 5.18: Graph of Nanoindentation Creep Test Human Lens Capsule 9 - Load to  $25 \mu\text{N}$ , Hold for 30 seconds. The pre-load force necessary to get contact with the lens capsule is the cause of the non-zero starting force.

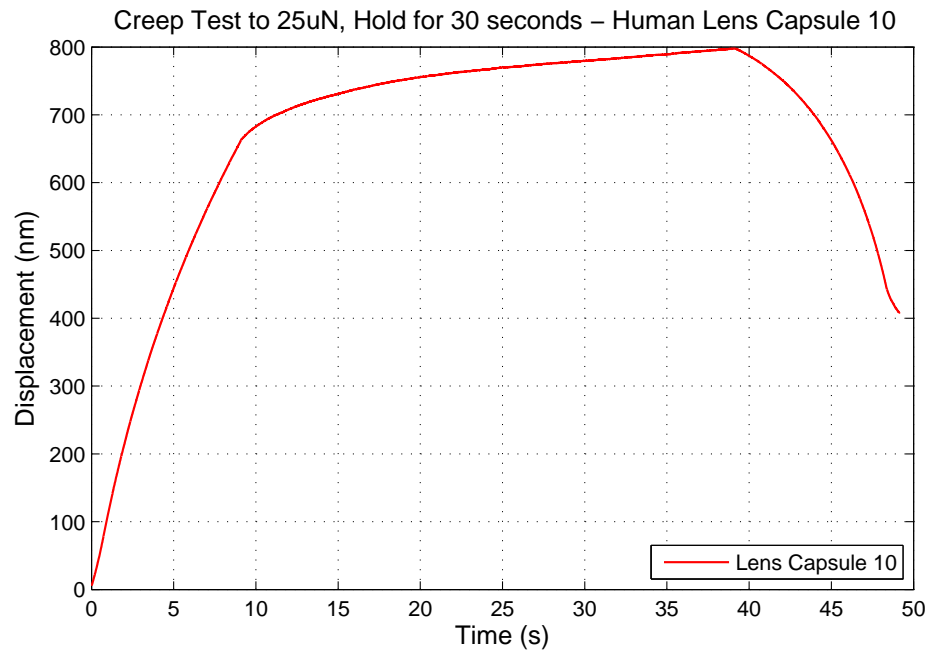


Figure 5.19: Graph of Nanoindentation Creep Test Human Lens Capsule 10 - Load to  $25 \mu\text{N}$ , Hold for 30 seconds. The pre-load force necessary to get contact with the lens capsule is the cause of the non-zero starting force.

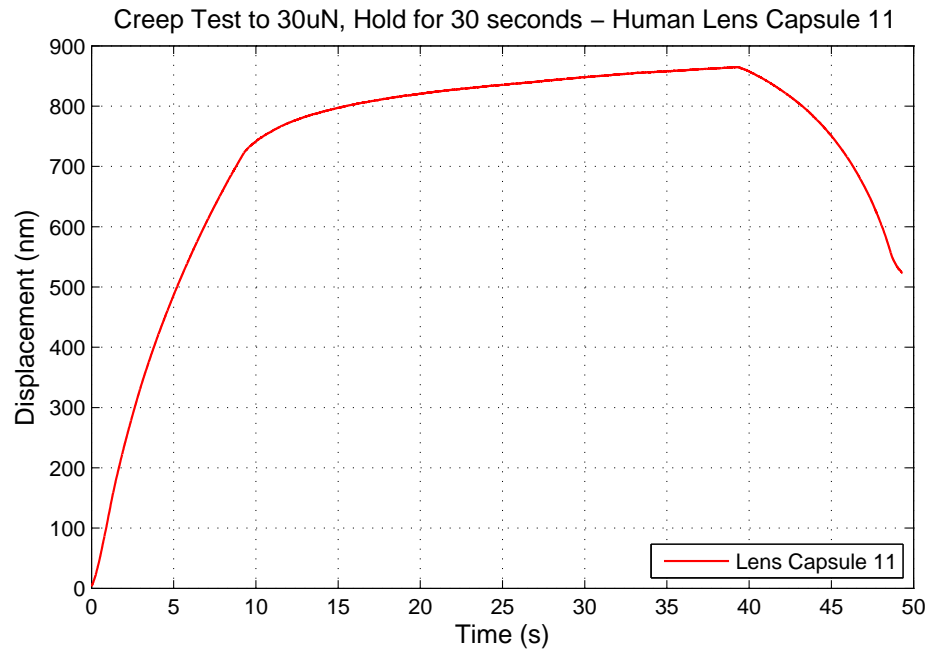


Figure 5.20: Graph of Nanoindentation Creep Test Human Lens Capsule 11 - Load to 30  $\mu\text{N}$ , Hold for 30 seconds. The pre-load force necessary to get contact with the lens capsule is the cause of the non-zero starting force.

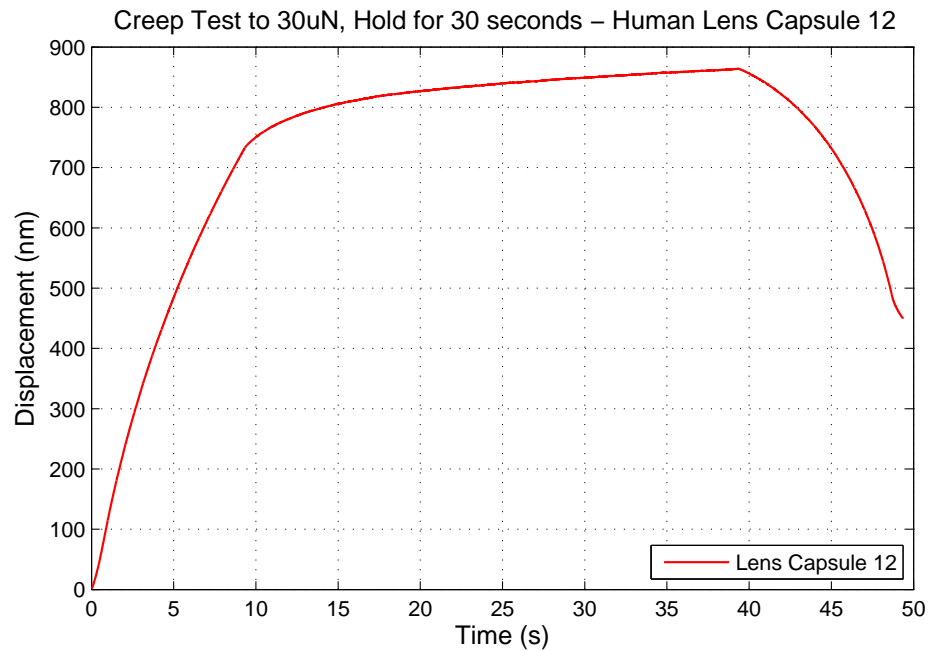


Figure 5.21: Graph of Nanoindentation Creep Test Human Lens Capsule 12 - Load to 30  $\mu\text{N}$ , Hold for 30 seconds. The pre-load force necessary to get contact with the lens capsule is the cause of the non-zero starting force.

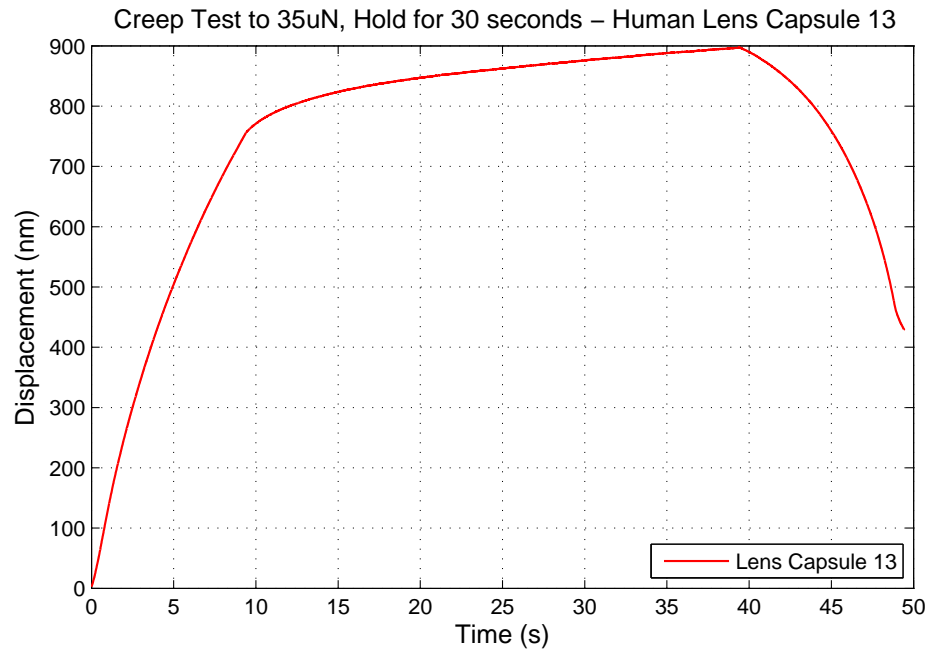


Figure 5.22: Graph of Nanoindentation Creep Test Human Lens Capsule 13 - Load to 35  $\mu$ N, Hold for 30 seconds. The pre-load force necessary to get contact with the lens capsule is the cause of the non-zero starting force.

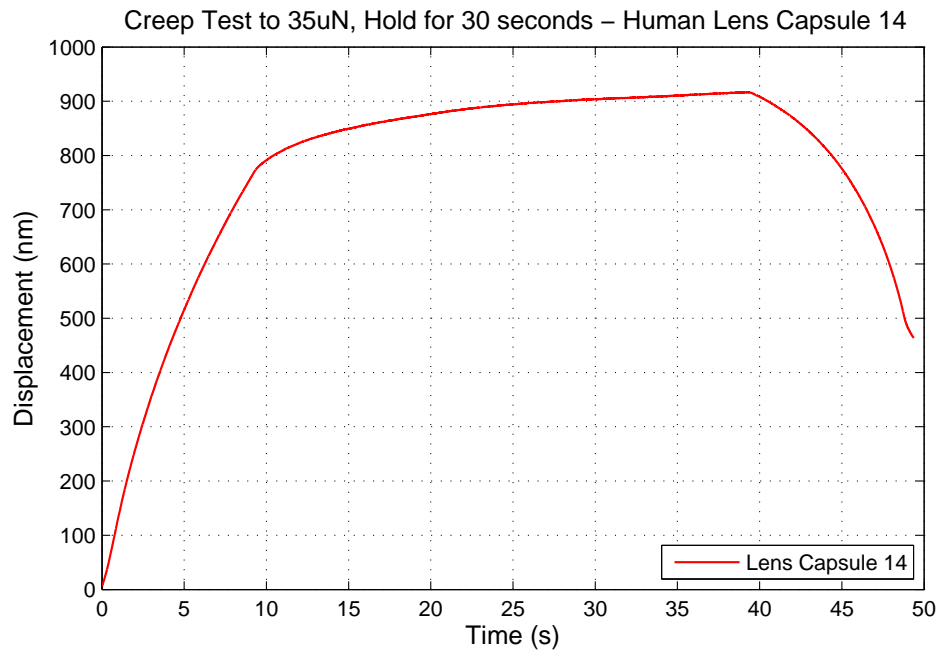


Figure 5.23: Graph of Nanoindentation Creep Test Human Lens Capsule 14 - Load to 35  $\mu$ N, Hold for 30 seconds. The pre-load force necessary to get contact with the lens capsule is the cause of the non-zero starting force.

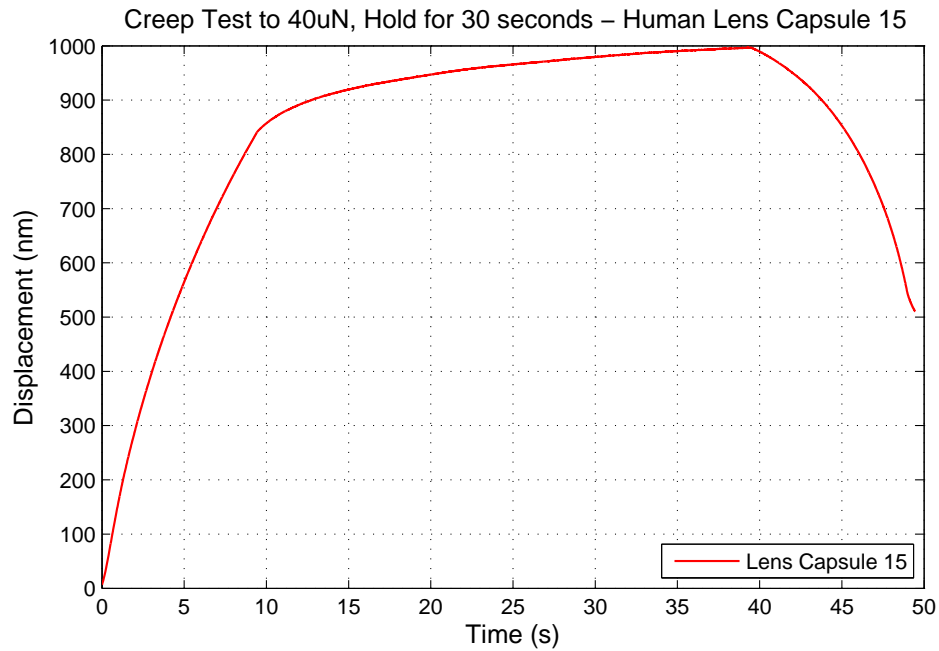


Figure 5.24: Graph of Nanoindentation Creep Test Human Lens Capsule 15 - Load to 40  $\mu\text{N}$ , Hold for 30 seconds. The pre-load force necessary to get contact with the lens capsule is the cause of the non-zero starting force.

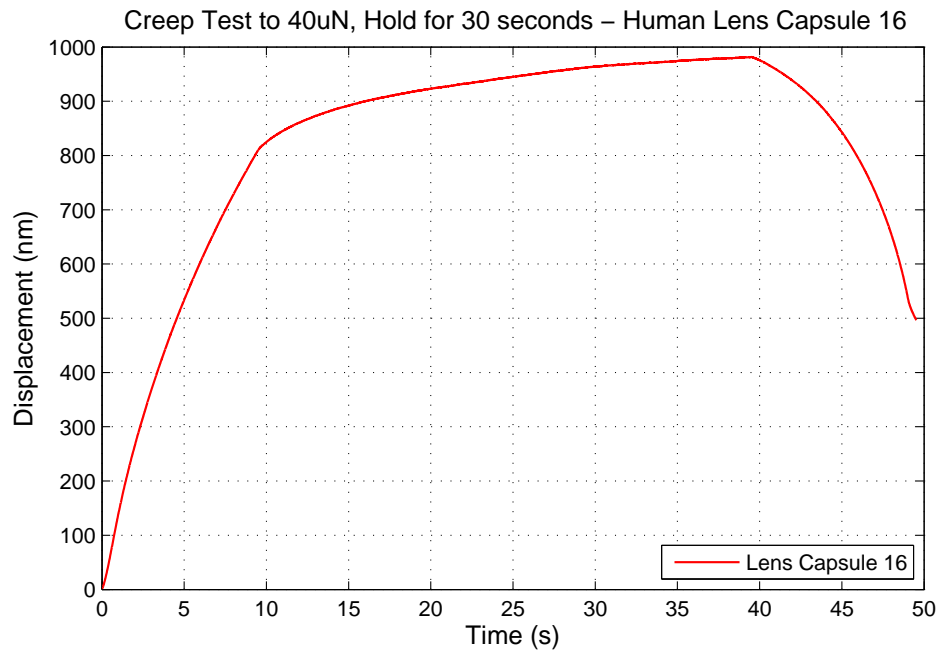


Figure 5.25: Graph of Nanoindentation Creep Test Human Lens Capsule 16 - Load to 40  $\mu\text{N}$ , Hold for 30 seconds. The pre-load force necessary to get contact with the lens capsule is the cause of the non-zero starting force.

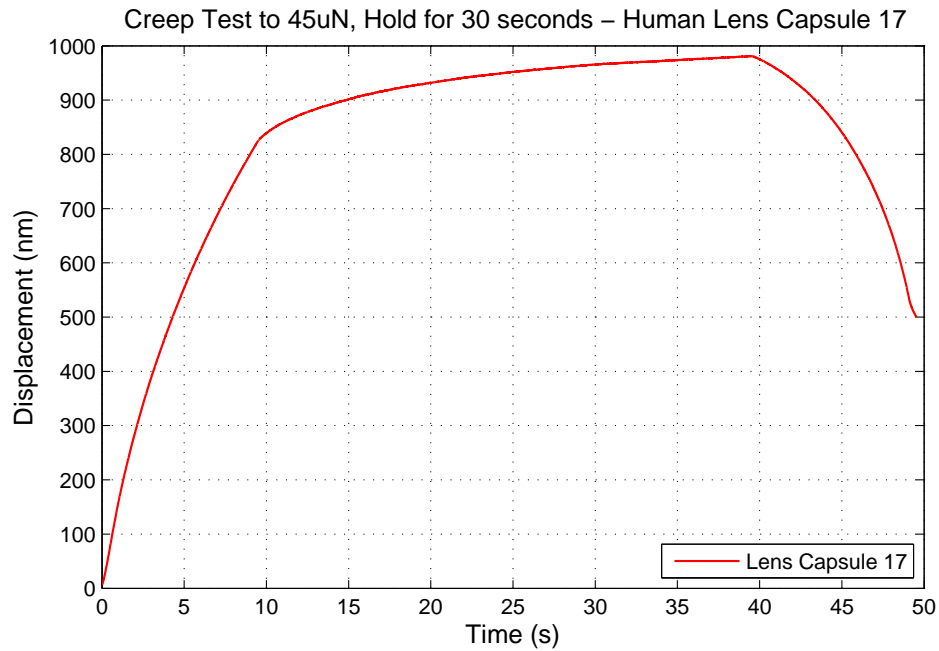


Figure 5.26: Graph of Nanoindentation Creep Test Human Lens Capsule 17 - Load to 45  $\mu$ N, Hold for 30 seconds. The pre-load force necessary to get contact with the lens capsule is the cause of the non-zero starting force.

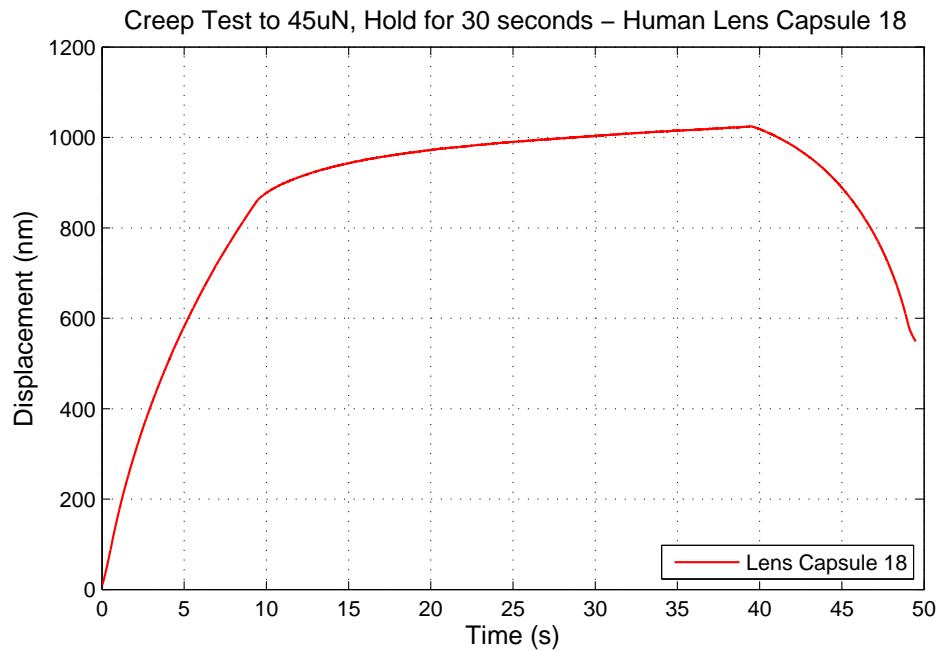


Figure 5.27: Graph of Nanoindentation Creep Test Human Lens Capsule 18 - Load to 45  $\mu$ N, Hold for 30 seconds. The pre-load force necessary to get contact with the lens capsule is the cause of the non-zero starting force.

## 5.5 Discussion

Overall, the creep test data from nanoindentation of the both the anterior porcine lens capsule and anterior human lens capsule looks promising. However, this data is just preliminary. The data would be improved with a longer hold section to better capture the viscoelastic dissipation of the force response. For the holding force of  $5\text{ }\mu\text{N}$ , the total creep for each porcine test fell approximately within the range of 800-1100 nm (see Figures 5.4-5.8). Additionally, the porcine creep test to  $15\text{ }\mu\text{N}$  had a total creep of approximately 1750 nm (see Figure 5.9). The fact that the total creep from the  $15\text{ }\mu\text{N}$  porcine creep test is greater than the total creep from any  $5\text{ }\mu\text{N}$  porcine test helps to validate that the test is working properly and we are indenting the porcine lens capsule and not just the fluid. Also, the loading curve for the  $15\text{ }\mu\text{N}$  porcine creep test looks smoother. This is due to the smaller proportion of the pre-load force to hold force compared to the  $5\text{ }\mu\text{N}$  porcine tests.

Looking at the human test data, we see a similar progression of smoother curves as the peak force is increased. Average (2 tests/peak force) total displacement as well as initial and final displacements can be seen in Table 5.1. As the peak force increased, the displacement into the tissue generally increased as well. The total displacement varied with each test, and more data is needed before an overall trend can be determined. At  $45\text{ }\mu\text{N}$  peak force, we achieved an indentation depth of approximately 5% strain, assuming the human anterior lens capsule to be approximately 11-33  $\mu\text{m}$  [Krag et al., 1997]. These data are usable and will be fit with Tahoe or Abaqus using methods similar to the fitting of the unconfined compression data.



Table 5.1: Average Displacement Values from Human Anterior Lens Capsule Creep Tests

Peak Force ( $\mu$ N)	Depth at Initial Peak Force (nm)	Depth After Creep (nm)	Total Displacement During Creep (nm)
5	96.9	159.7	62.8
10	317.5	429.8	112.3
15	680.3	824.7	144.4
20	620.6	756.7	136.1
25	689.4	828.3	138.9
30	727.8	864.3	136.5
35	764.8	906.9	142.1
40	825.6	989.1	163.5
45	843.4	1002.5	159.2

## Chapter 6

### Electron Microscopy and Tomography of the Lens Capsule

Electron Microscopy (EM) is used to image samples at very small scales (down to the nm scale in our research). Electron Tomography (ET) refers to imaging a sample by slices, allowing the collection of images in the z-axis resulting in a “stack” of images. Through EM and ET, the ultra-structure of the lens capsule can be determined for use in a computational model. To image the lens capsule, transmission electron microscopy (TEM) was used. A transmission electron microscope works by utilizing an electron gun to generate a beam of electrons which is then focused through a series of electrostatic and electromagnetic lenses onto the sample. The sample then allows electrons to pass through and scatters others, based upon its composition and structure. The resulting beam of electrons is then, in our case, collected by a CCD camera. Images are then post-processed with software to measure structure and other characteristics. In order to create stacks of images to allow for the 3-dimensional reconstruction of the sample, ET is employed. This is done by taking 2 tilt-series of the sample, along the x and y axis. During a tilt-series, the sample is rotated by a set amount along an axis to positive and negative limit of tilt. This allows images to be taken through the sample section at different angles. With the addition of the tilt-series along a perpendicular axis, the two data sets can then be combined with software to create a 3-D reconstruction of the sample. ET is used to image the lens capsule and, more specifically, the type-IV collagen mesh-work of the lens capsule.

Sample preparation for EM and ET involved one method of cryofixation. The cryofixation for cryo-ET differs from the process used for EM and ET. Both are described in detail below. Briefly,

for ET and EM the samples are frozen using a high pressure freezer (HPF). By using a HPF, the sample is frozen under approximately 30,000 PSI to the temperature of liquid nitrogen (-196 °C) in a few milliseconds. This process is used to prevent the formation of ice crystals, which would disrupt the native structure of the tissue and show up as artifacts in imaging. The samples then undergo freeze-substitution, described below, are embedded in resin, and sectioned. The difference from EM/ET to cryo-EM/cryo-ET is that instead of undergoing freeze-substitution, embedding, sectioning, and imaging (the last three being done at room temperature), the samples are kept at very low temperatures during sectioning and imaging, resulting in no need for freeze-substitution and embedding in resin. This allows for the imaging of a hydrated sample in its native state without possible alteration of the sample's structure. Cryo-EM/cryo-ET is a difficult technique and the process for our samples is still being figured out. The progress so far is presented below.

## 6.1 Sample Preparation

Anterior lens capsule was collected to be used for ET. This was done by first removing the cornea as previously described in the Puncture Testing of the Whole Lens Chapter. Then, while applying slight pressure to the whole globe, a small incision was made with a diamond-head scalpel in the anterior surface of the ocular lens, near the attachment of the zonules. By gently widening this incision with the scalpel, the interior lens fibers slide out, intact, from the slight pressure being applied to the globe. With the interior lens fibers removed, the anterior portion of the capsule is then lifted by a pair of tweezers inserted through the previously made incision. Once lifted, the anterior capsule is collected by using a pair of micro scissors to cut the capsule near the zonule attachments around the perimeter.

For EM/ET, the anterior lens capsule was then transported to the BalTec HPM 010 HPF (see Figure 6.1) in a vial of Alcon BSS.

At the HPF, a circular sample was cut out with a 2 mm diameter dermal punch. The sample was then placed in 150 mM mannitol in Alcon BSS for several minutes prior to freezing. The HPF specimen carrier (100  $\mu$ m circular stainless steel well) was then filled with the same solution. The



Figure 6.1: BalTec HPM 010 High Pressure Freezer.

sample was then placed in the carrier and frozen in the HPF. The sample was then immediately transferred to a container of liquid nitrogen in which the carrier was removed. The sample was kept in liquid nitrogen as it was transported to the freeze-substitution vessel. The freeze-substitution process was done with an acetone solution including 2% osmium tetroxide and 0.1% uranyl acetate. The sample and solution were kept at  $-90^{\circ}\text{C}$  over 36 hours while the substitution took place. The samples were then warmed to room temperature over 18 to 24 hours and washed with acetone before being fixed in epoxy resin for sectioning. The samples were sectioned on a Microtome to a thickness of 60-80 nm for EM and 150 nm for ET. Sections were placed in EM grids and taken to the scope for imaging.

For cryo-ET, dome-shaped carriers were used during high pressure freezing. These carriers were then mounted using a special chuck into the cryochamber of an Ultracut UCT microtome (Leica Inc., Vienna, Austria). Here they were cut into sections approximately 100 nm thick at  $-155^{\circ}\text{C}$ . After being placed on a grid, the sections were transported in liquid nitrogen to the cryo-transmission electron microscope. A cryo-holder (Gatan Inc., Warrendale, PA, USA) was used in the scope which kept the temperature of the sample at  $-180^{\circ}\text{C}$ .

## 6.2 Experimental Setup

For the initial EM images, a Phillips CM-100 Transmission Electron Microscope (see Figure 6.2) was used in the Molecular, Cellular, and Developmental Biology (MCDB) department at CU Boulder. The Phillips CM-100 TEM is equipped with a 100kV electron gun. It is setup to image plastic sections.

For the ET images, a FEI Tecnai TF30 300kV IVEM microscope (see Figure 6.3) was used in the The Boulder Laboratory For 3-D Electron Microscopy of Cells at CU ([bio3d.colorado.edu](http://bio3d.colorado.edu)). In its function at Boulder, this scope is used for both plastic and frozen-hydrated (cryo) electron tomography.



Figure 6.2: Phillips CM-100 Transmission Electron Microscope.



Figure 6.3: FEI Tecnai TF30 300kV IVEM Microscope.

## 6.3 Experimental Method

On the Phillips CM-100 TEM, images were taken at various magnifications (shown on each image in the results) of the initial samples to help provide an idea of what was visible with EM. The electron gun was set at 80kV for imaging of the thin, transparent samples to provide the most

contrast. The power of the electron beam was adjusted based off of the magnification to limit damage to the sample. Images were saved in .tiff format.

On the FEI Tecnai TF30 300kV IVEM microscope, the software SerialEM was used to take tilt-series (developed by The Boulder Laboratory For 3-D Electron Microscopy of Cells). Tilt-series were taken at 23,000x magnification and from  $-60^{\circ}$  to  $60^{\circ}$  on each axis in steps of  $1^{\circ}$ . The tilt-series were then aligned and assembled using IMOD (a software package developed by The Boulder Laboratory For 3-D Electron Microscopy of Cells). IMOD contains image processing, modeling and display programs specifically designed for tomographic and 3D reconstruction of EM images. In the reconstructed data, the space between images/slices was 1 nm. IMOD was also used for some preliminary modeling of the type-IV collagen mesh-work, shown in the results. “Nodes” of the mesh-work were selected manually based off of the darkness compared to the surrounding area of the image and apparent fibers coming into the node. Node coordinates and connectivity were exported from IMOD to be used in a future model in Tahoe.

## 6.4 Results

Below are images of the lens capsule taken with both EM and ET. Figure 6.4 is a picture from our initial attempts with EM. We aimed for a comparable settings that were used by Barnard [Barnard et al., 1992] in their images of a lens capsule replica. Figure 6.5 shows one of our initial ET attempts. The sample imaged was approximately 150 nm thick taken from the anterior portion of the porcine lens capsule. Figure 6.6 is a zoomed-in view of a section of the image in Figure 6.5. It has a scale bar of 100 nm. Figure 6.7 shows another sample that was imaged with ET with a scale bar of 100 nm.

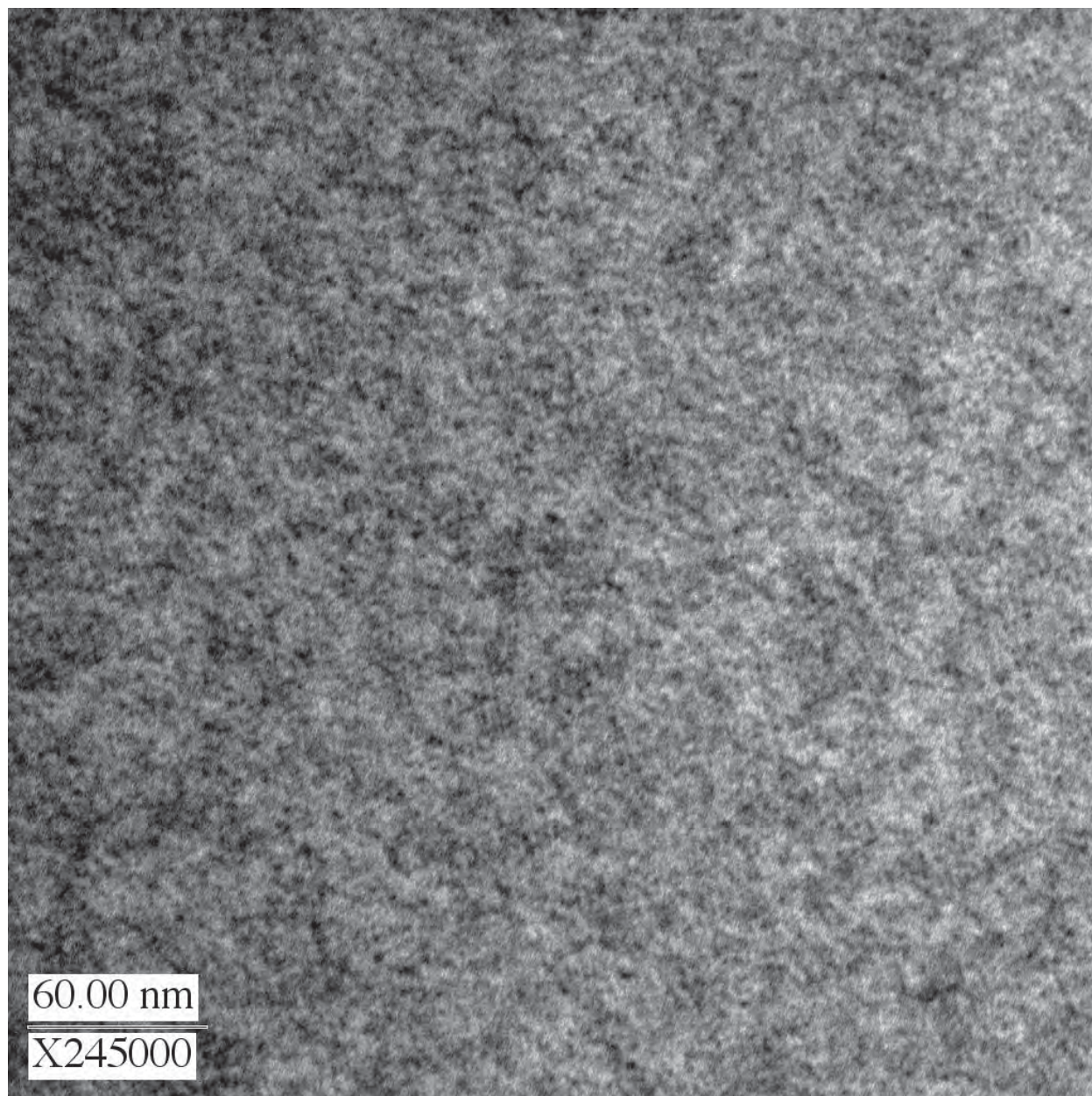


Figure 6.4: Initial Image Collected on Phillips CM-100 at 245,000X with 60 nm scale bar.



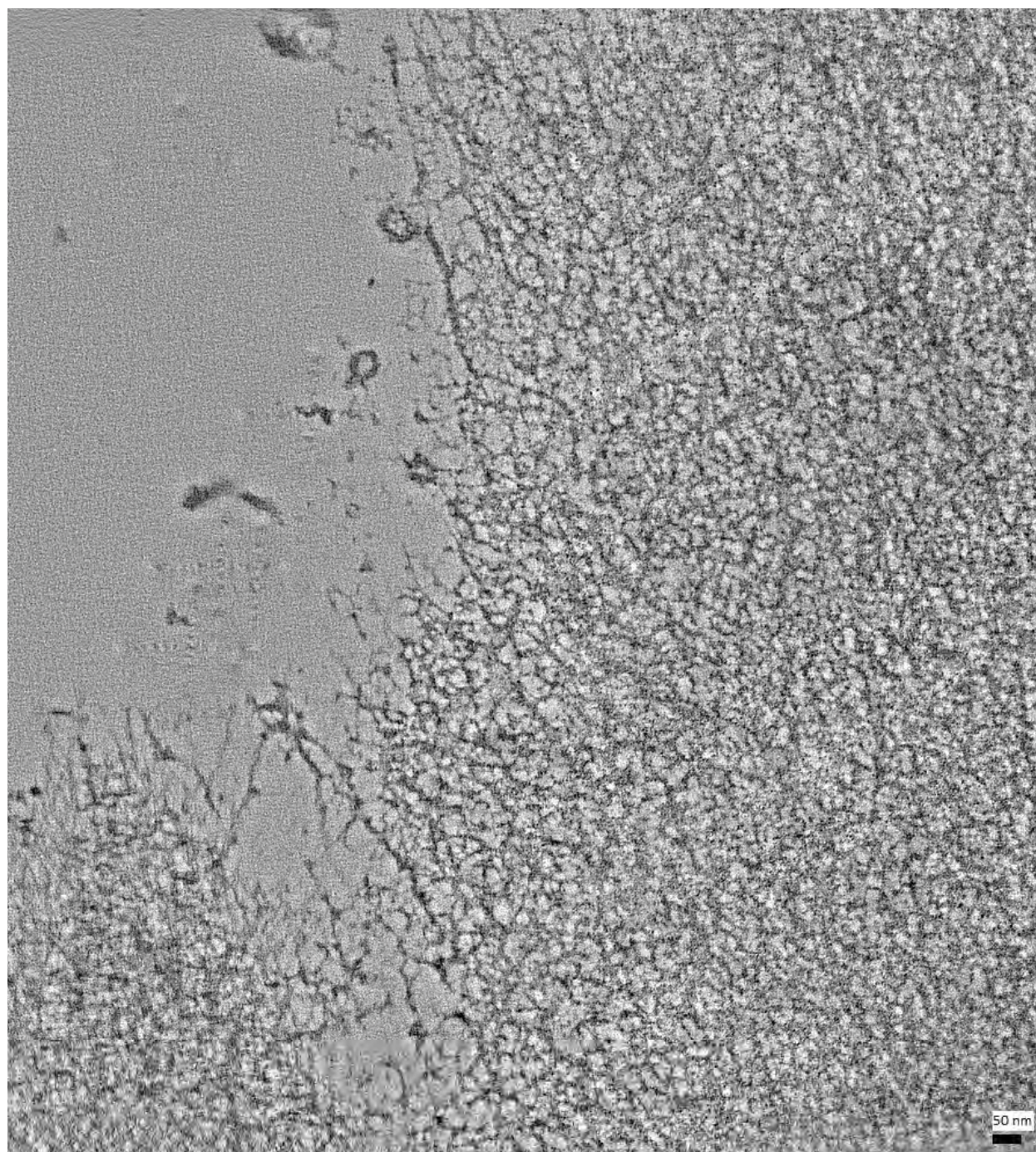


Figure 6.5: Reconstructed Image from Tilt-Series: taken at 23,000X, 1 image per degree from  $-60^\circ$  to  $60^\circ$  with 50 nm scale bar.



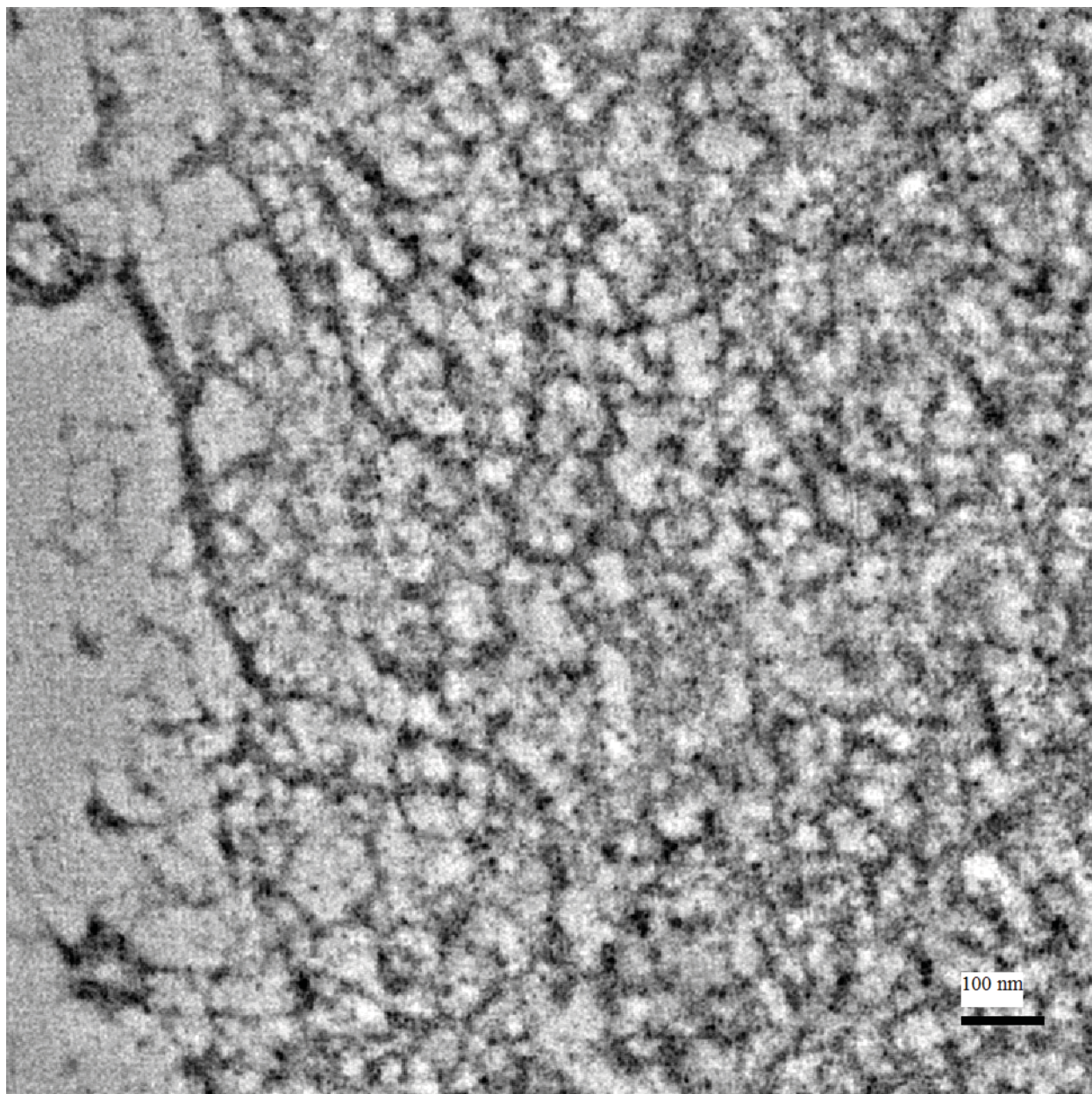


Figure 6.6: Zoomed in Region of Reconstructed Image from Tilt-Series: taken at 23,000X, 1 image per degree from  $-60^{\circ}$  to  $60^{\circ}$  with 100 nm scale bar.



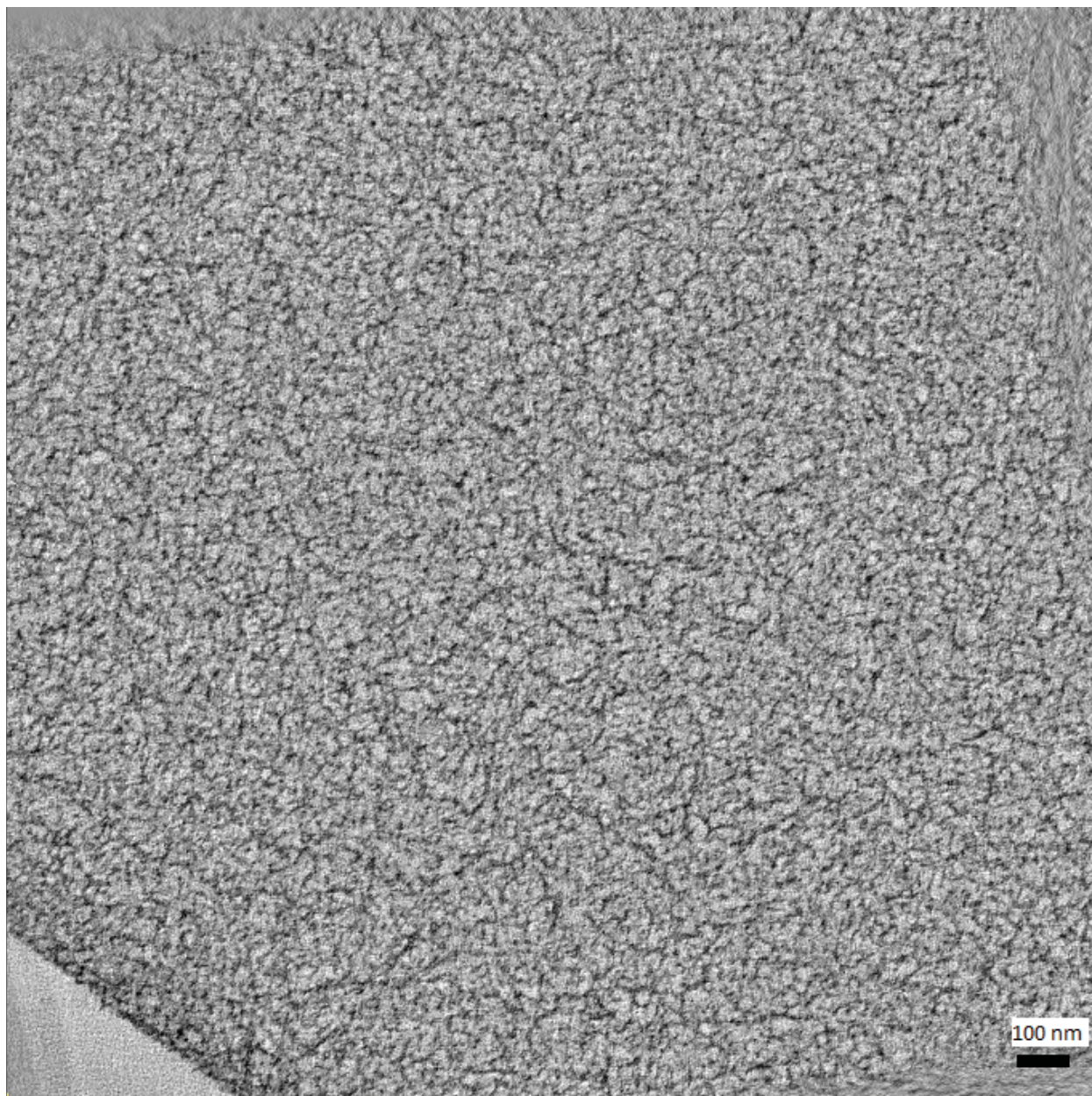


Figure 6.7: Reconstructed Image from Tilt-Series: taken at 23,000X, 1 image per degree from  $-60^\circ$  to  $60^\circ$  with 50 nm scale bar.

## 6.5 Discussion

Looking at Figure 6.4, there is little to no definition and no apparent structure visible. While we did mimic Barnard's [Barnard et al., 1992] imaging settings, we opted to not perform the extraction and platinum deposition that was done to their samples so we could better preserve the native structure. It appears that without extraction, no visible structure can be seen using 2-D TEM. These results led us to trying ET to image the lens capsule. Upon the initial examination of our ET results in Figure 6.5, we were inclined to believe that we had successfully imaged the type-IV collagen mesh-work structure of the porcine lens capsule. Furthermore, the comparison of the size of the fibers and gaps seen in our images to those of Barnard [Barnard et al., 1992] bolstered our belief that we had imaged the mesh-work structure. We imaged another sample and again, saw similar results (see Figure 6.7). However, after consulting with additional microscopists within the The Boulder Laboratory For 3-D Electron Microscopy of Cells, we cannot yet positively determine whether what we are seeing in the images is structure or artifact from the freezing/freeze-substitution process. Currently, work is being done to image more samples using the same process as well as using cryo-ET, which will hopefully provide us samples with the least possible artifacts in a nearest native state as we can achieve. Preliminary modeling work is being done using IMOD on the current images (see Figure 6.8). Whether the current images are showing structure or not, they are good practice for streamlining the modeling process. The nodes of the mesh-work are selected manually and the user searches for connections in both the x-y plane and through the stack in the z-axis. The node coordinates and connectivity are exported from IMOD to be processed by FEA simulation software.



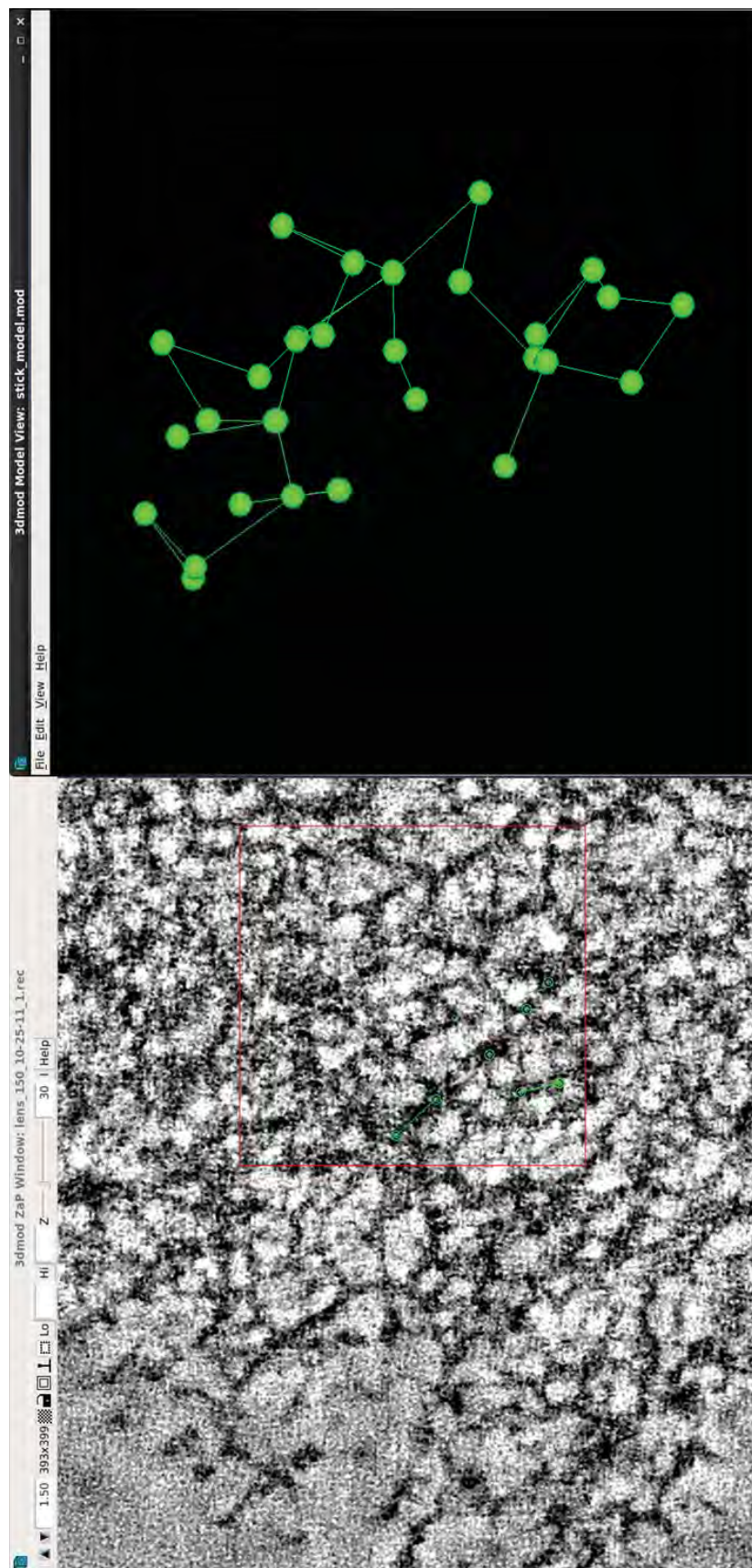


Figure 6.8: Modeling of Perceived Structure from ET Images using IMOD.

## Chapter 7

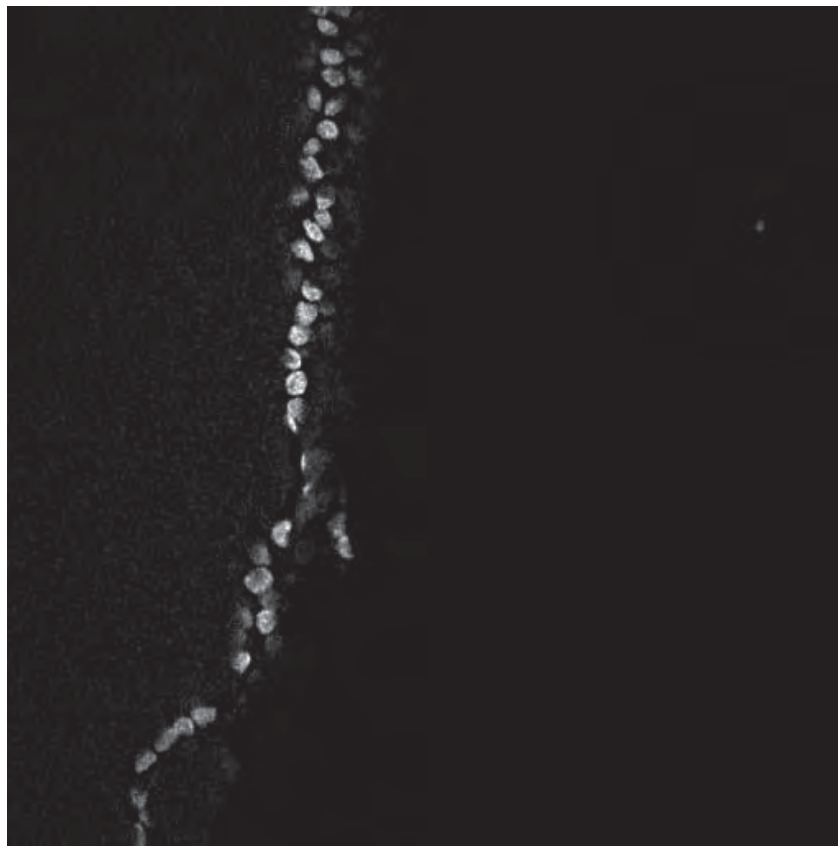
### Confocal Scanning Laser Microscopy of the Lens Fiber Cells

As mentioned earlier, the reason for using confocal LASER scanning microscopy (CLSM) is to image the ultra-structure of the interior lens fibers in 3 dimensions. The confocal images can be processed with software to recreate the structure of the lens fibers, which can then be employed in the computational mechanical model. CLSM works by staining a sample with binding-specific fluorescent molecules. These agents are then stimulated by LASER light and the resulting luminance is recorded. Since multiple wavelengths of LASER can be used, multiple agents bound to different sites can be imaged on one sample. Images of each fluorophore are taken on separate channels (see Figure 7.1).

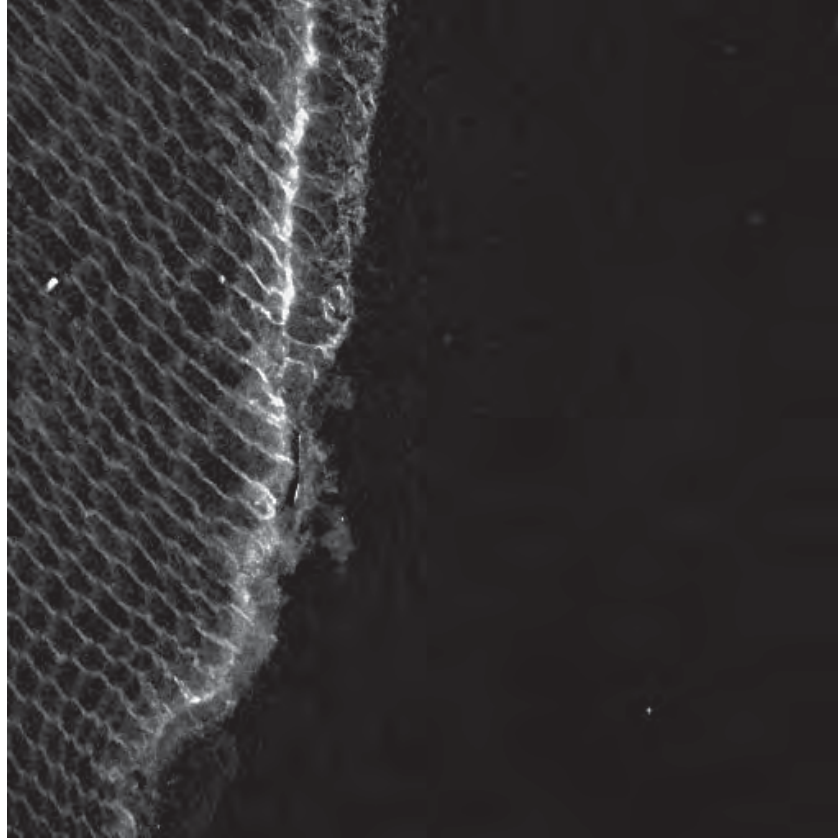
Using post-processing software, the color can be added to the channels to help view the different structures and the channels can be combined into one image (see Figure 7.2 and Figure 7.3). Of interest for the project were imaging the actin that is found in the structure of the crystalline lens fibers (to model the lens fiber shape and size) and the nuclei found in the epithelial cells along the anterior portion of the lens (to help orient the images and provide a landmark to reference).

#### 7.1 Sample Preparation

Upon receipt of eyes from Animal Technologies, Inc., the whole ocular lens was removed, as described previously in the Puncture Testing of the Whole Lens Chapter. The lenses were then placed in a sample tray and fixed with 4% paraformaldehyde for 36 hours at room temperature. After fixation, the lenses were washed in phosphate-buffered saline (PBS) and sectioned using a

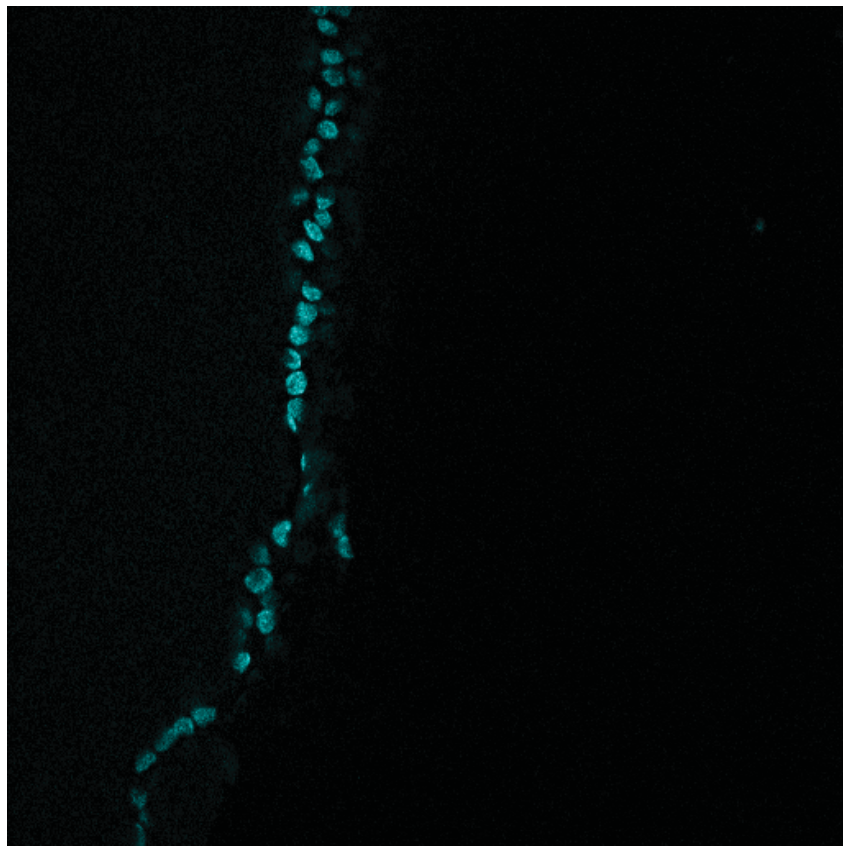


(a) Channel 1 Showing DAPI Staining of Porcine Lens Capsule.

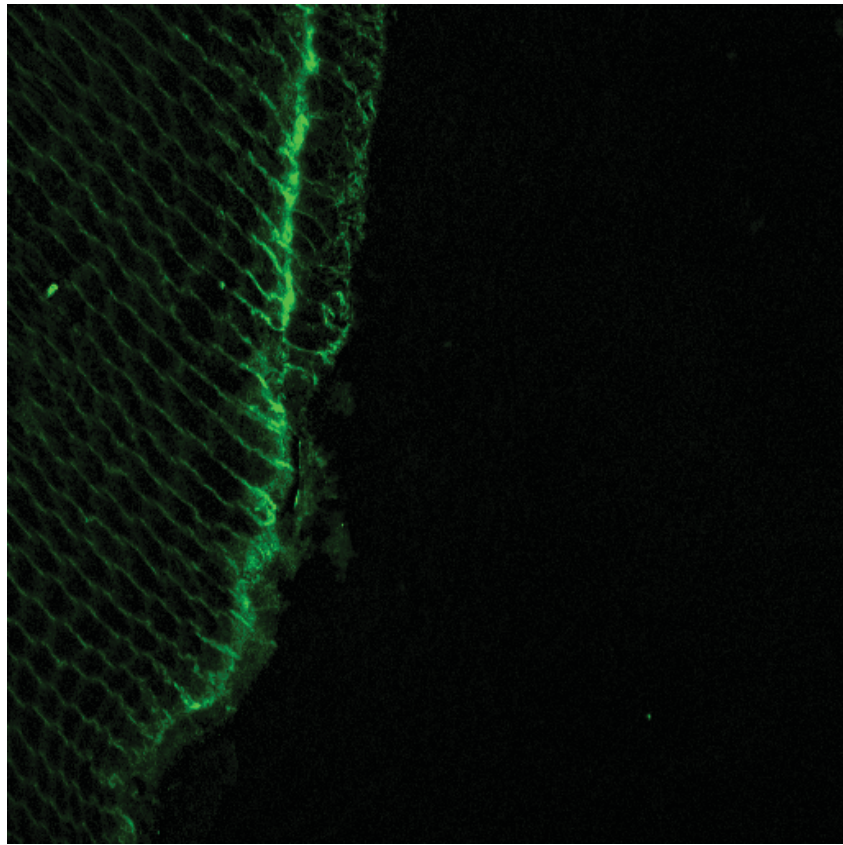


(b) Channel 2 Showing Phalloidin Staining of Porcine Lens Capsule.

Figure 7.1: Confocal LASER Scanning Microscopy Images of Porcine Lens Capsule.



(a) Channel 1 Showing DAPI Staining of Porcine Lens Capsule After Color Addition Through Post-Processing.



(b) Channel 2 Showing Phalloidin Staining of Porcine Lens Capsule After Color Addition Through Post-Processing.

Figure 7.2: Confocal LASER Scanning Microscopy Images of Porcine Lens Capsule After Color Addition Through Post-Processing.



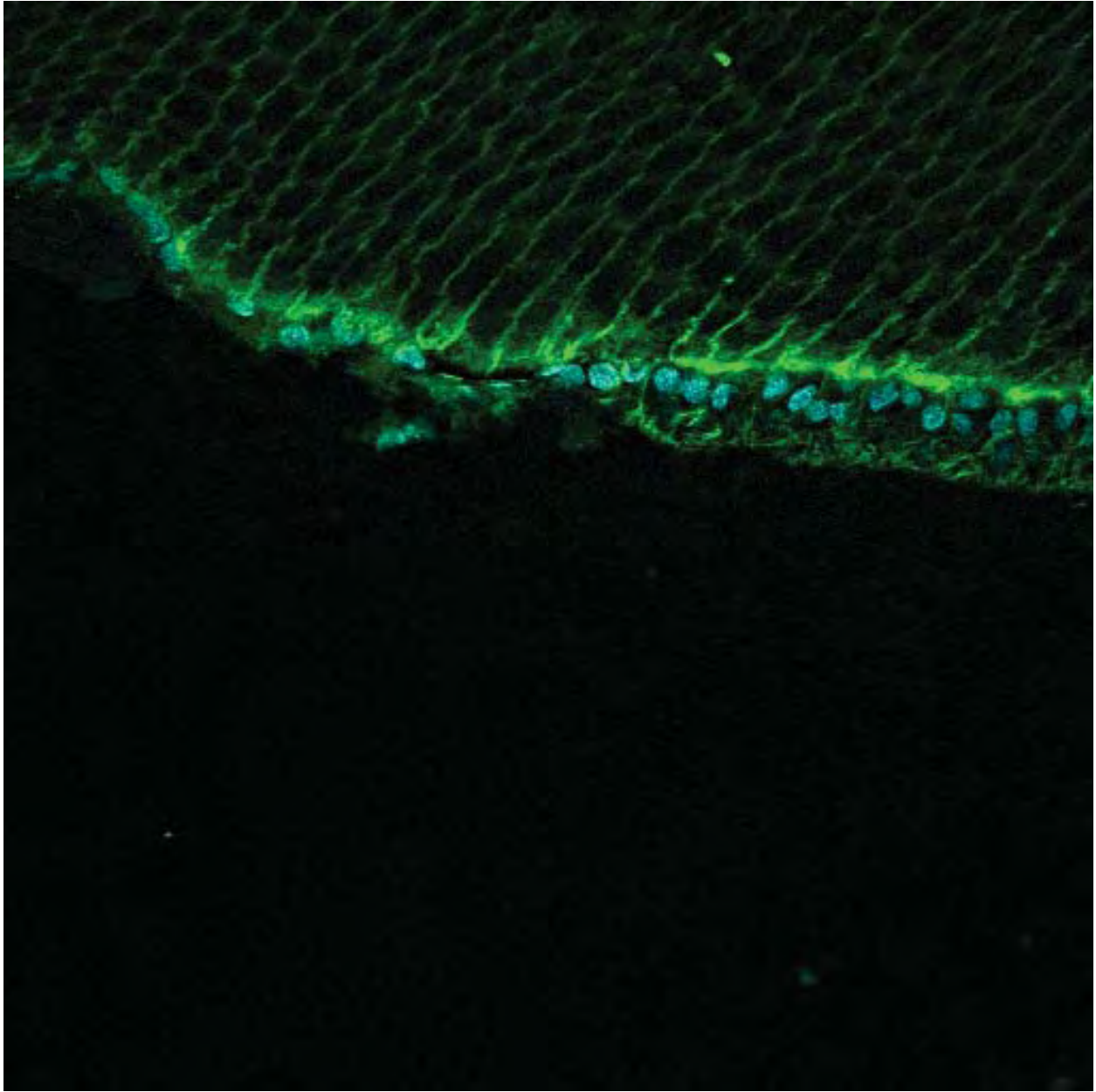


Figure 7.3: Channels 1 & 2 of Confocal LASER Scanning Microscopy Images of Porcine Lens Capsule Combined Into Composite Image With Post-Processing.



Vibratome to sections approximately  $70\ \mu\text{m}$  thick. To permeabilize the cells, the lens sections were blocked with phosphate-buffered saline Triton X-100 (PBST, 0.2% Triton X-100) for 12-18 hours at room temperature. The sections were then stained with Alexa Fluor® 488 Phalloidin from Life Technologies ([www.lifetechnologies.com](http://www.lifetechnologies.com)) in PBST (dilution 1:200). Sections were stained for 12-18 hours and then washed with PBST 5 times for 20 minutes each wash on an orbital shaker table. This was followed by one wash of PBS for 10 minutes on an orbital shaker table. Next, the sections were stained with DAPI (4',6-Diamidino-2-Phenylindole, Dihydrochloride) from Life Technologies ([www.lifetechnologies.com](http://www.lifetechnologies.com)) diluted in PBS (1:1000) for 15 minutes on an orbital shaker table. After the DAPI staining, the sections were washed 4 times in PBS for 10 minutes each on an orbital shaker table. The sections were then mounted on Fisherbrand Super Frost Plus microscope slides with Fluormount-G from Southern Biotech for imaging.

## 7.2 Experimental Setup

For imaging, an Olympus Fluoview FV1000 Confocal Microscope with a motorized stage was used (see Figure 7.4). Three lenses were used for imaging: 20X in air with a numerical aperture (NA) of 0.75, 40X in oil with a NA of 1.30, and 100X in oil with a NA of 1.40. Excitation LASERs of wavelengths 405 nm and 488 nm were used for the DAPI and Phalloidin, respectively.



Figure 7.4: Olympus Fluoview FV1000 Confocal Microscope.

### **7.3 Experimental Method**

Olympus' FV1000 ASW software was used to take the images. Details for each image are included in the captions. Images were exported from the FV1000 ASW software and were processed using ImageJ ([rsbweb.nih.gov/ij/](http://rsbweb.nih.gov/ij/)) and Fiji ([fiji.sc](http://fiji.sc)).

### **7.4 Results**

Below are the confocal images of the anterior porcine lens capsule. For purposed of determining the orientation of the samples, the cells stained with DAPI (cyan in the images) are located along the anterior surface of the lens capsule. These sections were cut parallel with the anterior pole/posterior-pole axis.

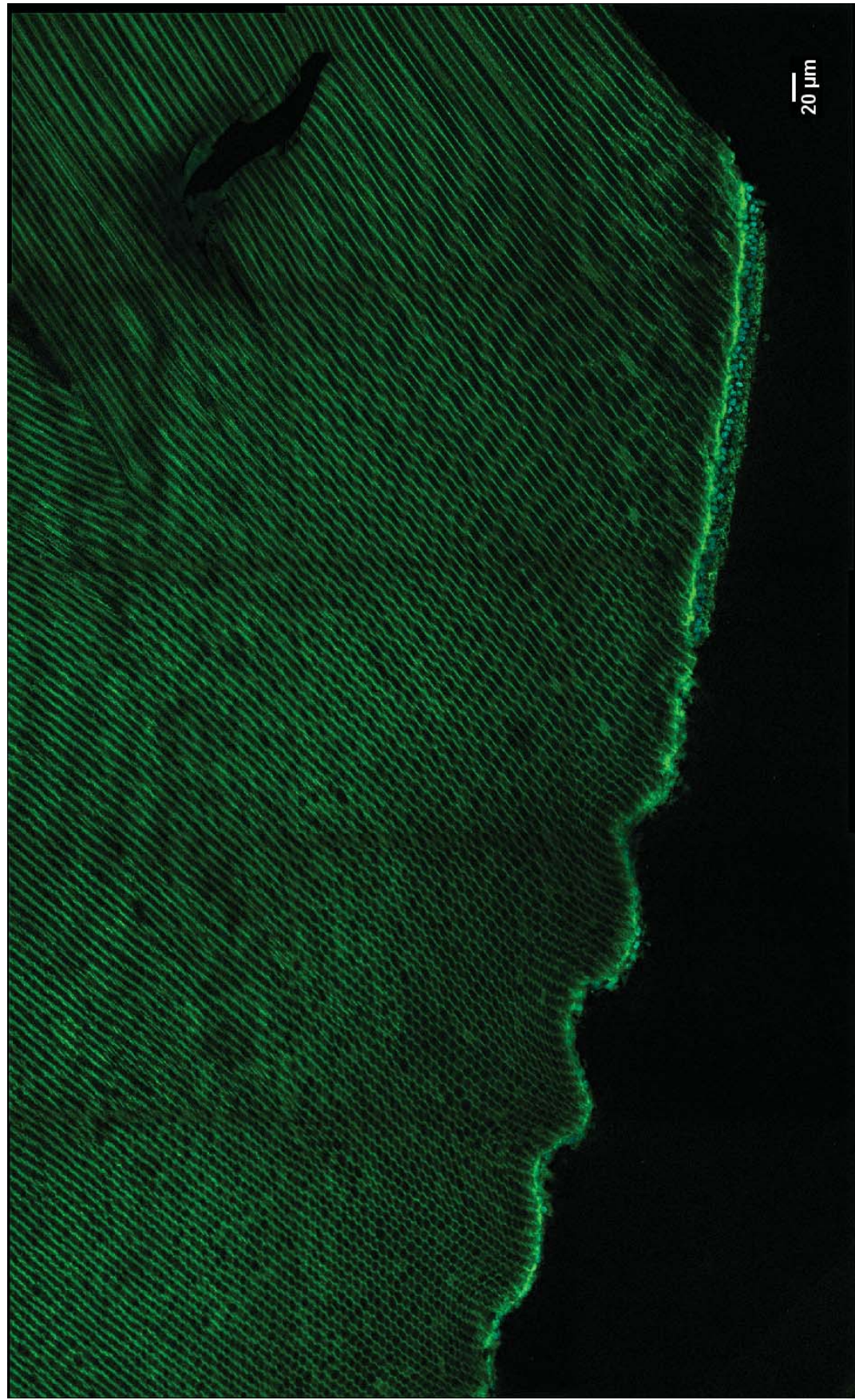


Figure 7.5: Confocal Image of Lens Fibers: 3x5 stitched image, each individual image was taken with the 40x( $NA=1.30$ ) objective in oil. Each image is 512 x 512 pixels and 317.331 x 317.331  $\mu m$ , resulting in an overall image size of 1586.655 x 951.993  $\mu m$ . The anterior surface can be identified at the bottom of the image by the nuclei stained with DAPI shown in cyan. The waves seen on the bottom of the sample are artifacts from the sectioning process. Notice the fine, honeycomb-like structure of the lens fibers in the bottom left area of the tissue.



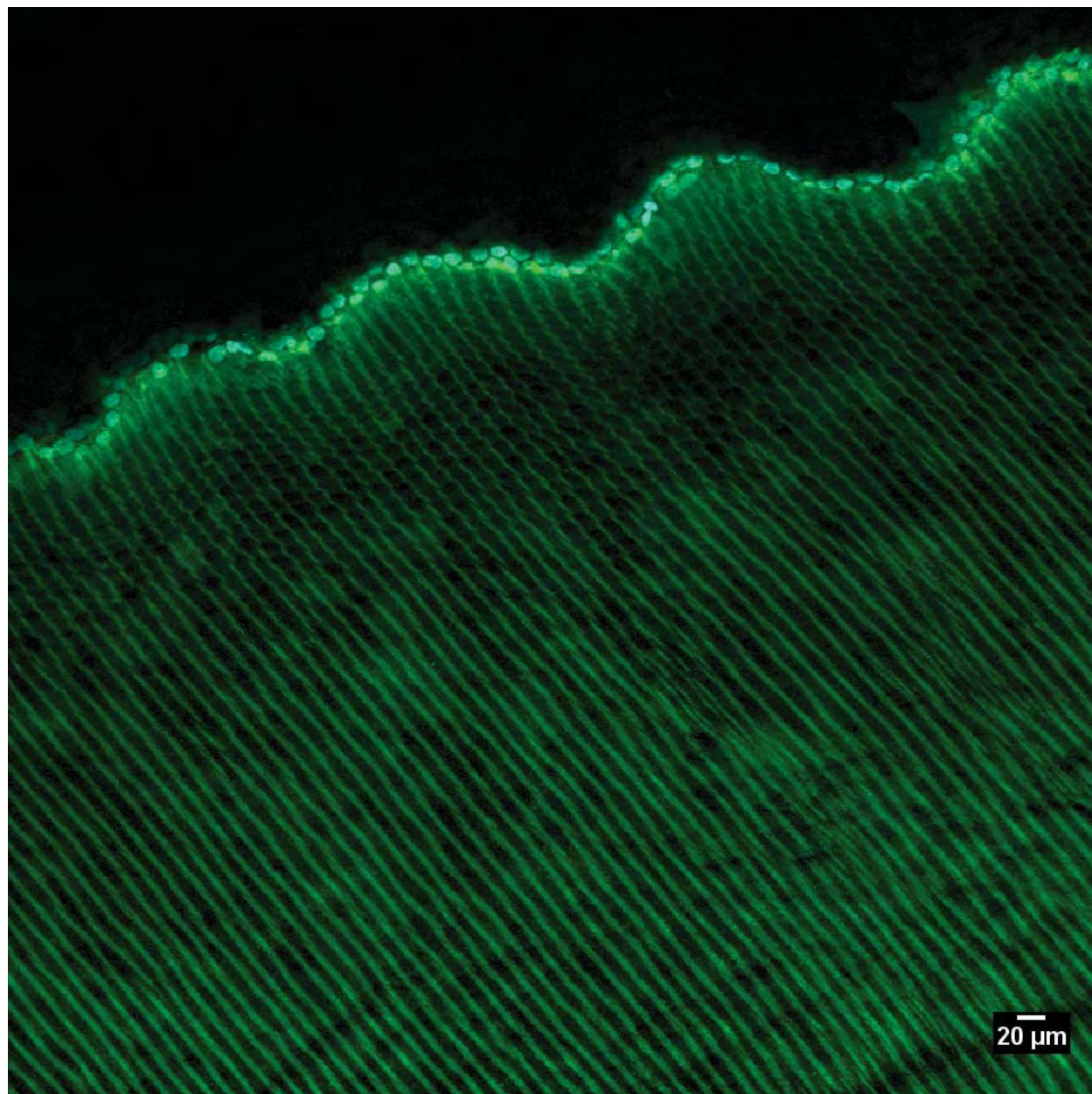


Figure 7.6: Confocal Image of Lens Fibers: Image was taken with the 20x(NA=0.75) objective in air. The image size is 800 x 800 pixels, or 635.205 x 635.205  $\mu\text{m}$ . Again, the anterior surface of the samples is identified by the stained nuclei in cyan. The fine structure of the lens fibers can be seen in the upper portion of the of the sample.

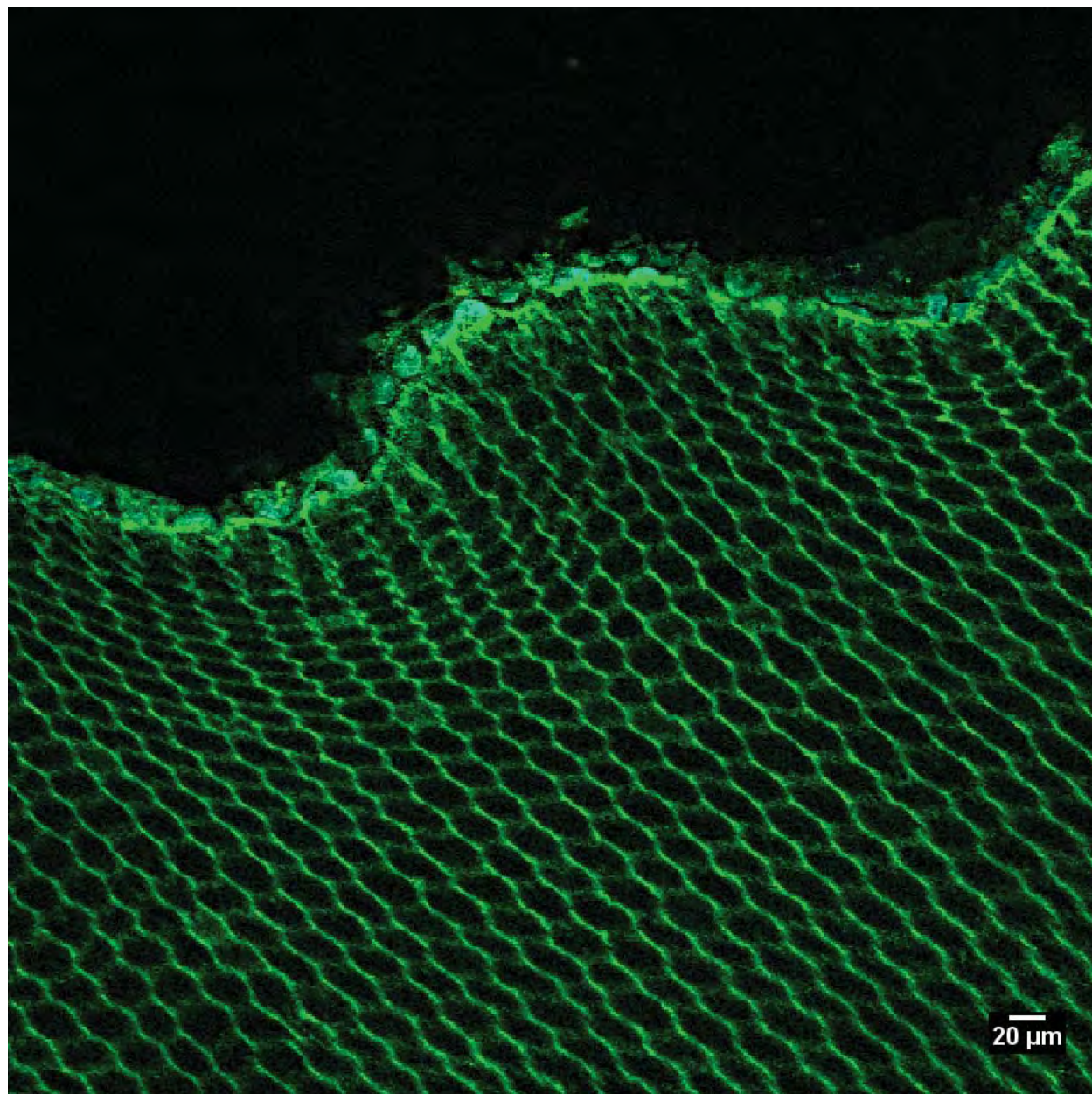


Figure 7.7: Confocal Image of Lens Fibers: Image was taken with the 40x(NA=1.30) objective in oil. The image is 512 x 512 pixels and has a size of 317.331 x 317.331  $\mu\text{m}$ . The lens fiber structure appears to be somewhat regular, with an exception along the anterior surface. This could be due to deformation of the tissue during the sectioning process.



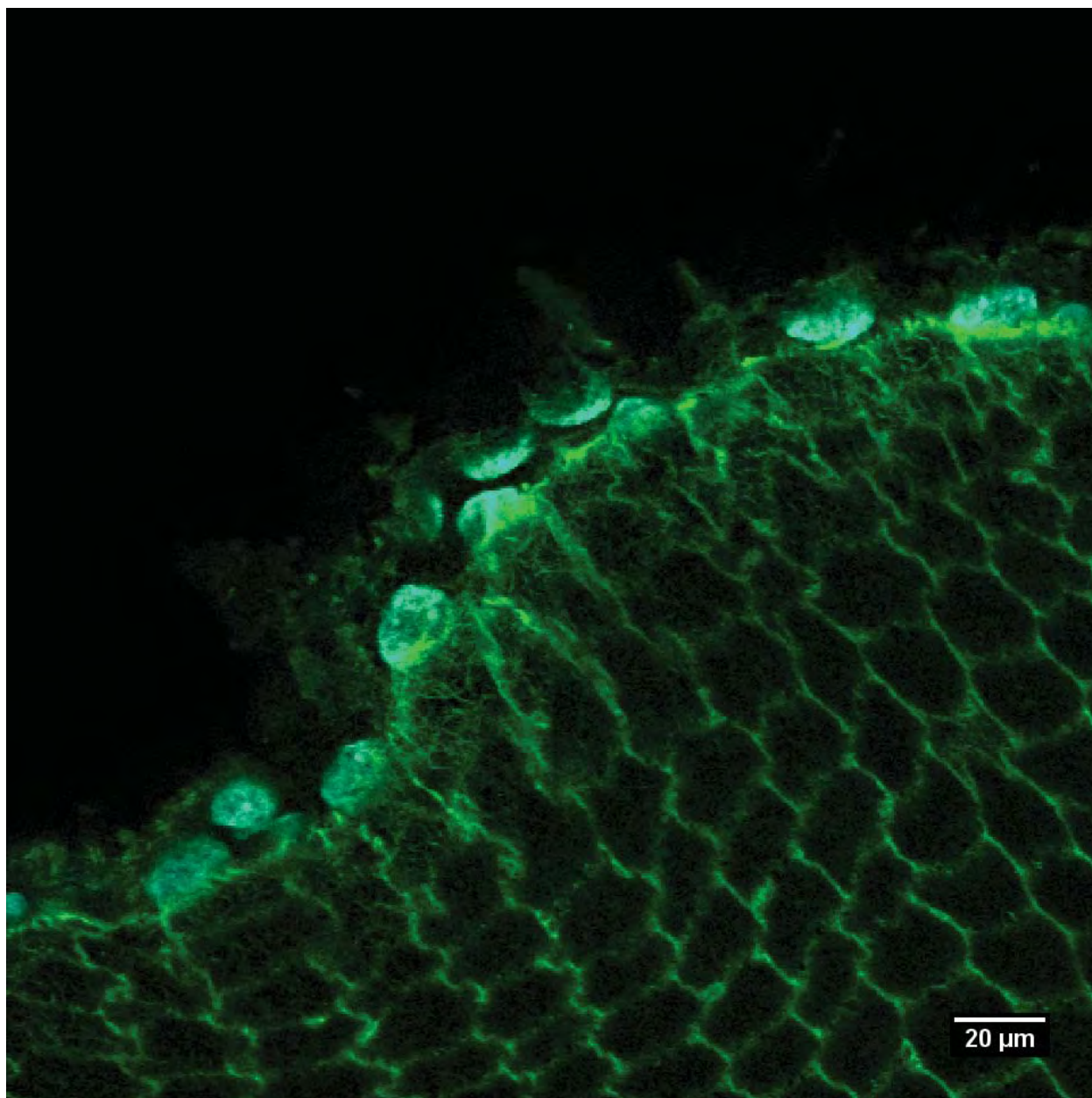


Figure 7.8: Confocal Image of Lens Fibers: Image was taken with the 100x(NA=1.40) objective in oil. The image is 512 x 512 pixels and has a size of 126.728 x 126.728  $\mu\text{m}$ . This image provides a detailed view of the lens fiber cells near the anterior surface.

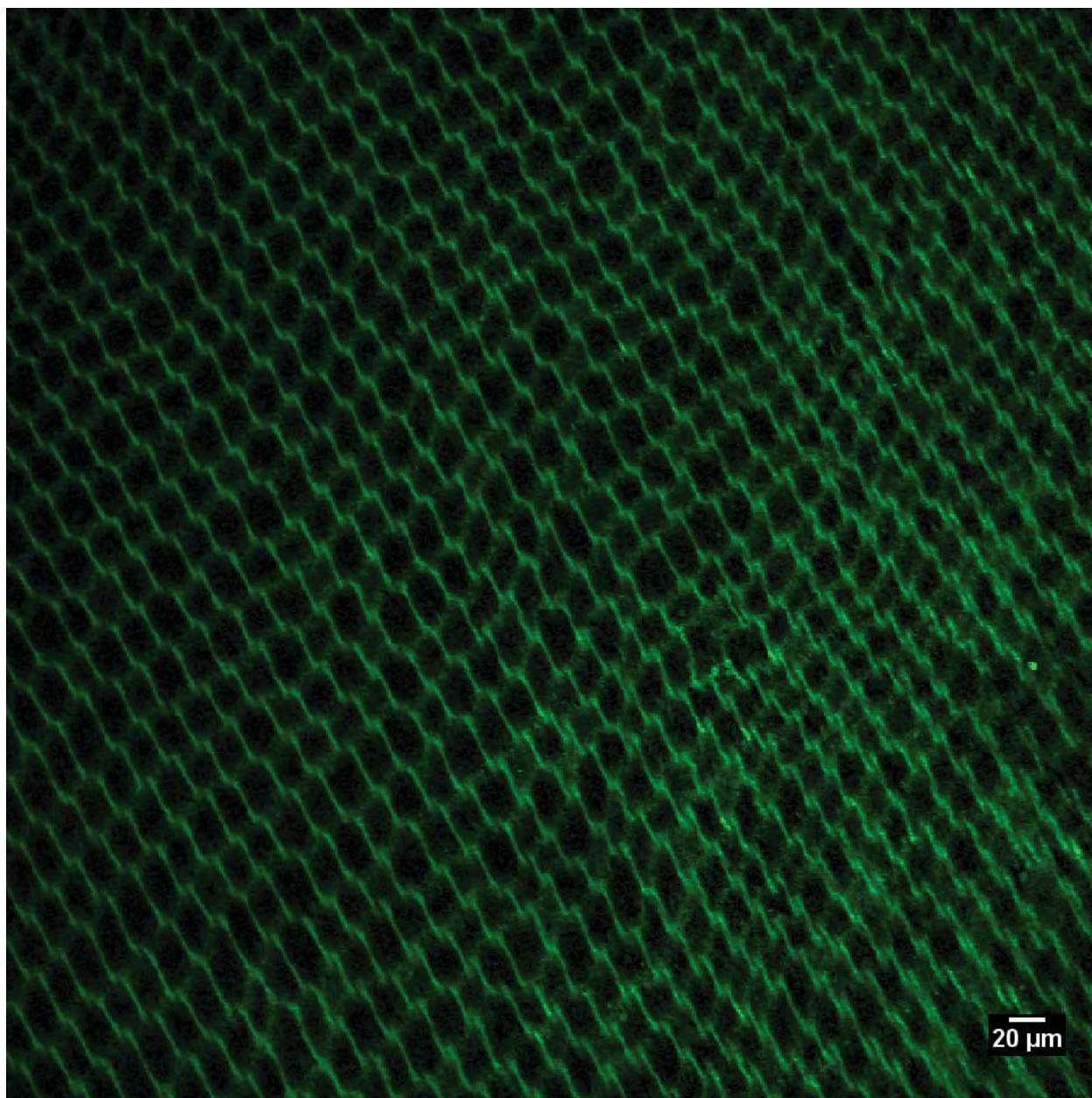


Figure 7.9: Confocal Image of Lens Fibers: Image was taken with the 40x(NA=1.30) objective in oil. The image is 512 x 512 pixels and has a size of 317.331 x 317.331  $\mu\text{m}$ . Lens fiber structure moving towards the middle of the section.





Figure 7.10: Confocal Image of Lens Fibers: Image was taken with the 40x(NA=1.30) objective in oil. The image is 512 x 512 pixels and has a size of 317.331 x 317.331  $\mu\text{m}$ . The structure of the lens fibers is harder to distinguish. This could be due to inadequate staining in the middle of the sample.



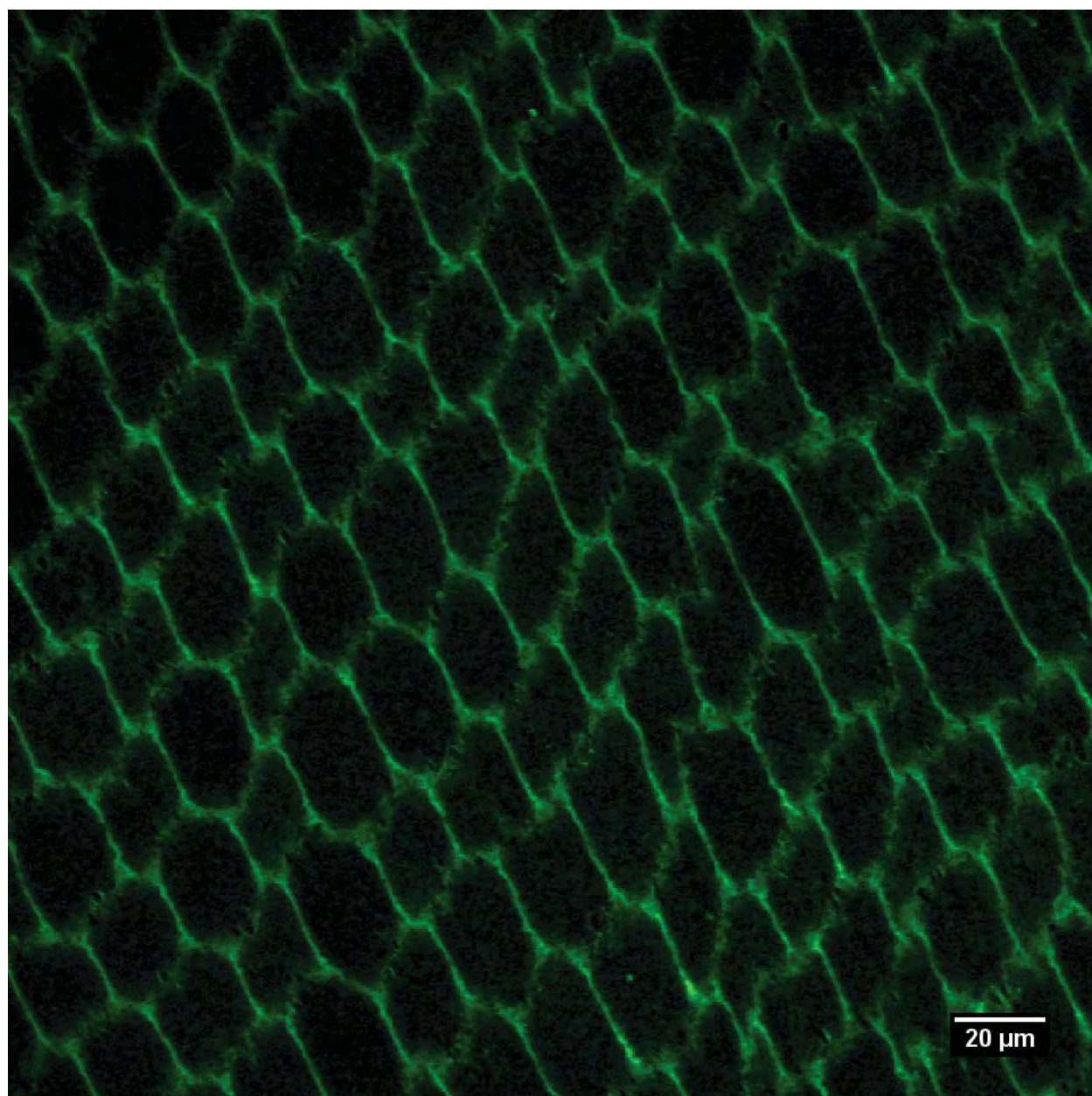


Figure 7.11: Confocal Image of Lens Fibers: Image was taken with the 100x(NA=1.40) objective in oil. The image is 512 x 512 pixels and has a size of 126.728 x 126.728  $\mu\text{m}$ . This image provides a detailed view of the lens fiber cells towards the middle of the section.

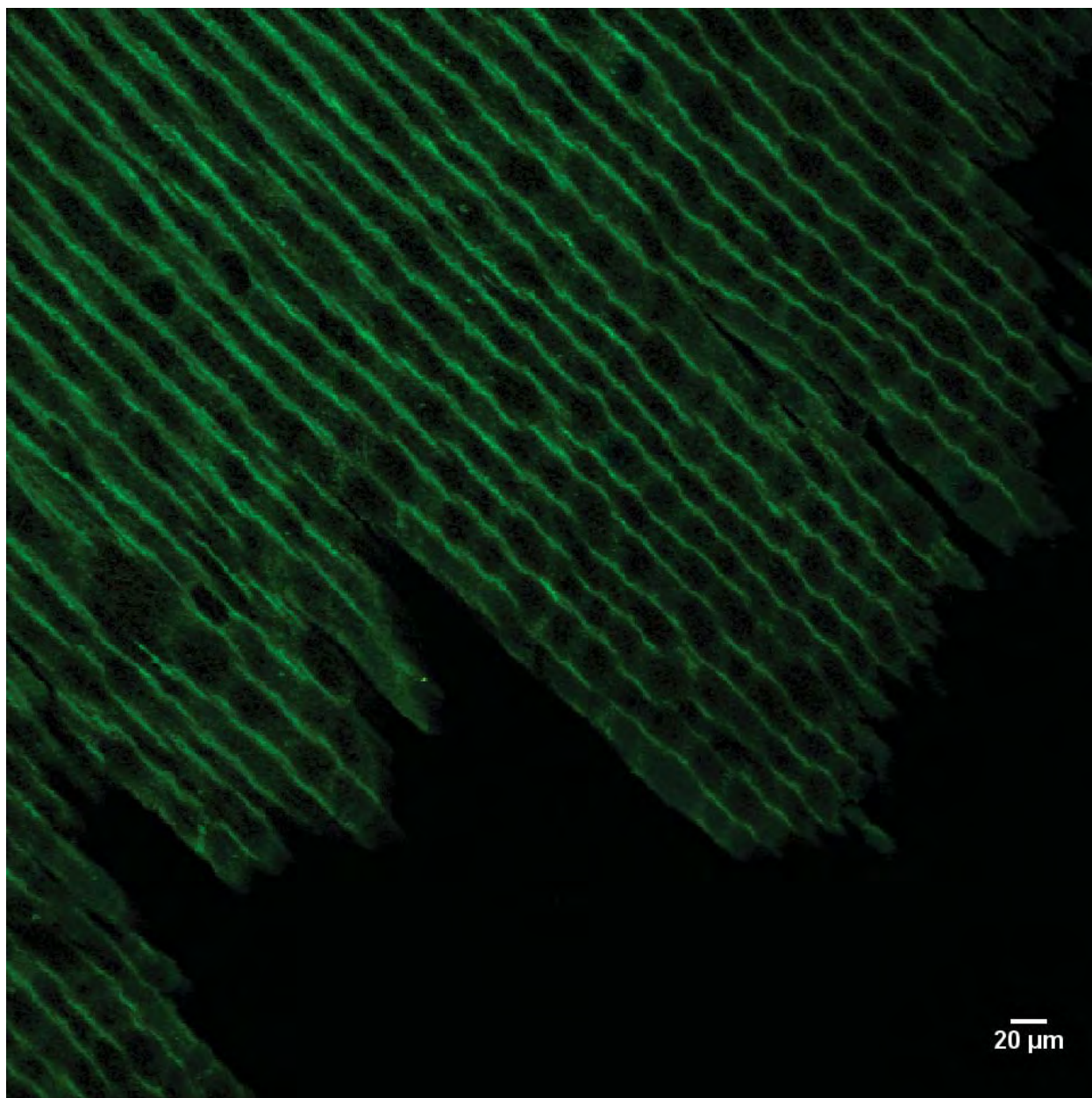


Figure 7.12: Confocal Image of Lens Fibers: Image was taken with the 40x(NA=1.30) objective in oil. The image is 512 x 512 pixels and has a size of 317.331 x 317.331  $\mu\text{m}$ . Image shows area where lens fibers were torn, near edge of sample.



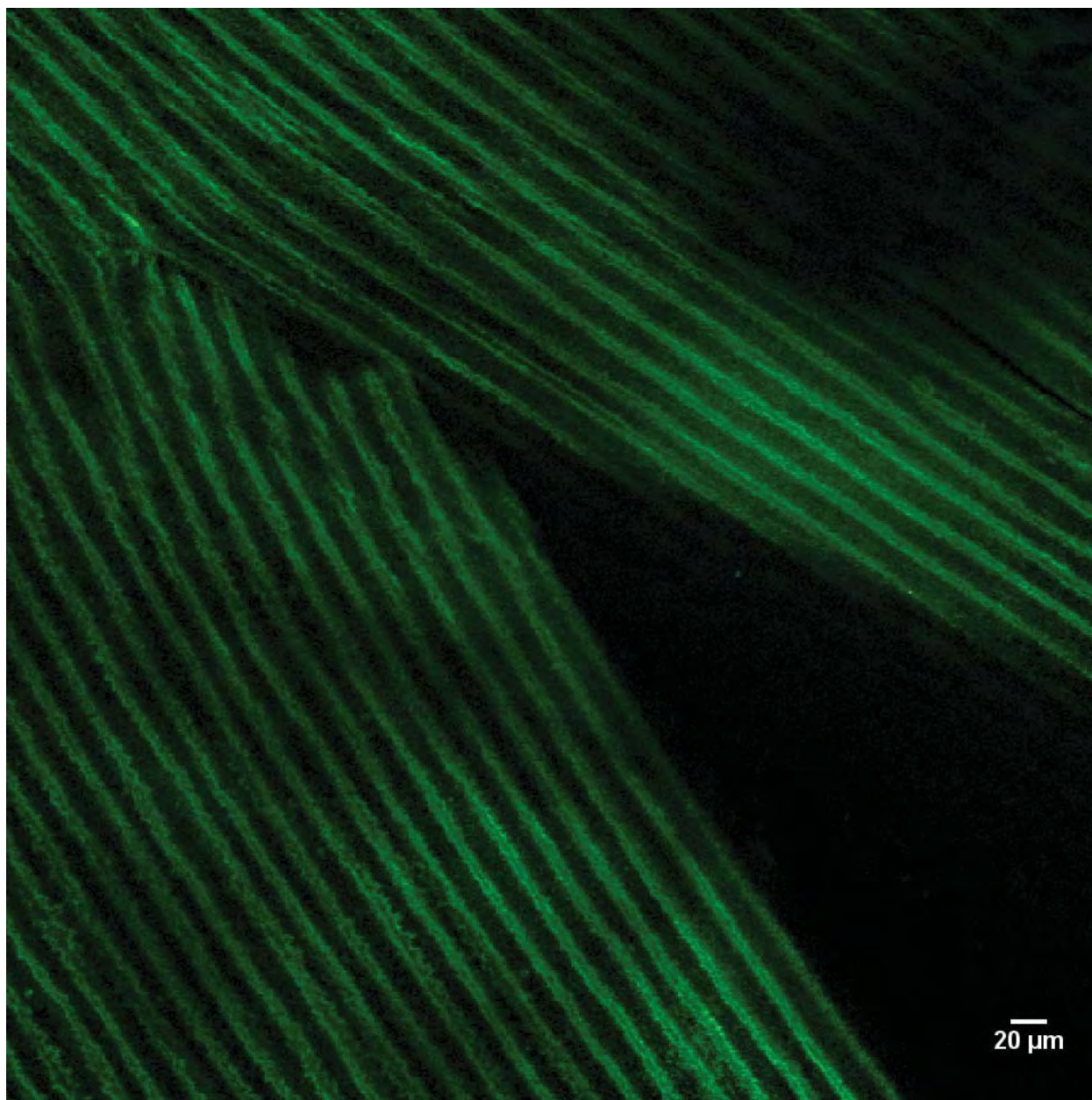


Figure 7.13: Confocal Image of Lens Fibers: Image was taken with the 40x(NA=1.30) objective in oil. The image is 512 x 512 pixels and has a size of 317.331 x 317.331  $\mu\text{m}$ . Potentially another tear in the sample, cleaner than in Figure 7.12.

## 7.5 Discussion

Looking at Figure 7.5, the structure of the lens fibers is easily observed. The lens fibers appear to be arranged in a fine honeycomb-like pattern, especially near the bottom of the tissue section. The waviness of the anterior surface of the section is believed to be caused by the sectioning process. The little definition of the honeycomb-like structure further from the edge of the sample could be from inadequate staining of the more interior lens fiber cells. It could also be from the angle of the lens fibers in relation to the plane of sectioning. If the fibers are more aligned with the plane of sectioning, they can appear as long channels, instead of hexagonal cross-sections. Figure 7.6 provides a better view of the structure near the anterior surface of the sample. In Figure 7.7 the honeycomb-like structure of the lens fiber cells appears rather regular in size and spacing, with exception of the cells near the anterior surface. Figure 7.8 shows the non-regular cells near the anterior surface. The different size of these cells could be a result of compression and deformation from the sectioning process. On the other hand, the size difference could be attributed to the formation of new fiber cells which occurs along the anterior lens capsule surface.

The area imaged by Figures 7.9, 7.10, and 7.11 were taken towards the middle of the section. The semi-regularity of the lens fiber structure can be seen in Figure 7.9 and the approximate diameter of  $20\text{ }\mu\text{m}$  can be seen in Figure 7.11. It appears there is little difference in the lens fibers from the more exterior regions to the more interior regions. It is important to note that these images are of sections from the cortex and do not include the nucleus of the lens fiber cells.

Figure 7.12 shows an area of the section that appears to be torn away. This is of significant interest with regard to understanding how the lens, and specifically lens fibers are damaged. Figure 7.13 is an image of a potential tear in the section. Again, this is of interest in studying lens trauma and injury.

A method has been developed to begin gathering geometrical data from the confocal images of the lens fiber cells for use in the generation of an ocular model. The structure is manually identified by selecting apparent intersections of the lens fibers (nodes) and the connectivity between the nodes

(see Figure 7.14). These coordinates and connectivity are then exported for use in the finite element modeling program Tahoe.

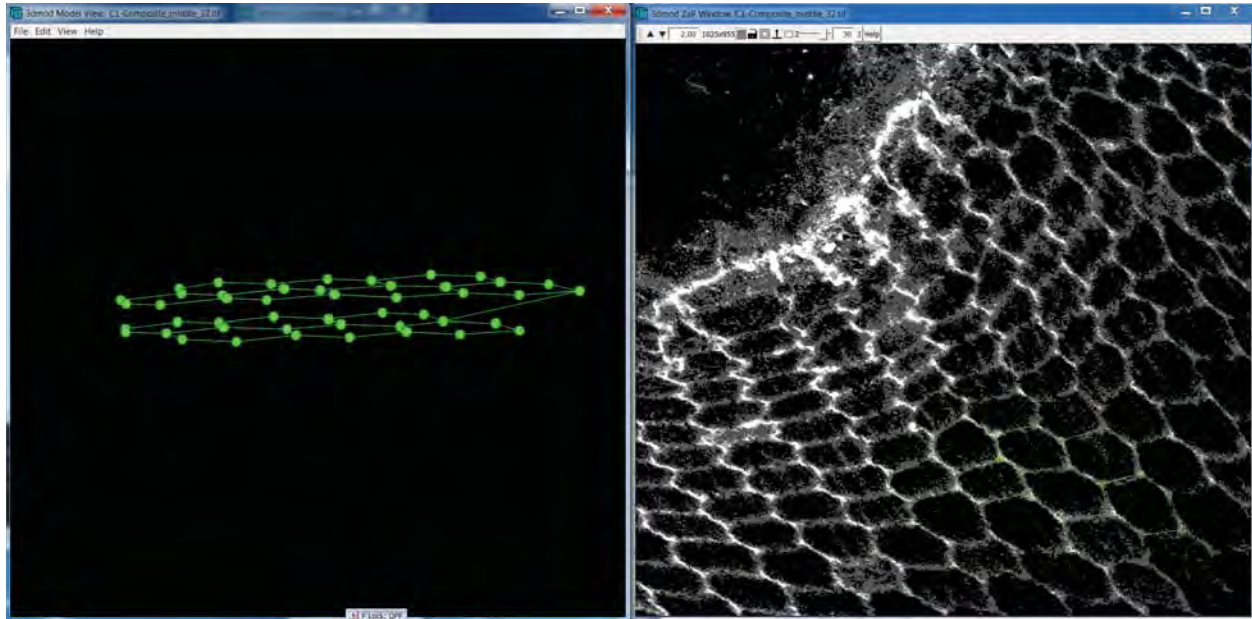


Figure 7.14: Modeling of Lens Fiber Ultrastructure using IMOD.

## Chapter 8

### Discussion

Progress has been made in regards to the determination of the material properties of the ocular lens. Our method for unconfined compression testing has produced good data. Preliminary fits have been completed for the preconditioned data. The calculated parameters show the older porcine lenses to be more viscous than the younger lenses that were tested. This complies with the theory that material properties of the lens change over time, possibly contributing to presbyopia. This change over time is supported by other research as well [Krag and Andreassen, 2003a]. We also noticed viscoelastic behavior in the whole porcine ocular lens. Additionally, data of lenses that did not undergo preconditioning has been generated to be fit and compare with the previous data. Preliminary models have been generated in Abaqus and Tahoe and will serve as a stepping stone to the creation of an ultrastructurally based computational finite element model. We also have developed a puncture testing method that has produced data that can be fitted from which to calculate material properties. A result of the testing is damaged tissue under controlled conditions that can be imaged and studied to investigate the mechanics of cutting, puncture, and IOFBs with regards to the lens. Our results support Yang's findings that the anterior lens capsule is stronger than the posterior lens capsule [Yang et al., 1998a]. A preliminary model of the puncture test has been developed in Abaqus as well. The nanoindentation of the anterior lens capsule in fluid is promising. The creep test data can be fit using Dakota and Tahoe, which will lead to the calculation of the material properties of the anterior lens capsule separate from the lens fiber cells. These calculations can then be used to verify the parameters from the compression and puncture

testing and allow back-calculation of the properties of the lens fibers. With additional testing, a strong data set can be developed, providing confidence in our material parameters for our model.

In terms of structure identification and geometrical data, the first steps have been made and with more work, we will have good data on which to base the model. The structure in the electron tomography images still remains to be confirmed. While they do look similar to the results produced by Barnard et al.'s imaging [Barnard et al., 1992], we want to be confident in our structure identification. A method has been developed to extract the coordinate data of the structure to include in our model. The confocal imaging has produced good images of the lens fiber structure. Our initial results show structure similar to that imaged by other work [Taylor et al., 1996]. A similar method for extracting the 3-dimensional coordinate data has been developed and the gathering of these data is currently in progress.

While more work remains to be done, much experimental progress has been made towards the generation of an ultrastructurally based computational finite element model. The work presented here is part of a larger project with the following research tasks: (1) the development of a model for type IV collagen mesh-work of lens capsule tissue; (2) the development of a multiscale model of the lens capsule in regards to its poromechanical characteristics; (3) the development of a multiscale lens fiber cell equivalent soft viscoelastic constitutive model of the internal lens substance; (4) unconfined compression testing of whole porcine lenses to estimate whole lens mechanical response; (5) nanoindentation testing on porcine lenses to approximate lens capsule parameters; and (6) imaging of lens fiber cell geometry using confocal laser scanning microscopy, and type IV collagen network ultrastructure in lens capsule using cryo-electron tomography. Significant work has been completed on tasks (4), (5), and (6) as well as limited preliminary modeling on tasks (1) and (2). The research described here contributes to the development of an ultrastructurally based computational finite element model that will contribute to the greater task of accurately modeling the lens to better understand accommodation, presbyopia, and ocular lens related injuries.



## **Chapter 9**

### **Recommendations**

#### **9.1 Determine Material Properties from Data**

While some parameter fitting has been completed, the data from the unconfined compression tests with no preconditioning and the puncture test data need to be fit as well. The same process used for the unconfined compression data with preconditioning can be used, with slight changes to the Tahoe setup. On top of fitting the other data, the constitutive framework should be adjusted and fine-tuned to better account for the lens's viscoelastic behavior, providing better fits and more accurate material properties or range of properties.

#### **9.2 Additional Imaging and Modeling**

More analysis needs to be done with the confocal images to provide more data on the structure of the lens fibers. This can be done with IMOD. Additional images of the lens should be taken to provide regional structure data throughout the lens. The lens fibers are already divided into 2 areas: the nucleus and the cortex. The structural differences of the two need to be found to include in a truly ultrastructurally based computational model.

With the ET images of the lens capsule, confirmation of whether what the images show are structure or artifact is needed. This can be accomplished through additional imaging and varying the freezing/preparation process, such as cryo-ET. Once the structure is identified, those images will need to be analyzed with IMOD to provide the structural data in a useful format to input into Tahoe. Again, the identification of the type-IV collagen mesh-work is important to accurately

model the lens capsule.

A large amount of work remains to be done in the modeling aspects of this research. Meshes of the lenses need to be generated with the information gathered from imaging. The sections of the model need to be decided on, such as anterior capsule, posterior capsule, lens fiber nucleus, and lens fiber cortex. The equations of the constitutive models for these different sections need to be adjusted and finalized. This can be done through further development of Tahoe, and is part of the current research.

### **9.3 Confocal Imaging of Deformed/Damaged Lenses**

It would be of interest to image a deformed lens, whether in compression or being indented (not to failure), potentially from one of the puncture tips. This could be done by utilizing the existing compression and puncture testing setups to deform the lens. Once deformed, the lens could be held in that state with the MTS Insight II, and fixed with the paraformaldehyde used in the confocal specimen preparation. Imaging the lens in a deformed state could lead to increased understanding of how the lens fibers interact as the lens accommodates. This imaging could also provide information on how lens fibers respond to trauma, either from blunt force contact or by blast wave loading (percussive waves generated by explosions that load the eye).

Punctured lenses should also be imaged, specifically around the puncture site and along any tears that occur. The damaged lens capsule could be imaged using a similar process as described in the EM/ET chapter. The damaged lens fibers could be imaged using the same process used to take confocal images of the normal lens fiber cells. Data from these images could lead to increased understanding of the interaction between the lens and intraocular foreign bodies (IOFBs), potentially resulting in improved treatment options for IOFB injuries.

### **9.4 Posterior Lens Capsule Testing**

Due to the differences between the anterior and posterior lens capsules, mainly thickness, curvature, and the lack of epithelial cells on the posterior lens capsule, the posterior lens capsule

needs to be tested as it's material properties may be different from those of the anterior lens capsule. This can be done through nanoindentation and ET. Nanoindentation can provide the material properties of the posterior lens capsule through creep testing similar to the testing done on the anterior lens capsule. This is important to include in the ultrastructurally based computational model to accurately predict the reactions of the lens.

## **9.5 Human Tissue Testing**

While tests can be calibrated on animal tissue, testing of human tissue is the ultimate goal. All tests and imaging processes should be repeated for human tissue in order to identify the structure and material properties of the human ocular lens. The processes and testing fixtures should not need to be modified, with the exception of the puncture well for anterior puncture tests due to the smaller size of the human lens when compared to the porcine lens. Additionally, the use of human data can provide insight into structure and material property differences between gender, something not provided with the porcine tissue. Also, with the range of age of human tissue, a better understanding of accommodation in different ages as well as presbyopia can be achieved.

## **9.6 Higher Strain Rate Testing**

In regards to the compression and puncture testing, higher strain testing should be performed. At higher loading rates, the lens may respond differently, resulting in different material properties. With the goal of being able to model blast wave loading on the eye, test data from high strain rate testing will ensure that the correct material properties are being used in the model. Currently a partnership is being formed with Dr. Tusit Weerasooriya at the Army Research Laboratory (ARL) in Aberdeen, Maryland, to utilize some of their high strain rate testing equipment. Intermediate strain rate (0.0125/s to 125/s) testing can be performed with their Bose Electroforce TestBench Instrument. Figure 9.1 shows a CAD drawing of a water bath and fixtures to allow for intermediate strain rate testing in fluid (Alcon BSS). To achieve high strain (greater than 125/s) testing, ARL has several split Hopkinson bar systems that could be utilized.

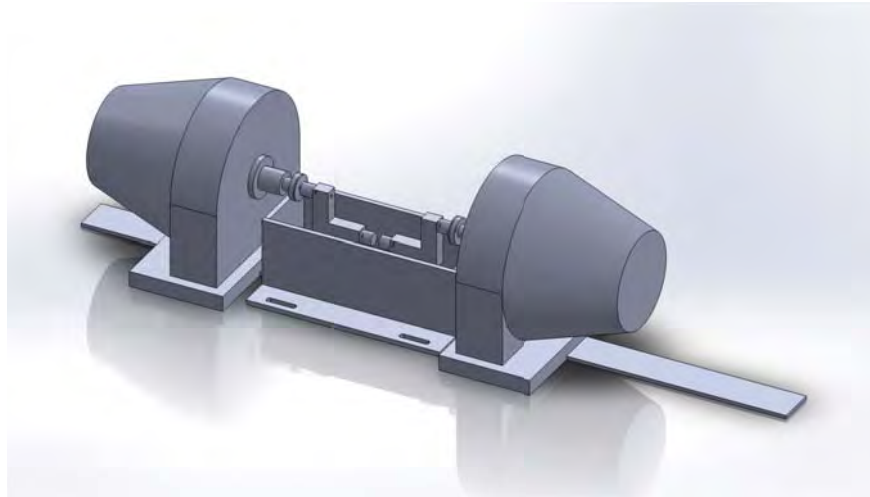


Figure 9.1: CAD Drawing of Environmental Bath and Test Fixtures Adapted to a Bose Electroforce TestBench System to Allow for Intermediate Strain Rate Testing in Fluid.

## 9.7 Determine Properties/Structure of Zonules/Ciliary Body

In order to create a model of the eye, the structure and material properties of all parts of the eye need to be known. To initially expand the model, parts of the eye that interact with the lens should be focussed on, specifically the suspensory zonules and the ciliary body. Testing opportunities for the zonules include using a lens stretcher clamped at the edges of the ciliary body, near the attachment of the zonules. The force would be recorded as the lens was stretched. With the force response of the lens/zonule assembly, the properties of the zonules could be back-calculated using the data from the whole lens tests performed (compression and puncture). Additionally, a fixture could be made to clamp and hold the ciliary body, suspending the lens in free air. The lens would then be displaced by a flat platen connected to a load cell measuring the force response, similar to the unconfined compressing testing procedure. A back-calculation of the properties of the zonules would again be necessary. A similar approach could possibly be used for the ciliary body, making sure to clamp at the exterior edge of the ciliary body. As for structure identification of the zonules and ciliary body, imaging processes would need to be investigated. With the material properties and structure of the zonules and ciliary body, the model could be coupled with other models and data on the other parts of the eye to further progress towards a complete computational model of the eye.

## Chapter 10

### Conclusion

There is much motivation to better understand the biomechanics of the ocular lens. The process of accommodation (the lens adjusting in optical power to focus an image) and presbyopia (the loss of accommodation over time) are not well understood. While the lens is an important part of the visual system, there has not been much focus until recently on the mechanics of accommodation and the mechanical characteristics of the ocular lens. This is mainly due to the possibility of the restoration of accommodation through surgical treatment (intraocular lens replacement surgery) and the improvement of cataract surgery. Through an increased understanding of the mechanics of the lens, IOLs and cataract surgery can be improved. Additionally, with recent military tours, an increase in ocular injuries has been recorded. This is largely due to the widespread use of improvised explosive devices (IEDs) and improved survival rates [Mader et al., 1993, Mader et al., 2006]. Management of ocular injuries in both soldiers and civilians as well as improved surgical treatments of the eye can be achieved with the development of an ultrastructurally based computational finite element model of the ocular lens.

In order to create such a model, the material properties and the ultrastructure of the components of the lens must be determined. While previous work has been done to understand the lens, more is needed for a consensus to be had. The work described above entailed mechanical testing as well as structure identification of the ocular lens with regard to the development of an accurate model. Data were analyzed from previous unconfined compression tests, producing material parameters by fitting the previous data curves. Additional data was generated through unconfined

compression tests without preconditioning, to provide more fitting data and the opportunity to compare the effects of preconditioning to those of lenses tested with none. Alongside compression testing, a puncture testing method was developed and data produced that can also be fit and allow the investigation of lens failure and the interaction between the ocular lens and intraocular foreign bodies (IOFBs). Both of these mechanical tests have provided data that will result in the determination of material properties of the whole porcine ocular lens. Nanoindentation was performed on the anterior porcine lens capsule to isolate the properties of the lens capsule. With said properties, the mechanical properties of the interior lens fibers can be back-calculated for the whole lens testing data.

The identification of the ultrastructure of the lens was also pursued. The type-IV collagen mesh-work that comprises the support structure of the lens capsule was imaged using electron tomography. More imaging is needed to confirm the observed structure, but a preliminary method (in need of some refining) has been developed to extract the geometrical data from the 3-dimensional reconstruction of the lens capsule samples. Confocal LASER scanning microscopy was employed to image the ultrastructure of the lens fiber cells. This was successful and many images of the fiber cell structure were obtained. A similar method has been developed to extract the geometrical data and that work is currently being completed.

This thesis is a presentation of results that are part of a larger research goal, that goal being the generation of an ultrastructurally based computational finite element model of the ocular lens. The results from this research are great progress towards that goal and will hopefully have lasting effects for soldiers, civilians, and anyone with visual impairment or injury involving the ocular lens.

## Bibliography

- [Abolmaali et al., 2007] Abolmaali, A., Schachar, R., and Le, T. (2007). Sensitivity study of human crystalline lens accommodation. Computer Methods and Programs in Biomedicine, 85(1):77–90.
- [Aggarwal et al., 2012] Aggarwal, P., Garg, P., Sidhu, H., and Mehta, S. (2012). Post-traumatic endophthalmitis with retained intraocular foreign body – a case report with review of literature. Nepalese Journal of Ophthalmology, 4(1).
- [Al-Amoudi et al., 2005a] Al-Amoudi, A., Dubochet, J., and Norl, L. (2005a). Nanostructure of the epidermal extracellular space as observed by Cryo-Electron microscopy of vitreous sections of human skin. Journal of Investigative Dermatology, 124(4):764–777.
- [Al-Amoudi et al., 2004] Al-Amoudi, A., Norlen, L. P., and Dubochet, J. (2004). Cryo-electron microscopy of vitreous sections of native biological cells and tissues. Journal of Structural Biology, 148(1):131 – 135.
- [Al-Amoudi et al., 2005b] Al-Amoudi, A., Studer, D., and Dubochet, J. (2005b). Cutting artefacts and cutting process in vitreous sections for cryo-electron microscopy. Journal of Structural Biology, 150(1):109 – 121.
- [Bailey et al., 1993] Bailey, A., Sims, T., Avery, N., and Miles, C. (1993). Chemistry of collagen cross-links: glucose-mediated covalent cross-linking of type-IV collagen in lens capsules. The Biochemical Journal, 296(2):489–496.
- [Bantseev and Sivak, 2005] Bantseev, V. and Sivak, J. G. (2005). Confocal laser scanning microscopy imaging of dynamic TMRE movement in the mitochondria of epithelial and superficial cortical fiber cells of bovine lenses. Molecular Vision, 11(December 2004):518–523.
- [Barnard et al., 1992] Barnard, K., Burgess, S., Carter, D., and Woolley, D. (1992). Three-dimensional structure of type IV collagen in the mammalian lens capsule. Journal of Structural Biology, 108(1):6–13.
- [Beers and van der Heijde, 1996] Beers, A. P. and van der Heijde, G. L. (1996). Age-related changes in the accommodation mechanism. Optometry and Vision Science: Official Publication of the American Academy of Optometry, 73(4):235–242. PMID: 8728490.
- [Bond et al., 1996] Bond, J., Green, C., Donaldson, P., and Kistler, J. (1996). Liquefaction of cortical tissue in diabetic and galactosemic rat lenses defined by confocal laser scanning microscopy. Investigative Ophthalmology & Visual Science, 37(8):1557–65.



- [Breitenfeld et al., 2005] Breitenfeld, P., Ripken, T., and Lubatschowski, H. (2005). Finite element method-simulation of the human lens during accommodation. In Bergh, H. v. d. and Vogel, A., editors, Therapeutic Laser Applications and Laser-Tissue Interactions II, volume 5863, page 586302. SPIE.
- [Burd, 2009] Burd, H. (2009). A structural constitutive model for the human lens capsule. Biomechanics and Modeling in Mechanobiology, 8(3):217–231. 10.1007/s10237-008-0130-5.
- [Burd et al., 2002] Burd, H., Judge, S., and Cross, J. (2002). Numerical modelling of the accommodating lens. Vision Research, 42(18):2235 – 2251.
- [Burd et al., 1999] Burd, H. J., Judge, S. J., and Flavell, M. J. (1999). Mechanics of accommodation of the human eye. Vision Research, 39(9):1591 – 1595.
- [Chen et al., 2007] Chen, X., Dunn, A. C., Sawyer, W. G., and Sarntinoranont, M. (2007). A biphasic model for Micro-Indentation of a Hydrogel-Based contact lens. Journal of Biomechanical Engineering, 129(2):156–163.
- [Chien et al., 2006] Chien, C. M., Huang, T., and Schachar, R. A. (2006). Analysis of human crystalline lens accommodation. Journal of Biomechanics, 39(4):672 – 680.
- [Colyer et al., 2008] Colyer, M. H., Chun, D. W., Bower, K. S., Dick, J. S. B., and Weichel, E. D. (2008). Perforating globe injuries during operation iraqi freedom. Ophthalmology, 115(11):2087–2093. PMID: 18672293.
- [David et al., 2007] David, G., Pedrigi, R. M., Heistand, M. R., and Humphrey, J. D. (2007). Regional multiaxial mechanical properties of the porcine anterior lens capsule. Journal of Biomechanical Engineering, 129(1):97–104.
- [Dhawahir-Scala and Kamal, 2005] Dhawahir-Scala, F. E. and Kamal, A. (2005). Intralenticular foreign body: a D-Day reminder. Clinical & Experimental Ophthalmology, 33(6):659–660.
- [Erpelding et al., 2005] Erpelding, T., Hollman, K., and O'Donnell, M. (2005). Spatially mapping the elastic properties of the lens using bubble-based acoustic radiation force. In Ultrasonics Symposium, 2005 IEEE, volume 1, page 613 – 616.
- [Fineman et al., 2000] Fineman, M. S., Fischer, D. H., Jeffers, J. B., Buerger, D. G., and Repke, C. (2000). Changing trends in paintball sport-related ocular injuries. Archives of Ophthalmology, 118(1):60–64. PMID: 10636415.
- [Fung, 1993] Fung, Y. (1993). Biomechanics: Mechanical Properties of Living Tissues. Springer.
- [Glasser and Campbell, 1998] Glasser, A. and Campbell, M. C. (1998). Presbyopia and the optical changes in the human crystalline lens with age. Vision Research, 38(2):209 – 229.
- [Glasser and Campbell, 1999] Glasser, A. and Campbell, M. C. (1999). Biometric, optical and physical changes in the isolated human crystalline lens with age in relation to presbyopia. Vision Research, 39(11):1991–2015.
- [Heistand et al., 2005] Heistand, M., Pedrigi, R., Delange, S., Dziezyc, J., and Humphrey, J. (2005). Multiaxial mechanical behavior of the porcine anterior lens capsule. Biomechanics and Modeling in Mechanobiology, 4(2):168–177. 10.1007/s10237-005-0073-z.

- [Helmholz, 1855] Helmholz, H. (1855). U. ber die accommodationes des auges. Arch. fur Ophthalmol., 1:1–74.
- [Hermans et al., 2006] Hermans, E., Dubbelman, M., Heijde, G. v. d., and Heethaar, R. (2006). Estimating the external force acting on the human eye lens during accommodation by finite element modelling. Vision Research, 46(21):3642 – 3650.
- [Heys et al., 2004a] Heys, K. R., Cram, S. L., and Truscott, R. J. W. (2004a). Massive increase in the stiffness of the human lens nucleus with age: the basis for presbyopia? Molecular Vision, 10:956–963. PMID: 15616482.
- [Heys et al., 2004b] Heys, K. R., Cram, S. L., and Truscott, R. J. W. (2004b). Massive increase in the stiffness of the human lens nucleus with age: the basis for presbyopia? Molecular Vision, 10:956–963. PMID: 15616482.
- [Hsieh et al., 2006] Hsieh, C., Leith, A., Mannella, C. A., Frank, J., and Marko, M. (2006). Towards high-resolution three-dimensional imaging of native mammalian tissue: Electron tomography of frozen-hydrated rat liver sections. Journal of Structural Biology, 153(1):1–13.
- [Hsieh et al., 2002] Hsieh, C., Marko, M., Frank, J., and Mannella, C. A. (2002). Electron tomographic analysis of frozen-hydrated tissue sections. Journal of Structural Biology, 138(1–2):63 – 73.
- [Jain et al., 2004] Jain, S. S., Rao, P., Nayak, P., and Kothari, K. (2004). Posterior capsular dehiscence following blunt injury causing delayed onset lens particle glaucoma. Indian Journal of Ophthalmology, 52(4):325–327. PMID: 15693327.
- [Kaufman and Alm, 2003] Kaufman, P. L. and Alm, A. (2003). Adler’s Physiology of the Eye. Mosby, St. Louis, MO, tenth edition edition.
- [Kessel and Kardon, 1979] Kessel, R. G. and Kardon, R. H. (1979). Tissues and Organs: a text-atlas of scanning electron microscopy. W.H. Freenman and Co., San Francisco, CA, first edition edition.
- [Kim et al., 2009] Kim, T. H., Kim, S. J., Kim, E., Chung, I. Y., Park, J. M., Yoo, J. M., Song, J. K., and Seo, S. W. (2009). Spontaneous anterior lens capsular dehiscence causing lens particle glaucoma. Yonsei Medical Journal, 50(3):452–454. PMID: 19568612 PMCID: PMC2703773.
- [Krag and Andreassen, 1996] Krag, S. and Andreassen, T. T. (1996). Biomechanical measurements of the porcine lens capsule. Experimental Eye Research, 62(3):253 – 260.
- [Krag and Andreassen, 2003a] Krag, S. and Andreassen, T. T. (2003a). Mechanical properties of the human lens capsule. Progress in Retinal and Eye Research, 22(6):749 – 767.
- [Krag and Andreassen, 2003b] Krag, S. and Andreassen, T. T. (2003b). Mechanical properties of the human posterior lens capsule. Investigative Ophthalmology & Visual Science, 44(2):691–696.
- [Krag et al., 1997] Krag, S., Olsen, T., and Andreassen, T. T. (1997). Biomechanical characteristics of the human anterior lens capsule in relation to age. Investigative Ophthalmology & Visual Science, 38(2):357–63.

- [Kremer et al., 1996] Kremer, J. R., Mastronarde, D. N., and McIntosh, J. R. (1996). Computer visualization of three-dimensional image data using IMOD. Journal of Structural Biology, 116(1):71–76. PMID: 8742726.
- [Kumar et al., 2005] Kumar, A., Kumar, V., and Dapling, R. B. (2005). Traumatic cataract and intralenticular foreign body. Clinical & Experimental Ophthalmology, 33(6):660–661.
- [Lam et al., 1998] Lam, D. S. C., Tham, C. C. Y., Kwok, A. K. H., and Gopal, L. (1998). Combined phacoemulsification, pars plana vitrectomy, removal of intraocular foreign body (IOFB), and primary intraocular lens implantation for patients with IOFB and traumatic cataract. Eye, 12:395–398.
- [Lee and Song, 2001] Lee, S. I. and Song, H. C. (2001). A case of isolated posterior capsule rupture and traumatic cataract caused by blunt ocular trauma. Korean Journal of Ophthalmology: KJO, 15(2):140–144. PMID: 11811583.
- [Liu et al., 2006] Liu, Z., Wang, B., Xu, X., and Wang, C. (2006). A study for accommodating the human crystalline lens by finite element simulation. Computerized Medical Imaging and Graphics, 30(6–7):371 – 376.
- [Ljubimova et al., 2008] Ljubimova, D., Eriksson, A., and Bauer, S. (2008). Aspects of eye accommodation evaluated by finite elements. Biomechanics and Modeling in Mechanobiology, 7(2):139–150. 10.1007/s10237-007-0081-2.
- [Mader et al., 1993] Mader, T. H., Aragonés, J. V., Chandler, A. C., Hazlehurst, J. A., Heier, J., Kingham, J. D., and Stein, E. (1993). Ocular and ocular adnexal injuries treated by united states military ophthalmologists during operations desert shield and desert storm. Ophthalmology, 100(10):1462–1467.
- [Mader et al., 2006] Mader, T. H., Carroll, R. D., Slade, C. S., George, R. K., Ritchey, J. P., and Neville, S. P. (2006). Ocular war injuries of the iraqi insurgency, January–September 2004. Ophthalmology, 113(1):97–104.
- [Martin et al., 2005] Martin, H., Guthoff, R., Terwee, T., and Schmitz, K. (2005). Comparison of the accommodation theories of coleman and of helmholtz by finite element simulations. Vision Research, 45(22):2910 – 2915.
- [Massig et al., 1994] Massig, J. H., Preissler, M., Wegener, A. R., and Gaida, G. (1994). Real-time confocal laser scan microscope for examination and diagnosis of the eye in vivo. Applied Optics, 33(4):690–694.
- [Masters, 1998] Masters, B. (1998). Three-dimensional microscopic tomographic imagings of the cataract in a human lens in vivo. Optics Express, 3(9):332–338.
- [Masters and Bohnke, 2002] Masters, B. R. and Bohnke, M. (2002). Three-dimensional confocal microscopy of the living human eye. Annual Review of Biomedical Engineering, 4:69–91. PMID: 12117751.
- [McCauley et al., 2008] McCauley, M. B., Anderson, D. M., and Johnson, A. J. (2008). Posterior chamber visian implantable collamer lens: stability and evaluation following traumatic grenade explosion. Journal of Refractive Surgery (Thorofare, N.J.: 1995), 24(6):648–651. PMID: 18581794.

- [McLeod et al., 2003] McLeod, S. D., Portney, V., and Ting, A. (2003). A dual optic accommodating foldable intraocular lens. British Journal of Ophthalmology, 87(9):1083–1085.
- [Muzaffar et al., 2000] Muzaffar, W., Khan, M. D., Akbar, M. K., Khan, M. D., Malik, A. M., and Durrani, O. M. (2000). Mine blast injuries: ocular and social aspects. British Journal of Ophthalmology, 84(6):626–630.
- [Nguyen et al., 2002] Nguyen, Q. D., Kruger, E. F., Kim, A. J., Lashkari, M. H., and Lashkari, K. (2002). Combat eye trauma: intraocular foreign body injuries during the Iran-Iraq war (1980–1988). International Ophthalmology Clinics, 42(3):167–177. PMID: 12131593.
- [O'Connor et al., 2008] O'Connor, M. D., Wederell, E. D., Iongh, R. d., Lovicu, F. J., and McAvoy, J. W. (2008). Generation of transparency and cellular organization in lens explants. Experimental Eye Research, 86(5):734 – 745.
- [Parver et al., 1993] Parver, L. M., Dannenberg, A. L., Blacklow, B., Fowler, C. J., Brechner, R. J., and Tielsch, J. M. (1993). Characteristics and causes of penetrating eye injuries reported to the national eye trauma system registry, 1985-91. Public Health Reports, 108(5):625–632. PMID: 8210260 PMCID: 1403438.
- [Pau and Kranz, 1991] Pau, H. and Kranz, J. (1991). The increasing sclerosis of the human lens with age and its relevance to accommodation and presbyopia. Graefe's Archive for Clinical and Experimental Ophthalmology, 229(3):294–296. PMID: 1869070.
- [Pedrigi et al., 2007] Pedrigi, R., David, G., Dziezyc, J., and Humphrey, J. (2007). Regional mechanical properties and stress analysis of the human anterior lens capsule. Vision Research, 47(13):1781 – 1789.
- [Pedrigi and Humphrey, 2011] Pedrigi, R. and Humphrey, J. (2011). Computational model of evolving lens capsule biomechanics following Cataract-Like surgery. Annals of Biomedical Engineering, 39(1):537–548. 10.1007/s10439-010-0133-0.
- [Powell et al., 2010] Powell, T. A., Amini, R., Oltean, A., Barnett, V. A., Dorfman, K. D., Segal, Y., and Barocas, V. H. (2010). Elasticity of the porcine lens capsule as measured by osmotic swelling. Journal of Biomechanical Engineering, 132(9):091008.
- [Ravi et al., 2006] Ravi, N., Wan, K., Swindle, K., Hamilton, P., and Duan, G. (2006). Development of techniques to compare mechanical properties of reversible hydrogels with spherical, square columnar and ocular lens geometry. Polymer, 47(11):4203 – 4209.
- [Reese and Govindjee, 1998] Reese, S. and Govindjee, S. (1998). A theory of finite viscoelasticity and numerical aspects. International Journal of Solids and Structures, 35(26–27):3455–3482.
- [Reilly and Ravi, 2009] Reilly, M. and Ravi, N. (2009). Microindentation of the young porcine ocular lens. Journal of Biomechanical Engineering, 131(4):044502.
- [Reilly et al., 2009] Reilly, M. A., Hamilton, P. D., Perry, G., and Ravi, N. (2009). Comparison of the behavior of natural and refilled porcine lenses in a robotic lens stretcher. Experimental Eye Research, 88(3):483 – 494.
- [Reilly et al., 2008] Reilly, M. A., Hamilton, P. D., and Ravi, N. (2008). Dynamic multi-arm radial lens stretcher: A robotic analog of the ciliary body. Experimental Eye Research, 86(1):157 – 164.

- [Richdale et al., 2008] Richdale, K., Bullimore, M. A., and Zadnik, K. (2008). Lens thickness with age and accommodation by optical coherence tomography. Ophthalmic & physiological optics : the journal of the British College of Ophthalmic Opticians (Optometrists), 28(5):441–447. PMID: 18761481 PMCID: PMC2857534.
- [Rofagha et al., 2008] Rofagha, S., Day, S., Winn, B. J., Ou, J. I., Bhisitkul, R. B., and Chiu, C. S. (2008). Spontaneous resolution of a traumatic cataract caused by an intralenticular foreign body. Journal of Cataract & Refractive Surgery, 34(6):1033–1035.
- [Shestopalov and Bassnett, 2000] Shestopalov, V. I. and Bassnett, S. (2000). Three-Dimensional organization of primary lens fiber cells. Investigative Ophthalmology & Visual Science, 41(3):859–863.
- [Stachs et al., 2005] Stachs, O., Martin, H., Behrend, D., Schmitz, K., and Guthoff, R. (2005). Three-dimensional ultrasound biomicroscopy, environmental and conventional scanning electron microscopy investigations of the human zonula ciliaris for numerical modelling of accommodation. Graefe’s Archive for Clinical and Experimental Ophthalmology, 244(7):836–844.
- [Stachs et al., 2007] Stachs, O., Zhivov, A., Kraak, R., Stave, J., and Guthoff, R. (2007). In vivo three-dimensional confocal laser scanning microscopy of the epithelial nerve structure in the human cornea. Graefe’s Archive for Clinical and Experimental Ophthalmology, 245(4):569–575. 10.1007/s00417-006-0387-2.
- [Strenk et al., 2004] Strenk, S. A., Strenk, L. M., Semmlow, J. L., and DeMarco, J. K. (2004). Magnetic resonance imaging study of the effects of age and accommodation on the human lens Cross-Sectional area. Investigative Ophthalmology & Visual Science, 45(2):539–545.
- [Szijarto et al., 2007] Szijarto, Z., Gaal, V., Kovacs, B., and Kuhn, F. (2007). Prognosis of penetrating eye injuries with posterior segment intraocular foreign body. Graefe’s Archive for Clinical and Experimental Ophthalmology, 246(1):161–165.
- [Taylor et al., 1996] Taylor, V. L., al-Ghoul, K. J., Lane, C. W., Davis, V. A., Kuszak, J. R., and Costello, M. J. (1996). Morphology of the normal human lens. Investigative Ophthalmology & Visual Science, 37(7):1396–1410.
- [Thim et al., 1993] Thim, K., Krag, S., and Corydon, L. (1993). Hydroexpression and viscoexpression of the nucleus through a continuous circular capsulorhexis. Journal of Cataract and Refractive Surgery, 19(2):209–212. PMID: 8487162.
- [WALTER, 1962] WALTER, W. L. (1962). Intralenticular foreign body as a cause of traumatic cataract. American Journal of Ophthalmology, 54:856–858. PMID: 13998693.
- [Weeber et al., 2005] Weeber, H. A., Eckert, G., Soergel, F., Meyer, C. H., Pechhold, W., and Van Der Heijde, R. G. L. (2005). Dynamic mechanical properties of human lenses. Experimental Eye Research, 80(3):425–434.
- [Weeber and Van Der Heijde, 2008] Weeber, H. A. and Van Der Heijde, R. G. L. (2008). Internal deformation of the human crystalline lens during accommodation. Acta Ophthalmologica, 86(6):642–647.
- [Weichel and Colyer, 2008] Weichel, E. D. and Colyer, M. H. (2008). Combat ocular trauma and systemic injury. Current Opinion in Ophthalmology, 19(6):519–525.

- [Weichel et al., 2008] Weichel, E. D., Colyer, M. H., Ludlow, S. E., Bower, K. S., and Eiseman, A. S. (2008). Combat ocular trauma visual outcomes during operations iraqi and enduring freedom. Ophthalmology, 115(12):2235–2245. PMID: 19041478.
- [Wong et al., 1997] Wong, T. Y., Seet, M. B., and Ang, C. (1997). Eye injuries in twentieth century warfare: A historical perspective. Survey of Ophthalmology, 41(6):433–459.
- [Yang et al., 1998a] Yang, X., Zou, L., Binrong, M., Dong, D., Dai, H., and Lu, X. (1998a). Tensile strength of lens capsules in eye-bank eyes. Journal of Cataract and Refractive Surgery, 24(4):543–546. PMID: 9584253.
- [Yang et al., 1998b] Yang, X., Zou, L., Binrong, M., Dong, D., Dai, H., and Lu, X. (1998b). Tensile strength of lens capsules in eye-bank eyes. Journal of Cataract and Refractive Surgery, 24(4):543–546. PMID: 9584253.
- [Ziebarth et al., 2011] Ziebarth, N. M., Arrieta, E., Feuer, W. J., Moy, V. T., Manns, F., and Parel, J. (2011). Primate lens capsule elasticity assessed using atomic force microscopy. Experimental Eye Research, 92(6):490–494.
- [Ziebarth et al., 2008] Ziebarth, N. M., Borja, D., Arrieta, E., Aly, M., Manns, F., Dortonne, I., Nankivil, D., Jain, R., and Parel, J. (2008). Role of the lens capsule on the mechanical accommodative response in a lens stretcher. Investigative Ophthalmology & Visual Science, 49(10):4490–4496.
- [Ziebarth et al., 2010] Ziebarth, N. M., Rico, F., and Moy, V. T. (2010). Structural and mechanical mechanisms of ocular tissues probed by AFM. In Bhushan, B., editor, Scanning Probe Microscopy in Nanoscience and Nanotechnology, page 363–393. Springer Berlin Heidelberg, Berlin, Heidelberg.